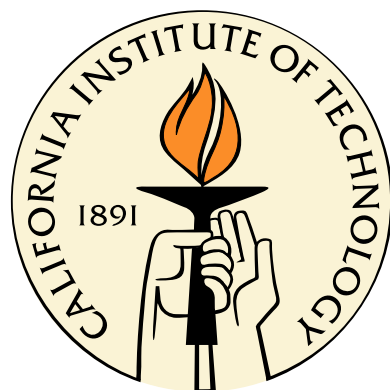


The Physics of Superconducting Microwave Resonators

Thesis by
Jiansong Gao

In Partial Fulfillment of the Requirements
for the Degree of
Doctor of Philosophy



California Institute of Technology
Pasadena, California

2008
(Defended May 28, 2008)

© 2008
Jiansong Gao
All Rights Reserved

This thesis is dedicated to my dearest wife, Yingyan, who has been a constant source of inspiration and support through all stages of my life since high school, and to our lovely boy, Logan, who came to our family just before the thesis was finished.

Acknowledgments

First, I would like to thank my advisor Professor Jonas Zmuidzinas for giving me the opportunity to work on this great project of MKID. I came to Caltech in 2002 and originally planned to work in the field of optics. Failing to join any optics group on campus, I luckily ran across Jonas in a talk on MKID he gave to the students in applied physics major. These detectors made of resonators immediately attracted my interest. I still remember the interview that took place at Jonas' office. Desperate to join a research group, I was advertising how good I was in both theory and experiment. At some point I mentioned that I had taken a mathematical course on stochastic process, which had caught Jonas' attention. He immediately gave me a quiz, asking me to state the Weiner-Kinchin theorem. Fortunately, I was able to give the correct answer promptly. He was very satisfied and said, "Let me show you the lab."

That was how I joined the MKID group and also where my journey of noise study started. It turns out that in the past five years, there wasn't a single day in which I wasn't dealing with the noise spectrum, stochastic process or the Weiner-Kinchin theorem. And of course, I enjoyed it very much. Noise in superconducting microwave resonators is a problem that has never been studied before. It is challenging but equally fascinating. Jonas has given me enough freedom in tackling the problem, as well as critical advice in times I could not find my way out. Every discussion with him boosted my knowledge, deepened my understanding and led to small or big progress in my research.

I also enjoy and benefit a lot from the collaboration with a group of great people. The cryostat and the measurement setup are all taken care of by Dr. Ben Mazin. This has saved me a huge amount of time on the hardware which I'm not good at. Also, as the first student on MKID project, his thesis is the starting point of my work and in some sense I am harvesting the fruits of his previous hard work. Thanks to the fact that an international student has no easy access to JPL. So I don't have to worry about the fabrication at all – Dr. Rick LeDuc at the microdevice lab in JPL will always turn my drawings into the best made devices. Some other devices are supplied by Miguel Daal, my collaborator and also my best friend from UC Berkeley. His devices appear to be more noisy than Rick's devices, which may be a bad thing for a detector but not bad for me, who study noise on purpose, at all. It turns out his devices has led to some of the most important progress. We also spent a lot of afternoons in front of Red Door Cafe, talking about ideas that were too crazy

or too stupid to be discussed with professors. Dr. Peter Day from JPL supervised me in the year when Jonas was ill. He has given me a lot of guidance both on theory and experiment, as well as on paper writing. Anastasios Vayonakis taught me a lot of things, from how to use a wire bonder to how to repair a car. Asking him about microwave engineering and cryogenic instrumentation has always been an shortcut for me to solve practical problems in these areas. I would like to give special thanks to Prof. John Martinis form UC Santa Barbara, who is very enthusiastic on the noise problem I am working on. Some of my work was inspired by his paper and discussions with him. Professor Sunil Golowala and Bernald Sadoulet, graduate students Megan Eckart, Shwetank Kumar, James Schlaerth, Omid Noroozian and David Moore have all given me many help and support to this thesis work.

I would also like to thank my parents, my sister and members in my extended family for their remote love and support.

Funding for this project has been provided by NASA, JPL DRDF, and the generous contributions of Alex Lidow, Caltech Trustee.

Abstract

Over the past decade, low temperature detectors have been of great interest to the astronomy community. These detectors work at very low temperatures, usually well below 1 K. Their ultra-high sensitivity has brought astronomers revolutionary new observational capabilities and led to many great discoveries, such as the demonstration that the geometry of the universe is flat[1, 2]. Although a single low temperature detector has very impressive sensitivity, a large array of them would be much more powerful and are highly demanded for the study of more difficult and fundamental problems in astronomy. However, current detector technologies, such as transition edge sensors (TESs) and superconducting tunnel junction (STJ) detectors, are difficult to integrate into a large array. When the pixel count becomes relatively large (> 1000), great technical challenges are encountered in fabricating and in reading out these detectors.

The microwave kinetic inductance detector (MKID) is a promising new detector technology invented at Caltech and JPL which provides both high sensitivity and an easy solution to the integration of detectors into a large array. It operates on the principle that the surface impedance of a superconductor changes as incoming photons break Cooper pairs. This change is read out by using high-Q superconducting microwave resonators capacitively coupled to a common feedline. This architecture allows thousands of detectors (resonators) to be easily integrated through passive frequency domain multiplexing. In addition, MKIDs are easy to fabricate and require minimal cryogenic electronics support (a single HEMT amplifier can potentially multiplex $10^3 - 10^4$ MKIDs).

In this thesis we will explore the rich and interesting physics behind these superconducting microwave resonators used in MKIDs. This study was carried out around two main topics, the responsivity and the noise of MKIDs.

In the discussion of the responsivity, the following physics are visited:

1. How does the surface impedance of a superconductor change with quasiparticle density?
2. What fraction of the distributed inductance of a superconducting transmission line is contributed by the superconductor?
3. What is the static and dynamic response of the microwave resonant circuit used in MKIDs?

The first question is answered in Chapter 2 by applying the Mattis-Bardeen theory to bulk and thin-film superconductors. The second question is answered in Chapter 3 by solving the quasi-TEM

mode of the coplanar wave guide (CPW) using the tool of conformal mapping. The third question is answered in Chapter 4 by applying the network theory to the readout circuit.

The experimental study of the noise is presented in Chapter 5, which is the focus of this thesis. Before noise was measured on the first MKID, the fundamental noise limit was understood to be the quasi-particle generation-recombination noise. Unexpectedly, a significant amount of excess noise was observed. From a large number of experiments, we have found this excess noise to be pure frequency noise (equivalent to a jitter in the resonance frequency), with the noise level depending on the microwave power, the bath temperature, the superconductor/substrate materials combination, and the geometry of the resonator. The observed noise properties suggest that the excess noise is not related to the superconductor but is caused by the two-level systems (TLS) in the dielectric materials in the resonator. The TLS are tunneling states which exist in amorphous solids and causes the anomalous properties of these solids at low temperatures. Several special experiments were designed to test the TLS hypothesis. From these experiments, we find that the effects of the TLS on the resonance frequency and the quality factor of the resonators are in good agreement with the TLS theory. In an important experiment we explored the geometrical scaling of TLS-induced frequency shift and noise. The results give direct experimental evidence that the TLS, responsible for the low temperature resonance frequency shift, dissipation, and frequency noise, are distributed on the surface of the resonator, but not in the bulk substrate. Guided by the measured noise scaling with geometry and power, we have come up with a semi-empirical noise model which assumes a surface distribution of independent TLS fluctuators. With this knowledge about TLS and excess noise, we propose a number of methods that can potentially reduce the excess noise.

Parallel to the experimental study, we have also taken great effort in working toward a theoretical model of the noise. It is likely that the noise is related to the dielectric constant fluctuation caused by the state switching (by absorption or emission of thermal phonons) or the energy level fluctuations of the TLS. However, at the time this thesis was finished, we still do not have a complete theory that can quantitatively explain all the experimental observations, and therefore the detailed physical noise mechanism is still not clear.

With the theoretical results of the responsivity and the semi-empirical model of the noise established in this thesis, a prediction of the detector sensitivity (noise equivalent power) and an optimization of MKID design are now possible, which was the original motivation of this thesis.

Contents

Acknowledgments	iv
Abstract	vi
List of Figures	xiv
List of Tables	xvii
1 Introduction	1
1.1 Microwave kinetic inductance detectors	1
1.1.1 Introduction to low temperature detectors	1
1.1.2 Principle of operation	2
1.1.3 Technical advantages	4
1.1.4 Applications and ongoing projects	5
1.1.4.1 Antenna-coupled MKIDs for millimeter and submillimeter imaging .	5
1.1.4.2 MKID strip detectors for optical/X-ray	6
1.1.4.3 MKID phonon sensor for dark matter search	7
1.2 Other applications of superconducting microwave resonators	9
1.2.1 Microwave frequency domain multiplexing of SQUIDS	9
1.2.2 Coupling superconducting qubits to microwave resonators	10
1.2.3 Coupling nanomechanical resonators to microwave resonators	11
2 Surface impedance of superconductor	13
2.1 Non-local electrodynamics of superconductor and the Mattis-Bardeen theory	13
2.2 Surface impedance of bulk superconductor	16
2.2.1 Solution of the Mattis-Bardeen kernel $K(q)$	16
2.2.2 Asymptotic behavior of $K(q)$	17
2.2.2.1 $K(q \rightarrow 0)$	18
2.2.2.2 $K(q \rightarrow \infty)$	18
2.2.2.3 A sketch of $K(q)$	19

2.2.3	Surface impedance Z_s and effective penetration depth λ_{eff} for specular and diffusive surface scattering	19
2.2.4	Surface impedance in two limits	21
2.2.4.1	Extreme anomalous limit	22
2.2.4.2	Local limit	23
2.2.5	Numerical approach	24
2.2.6	Numerical results	24
2.2.6.1	λ_{eff} of Al and Nb at zero temperature	24
2.2.6.2	Temperature dependence of Z_s	25
2.2.6.3	Frequency dependence of Z_s	27
2.3	Surface impedance of superconducting thin films	27
2.3.1	Equations for specular and diffusive surface scattering	27
2.3.2	Numerical approach	29
2.3.2.1	Implementing the finite difference method	29
2.3.2.2	Boundary condition	30
2.3.2.3	Retrieving the results	30
2.3.3	Numerical results	31
2.3.3.1	λ_{eff} of Al thin film	31
2.4	Complex conductivity $\sigma = \sigma_1 - j\sigma_2$	32
2.4.1	Surface impedance Z_s in various limits expressed by σ_1 and σ_2	33
2.4.1.1	Thick film, extreme anomalous limit	33
2.4.1.2	Thick film, local limit	33
2.4.1.3	Thin film	34
2.4.2	Change in the complex conductivity $\delta\sigma$ due to temperature change and pair breaking	34
2.4.2.1	Relating δZ_s to $\delta\sigma$	34
2.4.2.2	Effective chemical potential μ^*	34
2.4.2.3	Approximate formulas of Δ , n_{qp} , σ , and $d\sigma/dn_{qp}$ for both cases	36
2.4.2.4	Equivalence between thermal quasiparticles and excess quasiparticles from pair breaking	37
3	Kinetic inductance fraction of superconducting CPW	39
3.1	Theoretical calculation of α from quasi-static analysis and conformal mapping technique	39
3.1.1	Quasi-TEM mode of CPW	40
3.1.2	Calculation of geometric capacitance and inductance of CPW using conformal mapping technique	43

3.1.2.1	Zero thickness	44
3.1.2.2	Finite thickness with $t \ll a$	46
3.1.2.3	General case of finite thickness from a numerical approach	48
3.1.2.4	Results of L and C calculated using different methods	50
3.1.3	Theoretical calculation of α for thick films ($t \gg \lambda_{\text{eff}}$)	50
3.1.3.1	Kinetic inductance L_{ki} , kinetic inductance fraction α , and geometrical factor g	50
3.1.3.2	Approximate formula of g under the condition of $t \ll a$	52
3.1.3.3	Numerical calculation of g for general cases	53
3.1.3.4	A comparison of g calculated using different methods	54
3.1.4	Theoretical calculation of α for thin films ($t < \lambda_{\text{eff}}$)	54
3.1.5	Partial kinetic inductance fraction	56
3.2	Experimental determination of α	58
3.2.1	Principle of the experiment	58
3.2.2	α -test device and the experimental setup	59
3.2.3	Results of 200 nm Al α -test device ($t \gg \lambda_{\text{eff}}$ and $t \ll a$)	60
3.2.3.1	α of the smallest geometry	60
3.2.3.2	Retrieving values of α from $f_r(T)$ and $Q_r(T)$	60
3.2.3.3	Comparing with the theoretical calculations	62
3.2.4	Results of 20 nm Al α -test device ($t < \lambda_{\text{eff}}$)	63
3.2.4.1	α of the smallest geometry	63
3.2.4.2	Retrieving values of α from $f_r(T)$	63
3.2.4.3	Comparing with the theoretical calculations	64
3.2.5	A table of experimentally determined α for different geometries and thicknesses.	64
4	Analysis of the resonator readout circuit	66
4.1	Quarter-wave transmission line resonator	66
4.1.1	Input impedance and equivalent lumped element circuit	66
4.1.2	Voltage, current, and energy in the resonator	68
4.2	Network model of a quarter-wave resonator capacitively coupled to a feedline	69
4.2.1	Network diagram	70
4.2.2	Scattering matrix elements of the coupler's 3-port network	70
4.2.3	Scattering matrix elements of the extended coupler-resonator's 3-port network	71
4.2.4	Transmission coefficient t_{21} of the reduced 2-port network	71
4.2.5	Properties of the resonance curves	73
4.3	Responsivity of MKIDs I — shorted $\lambda/4$ resonator ($Z_l = 0$)	75

4.4 Responsivity of MKIDs II — $\lambda/4$ resonator with load impedance ($Z_l \neq 0$)	77
4.4.1 Hybrid resonators	77
4.4.2 Static response	78
4.4.3 Power dissipation in the sensor strip	79
4.4.4 Dynamic response	79
5 Excess noise in superconducting microwave resonators	83
5.1 A historical overview of the noise study	83
5.2 Noise measurement and data analysis	85
5.3 General properties of the excess noise	88
5.3.1 Pure phase (frequency) noise	88
5.3.2 Power dependence	90
5.3.3 Metal-substrate dependence	91
5.3.4 Temperature dependence	92
5.3.5 Geometry dependence	94
5.4 Two-level system model	95
5.4.1 Tunneling states	95
5.4.2 Two-level dynamics and the Bloch equations	97
5.4.3 Solution to the Bloch equations	99
5.4.4 Relaxation time T_1 and T_2	100
5.4.5 Dielectric properties under weak and strong electric fields	102
5.4.5.1 Weak field	103
5.4.5.2 Strong field	104
5.4.6 A semi-empirical noise model assuming independent surface TLS fluctuators	106
5.5 Experimental study of TLS in superconducting resonators	109
5.5.1 Study of dielectric properties and noise due to TLS using superconducting resonators	109
5.5.1.1 Silicon nitride (SiN_x) covered Al on sapphire device	109
5.5.1.2 Nb microstrip with SiO_2 dielectric on sapphire substrate	115
5.5.2 Locating the TLS noise source	119
5.5.2.1 Evidence for a surface distribution of TLS from frequency shift measurement	119
5.5.2.2 More on the geometrical scaling of frequency noise	123
5.6 Method to reduce the noise	126
5.6.1 Hybrid geometry	126
5.6.1.1 Two-section CPW	126

5.6.1.2	A design using interdigitated capacitor	128
5.6.2	Removing TLS	128
5.6.2.1	Coating with non-oxidizing metal	128
5.6.2.2	Silicides	128
5.6.3	Amplitude readout	129
6	Sensitivity of submm kinetic inductance detector	131
6.1	The signal chain and the noise propagation	131
6.1.1	Quasiparticle density fluctuations δn_{qp} under an optical loading p	132
6.1.1.1	Quasiparticle recombination $r(t)$	132
6.1.1.2	Thermal quasiparticle generation $g^{th}(t)$	133
6.1.1.3	Excess quasiparticle generation $g^{ex}(t)$ under optical loading	133
6.1.1.4	Steady state quasiparticle density \bar{n}_{qp}	134
6.1.1.5	Fluctuations in quasiparticle density δn_{qp}	135
6.2	Noise equivalent power (NEP)	136
6.2.1	Background loading limited NEP	136
6.2.2	Detector NEP limited by the HEMT amplifier	137
6.2.3	Requirement for the HEMT noise temperature T_n in order to achieve BLIP detection	138
6.2.4	Detector NEP limited by the TLS noise	139
A	Several integrals encountered in the derivation of the Mattis-Bardeen kernel $K(q)$ and $K(\eta)$	142
A.1	Derivation of one-dimensional Mattis-Bardeen kernel $K(\eta)$ and $K(q)$	142
A.2	$R(a, b)$ and $S(a, b)$	144
A.3	$RR(a, b)$, $SS(a, b)$, $RRR(a, b, t)$, and $SSS(a, b, t)$	145
B	Numerical tactics used in the calculation of surface impedance of bulk and thin-film superconductors	147
B.1	Dimensionless formula	147
B.2	Singularity removal	148
B.3	Evaluation of $K(\eta)$	149
C	j_t/j_z in quasi-TEM mode	150
D	Solution of the conformal mapping parameters in the case of $t \ll a$	152

E Fitting the resonance parameters from the complex t_{21} data	155
E.1 The fitting model	155
E.2 The fitting procedures	155
E.2.1 Step 1: Removing the cable delay term	156
E.2.2 Step 2: Circle fit	156
E.2.3 Step 3: Rotating and translating to the origin	158
E.2.4 Step 4: Phase angle fit	158
E.2.5 Step 5: Retrieving other parameters	159
E.3 Fine-tuning the fitting parameters	159
E.4 Fitting $ t_{21} ^2$ to the skewed Lorentzian profile	161
F Calibration of IQ-mixer and data correction	162
G Several integrals encountered in the calculation of $\epsilon_{\text{TLS}}(\omega)$	166
G.1 Integrating $\vec{\chi}_{\text{res}}(\omega)$ over TLS parameter space	166
G.2 $\epsilon_{\text{TLS}}(\omega)$ for weak field ($ \vec{E} \rightarrow 0$)	168
G.3 $\epsilon_{\text{TLS}}(\omega)$ for nonzero \vec{E} field	169
H Semi-empirical frequency noise formula for a transmission line resonator	172
Bibliography	174

List of Figures

1.1	Principle of operation of MKID	3
1.2	Pixel design of the antenna-coupled submm MKIDs	6
1.3	MKID strip detectors for optical/X-ray	7
1.4	Scheme of a dark matter MKID using CPW resonators	8
1.5	Scheme of a dark matter MKID using air-gapped microstrip resonators	9
1.6	Schematic of SQUID multiplexer	10
1.7	Integrated circuit for cavity QED	10
1.8	Device in which a nanomechanical resonator is coupled to a microwave resonator	11
2.1	Configuration of a plane wave incident onto a bulk superconductor	16
2.2	A sketch of $K(q)$	19
2.3	The temperature dependence of the surface impedance of Al	25
2.4	$\frac{\delta f_r}{f_r}$ and $\delta \frac{1}{Q_r}$ as a function of temperature	26
2.5	Frequency dependance of effective penetration depth λ_{eff} of Al bulk superconductor . .	27
2.6	Configuration of a plane wave incident onto a superconducting thin film	28
2.7	Field configuration used by Sridhar to calculate Z_s of a thin film	28
2.8	A thin film divided into N slices	29
2.9	Effective penetration depth λ_{eff} of Al thin film as a function of the film thickness d . .	32
2.10	$d\sigma/dn_{qp}$ vs. T calculated for thermal and external quasiparticles	37
3.1	Coplanar waveguide geometry	40
3.2	Schwarz-Christoffel mapping	43
3.3	SC-mapping of a zero-thickness CPW into a parallel-plate capacitor	44
3.4	SC-mapping of a finite-thickness CPW into a parallel plate capacitor	46
3.5	Constructing the capacitance of a CPW with thickness t	47
3.6	Mapping a quadrant of a finite-thickness CPW into a rectangle	48
3.7	Calculation of the exact capacitance of a CPW	49
3.8	\vec{E} and \vec{H} fields near the surface of a bulk superconducting CPW	51
3.9	Total inductance L as a function of the surface inductance L_s for a thin-film CPW . .	55

3.10	Coupler structure of the α -test device	58
3.11	Measured $\delta f_r/f_r$ and $\delta(1/Q_r)$ as a function of T from the 200 nm α -test device	61
3.12	$\delta f_r/f_r$ normalized by group 1 from the 200 nm α -test device	61
3.13	Fitting $\delta f_r/f_r$ and $\delta(1/Q_r)$ data to the Mattis-Bardeen theory	62
3.14	Measured $\delta f_r/f_r$ as a function of T from the 20 nm α -test device	63
3.15	$\delta f_r/f_r$ normalized by group-1 from the 20 nm α -test device	63
3.16	Fitting $\delta f_r/f_r$ data to the Mattis-Bardeen theory	64
4.1	A short-circuited $\lambda/4$ transmission line and its equivalent circuit	67
4.2	Network model of a $\lambda/4$ resonator capacitively coupled to a feedline	69
4.3	Plot of $t_{21}(f)$ and its variation $t'_{21}(f)$	74
4.4	A hybrid design of MKID.	78
4.5	Equivalent circuits for $\delta R(t)$ and $\delta L(t)$ perturbations	80
5.1	A diagram of the homodyne readout system	86
5.2	Resonance circle and noise ellipse	86
5.3	Phase and amplitude noise spectra	88
5.4	Excess phase noise under different readout power	90
5.5	Frequency noise at 1 kHz vs. internal power	91
5.6	Power and material dependence of the frequency noise	92
5.7	Phase noise at temperatures between 120 mK and 1120 mK	93
5.8	Temperature and power dependence of frequency noise	94
5.9	Resonance frequency and quality factor as a function of temperature	95
5.10	Geometry dependence of frequency noise	96
5.11	A particle in a double-well potential	97
5.12	Spectral diffusion	102
5.13	Temperature dependence of TLS-induced loss tangent and dielectric constant	104
5.14	Electric field strength dependence of δ_{TLS}	105
5.15	An illustration of the SiN_x -covered CPW resonator	110
5.16	Internal loss Q_i^{-1} as a function of P_{int}	111
5.17	Joint fit of Q_i^{-1} and f_r vs. T at lowest readout power	113
5.18	Excess noise measured on Res 1 of the SiN_x -covered device	114
5.19	Temperature dependence of frequency noise	115
5.20	Measured power and temperature dependence of f_r and Q_i	116
5.21	Frequency noise at 30 Hz as a function of temperature	117
5.22	Frequency noise spectrum and the derived noise coefficient κ	118
5.23	Possible locations of TLS noise source	119

5.24	An illustration of the CPW coupler and resonator	120
5.25	Fractional frequency shift $\Delta f_r/f_r$ as a function of temperature	121
5.26	The geometrical scaling of α , F^* , g_m , and g_g	122
5.27	Frequency noise of the four CPW resonators measured at $T = 55$ mK	123
5.28	Geometrical scaling of frequency noise	124
5.29	The scaling of the calculated dimensionless noise scaling function $F_3^m(t/s_r)$	125
5.30	An illustration of the two-section CPW design	127
5.31	An illustration of the MKID design using interdigitated capacitor	127
5.32	Detector response to a single UV photon event	129
5.33	NEP calculated for the phase and amplitude readout	130
6.1	A diagram of the signal chain and the noise propagation in a hybrid MKID	132
C.1	Current and charge distribution	150
E.1	Fitting the resonance circle step by step in the complex plain	156
E.2	Fitting the phase angle	158
E.3	Geometrical relationships used to determine Q_c and ϕ_0	159
E.4	Refining the fitting result	160
E.5	Fitting $ t_{21} $ to the skewed Lorentzian profile	161
F.1	IQ ellipse	163
F.2	Geometric relationships	164
F.3	IQ ellipses from beating two synthesizers	165
G.1	$F(a)$ and $1/(a^2 + 3)$	167
G.2	$\delta\epsilon'$, $\delta\epsilon'_1$, and $\delta\epsilon'_2$ as a function of temperature	171

List of Tables

2.1	λ_{eff} of bulk Al and Nb	25
3.1	A comparison of L and C calculated using different methods.	50
3.2	L_m , g , L_{ki} , and α calculated from the approximate formula	54
3.3	L_m , g , L_{ki} , and α calculated from the numerical method	54
3.4	Ratio of α^*/α calculated using the two methods	57
3.5	Ratio of α^*/α calculated using “induct” program	57
3.6	Design parameters of the α -test device	59
3.7	Results of α from the 200 nm α -test device	62
3.8	Results of α from the 20 nm α -test device	64
3.9	A list of experimentally determined α for different geometries and thicknesses	65
5.1	Resonance frequency before and after the deposition of SiN_x	110
5.2	Results of δ_{TLS}^0 and f_r from a joint fit to the $Q_i^{-1}(T)$ and $f_r(T)$ data	112
5.3	Parameters of Nb/SiO ₂ /Nb microstrip	117
5.4	Values and ratios	123
6.1	Required HEMT noise temperature in order to achieve BLIP detection	139
6.2	Parameters involved in the calculation of TLS limited detector NEP	141

Chapter 1

Introduction

1.1 Microwave kinetic inductance detectors

1.1.1 Introduction to low temperature detectors

Over the past decade, low temperature detectors have been of great interest to the astronomy community. These detectors work at very low temperatures, usually well below 1 K. Their ultra-high sensitivity have brought astronomers with revolutionary new observational capabilities and led to many great discoveries throughout a broad wavelength range—from submillimeter, optical/UV to X-ray and gamma-ray.

The basic idea behind a traditional low temperature detector is quite simple [3]. It's well known that the heat capacity of an insulating crystal (or a superconducting metal well below its transition temperature T_c) decreases as T^3 . Therefore at a sufficient low temperature, any small amount of heat (energy) deposited in a crystal would be in principle resolvable by using a thermometer. A straightforward implementation of this idea, which a large family of low temperature detectors work on today, is an absorber-thermometer scheme: an absorber is connected to a heat bath through a weak heat link and a thermometer of some kind, attached to the absorber, is used to measure the temperature change, from which the absorbed energy can be calculated.

Several types of thermometers have been developed and used in different applications. Neutron-transmutation-doped (NTD) Ge thermistors were among the earliest developed detectors[4], and are used in the Bolocam, a mm-wave camera at the Caltech Submillimeter Observatory (CSO)[5]. To make these thermistors, semiconductor Ge is irradiated with slow neutrons. After irradiation, transmutation occurs and the radioactive nuclei decay into a mixing of n and p impurities. Because of the high impedance of the NTD-Ge thermistor, low noise JFET amplifiers cooled down to 100 K are usually used to read out these detectors.

A second type of thermometer, which make the most sensitive low temperature detectors of today at almost all wavelengths, is the transition edge sensor (TES)[6, 7, 8, 9, 10]. These sensors use a thin

strip of superconductor and operate at a temperature right on the superconducting transition edge ($T \approx T_c$), where the slope dR/dT is extremely steep. Due to the low impedance, and for stability considerations, TES is usually voltage biased, and the current flowing through the sensor is usually measured by using a superconducting quantum interference device (SQUID), which serves as a cold low noise amplifier.

More recently, magnetic microcalorimeters (MMCs) have emerged as an alternative to TES for some applications[11]. In a MMC, rare earth ions are embedded in a metal and the magnetization of the metal in an external magnetic field sensitively changes with temperature. The magnetization is again measured with a SQUID.

There is another category of low temperature detectors called quasiparticle detectors that do not operate on the absorber-thermometer scheme. Instead of measuring the temperature change of the absorber caused by the energy deposited by a photon, it directly measures the quasiparticles created when a photon breaks Cooper pairs in a superconductor. Superconducting tunnel junction (STJ)[12, 13] detectors and kinetic inductance detectors (MKIDs) are two examples in this category. The STJs use a superconductor-insulator-superconductor (SIS) junction, which has a very thin insulating tunnel barrier in between the two superconducting electrodes. Under a dc voltage bias, the tunneling current changes when excess quasiparticles are generated in one of the electrodes. STJs have a comparably high dynamic resistance and capacitance, and can be read out with FET-based low-noise preamplifiers operated at room temperature. In addition, a magnetic field must be applied to STJs to suppress the Josephson current.

Although a single low temperature detector has demonstrated very impressive sensitivity, a large array of them would be much more powerful and are highly demanded for the study of more difficult and fundamental problems in astronomy, with the cosmic microwave background (CMB) polarization problem being one example. Although researchers are working on increasing the pixel count of all type of low temperature detectors introduced above (NTD-Ge, TES, MMC, STJ), great technical challenges exist in building and reading out these detectors when the pixel count becomes relatively large ($\gtrsim 1000$).

MKID is a promising detector technology invented in Caltech and JPL which provides both high sensitivity and an easy solution to the integration of these detectors into a large pixel array[14, 15, 16, 17, 18]. A brief introduction of MKID will be given in the following sections of this chapter, and the physics behind the detector will be explored in the rest of this thesis.

1.1.2 Principle of operation

In order to understand the principle of operation of MKID, let's first explain the concept of kinetic inductance of a superconductor. It is well known that a superconductor has zero dc resistance ($\sigma_{dc} \rightarrow \infty$) at $T \ll T_c$. This is because the supercurrent is carried by pairs of electrons—the Cooper

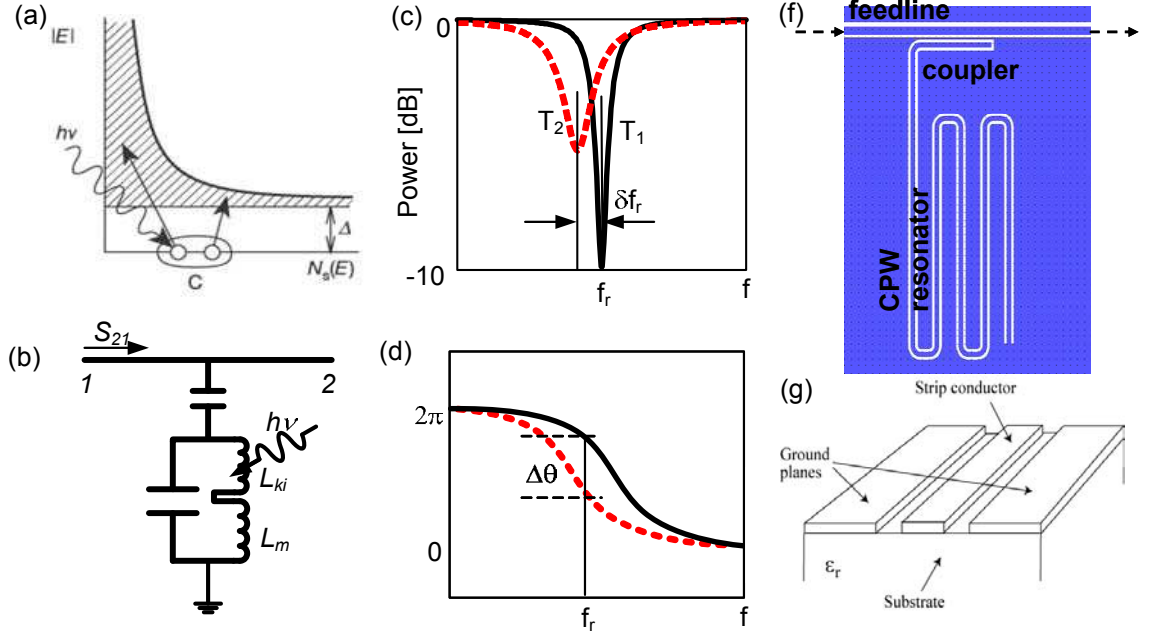


Figure 1.1: Detection principle of MKIDs. a) A photon with energy $h\nu > 2\Delta$ breaks Cooper pairs and creates quasiparticles in a superconducting strip cooled to $T < T_c$. b) The superconducting strip is used as an inductive element with a variable kinetic inductance L_{ki} and a fixed inductance L_m in a microwave resonant circuit. The increase in the quasiparticle density changes the surface impedance Z_s (mainly surface inductance L_s) which leads to a change in L_{ki} . c) The transmission through the resonant circuit has a narrow dip at the resonance frequency f_r which moves when L_{ki} changes. d) The microwave probe signal acquires a phase shift when f_r changes. e) Schematic illustration (not to scale) of the coplanar waveguide resonator and feedline which implement the LC resonant circuit of (b). Blue represents the superconducting film and white represents bare substrate. f) A cross-sectional view of the coplanar waveguide geometry

pairs which can move freely in the superconductor without being scattered.

However, because Cooper pairs have inertia, superconductors have a nonzero ac impedance. The effect of the inertia of the electrons to the conductivity is included in Drude's model and the ac conductivity $\sigma(\omega)$ is given by:

$$\sigma(\omega) = \frac{\sigma_{dc}}{1 + j\omega\tau} \quad (1.1)$$

where ω is the frequency, τ is the scattering time, and the $j\omega\tau$ term arises from the phase lag between the current and the electric field due to the inertia of the electrons. In a normal metal at room temperature, the electron scattering time τ is very short, on the order of 10^{-14} s. So up to the microwave frequencies, $\omega\tau \ll 1$ and the conductivity appears almost purely resistive. In a superconductor at $T \ll T_c$, both $\sigma_{dc} \rightarrow \infty$ and $\omega\tau \rightarrow \infty$, but the ratio $\sigma_{dc}/\omega\tau$ remains finite. As a result, the ac conductivity $\sigma(\omega)$ of a superconductor is almost purely inductive, which gives rise to a surface impedance $Z_s = |\vec{E}|/|\int \vec{J} dz| = R_s + j\omega L_s$ (see Chapter 2) that is also almost purely inductive, $\omega L_s \gg R_s$. When a superconductor is used as a component in an ac circuit, the

surface inductance L_s will contribute an inductance L_{ki} called kinetic inductance, in addition to the conventional magnetic inductance L_m . From an energy point of view, the inductance L_{ki} accounts for the energy stored in the supercurrent as the kinetic energy of the Coopers.

Cooper pairs are bound together by the electron-phonon interaction, with a binding energy $2\Delta \approx 3.52kT_c$ [19]. At finite temperature $T > 0$, a small fraction of electrons are thermally excited from the Cooper pair state. These excitations are called “quasiparticles” which are responsible for small ac losses and a nonzero surface resistance R_s of the superconductor.

Photons with sufficient energy ($h\nu > 2\Delta$) may also break apart one or more Cooper pairs (Fig. 1.1a). These “excess” quasiparticles will subsequently recombine into Cooper pairs on time scales $\tau_{qp} \approx 10^{-3} - 10^{-6}$ s. During this time period, the quasiparticle density will be increased by a small amount δn_{qp} above its thermal equilibrium value, resulting in a change in the surface impedance δZ_s . Although δZ_s is quite small, it may be sensitively measured by using a resonant circuit (Fig. 1.1b). Changes in L_s and R_s affect the frequency and width of the resonance, respectively, changing the amplitude and phase of a microwave signal transmitted through the circuit (Fig. 1.1c and Fig. 1.1d).

Although the schematic depicted in Fig. 1.1b directly suggests a lumped-element implementation, a distributed resonant circuit with a quarter wavelength coplanar waveguide (CPW) resonator capacitively coupled to a CPW feedline (Fig. 1.1f) is mostly used in MKIDs, due to the technical advantages that will be discussed shortly.

1.1.3 Technical advantages

MKIDs have several technical advantages:

- The fundamental noise in MKIDs is limited by the fluctuations in the quasiparticle density caused by the random breaking of Cooper pairs into quasiparticles and recombination of quasiparticles into Cooper pairs by thermal phonons. Because of the Poisson nature of these two processes, this generation-recombination noise (g-r noise) is proportional to the quasiparticle density itself, which decreases as $\exp(-\Delta/kT)$ when T goes to zero. Therefore, by operating at $T \ll T_c$, in theory MKIDs can achieve a very high detector sensitivity.
- The CPW resonators are a simple planar structure that can be easily fabricated by standard lithography from a single layer of superconducting film. Because it has no junctions, bilayers or other difficult structures to make, even the fabrication of a large detector array is straightforward. Therefore, MKIDs have the advantages of low cost, high yield, and good uniformity for the fabrication of a large detector array.
- The most attractive aspect of MKIDs is its capability for large scale frequency domain multiplexing. In MKIDs, an array of resonators, each with a different resonance frequency, are

coupled to a common feedline. The detectors are read out by sending a probe microwave signal containing a comb of frequencies tuned to the unique resonance frequency of each resonator, amplifying the transmitted signal with a cryogenic high electron mobility transistor (HEMT) amplifier, and demultiplexing the signal at room temperature. Only one input and output transmission line (coaxial cable) and a single HEMT is needed for the readout of the entire array, which largely simplifies the design of readout circuits and reduces the power dissipation at the cold stage. In contrast, the direct multiplexing of TES or STJ detectors requires several biasing wires per detector be made and one amplifier per detector be deployed.

Recent advances in the software defined radio (SDR) technology have provided a more elegant solution for the readout of large MKID arrays[20]. On the transmitter side, the microwave probe signal consisting of multiple tones can be generated by upconverting (mixing an IF signal with an local microwave oscillation signal) an IF signal, which is produced by playing a preprogrammed waveform stored in the computer memory through a fast D/A card. On the receiver side, the transmitted microwave signal is first downconverted and then digitized by a fast A/D card. The demodulation can be done digitally using signal processing algorithms operating a field programmable gate array (FPGA).

1.1.4 Applications and ongoing projects

1.1.4.1 Antenna-coupled MKIDs for millimeter and submillimeter imaging

One of the ongoing projects in our group is the development of MKIDCam[21, 22], a MKID camera with 600 pixels, each sensing 4 colors at mm/submm wavelength (see Table 6.1), which is to be installed at CSO in 2010.

Fig. 1.2 illustrates the design concept of a single pixel in the array. Each pixel consists of a single slot antenna, a band-pass filter and a quarter-wave CPW resonator coupled to the feedline. The mm/submm radiation is first collected by the slot antenna. One can think of a lot of voltage sources being placed at the points where the microstrip lines run over across the slots. These small voltage signals are combined by the binary microstrip summing network to deliver a stronger signal to the filter. The path lengths between the root of the summing tree and the microstrip crossing point of each slot are designed to be the same, which ensures that only plane waves normally incident onto the antenna will be coherently added up, thus defineing the directionality of the antenna. The band-pass filters used here are superconducting filters which are a compact on-chip implementation of the lumped-element LC filter networks. Both the antenna and the filters are made of superconductor Nb, which has a $T_c = 9.2$ K and gives very small loss for the mm/submm wave. The desired in-band mm/submm signal is selected by the filter and delivered to the CPW resonator by a Nb microstrip overlapping with the center strip of the CPW resonator near its shorted end. Because the center

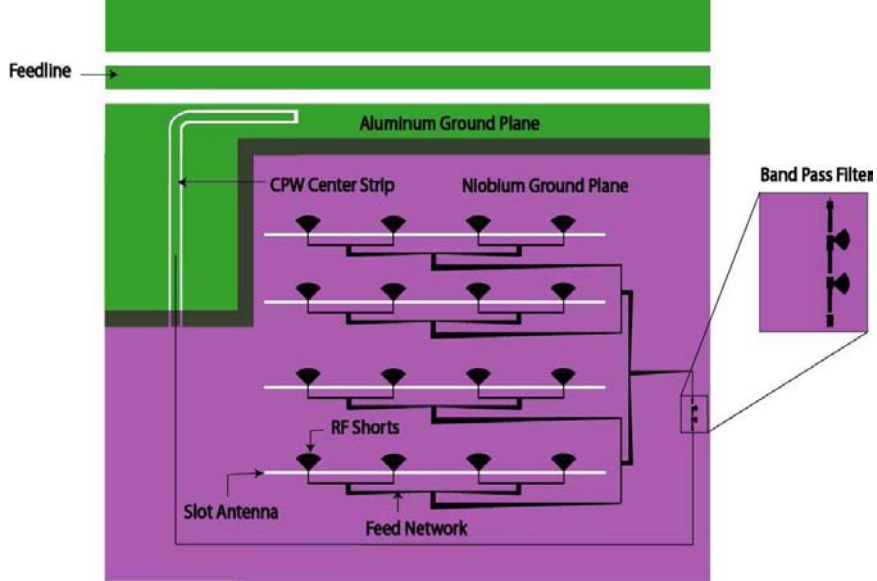


Figure 1.2: An illustration of the pixel design in an antenna-coupled submm MKIDs array. The slot antenna, on-chip filter, CPW resonator, and feedline are shown in this illustration. This pixel uses a single slot antenna and has one filter, which is able to sense one polarization at one wavelength (color). The actual pixel used in the MKIDCam has four filters, each followed by one CPW resonator.

strip is made of superconductor Al ($T_c = 1.2$ K), the submm/mm wave from the Nb microstrip will break Cooper pairs in the Al strip in the overlapping region, change the local surface impedance Z_s , and be sensed by the resonator readout circuit.

The pixel design shown in Fig. 1.2 is slightly different from the actual pixel design used in the MKIDCam array. The pixel shown here uses one filter and can therefore sense only one color, while the pixel in MKIDCam uses 4 filters to sense the 4 colors, with each filter followed by a CPW resonator. In Fig. 1.2, the entire CPW resonator as well as the feedline are made of Al, while in a MKIDCam pixel only the center strip near the shorted end, where the microstrip overlaps with CPW, is made of Al, and the remaining part is made of Nb. This “hybrid” resonator design helps to confine Al quasiparticles in a small sensitive region and increase the quality factor of the resonator. More discussions on the hybrid mm/submm MKIDs will be given in Chapter 4 and Chapter 6.

1.1.4.2 MKID strip detectors for optical/X-ray

Also under development in our group is the MKID detector array for optical and X-ray detection[23]. The optical and X-ray MKIDs share a common position-sensitive strip detector design as shown in Fig. 1.3, which is borrowed from a scheme originally used by the STJ detectors. In this scheme, an absorber strip made of a higher-gap superconductor with a large atomic number, usually Ta ($T_c = 4.4$ K and $Z = 181$), is used to absorb the optical/X-ray photons. These high energy photons break Cooper pairs and generate quasiparticles in the Ta absorber. The Ta quasiparticles (with

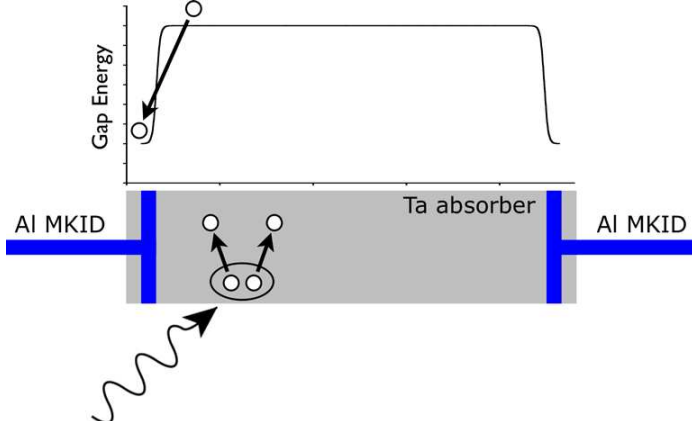


Figure 1.3: An illustration of the strip detector design used in Optical/X-ray MKIDs. The optical/X-ray photon breaks Cooper pairs and generates quasiparticles in the Ta absorber. The Ta quasiparticles (with energy $\sim \Delta_{\text{Ta}}$) diffuse to the edges of the absorber and are down-converted to Al quasiparticles (with energy $\sim \Delta_{\text{Al}}$) in the Al sensor strips attached to the Ta absorber. Because $\Delta_{\text{Al}} < \Delta_{\text{Ta}}$, the Al quasiparticles are trapped in the sensor strip and cause a change in the Al quasiparticle density, which is sensed by the resonator circuit.

energy $\sim 2\Delta_{\text{Ta}}$) diffuse to the edges of the absorber and are downconverted (by breaking Cooper pairs with lower gap energy) to Al quasiparticles (with energy $\sim 2\Delta_{\text{Al}}$) in the Al sensor strips that are attached to the absorber on both edges. Because $\Delta_{\text{Al}} < \Delta_{\text{Ta}}$, a natural quasiparticle trap forms which prevent the Al quasiparticles from leaving the Al sensor strip. These excess quasiparticles change the Al quasiparticle density, which is sensed by the resonator circuit. Each single photon absorbed will give rise to two correlated pulses in the readout signals from the two resonators. The energy deposited by the photon can be resolved by looking at the sum of the two pulse heights, while the position where the photon is absorbed can be resolved by examining the ratio between the two pulse heights, or the arrival time difference between the two pulses. Therefore, this scheme makes a position-sensitive spectrometer. An energy resolution of $\delta E = 62$ eV at 5.899 keV from a X-ray MKID strip detector has been demonstrated[24].

1.1.4.3 MKID phonon sensor for dark matter search

Dark matter, the unknown form of matter that accounts for 25 percent of the entire mass of the universe, has long been a fascinating problem to the theoretical physicists and astrophysicists, while the search for dark matter has been one of the most challenging experiments to the experimentalists. Weakly interacting massive particles (WIMPs) are leading candidates for the building blocks of dark matter. These particles have mass and interact with gravity, but do not have electromagnetic interaction with normal matter.

It is predicted that WIMP dark matter may be directly detected through its elastic-scattering interaction with nuclei. One of the popular detection schemes, which sets the lowest constraint for

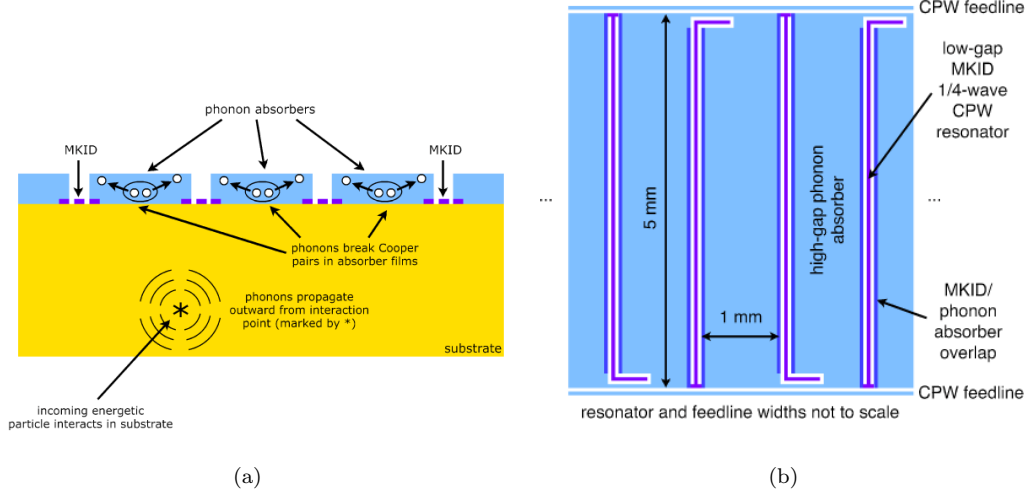


Figure 1.4: A proposed detector scheme of kinetic inductance phonon sensor for dark matter detection using CPW ground plane trapping. (a) Cross-sectional view and (b) top view of the detector [25].

the WIMP-nucleon cross section today, is to jointly measure the effects of ionization and lattice vibrations (or phonons) caused by the nuclear recoil from a WIMP impact event, using a crystalline Ge or Si absorber (also called a target). By examining the ionization signal and the phonon signal, WIMP events can be discriminated from non-WIMP events.

Currently the Cryogenic Dark Matter Search (CDMS) experiment uses 19 Ge targets (a total mass of 4.75 kg) and 11 Si targets (a total mass of 1.1 kg), with TES phonon sensors covering the surface of each target. As the total target mass will be significantly increased (> 100 kg) in the next generation of CDMS experiments, how to instrument such a large target at low cost while maintaining a high sensitivity becomes a big challenge.

MKID phonon sensors offer an interesting solution to this scaling problem. Fig. 1.4 shows a detector scheme proposed by Golwala[25]. In this scheme, the surface of the target is covered by frequency domain multiplexed CPW resonators. Phonons generated by the nuclear recoil arrive at the surface and break Cooper pairs mostly in the Al ground planes. The Al quasiparticles then diffuse to the edges of the CPW ground plane, where a narrow strip of lower gap superconductor (Ti or W) overlaps with the Al ground planes. The Al quasiparticles will be downconverted Ti or W quasiparticles which are trapped in the edge region and sensed by the resonator.

In another scheme proposed by the CDMS group in UC Berkeley[26], Nb strip resonators are placed in a separate wafer as shown in Fig. 1.5. The Ge target is first coated with a thin Al film on the surface serving as a ground plane. The strip resonators are then suspended over the ground plane at the desired separation using spacers. The structure becomes a air-gapped microstrip (inverted microstrip). The quasiparticles are generated in the Al ground plane and are sensed when they

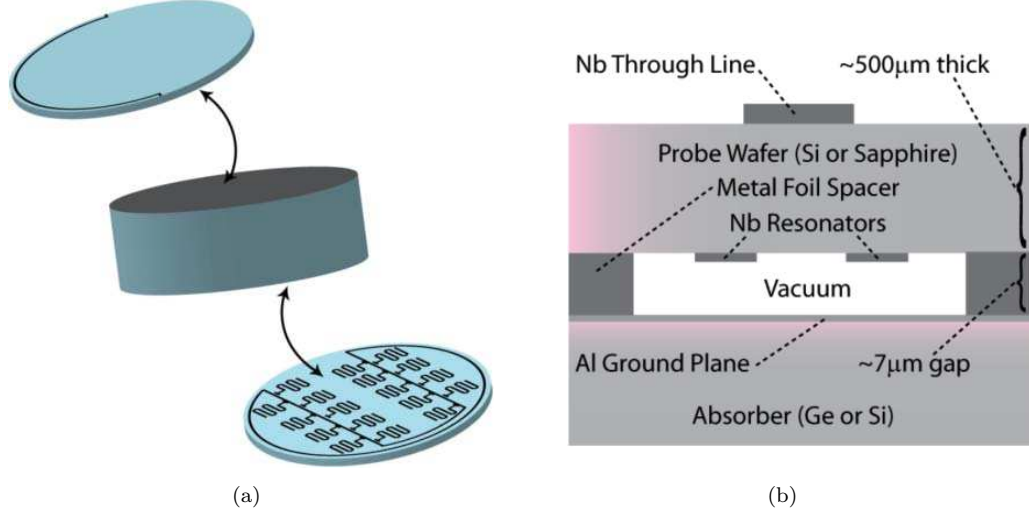


Figure 1.5: The detector scheme of the kinetic inductance phonon sensor using air-gapped microstrip resonators for dark matter detection. (a) Separation of function: resonators are patterned onto a standard sized wafer, which is then affixed to the thick absorber. The absorber receives minimal processing. (b) Cross-sectional view of kinetic inductance phonon sensor test device. The probe wafer, containing the resonators, is suspended above the absorber using metal foil spacers. Figure from [26]

diffuse to the region underneath the top Nb strip. One of the advantages of this scheme is that no lithography is required on the large target, because of the separation of resonator wafer from the target. Fairly high-Q resonators ($Q_r \sim 40,000$) using this structure have been demonstrated[26].

1.2 Other applications of superconducting microwave resonators

Ever since the original work on MKIDs was started, superconducting microwave resonators have attracted great attention both inside and outside the low temperature detector community. The following shows a number of successful applications of superconducting microwave resonators, which have been inspired by MKIDs.

1.2.1 Microwave frequency domain multiplexing of SQUIDs

The traditional time domain multiplexing of SQUID uses switching circuit to periodically select a sensor in an array for readout. This scheme is still rather complicated in terms of fabrication and operation. Recently, researchers in NIST[27, 28] and JPL[29, 30] are investigating the frequency domain multiplexing of SQUIDs using superconducting resonators.

The circuit schematic of the SQUID multiplexer developed in NIST is illustrated in Fig. 1.6. The quarterwave resonator is terminated with a single junction SQUID loop, instead of being directly

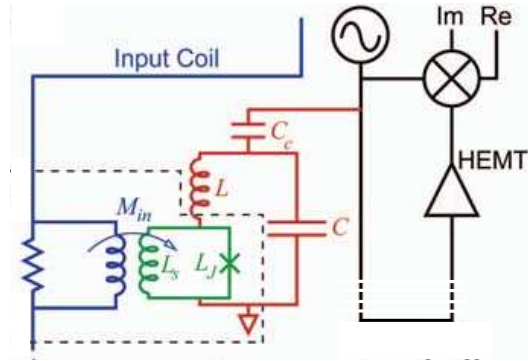


Figure 1.6: Schematic of the SQUID multiplexer using the quarterwave CPW resonators (modeled as parallel LC resonators). Figure from [28]

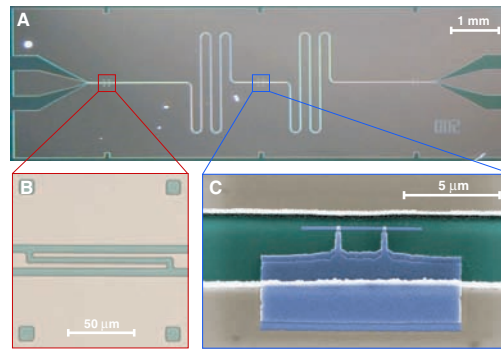


Figure 1.7: Integrated circuit for cavity QED. Panel A, B, and C show the entire device consisting of the CPW resonator and the feedline, the coupling capacitor, and the Cooper pair box, respectively. Figure from [31]

short circuited as in MKIDs. Because of the flux-dependent Josephson inductance, the SQUID loop acts as a flux-variable inductor. Therefore a change of the flux in the SQUID loop will modify the total inductance, leading to a resonance frequency shift that can be read out. A prototype of this multiplexer with high-Q ($\sim 18,000$) resonators has been demonstrated by the NIST group.

1.2.2 Coupling superconducting qubits to microwave resonators

The cavity quantum electrodynamic (CQED) experiments, which study the interaction between photons and atoms (light and matter), are usually performed with laser and two-level atoms in an optical cavity. For the first time, Wallraff et al.[31] have demonstrated that these experiments can also be carried out with microwave photons and superconducting qubits (Cooper pair box) in a superconducting microwave resonator. They call it “circuit QED”.

A picture of such a device is shown in Fig. 1.7. In this device, a full-wave Nb CPW resonator is capacitively coupled to the input and output transmission lines. A Cooper pair box is fabricated in the gap between the center strip and the ground planes and in the middle of the full-wave resonator,

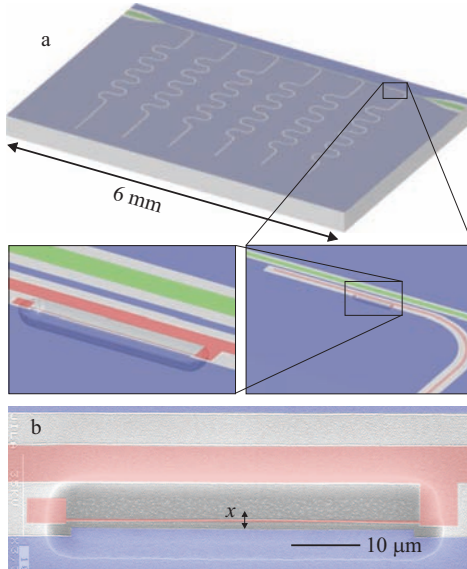


Figure 1.8: (a) Device drawing showing frequency multiplexed quarterwave CPW resonators. (b) A zoom-in view of a suspended nanomechanical beam clamped on both ends (with Si substrate underneath etched off) and electrically connected to the center strip of the CPW. Figure from [36]

where the electric field is maximal, allowing a strong coupling between the qubit and the cavity. The two Josephson tunnel junctions are formed at the overlap between the long thin island parallel to the center conductor and the fingers extending from the much larger reservoir coupled to the ground plane.

The coupled circuit of qubit and resonator can be described by the well-known Jaynes-Cummings Hamiltonian[32]. It can be shown that for weak coupling g or large detuning $\Delta = \varepsilon/h - f_r$ (ε is the two-level energy of the qubit and f_r is the resonance frequency), $g \ll \Delta$, the reactive loading effect of the qubit will cause the resonator frequency to shift by $\pm g^2/\Delta$ depending on the quantum state of the qubit. This shift can be measured by a weak microwave probe signal. Therefore, this dispersive measurement scheme performs a quantum non-demolition read-out of the qubit state.

Circuit-QED opens up a new path to perform quantum optics and quantum computing experiments in a solid state system. Currently, circuit-QED has become a very hot area of quantum computing research[33, 34, 35].

1.2.3 Coupling nanomechanical resonators to microwave resonators

A superconducting microwave resonator is also used in an recent experiment to read out the motion of a nanomechanical beam, or the quantum mechanical state of a mechanical harmonic oscillator[36]. The device used for this experiment is shown in Fig. 1.8. A nanomechanical beam (50 μm long with a 100 nm by 130 nm crosssection) is formed by electron beam lithography of an Al film deposited on

a Si substrate. The beam is suspended by etching off the Si substrate underneath it. Because the Al beam is electrically connected to the center strip, the local centerstrip-to-ground capacitance depends on the position of the beam. If the beam has a displacement or deformation, it will cause a shift in the resonance frequency, which can be read out from the transmission measurement. In addition to the detection of the nanomechanical motion, researchers are working on cooling the nanomechanical resonators towards their ground state, by making use of the radiation pressure effect.

Chapter 2

Surface impedance of superconductor

2.1 Non-local electrodynamics of superconductor and the Mattis-Bardeen theory

It is well known that an electromagnetic field penetrates into the normal metal with a finite skin depth δ . The skin depth can be calculated using Maxwell's equations and Ohm's law, which expresses a local relationship between the current density \vec{J}_n and the electric field \vec{E} in the normal metal:

$$\vec{J}_n(\vec{r}) = \sigma \vec{E}(\vec{r}) = \frac{\sigma_{dc}}{1 + j\omega\tau} \vec{E}(\vec{r}), \quad (2.1)$$

where σ_{dc} is the DC conductivity and τ is the relaxation time of the electrons, related by $\tau = l/v_0$ to the mean free path l and the Fermi velocity v_0 . Because τ is usually below a picosecond at room temperature, the condition $\omega\tau \ll 1$ holds at microwave frequency $\omega\tau \ll 1$, and so $\sigma \approx \sigma_{dc}$. The skin depth δ is derived to be

$$\delta \approx \sqrt{\frac{2}{\omega\mu\sigma_{dc}}}, \quad (2.2)$$

where μ is the magnetic permeability of the metal; usually $\mu \approx \mu_0$.

The local relationship Eq. 2.1 and the classic skin depth (Eq. 2.2) are valid when the electric field \vec{E} varies little within a radius l around some point \vec{r} , which translates to $l \ll \delta$. Because δ decreases at higher frequencies and l increases at lower temperatures, a non-local relationship between \vec{J}_n and \vec{E} may occur at high enough frequency or low enough temperature. A non-local relationship replacing Eq. 2.1 was proposed by Chambers[37]:

$$\vec{J}_n(\vec{r}) = \frac{3\sigma_{dc}}{4\pi l} \int_V \frac{\vec{R}\vec{R} \cdot \vec{E}(\vec{r}') e^{-R/l}}{R^4} d\vec{r}', \quad (2.3)$$

where $\vec{R} = \vec{r}' - \vec{r}$. Eq. 2.3 is non-local because \vec{J}_n at point \vec{r} depends on \vec{E} not just at that point, but is instead a weighted average of \vec{E} in a volume around \vec{r} . If \vec{E} varies little in the vicinity of \vec{r} so that \vec{E} can be taken out of the integral, Eq. 2.3 returns to the local relationship.

Due to the Meissner effect, an electromagnetic field also penetrates into a superconductor over a distance called the penetration depth λ . Similar to the classical skin effect, in the calculation of λ both local and non-local behavior may occur. Equations reflecting a local relationship between the supercurrent J_s (assuming the two fluid model with $\vec{J} = \vec{J}_s + \vec{J}_n$) and the fields were proposed by London[38] (known as the famous London equations):

$$\frac{\partial}{\partial t} \vec{J}_s = \frac{\vec{E}}{\mu_0 \lambda_L^2}, \quad (2.4)$$

$$\nabla \times \vec{J}_s = -\frac{1}{\lambda_L^2} \vec{H}, \quad (2.5)$$

where μ_0 is the vacuum permeability, \vec{H} is the magnetic field, and λ_L is the London penetration depth. At zero temperature, the London penetration depth λ_{L0} is given by

$$\lambda_{L0} = \sqrt{\frac{m}{\mu_0 n e^2}}, \quad (2.6)$$

where m , n , and e are the mass, density, and charge of the electron, respectively. In the London gauge $\nabla \cdot \vec{A} = 0$, the second London equation can be written as¹

$$\vec{J}_s = -\frac{1}{\lambda_L^2} \vec{A}. \quad (2.7)$$

These equations apply to superconductors where the local condition is satisfied. In general, a non-local relationship is more appropriate, because the mean free path l may become large in high quality superconductors at low temperatures. Based on the observation of increasing penetration depth with increasing impurity density or decreasing mean free path, Pippard proposed an empirical non-local equation [41]:

$$\vec{J}_s(\vec{r}) = -\frac{3}{4\pi\xi_0\lambda_L^2} \int_V \frac{\vec{R}\vec{R} \cdot \vec{A}(\vec{r}') e^{-R/\xi}}{R^4} d\vec{r}' \quad (2.8)$$

with

$$\frac{1}{\xi} = \frac{1}{\xi_0} + \frac{1}{\alpha_p l} \quad (2.9)$$

where ξ_0 , ξ are the coherence lengths of the pure and impure superconductor and α_p is an empirical

¹Throughout this thesis, the magnetic vector potential is defined as $\vec{H} = \nabla \times \vec{A}$, which is used by Mattis and Bardeen[39] and Popel[40].

constant. The coherence length ξ_0 is related to v_0 and Δ_0 by

$$\xi_0 = \frac{\hbar v_0}{\pi \Delta_0}, \quad (2.10)$$

where Δ_0 is the gap parameter at zero temperature introduced by the BCS theory[42]. The coherence length ξ_0 may be thought as the minimum size of a Cooper pair as dictated by the Heisenburg uncertainty principle.

From the BCS theory, Mattis and Bardeen have derived a non-local equation between the total current density \vec{J} (including the supercurrent and the normal current) and the vector potential \vec{A} [39]:

$$\vec{J}(\vec{r}) = \frac{3}{4\pi^2 v_0 \hbar \lambda_{L0}^2} \int_V \frac{\vec{R} \vec{R} \cdot \vec{A}(\vec{r}') I(\omega, R, T) e^{-R/l}}{R^4} d\vec{r}' \quad (2.11)$$

with

$$\begin{aligned} I(\omega, R, T) = & - j\pi \int_{\Delta - \hbar\omega}^{\Delta} [1 - 2f(E + \hbar\omega)][g(E) \cos \alpha\Delta_2 - j \sin \alpha\Delta_2] e^{j\alpha\Delta_1} dE \\ & - j\pi \int_{\Delta}^{\infty} [1 - 2f(E + \hbar\omega)][g(E) \cos \alpha\Delta_2 - j \sin \alpha\Delta_2] e^{j\alpha\Delta_1} dE \\ & + j\pi \int_{\Delta}^{\infty} [1 - 2f(E)][g(E) \cos \alpha\Delta_1 + j \sin \alpha\Delta_1] e^{-j\alpha\Delta_2} dE, \end{aligned}$$

and

$$\Delta_1 = \begin{cases} \sqrt{E^2 - \Delta^2}, & |E| > \Delta \\ j\sqrt{\Delta^2 - E^2}, & |E| < \Delta \end{cases}, \quad \Delta_2 = \sqrt{(E + \hbar\omega)^2 - \Delta^2}, \quad g(E) = \frac{E^2 + \Delta^2 + \hbar\omega E}{\Delta_1 \Delta_2}, \quad \alpha = R/(\hbar v_0), \quad (2.12)$$

where $\Delta = \Delta(T)$ is the gap parameter at temperature T and $f(E)$ is the Fermi distribution function given by

$$f(E) = \frac{1}{1 + e^{\frac{E}{kT}}}. \quad (2.13)$$

The function $I(\omega, R, T)$ decays on a characteristic length scale $R \sim \xi_0$, which arises from the fact that the superconducting electron density cannot change considerably within a distance of the coherence length. Eq. 2.11 is consistent (qualitatively) with Eq. 2.8, because both the Pippard kernel $e^{R/\xi}$ and the full Mattis-Bardeen kernel $I(\omega, R, T) e^{R/l}$ express a decaying profile with a characteristic length dictated by the smaller of l and ξ_0 .

In the next section of this chapter, we will start from Eq. 2.11 and evaluate the surface impedance of superconductor step by step.

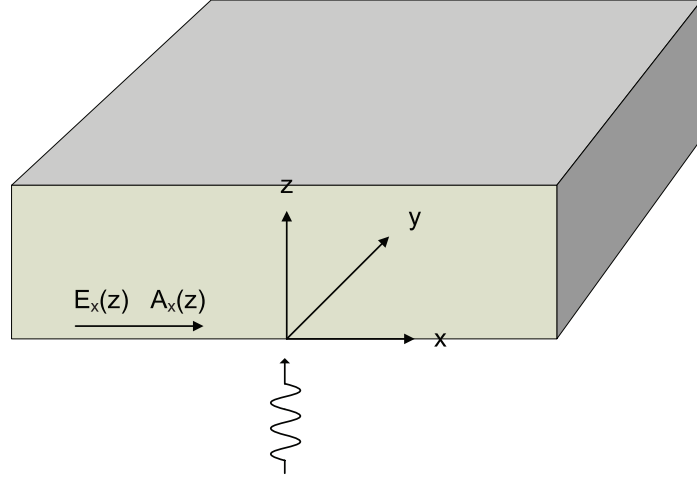


Figure 2.1: Configuration of a plane wave incident onto a bulk superconductor

2.2 Surface impedance of bulk superconductor

2.2.1 Solution of the Mattis-Bardeen kernel $K(q)$

Consider the problem of a plane wave incident onto a bulk superconductor as illustrated in Fig. 2.1. The bulk superconductor has its surface in the $x - y$ plane and fills the half space of $z > 0$. The plane wave $\vec{E} = E_x(z)\hat{x}$ is polarized in the x direction and is only a function of z , as are the vector potential $\vec{A} = A_x(z)\hat{x}$ and current density $\vec{J} = J_x(z)\hat{x}$.

By introducing the one-dimensional Fourier transform of $J_x(z)$ and $A_x(z)$:

$$\begin{aligned} J_x(z) &= \int_{-\infty}^{+\infty} J_x(q) e^{jqz} dq \\ A_x(z) &= \int_{-\infty}^{+\infty} A_x(q) e^{jqz} dq , \end{aligned} \quad (2.14)$$

Eq. 2.11, which takes a form of spatial convolution, can be converted into a product in Fourier domain:

$$J_x(q) = -K(q)A_x(q) \quad (2.15)$$

with the Mattis-Bardeen kernel (see Appendix A):

$$K(q) = -\frac{3}{\pi\hbar v_0\lambda_{L0}^2 q} \int_0^\infty \left[\frac{\sin x}{x^3} - \frac{\cos x}{x^2} \right] I(\omega, x/q, T) e^{-x/q} dx \quad (2.16)$$

where $x = qR$.

When further simplifying $K(q)$, one will encounter the following integrals:

$$\int_0^\infty e^{-bx} \left[\frac{\sin x}{x^3} - \frac{\cos x}{x^2} \right] \cos(ax) dx = R(a, b) \quad (2.17)$$

$$\int_0^\infty e^{-bx} \left[\frac{\sin x}{x^3} - \frac{\cos x}{x^2} \right] \sin(ax) dx = S(a, b). \quad (2.18)$$

These integrals can be worked out by the method of Laplace transformation. The result is:

$$W(s = b - ja) = R(a, b) + jS(a, b) = -\frac{s}{2} + \frac{1}{2}(s^2 + 1) \arctan \frac{1}{s}.$$

The derivation and the detailed expressions of $R(a, b)$ and $S(a, b)$ are given in Appendix A.

Finally, the kernel $K(q)$ works out to be

$$\begin{aligned} \text{Re}\{K(q)\} &= \frac{3}{\hbar v_0 \lambda_{L0}^2 q} \times \\ &\left\{ \int_{\max\{\Delta-\hbar\omega, -\Delta\}}^{\Delta} [1 - 2f(E + \hbar\omega)] \left\{ \frac{E^2 + \Delta^2 + \hbar\omega E}{\sqrt{\Delta^2 - E^2} \sqrt{(E + \hbar\omega)^2 - \Delta^2}} R(a_2, a_1 + b) + S(a_2, a_1 + b) \right\} dE \right. \\ &+ \frac{1}{2} \int_{\Delta-\hbar\omega}^{-\Delta} [1 - 2f(E + \hbar\omega)] \{[g(E) + 1]S(a^-, b) - [g(E) - 1]S(a^+, b)\} dE \\ &- \int_{\Delta}^{\infty} [1 - f(E) - f(E + \hbar\omega)][g(E) - 1]S(a^+, b) dE \\ &+ \left. \int_{\Delta}^{\infty} [f(E) - f(E + \hbar\omega)][g(E) + 1]S(a^-, b) dE \right\} \end{aligned} \quad (2.19)$$

$$\begin{aligned} \text{Im}\{K(q)\} &= \frac{3}{\hbar v_0 \lambda_{L0}^2 q} \times \\ &\left\{ -\frac{1}{2} \int_{\Delta-\hbar\omega}^{-\Delta} [1 - 2f(E + \hbar\omega)] \{[g(E) + 1]R(a^-, b) + [g(E) - 1]R(a^+, b)\} dE \right. \\ &+ \left. \int_{\Delta}^{\infty} [f(E) - f(E + \hbar\omega)] \{[g(E) + 1]R(a^-, b) + [g(E) - 1]R(a^+, b)\} dE \right\} \end{aligned} \quad (2.20)$$

where $b = 1/ql$, $a^+ = a_1 + a_2$, $a^- = a_2 - a_1$, $a_1 = \Delta_1/(\hbar v_0 q)$, and $a_2 = \Delta_2/(\hbar v_0 q)$. When $\hbar\omega < 2\Delta$, the first integrals in both the real and the imaginary parts of $K(q)$ vanish. Physically, these two integrals represent the breaking of Cooper pairs that have a binding energy of 2Δ with photons of energy $\hbar\omega$.

2.2.2 Asymptotic behavior of $K(q)$

It can be shown from Eq. 2.19 that to the lowest order

$$W(s) = \begin{cases} \frac{\pi}{4} & |s| \rightarrow 0 \\ \frac{1}{3s} & |s| \rightarrow \infty \end{cases} \quad (2.21)$$

and thus

$$R(a, b) = \frac{\pi}{4}, \quad S(a, b) = 0 \quad a^2 + b^2 \rightarrow 0 \quad (2.22)$$

$$R(a, b) = \frac{b}{3(a^2 + b^2)}, \quad S(a, b) = \frac{b}{3(a^2 + b^2)} \quad a^2 + b^2 \rightarrow \infty. \quad (2.23)$$

The asymptotic behavior of $K(q)$ at $q \rightarrow 0$ and $q \rightarrow \infty$ can be derived from the asymptotic form of $W(s)$.

2.2.2.1 $K(q \rightarrow 0)$

In this limit, we have

$$a \sim \frac{1}{v_0 q} \sim \frac{1}{q \xi_0} \rightarrow \infty \quad (a = a_1, a_2, a^+, a^-), \quad b \sim \frac{1}{q l} \rightarrow \infty. \quad (2.24)$$

Thus $a^2 + b^2 \rightarrow \infty$ is satisfied and from Eq. 2.23

$$R(a, b) = \frac{b}{3(a^2 + b^2)} \propto q, \quad S(a, b) = \frac{b}{3(a^2 + b^2)} \propto q. \quad (2.25)$$

It turns out that the terms of R and S in Eq. 2.19 and Eq. 2.20 cancel the factor $1/q$ in front of the integrals. The result is that $K(q)$ approaches a constant as q goes to zero. Because the condition $a^2 + b^2 \gg 1$ requires either argument be large, we arrive at the following conclusion:

$$K(q) = K_0(\xi_0, l, T), \quad q \ll \max\left\{\frac{1}{\xi_0}, \frac{1}{l}\right\} \quad (2.26)$$

where $K_0(\xi_0, l, T)$ is a constant dependent on the parameters such as ξ_0 , l , and T .

2.2.2.2 $K(q \rightarrow \infty)$

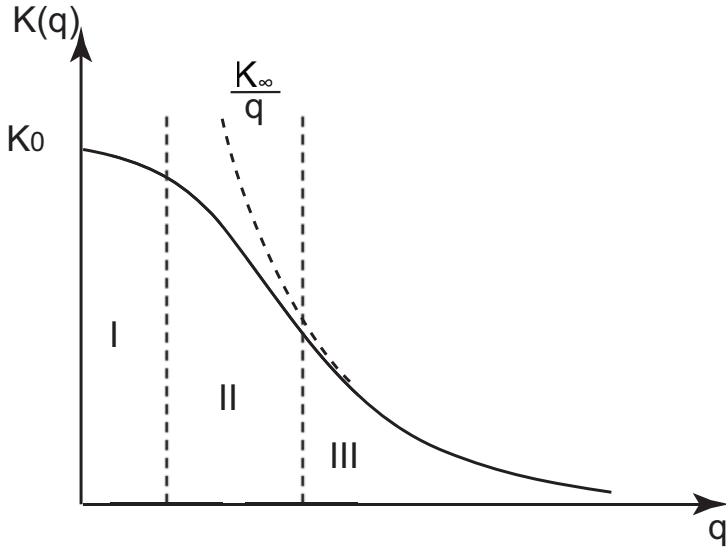
In this limit, we have

$$a \sim \frac{1}{q \xi_0} \rightarrow 0 \quad (a = a_1, a_2, a^+, a^-), \quad b \sim \frac{1}{q l} \rightarrow 0. \quad (2.27)$$

Thus $a^2 + b^2 \rightarrow 0$ is satisfied. Inserting Eq. 2.22 into Eq. 2.19, we find that $K(q)$ goes as $1/q$ as q becomes very large. Because the condition $a^2 + b^2 \ll 1$ requires both arguments be small, we arrive at the following conclusion:

$$K(q) = \frac{K_\infty(\xi_0, l, T)}{q}, \quad q \gg \max\left\{\frac{1}{\xi_0}, \frac{1}{l}\right\} \quad (2.28)$$

where $K_\infty(\xi_0, l, T)$ is another constant.

Figure 2.2: A sketch of $K(q)$

2.2.2.3 A sketch of $K(q)$

Fig. 2.2 depicts the general behavior of $K(q)$, which divides into three regimes. In regime I, where $q \ll \max\{\frac{1}{\xi_0}, \frac{1}{l}\}$, $K(q)$ approaches the constant $K_0(\xi_0, l, T)$. In regime III, where $q \gg \max\{\frac{1}{\xi_0}, \frac{1}{l}\}$, $K(q)$ goes as $K_\infty(\xi_0, l, T)/q$. Regime II is the transition regime.

The behavior of $K(q)$ shown in Fig. 2.2 agrees with our earlier discussion of the spatial domain Mattis-Bardeen kernel $I(\omega, R, T)e^{-R/l}$. Because the kernel $I(\omega, R, T)e^{-R/l}$ decays on a characteristic length of $R \sim \min\{\xi_0, l\}$, its Fourier transform $K(q)$ will span a width of $q \sim \max\{1/\xi_0, 1/l\}$.

2.2.3 Surface impedance Z_s and effective penetration depth λ_{eff} for specular and diffusive surface scattering

The surface impedance Z_s is usually defined as the ratio between the transverse components of \vec{E} field and \vec{H} field on the surface of the metal. In our configuration, as shown in Fig. 2.1,

$$Z_s = \frac{E_x}{H_y}|_{z=0}. \quad (2.29)$$

In the following, we will derive expressions which relate Z_s to the Fourier domain Mattis-Bardeen kernel function $K(q)$.

From the Maxwell equation $\nabla \times \vec{E} = -j\omega\mu_0\vec{H}$ and the relationship $\vec{H} = \nabla \times \vec{A}$, we find for our

configuration

$$\begin{aligned} E_x(z) &= -j\omega\mu_0 A_x(z) \\ H_y(z) &= \frac{dA_x(z)}{dz} \\ Z_s &= -j\omega\mu_0 \left. \frac{A_x(z)}{dA_x(z)/dz} \right|_{z=0}. \end{aligned} \quad (2.30)$$

Using another Maxwell Equation $\nabla \times \vec{H} = j\omega\epsilon_0 \vec{E} + \vec{J}$ and neglecting the displacement current term (which is much smaller than \vec{J} in metal), we get

$$J_x(z) = -\frac{d^2 A_x(z)}{dz^2}. \quad (2.31)$$

On the other hand, we have derived in Appendix A the one-dimensional form of the Mattis-Bardeen equation equivalent to Eq. 2.11:

$$\begin{aligned} J_x(z) &= \int K(\eta) A_x(z') dz' \\ K(\eta) &= \frac{3}{4\pi\hbar v_0 \lambda_L^2} \int_1^\infty du \left(\frac{1}{u} - \frac{1}{u^3} \right) I(\omega, |\eta|u, T) e^{-|\eta|u/l} \end{aligned} \quad (2.32)$$

with $\eta = z' - z$. Here $K(\eta)$ is the inverse Fourier transform of $-K(q)$ discussed in Section 2.2.1.

There is some subtlety in combining Eq. 2.31 and Eq. 2.32 to obtain a workable equation for $A_x(z)$. It turns out that how the electrons scatter from the surface matters, because we are studying the current distribution in a region very close to the surface. The usual assumption is that a portion p of the electrons reflect from the surface specularly (after reflection, the normal component of the momentum of the electron flips its sign) and the remaining portion $1 - p$ of the electrons scatter diffusively (after scattering the momentum of the electron is randomized)[43].

For the perfect specular scattering case ($p = 1$), one can make a even continuation of the field and current into the $z < 0$ space which leads to the following integro-differential equation:

$$-\frac{d^2 A_x(z)}{dz^2} = \int_{-\infty}^\infty K(\eta) A_x(z') dz'. \quad (2.33)$$

For the perfect diffusive scattering case ($p = 0$), one can derive another integro-differential equation:

$$-\frac{d^2 A_x(z)}{dz^2} = \int_0^\infty K(\eta) A_x(z') dz'. \quad (2.34)$$

A complete solution of the equation is not necessary for the purpose of evaluating the surface impedance, because only the ratio of A and its derivative on the surface is needed, according to

Eq. 2.30. However, even solving for this ratio from the two integro-differential equations is non-trivial. The solution is obtained in Fourier domain, and only the ultimate results are quoted here:

$$\text{Perfect specular scattering: } Z_s = \frac{j\mu_0\omega}{\pi} \int_{-\infty}^{\infty} \frac{dq}{q^2 + K(q)} \quad (2.35)$$

$$\text{Perfect diffusive scattering: } Z_s = \frac{j\mu_0\omega\pi}{\int_0^{\infty} \ln(1 + \frac{K(q)}{q^2}) dq} \quad (2.36)$$

where $K(q)$ is the one-dimensional Mattis-Bardeen kernel in Fourier space. Please refer to Reuter and Sondheimer [43] and Hook [44] for the detailed derivations of these two equations.

Although formula for the specular scattering case is mathematically simpler than the diffusive scattering case, the latter is considered to better represent the real situation of electron scattering at the metal surface and is more widely used. In this thesis, we adopt the diffusive scattering assumption and use Eq. 2.36 to evaluate surface impedance.

The surface impedance Z_s generally has a real and imaginary part

$$Z_s = R_s + jX_s = R + j\omega L_s = R_s + j\omega\mu_0\lambda_{\text{eff}} \quad (2.37)$$

where R_s , X_s , and L_s are called surface resistance, surface reactance, and surface inductance, respectively, and λ_{eff} is called the effective penetration depth. For temperature much lower than T_c , usually $R_s \ll X_s$. If we assume that $J_x(z)$, $H_y(z)$, and $A_x(z)$ all decay into the superconductor exponentially as $e^{-z/\lambda_{\text{eff}}}$, and ignoring R_s , we can immediately see from Eq. 2.30 that

$$Z_s \approx j\omega\mu_0\lambda_{\text{eff}} . \quad (2.38)$$

For diffusive scattering, according to Eq. 2.36, λ_{eff} can be calculated by

$$\lambda_{\text{eff}} = \frac{\pi}{\text{Re} \left[\int_0^{\infty} \ln(1 + \frac{K(q)}{q^2}) dq \right]} . \quad (2.39)$$

2.2.4 Surface impedance in two limits

It is useful to rewrite Eq. 2.36 into the following form

$$Z_s = j\mu_0\omega\lambda_{\text{L0}} \frac{\pi}{\int_0^{\infty} \ln(1 + \frac{\lambda_{\text{L0}}^2 K(Q/\lambda_{\text{L0}})}{Q^2}) dQ} \quad (2.40)$$

where both $\lambda_{\text{L0}}^2 K(Q/\lambda_{\text{L0}})$ and Q are dimensionless.

According to Eq. 2.26 and Eq. 2.28, $K(Q/\lambda_{\text{L0}})$ has the following asymptotic behavior for small and large Q :

$$\text{Regime I: } Q \ll \max\left\{\frac{\lambda_{L0}}{\xi_0}, \frac{\lambda_{L0}}{l}\right\}, \quad K(Q/\lambda_{L0}) = K_0(\xi_0, l, T) \quad (2.41)$$

$$\text{Regime III: } Q \gg \max\left\{\frac{\lambda_{L0}}{\xi_0}, \frac{\lambda_{L0}}{l}\right\}, \quad K(Q/\lambda_{L0}) = \lambda_{L0} K_\infty(\xi_0, l, T)/Q. \quad (2.42)$$

2.2.4.1 Extreme anomalous limit

In the extreme anomalous approximation, one assumes that Regime III holds for all Q of importance in the integral in Eq. 2.40, so $K(Q)$ can be replaced by its asymptotic form of Eq. 2.42.

$$\begin{aligned} Z_s &= j\mu_0\omega\lambda_{L0} \frac{\pi}{\int_0^\infty \ln(1 + \frac{\lambda_{L0}^3 K_\infty(\xi_0, l, T)}{Q^3}) dQ} \\ &= j\mu_0\omega \left[\frac{\sqrt{3}}{2} K_\infty(\xi_0, l, T)^{-1/3} \right] \end{aligned} \quad (2.43)$$

$$\lambda_{\text{eff}} = \text{Re} \left[\frac{\sqrt{3}}{2} K_\infty(\xi_0, l, T)^{-1/3} \right] \quad (2.44)$$

where $\int_0^\infty \ln(1 + 1/x^3) dx = 2\pi/\sqrt{3}$ is used.

According to Eq. 2.42, the condition for the extreme anomalous limit is

$$\xi_0 \gg \lambda_{L0} \text{ AND } l \gg \lambda_{L0}. \quad (2.45)$$

In fact, this condition can be relaxed to

$$\xi_0 \gg \lambda_{\text{eff}} \text{ AND } l \gg \lambda_{\text{eff}}. \quad (2.46)$$

This is because the lower limit of the integral $\int_0^\infty \ln(1 + 1/x^3) dx$ can be set to a small number ϵ instead of 0 without significant error. For qualitative discussion, let's take $\epsilon = 1$, which corresponds to a lower limit of $Q_l \approx \sqrt[3]{\lambda_{L0}^3 K_\infty(\xi_0, l, T)} \approx \lambda_{L0}/\lambda_{\text{eff}}$ in the integral of Eq. 2.40. For self consistency, $K(Q)$ for $Q > Q_l$ must be all in Regime III and therefore Q_l must satisfy the condition $Q_l \approx \lambda_{L0}/\lambda_{\text{eff}} \gg \max\left\{\frac{\lambda_{L0}}{\xi_0}, \frac{\lambda_{L0}}{l}\right\}$, which leads to the condition Eq. 2.46.

According to the condition given by Eq. 2.45, the extreme anomalous limit occurs when the effective penetration depth λ_{eff} , which is the characteristic length scale of the penetrating magnetic field, is much less than the smaller of ξ_0 and l , which is the decay length of the Mattis-Bardeen kernel. Extreme anomalous effect may also occur in a normal metal at high frequency and low temperature, when the classical skin depth δ becomes shorter than the scattering length l .

2.2.4.2 Local limit

In the local approximation, one assumes that Regime I holds for all Q of importance in the integral in Eq. 2.40; $K(Q)$ can be replaced by its asymptotic form in Eq. 2.41.

$$\begin{aligned} Z_s &= j\mu_0\omega\lambda_{L0}\frac{\pi}{\int_0^\infty \ln(1 + \frac{\lambda_{L0}^2 K_0(\xi_0, l, T)}{Q^2})dQ} \\ &= j\mu_0\omega[K_0(\xi_0, l, T)^{-1/2}] \\ \lambda_{\text{eff}} &= \text{Re}[K_0(\xi_0, l, T)^{-1/2}] \end{aligned} \quad (2.47)$$

where $\int_0^\infty \ln(1 + 1/x^2)dx = \pi$ is used.

The condition for this approximation to be valid, according to Eq. 2.41, is

$$\xi_0 \ll \lambda_{L0} \text{ OR } l \ll \lambda_{L0}. \quad (2.48)$$

Similar to the extreme anomalous case, this condition can be relaxed to

$$\xi_0 \ll \lambda_{\text{eff}} \text{ OR } l \ll \lambda_{\text{eff}}. \quad (2.49)$$

Another widely used definition of local (or dirty) limit in the literature is

$$l \ll \xi_0 \text{ AND } l \ll \lambda_{\text{eff}} \quad (2.50)$$

which is stronger than condition of Eq. 2.49. So the local approximation and result of effective penetration Eq. 2.47 is guaranteed to be valid in such defined local limit.

According to the condition given by Eq. 2.48, the local limit occurs when the characteristic length scale of the Mattis-Bardeen kernel (the smaller of ξ_0 and l) is much smaller than the length scale of the penetrating magnetic field (λ_{eff}). Therefore, the vector potential $A_x(z') \approx A_x(z)$ can be taken out of the integral in Eq. 2.32 as a constant, leading to a local equation. The local equation can be expressed in terms of $K_0(\xi_0, l, T)$. With $K(q) \approx K_0(\xi_0, l, T)$ for all q , $K(\eta) = K_0(\xi_0, l, T)\delta(\eta)$. The one-dimensional Eq. 2.32 reduces to

$$J_x(z) = -K_0(\xi_0, l, T)A_x(z) = \frac{K_0(\xi_0, l, T)}{j\mu_0\omega}E_x(z). \quad (2.51)$$

If a complex conductivity

$$\sigma = \frac{K_0(\xi_0, l, T)}{j\mu_0\omega} \quad (2.52)$$

is defined, the problem can be solved by using Ohm's law $J = \sigma E$, as if it were a normal metal with conductivity σ . This complex conductivity will be discussed in more detail later in this chapter.

2.2.5 Numerical approach

Analytical formulas for Z_s may be derived for a few special cases under certain approximations, which will be discussed later in this chapter. In general, Z_s has to be evaluated by numerical approach. The task for such a numerical program is to calculate a two-fold integral: for a given q the evaluation of $K(q)$ involves 6 energy integrals for $\hbar\omega > 2\Delta$ or 4 integrals for $\hbar\omega < 2\Delta$, according to Eq. 2.19 and Eq. 2.20; then an integral of $K(q)$ over q gives Z_s , as defined in Eq. 2.36. To carry out these numerical integrals efficiently and robustly, a few tactics have been used, which are briefly discussed in Appendix B.

2.2.6 Numerical results

A numerical program “surimp” was developed in the C++ language to implement the theory and algorithm discussed above. To calculate the surface impedance, the program takes frequency ω and temperature T as two independent variables, and requires five material-dependent parameters to be specified: the transition temperature T_c , the energy gap at zero temperature Δ_0 (or the ratio of Δ_0 to kT), the London penetration depth at zero temperature λ_{L0} , the mean free path l and the coherence length ξ_0 (or the Fermi velocity v_0).

In addition, the temperature dependent gap function $\Delta(T)$ is calculated using a subroutine borrowed from the “Supermix” software, a package developed at Caltech originally for the superconducting SIS mixer design[45]. In “Supermix”, the reduced energy gap $\Delta(T)/\Delta_0$ as a function of T/T_c is interpolated from a table of experimentally measured values given by Muhlschlegel[46] for $T/T_c > 0.18$, and from the low temperature approximate expression (see Eq. 2.88)

$$\frac{\Delta(T)}{\Delta_0} \approx \exp\left[-\sqrt{\frac{2\pi kT}{\Delta_0}} \exp\left(-\frac{\Delta_0}{kT}\right)\right] \approx \exp\left[-\sqrt{3.562x} \exp(-1.764/x)\right] \quad (2.53)$$

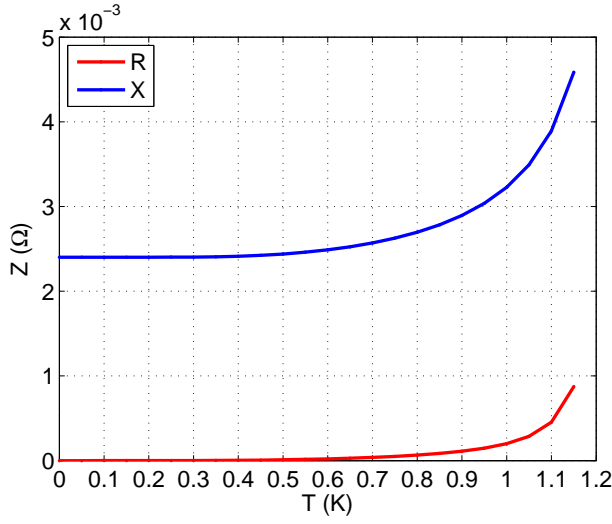
for $x = T/T_c < 0.18$, where the BCS value $\Delta_0 = 1.762kT_c$ is assumed in the right-hand side of Eq. 2.53.

2.2.6.1 λ_{eff} of Al and Nb at zero temperature

As a first application of the program “surimp”, we calculate the surface impedance Z_s of Al and Nb at $T = 0$ K and $f = 6$ GHz. The material parameters are taken from Popel [40] and are listed in Table 2.1, except that the BCS ratio of $\Delta_0/kT = 1.76$ is used. The program gives $\lambda_{\text{eff}} = 51.4$ nm for Al and $\lambda_{\text{eff}} = 63.5$ nm for Nb. From the listed material dependent parameters, we see that Al is in the extreme anomalous limit case while Nb is in the local limit case.

Table 2.1: λ_{eff} of bulk Al and Nb.

	Al	Nb
T_c [K]	1.2	9.2
λ_{L0} [nm]	15.4	33.3
v_0 [10^6 m/s]	1.34	0.28
ξ_0 [nm]	1729	39
l [nm]	10000	20
Δ_0 [meV]	0.182	1.395
$\frac{\Delta_0}{kT_c}$	1.76	1.76
λ_{eff} (0 K, 6 GHz) [nm]	51.4	63.5

Figure 2.3: Surface resistance R_s and surface reactance X_s of aluminum as a function of temperature T . The material parameters used in the calculation are from Table 2.1

2.2.6.2 Temperature dependence of Z_s

In this example, we use the program “surimp” to calculate the temperature dependence of surface impedance. The surface resistance R_s and surface inductance X_s (or the real and imaginary part of Z_s) of Al are calculated for T from 0 to 1.15 K (slightly below $T_c = 1.2K$) and the results are plotted in Fig. 2.3. As expected from the theory, we see that R_s goes to zero as $T \rightarrow 0$ while X_s approaches a nonzero finite value $X_s(0)$.

The temperature dependence of Z_s predicted by “surimp” can be tested by fitting it to the data of variation of resonance frequency f_r and quality factor Q_r of a superconducting resonators as a function of bath temperature. The relationships between f_r , Q_r and X_s , R_s are

$$\begin{aligned} \frac{\delta f_r}{f_r} &= \frac{f_r(T) - f_r(0)}{f_r(0)} = -\frac{\alpha}{2} \frac{X_s(T) - X_s(0)}{X_s(0)} = -\frac{\alpha}{2} \frac{\delta \lambda_{\text{eff}}}{\lambda_{\text{eff}}} \\ \delta \frac{1}{Q_r} &= \frac{1}{Q_r(T)} - \frac{1}{Q_r(0)} = \alpha \frac{R_s(T) - R_s(0)}{X_s(0)} \end{aligned} \quad (2.54)$$

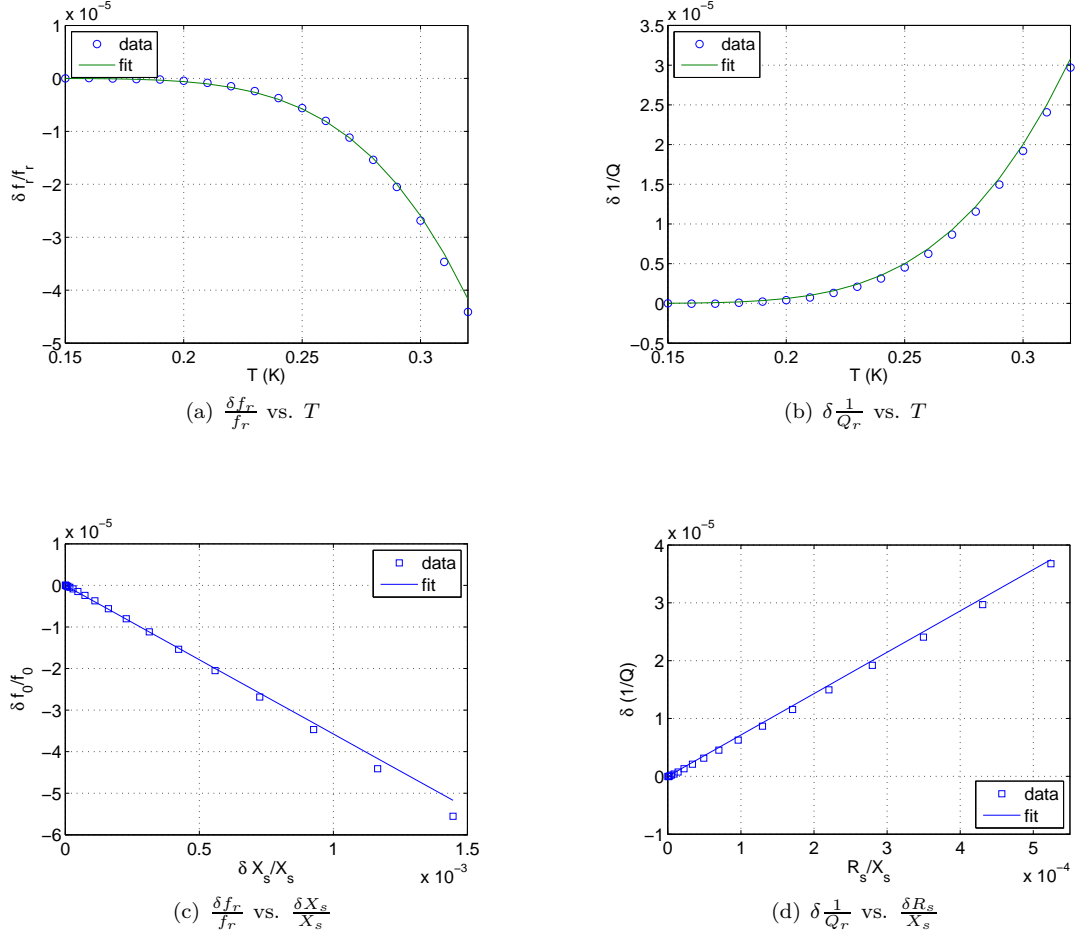


Figure 2.4: Fractional resonance frequency shift $\frac{\delta f_r}{f_r}$ and change in inverse quality factor $\delta \frac{1}{Q_r}$ vs. temperature T . Data measured from a Al resonator with film thickness $d = 220$ nm, center strip width $s = 3 \mu\text{m}$, gap width $g = 2 \mu\text{m}$, $f_r = 6.911$ GHz, $Q_r = 68000$, and $T_c = 1.25$ K. $\Delta_0 = 0.181$ meV and $\alpha = 0.07$ is obtained from the best fit. Other material-related parameters are from Table 2.1.

where α is the kinetic inductance fraction. Eq. 2.54 will be derived in the next two chapters. The measured $\delta f_r/f_r$ and $\delta 1/Q_r$ can be fitted to the calculated $\delta X_s/X_s$ and $\delta R_s/X_s$ with a simple linear fitting model according to Eq. 2.54. The energy gap Δ_0 and the kinetic inductance fraction α are taken as two fitting parameters. T_c can be measured by experiment. Other parameters are taken from the literature and set fixed. The data of $f_r(T)$ and $Q_r(T)$ from an Al resonator is fitted in this way and the result is shown in Fig. 2.4, which shows a good agreement between data and calculation.

2.2.6.3 Frequency dependence of Z_s

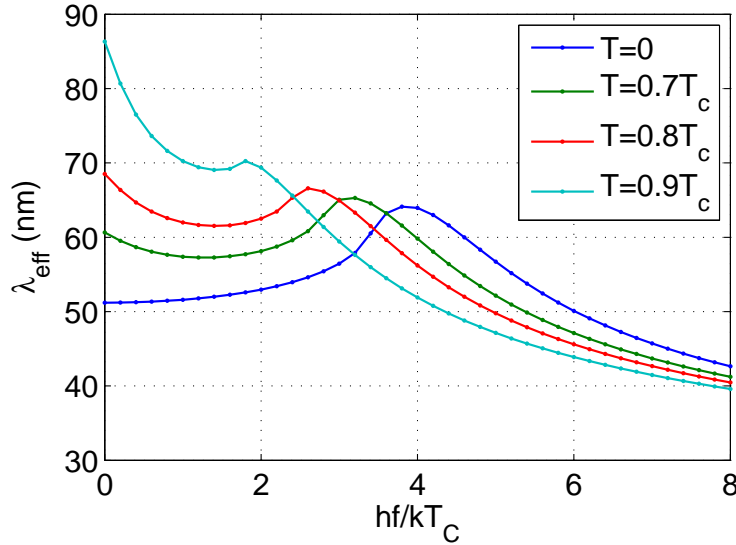


Figure 2.5: Frequency dependance of the effective penetration depth λ_{eff} of an Al bulk superconductor. The material parameters are from Table 2.1 except $\Delta_0 = 1.70kT_C$.

The frequency dependance of effective penetration depth of Al is calculated and plotted in Fig. 2.5. As a verification of our calculation, we use exactly the same material parameters used by Popel in Fig. 15 of Ref. [40]. Comparing Fig. 2.5 to Fig. 15 of Ref. [40], we find that the frequency dependence calculated by “surimp” is identical to that calculated by Popel.

2.3 Surface impedance of superconducting thin films

2.3.1 Equations for specular and diffusive surface scattering

One can also apply the Mattis-Bardeen equations to the case of thin films. Consider a plane superconductor with thickness d as shown in Fig. 2.6. If the film is thin enough, the magnetic field can penetrate through the film and both \vec{H} and \vec{J} can be nonzero inside the film, which is different from the bulk case.

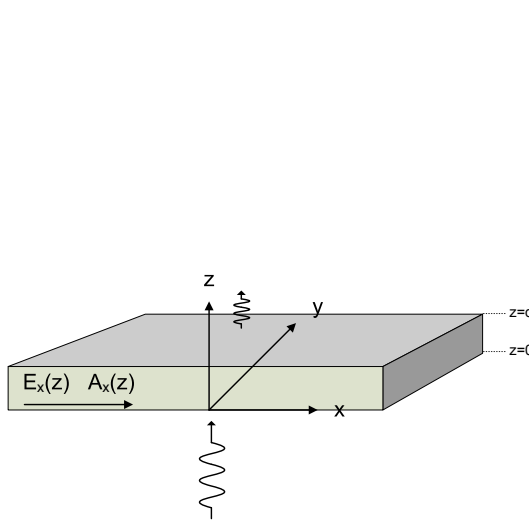


Figure 2.6: Configuration of a plane wave incident onto a superconducting thin film

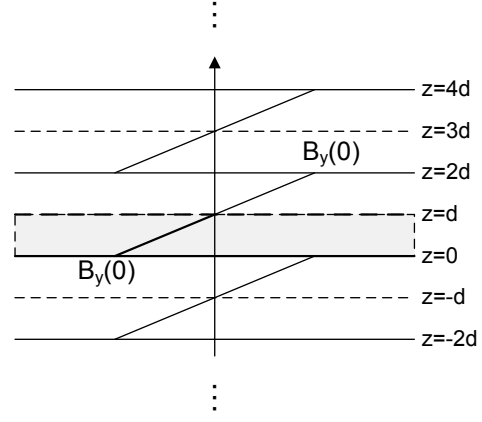


Figure 2.7: Field configuration used by Sridhar to calculate Z_s of a thin film assuming specular scattering boundary condition at both interfaces

Again, to apply the Mattis-Bardeen equations one has to assume either specular scattering or diffusive scattering at the surface. For specular scattering boundary at both sides of the film, the problem can be solved by mirroring the field and current repeatedly to fill the entire space (see Fig. 2.7) and applying the equation

$$-\frac{d^2 A_x(z)}{dz^2} = \int_{-\infty}^{\infty} K(\eta) A_x(z') dz', \quad \eta = z' - z \quad (2.55)$$

which can easily be solved in a similar manner as in the bulk case. The result is derived by Sridhar[47] to be

$$Z_s = \frac{i\mu_0\omega}{d} \sum_{n=-\infty}^{+\infty} \frac{1}{q_n^2 + K(q_n)} \quad (2.56)$$

where $q_n = n\pi/d$. Comparing Eq. 2.56 to Eq. 2.35, we see that the only change is that the integral in the bulk case has been replaced by an infinite series in the thin film case.

For the diffusive scattering boundary condition, the equation is

$$-\frac{d^2 A_x(z)}{dz^2} = \int_0^d K(\eta) A_x(z') dz', \quad \eta = z' - z \quad (2.57)$$

and unfortunately has to be solved numerically.

2.3.2 Numerical approach

There are two tasks in the numerical calculation of surface impedance of a thin film: evaluating the kernel function $K(\eta)$ and solving the integro-differential equation of Eq. 2.57.

2.3.2.1 Implementing the finite difference method

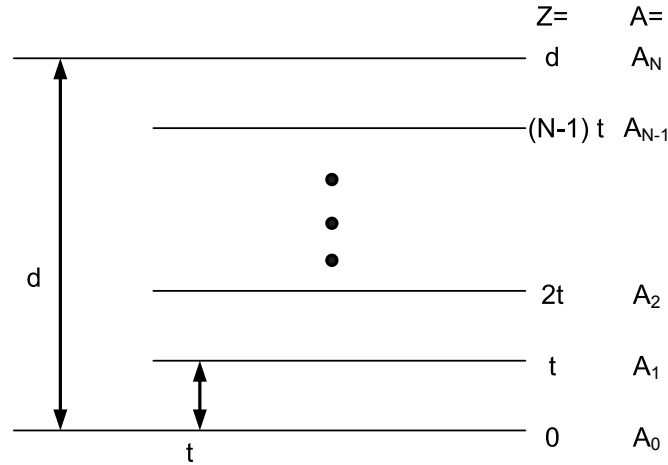


Figure 2.8: Thin film divided into N slices

The integro-differential equation of Eq. 2.57 can be solved numerically by the finite difference method (FD). To implement FD method, we first divide the film into N thin slices of equal thickness $t=d/N$ (see Fig. 2.8). Then we follow the standard procedures to convert Eq. 2.57 into a discrete FD equation. On the left-hand side, we employ the simple three-point approximation formula

$$\frac{d^2 A_x(z)}{dz^2} \approx (A_{n+1} - 2A_n + A_{n-1})/t^2. \quad (2.58)$$

On the right-hand side, we apply the simple extended trapezoidal rule to approximate the integral as a sum

$$\int_0^d K(\eta) A_x(z') dz' \approx t \sum_{n'=0}^N K_{nn'} A(n') \quad (2.59)$$

where

$$K_{nn'} = \begin{cases} \frac{1}{2} K(|n - n'| t) & \text{if } n' = 0 \text{ or } N \\ \frac{1}{t} \int_{(n-1/2)t}^{(n+1/2)t} K(|nt - x'|) dx' & \text{if } n' = n \\ K(|n - n'| t) & \text{otherwise} \end{cases}. \quad (2.60)$$

So we get the following FD equations

$$A_{n+1} - 2A_n + A_{n-1} = -t^3 \sum_{n'=0}^N K_{nn'} A(n'), \quad n = 1, \dots, N-1. \quad (2.61)$$

2.3.2.2 Boundary condition

Eq. 2.61 provides $N-1$ linear equations with $N+1$ unknowns ($A_0 \dots A_N$), so two more equations are needed. The two additional equations come from the boundary conditions at the interfaces at $z=0$ and $z=d$. In the configuration of Fig. 2.6, both sides of the film are connected to free space and the electromagnetic wave is incident from $z=0$ into the film. In this case, at $z=0$ one can assume either boundary conditions of the first kind

$$A(z)|_{z=0} = 1 \Rightarrow A_0 = 1 \quad (2.62)$$

or of the second kind

$$H_y(0) = \frac{dA(z)}{dz} \Big|_{z=0} = 1 \Rightarrow A_1 - A_0 = t \quad (2.63)$$

where a two point formula for $dA(z)/dz$ is used. Physically, the former specifies a vector potential and the latter specifies a magnetic field on the $z=0$ surface.

At the interface of $z=d$, one usually assumes that the transmitted wave sees the free space impedance

$$Z_0 = -j\omega\mu_0 \frac{A(z)}{\frac{dA(z)}{dz}} \Big|_{z=d} \Rightarrow (1 + \frac{j\omega\mu_0}{Z_0} t) A_N - A_{N-1} = 0, \quad (2.64)$$

Because the free space impedance $Z_0 \approx 377 \Omega$ is usually much larger than the surface impedance of the film, boundary condition Eq. 2.64 is virtually equivalent to

$$H_y(d) = \frac{dA(z)}{dz} \Big|_{z=d} = 0 \Rightarrow A_N = A_{N-1} \quad (2.65)$$

which physically forces a zero magnetic field on the $z=d$ surface.

2.3.2.3 Retrieving the results

With proper boundary conditions, the FD problem is ready to solve. The $N+1$ linear equations can easily be solved with standard numerical algorithms. Unfortunately, we can not utilize a sparse algorithm to accelerate the calculation.

For thin films, the transmitted wave is often important and can not be neglected. In these cases, it is often not enough to consider only the surface impedance at the surface $z=0$. We can generalize

the concept of surface impedance and define a pair of impedances for the thin film

$$Z_{11} = \frac{E_x(0)}{H_y(0)} = -j\omega\mu_0 \frac{A_x(z)|_{z=0}}{dA_x(z)/dz|_{z=0}} = -j\omega\mu_0 t \frac{A_0}{A_1 - A_0} \quad (2.66)$$

$$Z_{21} = \frac{E_x(d)}{H_y(0)} = -j\omega\mu_0 \frac{A_x(z)|_{z=d}}{dA_x(z)/dz|_{z=0}} = -j\omega\mu_0 t \frac{A_N}{A_1 - A_0} \quad (2.67)$$

Instead of returning one impedance, both Z_{11} and Z_{21} are calculated from the solution and reported by our numerical program.

In the case that the electromagnetic wave is incident from one side of the thin film ($d < \lambda_{\text{eff}}$), with the other side exposed to the free space, we have $H_y(d) \approx 0$ (see the previous discussion of Eq. 2.65) and $H_y(0) = K = \int_0^d J_x dz$ according to Ampere's law, where K represents the sheet current (current flowing in the entire film thickness). Therefore the electric fields at the two surfaces are given by

$$E_x(0) = Z_{11}K, \quad E_x(d) = Z_{21}K. \quad (2.68)$$

In the anti-symmetric excitation case, as in a TEM mode of a superconducting coplanar waveguide (discussed in more detail in the next chapter), the electromagnetic wave is incident from both sides of the film with $H_y(0) = -H_y(d)$. One can decompose this problem into two problems, each with a wave incident from one side. It can be shown that in this anti-symmetric excitation case,

$$\begin{aligned} H_y(0) &= -H_y(d) = K/2 \\ E_x(0) &= E_x(d) = (Z_{11} + Z_{21})K/2. \end{aligned} \quad (2.69)$$

2.3.3 Numerical results

With slight modification to “surimp”, a program “surimpfilm” is developed to calculate the surface impedance of a superconducting thin film. The program takes ω and T as independent variables and the same 5 material parameters. It takes the film thickness d and the number of subdivisions to the film N as two additional parameters. Besides, all 3 types of boundary conditions (specifying value of A , value of H or the load impedance Z) can be applied to both the top side and the bottom side of the film. The values of generalized surface impedance Z_{11} and Z_{12} are returned from the program.

2.3.3.1 λ_{eff} of Al thin film

We use “surimpfilm” to calculate the thickness dependence of surface impedance for Al at $T = 0$ K and $f = 6$ GHz. The result is shown in Fig. 2.9. We see that Z_{11} approaches its bulk value when the thickness is large compared to the bulk penetration depth (roughly $d > 3\lambda_{\text{eff}}$) and Z_{12} goes to zero, implying no magnetic field penetrates through. As the thickness of the film is reduced, both Z_{11}

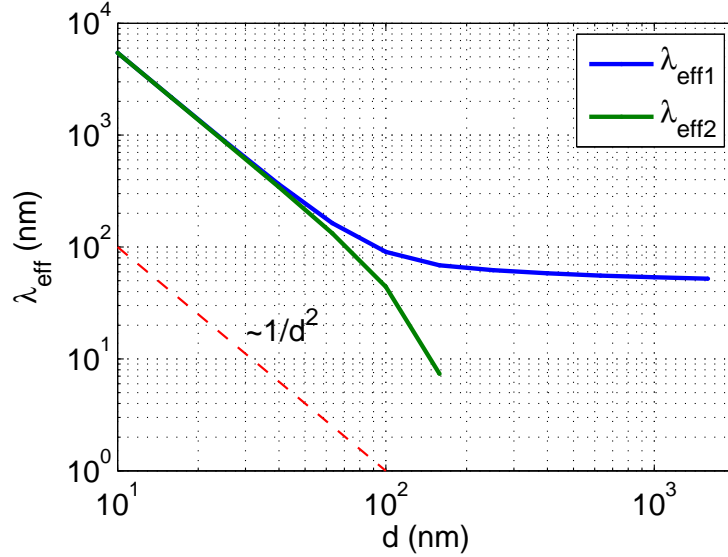


Figure 2.9: Effective penetration depth of Al thin film vs. thickness. $f = 6$ GHz, $T = 0$ K, and other material related parameters are from Table 2.1, except that the mean free path l is set to the film thickness d . In the calculation, $N = 400$ division is used. The two effective penetration depths are defined as $\lambda_{\text{eff}1} = \frac{Z_{11}}{j\omega\mu_0}$ and $\lambda_{\text{eff}2} = \frac{Z_{21}}{j\omega\mu_0}$.

and Z_{21} increase. Ultimately when the film is very thin, Z_{11} and Z_{21} become equal, which implies that the film is completely penetrated. We also notice that the impedance goes as $1/d^2$, which will be explained later in this chapter.

2.4 Complex conductivity $\sigma = \sigma_1 - j\sigma_2$

The concept of complex conductivity $\sigma = \sigma_1 - j\sigma_2$ was first introduced by Glover and Tinkham[48] for the superconducting states. σ_1 and σ_2 are expressed by two integrals[39]

$$\begin{aligned} \frac{\sigma_1}{\sigma_n} &= \frac{2}{\hbar\omega} \int_{\Delta}^{\infty} \frac{[f(E) - f(E + \hbar\omega)](E^2 + \Delta^2 + \hbar\omega E)}{\sqrt{E^2 - \Delta^2} \sqrt{(E + \hbar\omega)^2 - \Delta^2}} dE \\ &\quad + \frac{1}{\hbar\omega} \int_{\Delta - \hbar\omega}^{-\Delta} \frac{[1 - 2f(E + \hbar\omega)](E^2 + \Delta^2 + \hbar\omega E)}{\sqrt{E^2 - \Delta^2} \sqrt{(E + \hbar\omega)^2 - \Delta^2}} dE \end{aligned} \quad (2.70)$$

$$\frac{\sigma_2}{\sigma_n} = \frac{1}{\hbar\omega} \int_{\max\{\Delta - \hbar\omega, -\Delta\}}^{\Delta} \frac{[1 - 2f(E + \hbar\omega)](E^2 + \Delta^2 + \hbar\omega E)}{\sqrt{\Delta^2 - E^2} \sqrt{(E + \hbar\omega)^2 - \Delta^2}} dE. \quad (2.71)$$

We recall that the expression for $K(q)$ in Eq. 2.19 and Eq. 2.20 generally has 4 integrals in the real part and 2 integrals in the imaginary part. We will show that under certain conditions some of the integrals vanish and the total 6 integrals reduce to the 3 integrals of σ_1 and σ_2 . In these cases, Z_s and λ_{eff} have simplified expressions in terms of σ_1 and σ_2 .

2.4.1 Surface impedance Z_s in various limits expressed by σ_1 and σ_2

2.4.1.1 Thick film, extreme anomalous limit

In the extreme anomalous limit, both Z_s and λ_{eff} are related only to the value of $K_\infty(\xi_0, l, T)$ according to Eq. 2.44. It can be shown by comparing the asymptotic expression of $K(q)$ at $q \rightarrow \infty$ to the expression of σ in Eq. 2.70 and 2.71 that

$$K_\infty(\xi_0, l, T) = \frac{3\pi\omega}{4v_0\lambda_{L0}^2} \frac{\sigma_2 + j\sigma_1}{\sigma_n}. \quad (2.72)$$

Thus

$$Z_s = \frac{j\sqrt{3}\mu_0\omega}{2} \left[\frac{3\pi\omega}{4v_0\lambda_{L0}^2} \frac{\sigma_2 + j\sigma_1}{\sigma_n} \right]^{-1/3}. \quad (2.73)$$

2.4.1.2 Thick film, local limit

In the local limit, both Z_s and λ_{eff} are related only to the value of $K_0(\xi_0, l, T)$ according to Eq. 2.47. It can be shown by comparing the asymptotic expression of $K(q)$ at $q \rightarrow 0$ to the expression of σ in Eq. 2.70 and 2.71 that

$$K_0(\xi_0, l, T) = \frac{\omega l}{v_0\lambda_{L0}^2} \frac{\sigma_2 + j\sigma_1}{\sigma_n}. \quad (2.74)$$

From Eq. 2.6 and the expression of σ_n

$$\sigma_n = \frac{ne^2\tau}{m} \quad (2.75)$$

where n , e , and m are the density, charge, and mass of the electron, respectively, it can be derived that

$$\lambda_{L0} = \sqrt{\frac{l}{\mu_0\sigma_nv_0}}. \quad (2.76)$$

Inserting Eq. 2.76 into Eq. 2.74, we get another equivalent expression of $K_0(\xi_0, l, T)$

$$K_0(\xi_0, l, T) = j\omega\mu_0(\sigma_1 - j\sigma_2) \quad (2.77)$$

which is consistent with Eq. 2.52. It follows from Eq. 2.47 that

$$\begin{aligned} Z_s &= j\mu_0\omega \left[\frac{\omega l}{v_0\lambda_{L0}^2} \frac{\sigma_2 + j\sigma_1}{\sigma_n} \right]^{-1/2} \\ \text{or} \\ Z_s &= \sqrt{\frac{j\mu_0\omega}{\sigma_1 - j\sigma_2}}. \end{aligned} \quad (2.78)$$

We again see that Z_s of a superconductor in the local limit can be directly obtained by substituting $\sigma = \sigma_1 - j\sigma_2$ for σ_n in the corresponding classical formulas.

2.4.1.3 Thin film

If the film thickness t is smaller than the electron mean free path in the bulk case l_∞ , l will be limited by surface scattering and $l \approx d$. If in addition the local condition $l \ll \xi_0$ and $l \ll \lambda_{L0}$ are satisfied, the local equation $\vec{J} = \sigma \vec{E}$ applies. Moreover, if the film thickness satisfies $d \ll \lambda_{\text{eff}}$, the field penetrates through the entire film and the current distribution is almost uniform across the film with $J_x(z) \approx J_x(0)$, as is the electric field $E_x(z) \approx E_x(0)$. The following expression of Z_s can be derived

$$Z_s = Z_{11} = Z_{21} = \frac{E_x(0)}{\int_0^d J_x(z) dz} = \frac{1}{(\sigma_1 - i\sigma_2)d}, \quad (2.79)$$

where Z_{11} and Z_{12} are defined in Eq. 2.66 and 2.67. Because σ goes as $1/l \sim 1/d$, Z_s has a $1/d^2$ dependence on the film thickness d .

2.4.2 Change in the complex conductivity $\delta\sigma$ due to temperature change and pair breaking

2.4.2.1 Relating δZ_s to $\delta\sigma$

MKIDs operate on a principle that the surface impedance Z_s of a superconducting film changes when photons break Cooper pairs and generate quasiparticles (QPs)[14, 16]. The responsivity of MKIDs is related to dZ_s/dn_{qp} , where n_{qp} is the QP density.

It follows from the discussion in the previous section that the change in Z_s is related to the change in σ by

$$\frac{\delta Z_s}{Z_s} = \gamma \frac{\delta\sigma}{\sigma}, \quad \gamma = \begin{cases} -1/2 & \text{Thick film, local limit} \\ -1/3 & \text{Thick film, extreme anomalous limit} \\ -1 & \text{Thin film, local limit} \end{cases}. \quad (2.80)$$

Thus, $d\sigma/dn_{qp}$ becomes an important quantity in discussing responsivity of MKIDs.

2.4.2.2 Effective chemical potential μ^*

One straightforward way of calculating $d\sigma/dn_{qp}$ is through $d\sigma/dn_{qp} = \frac{\partial\sigma(T)/\partial T}{\partial n_{qp}(T)/\partial T}$ (the ratio between the change in the conductivity and the change in the quasiparticle density, both caused by a change

in the bath temperature) from Eq. 2.70, Eq. 2.71, and

$$n_{qp} = 4N_0 \int_0^\infty \frac{1}{1 + e^{\frac{E-\mu^*}{kT}}} d\epsilon, \quad \epsilon = \sqrt{E^2 - \Delta^2} \quad (2.81)$$

where N_0 is the single spin density of states. The result from such a calculation gives $\delta\sigma$ due to a change in thermal QP density from a change in bath temperature, which does not directly apply to excess QPs from pair breaking. To account for excess QPs, we adopt Owen and Scalapino's treatment[49] and introduce an effective chemical potential μ^* to the Fermi distribution function

$$f(E; \mu^*, T) = \frac{1}{1 + e^{\frac{E-\mu^*}{kT}}}. \quad (2.82)$$

Physically, Eq. 2.82 treats the QPs as a Fermi gas with a thermal equilibrium distribution characterized by the chemical potential μ^* and the temperature T . This assumption is valid because at low temperatures, phonons with energy less than 2Δ (under-gap phonons) are much more abundant than the phonons with energy larger than 2Δ (over-gap phonons); therefore the time scale τ_l for excess QPs to thermalize with the lattice (phonon) temperature T (assisted by under-gap phonons) is much shorter than the time scale τ_{qp} for excess QPs to recombine (assisted by over-gap phonons); as a result, during the time $\tau_l < t < \tau_{qp}$, the QPs may be described using the Fermi function given by Eq. 2.82.

With the introduction of μ^* , the total QP density n_{qp} (including both thermal and excess QPs), the superconducting gap Δ , and the complex conductivity σ can be rederived by substituting $f(E; \mu^*, T)$ for $f(E; T)$ in the corresponding BCS formula and the Mattis-Bardeen formula. The relevant equations now modify to

$$n_{qp} = 4N_0 \int_0^\infty \frac{1}{1 + e^{\frac{E-\mu^*}{kT}}} d\epsilon, \quad \epsilon = \sqrt{E^2 - \Delta^2} \quad (2.83)$$

$$\frac{1}{N_0 V} = \int_0^{\hbar\omega_c} \frac{\tanh \frac{E-\mu^*}{2kT}}{E} dE \quad (2.84)$$

$$\begin{aligned} \frac{\sigma_1}{\sigma_n} &= \frac{2}{\hbar\omega} \int_\Delta^\infty \frac{[f(E; \mu^*, T) - f(E + \hbar\omega; \mu^*, T)](E^2 + \Delta^2 + \hbar\omega E)}{\sqrt{E^2 - \Delta^2} \sqrt{(E + \hbar\omega)^2 - \Delta^2}} dE \\ &\quad + \frac{1}{\hbar\omega} \int_{\Delta - \hbar\omega}^{-\Delta} \frac{[1 - 2f(E + \hbar\omega; \mu^*, T)](E^2 + \Delta^2 + \hbar\omega E)}{\sqrt{E^2 - \Delta^2} \sqrt{(E + \hbar\omega)^2 - \Delta^2}} dE \end{aligned} \quad (2.85)$$

$$\frac{\sigma_2}{\sigma_n} = \frac{1}{\hbar\omega} \int_{\Delta - \hbar\omega}^\Delta \frac{[1 - 2f(E + \hbar\omega; \mu^*, T)](E^2 + \Delta^2 + \hbar\omega E)}{\sqrt{\Delta^2 - E^2} \sqrt{(E + \hbar\omega)^2 - \Delta^2}} dE. \quad (2.86)$$

2.4.2.3 Approximate formulas of Δ , n_{qp} , σ , and $d\sigma/dn_{qp}$ for both cases

Under the condition that $\hbar\omega \ll \Delta$ (Cond. 1), $kT \ll \Delta$ (Cond. 2) and $e^{-\frac{E-\mu^*}{kT}} \ll 1$ (Cond. 3), Eq. 2.83–2.86 have the following analytical approximate formula[50]:

$$n_{qp} = 2N_0\sqrt{2\pi kT\Delta}e^{-\frac{\Delta-\mu^*}{kT}} \quad (2.87)$$

$$\frac{\Delta}{\Delta_0} = 1 - \sqrt{\frac{2\pi kT}{\Delta}}e^{-\frac{\Delta-\mu^*}{kT}} = 1 - \frac{n_{qp}}{2N_0\Delta} \quad (2.88)$$

$$\frac{\sigma_1}{\sigma_n} = \frac{4\Delta}{\hbar\omega}e^{-\frac{\Delta-\mu^*}{kT}} \sinh(\xi)K_0(\xi), \quad \xi = \frac{\hbar\omega}{2kT} \quad (2.89)$$

$$\frac{\sigma_2}{\sigma_n} = \frac{\pi\Delta}{\hbar\omega}[1 - 2e^{-\frac{\Delta-\mu^*}{kT}}e^{-\xi}I_0(\xi)] \quad (2.90)$$

where I_n , K_n are the n th order modified Bessel function of the first and second kind, respectively

The first two conditions (Cond. 1 and Cond. 2) are apparently satisfied by a typical Al MKID with $T_c = 1.2$ K and microwave frequency $\omega/2\pi$ below 10 GHz. Meanwhile, the QP density due to pair breaking from a photon with energy $h\nu$ is estimated by $n_{qp} \approx \frac{h\nu}{\Delta V}$. Assuming a sensing volume $V \sim 3 \mu m \times 0.2 \mu m \times 100 \mu m$ (center strip width \times film thickness \times quasiparticle diffusion length) and taking $T=0.1$ K, $N_0 = 1.72 \times 10^{10} \mu m^{-3} eV^{-1}$, and $\Delta = 0.18$ meV for Al, $e^{-\frac{E-\mu^*}{kT}}$ is estimated from Eq. 2.87 to be 0.1 for a 6 keV photon and 1.4×10^{-5} for a 1 eV photon, both much less than 1. Thus for Al MKIDs up to X-ray band, the third condition (Cond. 3) is also satisfied.

Now we are ready to derive σ and its derivative for the two cases.

Case 1: thermal QPs due to temperature change

In Eq. 2.87–2.90, only two of the four variables Δ , n_{qp} , μ^* , and T are independent. By taking μ^* and T as independent variables, setting $\mu^* = 0$, and keeping only the lowest-order terms in Eq. 2.87–2.90, we arrive at the following results

$$\frac{\sigma_1(T)}{\sigma_n} = \frac{4\Delta_0}{\hbar\omega}e^{-\frac{\Delta_0}{kT}} \sinh(\xi)K_0(\xi) \quad (2.91)$$

$$\frac{\sigma_2(T)}{\sigma_n} = \frac{\pi\Delta_0}{\hbar\omega}[1 - \sqrt{\frac{2\pi kT}{\Delta_0}}e^{-\frac{\Delta_0}{kT}} - 2e^{-\frac{\Delta_0}{kT}}e^{-\xi}I_0(\xi)] \quad (2.92)$$

$$n_{qp}(T) = 2N_0\sqrt{2\pi kT\Delta_0}e^{-\frac{\Delta_0}{kT}} \quad (2.93)$$

$$\frac{d\sigma_1}{dn_{qp}} = \sigma_n \frac{1}{N_0\hbar\omega} \sqrt{\frac{2\Delta_0}{\pi kT}} \sinh(\xi)K_0(\xi) \left\{ \frac{\frac{\Delta_0}{kT} - \xi \frac{\cosh(\xi)}{\sinh(\xi)} + \xi \frac{K_1(\xi)}{K_0(\xi)}}{\frac{\Delta_0}{kT} + \frac{1}{2}} \right\} \quad (2.94)$$

$$\frac{d\sigma_2}{dn_{qp}} = \sigma_n \frac{-\pi}{2N_0\hbar\omega} [1 + \sqrt{\frac{2\Delta_0}{\pi kT}}e^{-\xi}I_0(\xi) \left\{ \frac{\frac{\Delta_0}{kT} + \xi - \xi \frac{I_1(\xi)}{I_0(\xi)}}{\frac{\Delta_0}{kT} + \frac{1}{2}} \right\}] \quad (2.95)$$

where the directives are evaluated by $d\sigma/dn_{qp} = \frac{\partial\sigma(T)/\partial T}{\partial n_{qp}(T)/\partial T}$.

Case 2: excess QPs due to pair breaking

Using Eq. 2.87 to suppress the explicit dependence of μ^* , taking n_{qp} and T as independent variables and keeping the lowest-order terms in Eq. 2.88–2.90, we arrive at the following result

$$\frac{\sigma_1(n_{qp}, T)}{\sigma_n} = \frac{2\Delta_0}{\hbar\omega} \frac{n_{qp}}{N_0\sqrt{2\pi kT\Delta_0}} \sinh(\xi) K_0(\xi) \quad (2.96)$$

$$\frac{\sigma_2(n_{qp}, T)}{\sigma_n} = \frac{\pi\Delta_0}{\hbar\omega} [1 - \frac{n_{qp}}{2N_0\Delta_0} (1 + \sqrt{\frac{2\Delta_0}{\pi kT}} e^{-\xi} I_0(\xi))] \quad (2.97)$$

$$\frac{d\sigma_1}{dn_{qp}} = \sigma_n \frac{1}{N_0\hbar\omega} \sqrt{\frac{2\Delta_0}{\pi kT}} \sinh(\xi) K_0(\xi) \quad (2.98)$$

$$\frac{d\sigma_2}{dn_{qp}} = -\sigma_n \frac{\pi}{2N_0\hbar\omega} [1 + \sqrt{\frac{2\Delta_0}{\pi kT}} e^{-\xi} I_0(\xi)] \quad (2.99)$$

where the directives are evaluated by $d\sigma/dn_{qp} = \partial\sigma(n_{qp}, T)/\partial n_{qp}$. In this case, we find that σ is a linear function of n_{qp} and

$$\kappa = \frac{\delta\sigma/|\sigma|}{\delta n_{qp}} \approx \frac{1}{\pi N_0} \sqrt{\frac{2}{\pi kT\Delta_0}} \sinh(\xi) K_0(\xi) + j \frac{1}{2N_0\Delta_0} [1 + \sqrt{\frac{2\Delta_0}{\pi kT}} e^{-\xi} I_0(\xi)]. \quad (2.100)$$

It can be derived from Eq. 2.80 that

$$\frac{\delta Z_s}{|Z_s|} = \kappa |\gamma| \delta n_{qp}. \quad (2.101)$$

2.4.2.4 Equivalence between thermal quasiparticles and excess quasiparticles from pair breaking

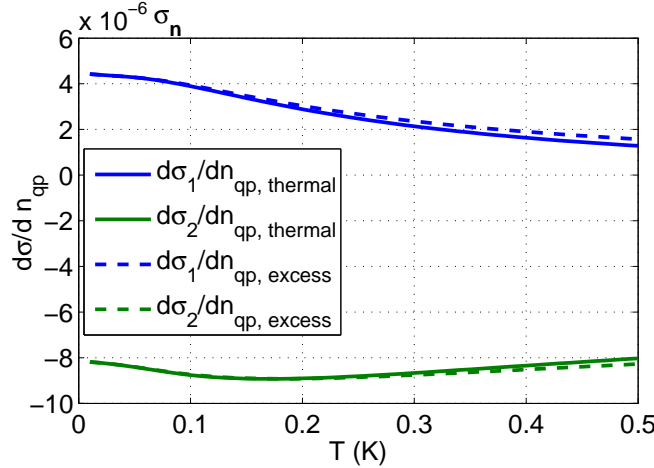


Figure 2.10: $d\sigma/dn_{qp}$ vs. T calculated for two cases. $\frac{\partial\sigma_1(T)/\partial T}{\partial n_{qp}(T)/\partial T}$ and $\frac{\partial\sigma_2(T)/\partial T}{\partial n_{qp}(T)/\partial T}$ are plotted by the upper and lower solid lines, $\frac{\partial\sigma_1(n_{qp}, T)}{\partial n_{qp}}$ and $\frac{\partial\sigma_2(n_{qp}, T)}{\partial n_{qp}}$ by dashed lines. Other parameters are $f = 6$ GHz, $N_0 = 1.72 \times 10^{10} \mu\text{m}^{-3}\text{eV}^{-1}$, and $\Delta_0 = 0.18$ meV for Al.

Comparing Eq. 2.94 and Eq. 2.95 to Eq. 2.98 and Eq. 2.99, we find the two cases only differ from

each other by the factors inside the curly brackets, which are found to be close to unity over the temperature and frequency range that MKIDs operate in.

The values of $d\sigma/dn_{qp}$ of the two cases are evaluated for Al and plotted in Fig. 2.10. We see that the thermal QP curves (solid lines) separates very little from the excess QP curves (dashed lines), which means that adding a thermal quasiparticle (by slightly changing the temperature) and adding a non-thermal quasiparticle (by breaking Cooper pairs) have the same effect on changing the complex conductivity. The equivalence between thermal and excess QPs allows us to use bath temperature sweep to calibrate the responsivity of MKIDs instead of using a external source.

Chapter 3

Kinetic inductance fraction of superconducting CPW

3.1 Theoretical calculation of α from quasi-static analysis and conformal mapping technique

In Chapter 2 we discussed how the electromagnetic properties of a superconductor changes with temperature or external Cooper-pair breaking. The topic of this chapter is how such a change will affect the transmission properties of a superconducting transmission line.

In this chapter, we first introduce and validate the quasi-static assumption for the superconducting CPW (SCPW). Under this assumption, the SCPW is fully characterized by its distributed inductance L and capacitance C according to the transmission line theory. As a common practice, we first treat the SCPW as a perfect-conductor CPW and calculate its geometric inductance L_m . The effect of superconductivity is then included perturbatively as an additional inductance L_{ki} called kinetic inductance. The ratio of L_{ki} to the total inductance $L = L_m + L_{ki}$ is called the kinetic inductance fraction α , which is an important parameter related to the MKID responsivity.

This chapter is divided into two parts. The first half mainly discusses the theoretical calculation of α , including the calculation of L_m , C , and a geometrical factor g which relates L_{ki} to the penetration depth λ_{eff} . Throughout these calculations, the powerful tool of conformal mapping is widely applied and both analytical formulas and numerical methods are derived. The second half of this chapter discusses the experimental technique used to determine α . The experimental results are compared to the theoretical calculations. Both thick film and thin film cases are covered in the theory part as well as in the experimental part.

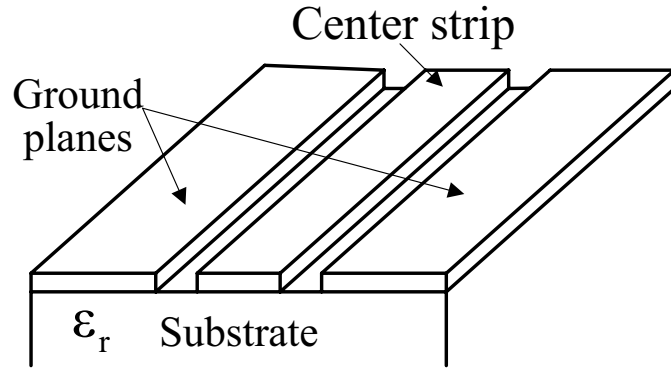


Figure 3.1: Coplanar waveguide geometry

3.1.1 Quasi-TEM mode of CPW

Consider an electromagnetic wave propagating on a transmission line along the z -axis. The field quantities \vec{E} , \vec{H} , and the current density \vec{J} can be written in a general form as (with a harmonic time dependence $e^{j\omega t}$ omitted):

$$\vec{X}(x, y, z) = [\vec{x}_t(x, y) + x_z(x, y)\hat{z}]e^{-j\beta z} \quad (3.1)$$

where β is the propagation constant and the vector \vec{X} is decomposed into its transverse component \vec{x}_t and longitudinal component $x_z\hat{z}$.

The solutions to Maxwell's equations show that a CPW made of perfect conductor (perfect CPW) immersed in a homogenous media can support a TEM mode. In this “pure” TEM mode, the longitudinal components of \vec{E} and \vec{H} vanish while the transverse component of current density \vec{J} vanishes:

$$e_z = 0, h_z = 0, j_t = 0. \quad (3.2)$$

A superconducting CPW differs from the above case in two aspects. First, a conventional CPW is usually made on a substrate (see Fig. 3.1), so the regions on the top and bottom of the CPW are filled with media of different dielectric constants. This inhomogeneity gives rise to longitudinal components e_z , h_z and transverse component j_t . Second, the superconductor has a finite surface impedance which gives rise to longitudinal components e_z on the surface. The conclusion is that a superconducting CPW cannot support a pure TEM mode.

However, both theory and lab measurements show that the propagation mode in a superconducting CPW is quasi-TEM, where non-TEM field components are much smaller than the TEM components. For instance, j_t contributed by the inhomogeneity from the substrate/air interface is

estimated to be on the order of (see Appendix C)

$$\frac{j_t}{j_z} \sim \frac{w}{\lambda} \quad (3.3)$$

where w is the transverse dimension of the transmission line and λ is the actual wavelength of the wave in propagation. A lithographed CPW line used in MKIDs usually has a transverse dimension of 10–100 μm (the distance between the two ground planes) while the wavelength is usually thousands of microns. Thus, $j_t/j_z \sim 1\%$ and j_t is indeed small as compared to j_z .

On the other hand, according to the definition of surface impedance, superconductor contributes an e_z on the metal surface that is estimated by

$$\frac{e_z}{e_t} \approx \frac{Z_s}{Z_0} \quad (3.4)$$

where Z_s is the surface impedance and Z_0 is the characteristic impedance of the transmission line. For CPW made of superconducting Al, Z_s is on the order of $\text{m}\Omega$ (e.g., surface reactance $X_s \approx 2 \text{ m}\Omega$ for $T=0 \text{ K}$, $f=5 \text{ GHz}$, and $\lambda_{\text{eff}} = 50 \text{ nm}$) and $Z_0 = 50 \Omega$. Thus, $e_z/e_t \sim 10^{-4}$ in our case. Even for a normal metal, Z_s is usually much smaller than Z_0 and so e_z is always much smaller than e_t .

It can be shown [51] that for the quasi-TEM mode of CPW, the transverse fields \vec{e}_t and \vec{h}_t are solutions to two-dimensional static problems, from which the distributed capacitance C and inductance L can be derived.

In the electrostatic problem, because \vec{e}_t quickly attenuates to zero over the Thomas-Fermi length (on the order of one \AA , which is always much smaller than the film thickness that we use) into the superconductor, the electric energy inside the superconductor has a negligible contribution to the capacitance C and the electric field \vec{e}_t outside the superconductor is almost identical to that for a perfect conductor. Therefore, \vec{e}_t can be solved with the introduction of an electric potential Φ , which satisfies the Laplace's equation

$$\nabla^2 \Phi = 0 \quad (3.5)$$

outside the superconductor, and has constant values at the surfaces of the superconductors which are now treated as perfect conductors. For a CPW, we assume $\Phi = V$ on the center strip and $\Phi = 0$ on the two ground planes. \vec{e}_t is given by $\vec{e}_t = \nabla \Phi$. The distributed capacitance C can be obtained either from $C = Q/V$ where Q is the total charge on the center strip, or from $C = 2w_e/V^2$ where w_e is the total electric energy (per unit length).

In the magnetostatic problem, \vec{h}_t penetrates into the superconductor by a distance given by the effective penetration depth λ_{eff} . In general, the magnetic field can be derived by solving the Maxwell equations together with the Mattis-Bardeen equation (Eq. 2.11). This leads to the following two

equations of the vector potential $A_z(x, y)$:

$$\begin{cases} \nabla^2 A_z = 0 & \text{outside the superconductor} \\ \nabla^2 A_z = \int K(x - x', y - y') A_z(x', y') dx' dy' & \text{inside the superconductor} \end{cases} \quad (3.6)$$

where $K(x - x', y - y')$ is the Mattis-Bardeen kernel appropriate for the two dimensional problems. To join these two equations, we require \vec{h}_t to be continuous at the superconductor surfaces.

Similar to the electrostatic problem, if the penetration depth is much smaller than the film thickness, $\lambda_{\text{eff}} \ll t$, the magnetic field outside the superconductor is almost identical to that for a perfect conductor. Therefore, \vec{h}_t can be solved from the first Laplace equation in Eq. 3.6, with the perfect conductor boundary condition— A_z is constant at superconductor surfaces or \vec{h}_t is parallel to the surfaces, and with the constraint that a total current I is flowing in the center strip and returns in the two ground planes for a CPW. The transverse field \vec{h}_t can be obtained from $\vec{h}_t = \nabla \times A_z$. The (distributed) geometric inductance L_m can be obtained either from $L_m = \phi/I$ where ϕ is the total magnetic flux per unit length going through the gap between the center strip and the ground planes, or from $L_m = 2w_m/I^2$ where w_m is the total magnetic energy. To account for the stored energy and dissipation inside the superconductor, we use the surface current derived for the perfect conductor (equal to \vec{h}_t on the surface) and apply the surface impedance Z_s of the superconductor to the calculation of the (distributed) kinetic inductance L_{ki} and (distributed) resistance R .

However, if the penetration depth is much larger than the film thickness, $\lambda_{\text{eff}} \gg t$, so that the film is fully penetrated by the magnetic field, the perfect-conductor approximation for the surface current and the near magnetic field outside the superconductor is no longer a good approximation, because the perfect-conductor boundary condition— h_t parallel to the superconductor surfaces—fails at the edges of the superconducting film; as the film becomes thinner and thinner, the surface current derived for a perfect conductor will become more and more singular at these edges, while in fact both the magnetic field and current density will become less and less singular due to the longer penetration. In this case, one has to solve faithfully the two equations in Eq. 3.6. However, for $\lambda_{\text{eff}} \gg t$, the relationship between \vec{J} and \vec{A} becomes local (see Section 2.4.1.3) and the second equation in Eq. 3.6 can be replaced by the London equation:

$$\nabla^2 A_z = \frac{1}{\lambda_L^2} A_z \quad (3.7)$$

which is easier to solve than the original differential-integral equation.

So far the electrostatic problem and the magnetostatic problem are independent, which is enough in many cases where only the distributed parameters L and C , or the characteristic impedance $Z_0 = \sqrt{L/C}$ and the phase velocity $v_p = 1/\sqrt{LC}$ are required. The two static problems can be further linked by applying the relationships between the voltage and current given by the transmission line

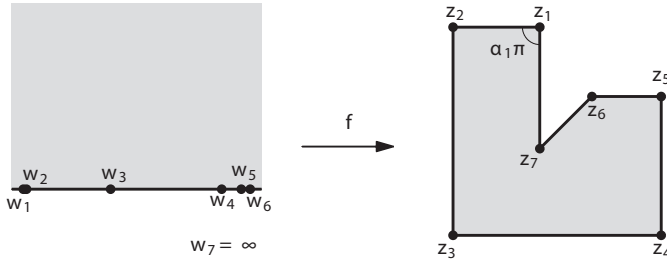


Figure 3.2: Schwarz-Christoffel mapping

equations.

3.1.2 Calculation of geometric capacitance and inductance of CPW using conformal mapping technique

A powerful tool for solving a two-dimensional static problem is the conformal mapping technique. Consider a potential problem

$$\frac{\partial^2 \Phi}{\partial u^2} + \frac{\partial^2 \Phi}{\partial v^2} = 0 \quad (3.8)$$

in domain W with spatial coordinates (u, v) . A complex function

$$z = f(w), \quad w = u + jv, \quad z = x + jy \quad (3.9)$$

maps (u, v) to a new domain Z with coordinates (x, y) . The theory of complex analysis tells us if the mapping function f is analytical, it is also conformal (or angle-preserving), and so Laplace's equation is invariant:

$$\frac{\partial^2 \Phi}{\partial x^2} + \frac{\partial^2 \Phi}{\partial y^2} = 0. \quad (3.10)$$

Often Laplace's equation is difficult to solve in the original domain but relatively easy in the other domain that is specially chosen.

A type of conformal mapping that is particularly useful in microwave engineering is called the Schwarz-Christoffel mapping (SC-mapping), and maps a half of the complex plane into the interior of a polygon. Fig. 3.2 shows the general configuration of SC mapping. The required mapping function is

$$z = f(w) = f(w_0) + c \int_{w_0}^w \prod_{j=1}^{n-1} (w' - w_j)^{\alpha_j - 1} dw' \quad (3.11)$$

where $\pi\alpha_j, j = 1, \dots, n-1$ are the internal angles of the polygon. As we can see in Fig. 3.2, the points w_i on the real axis, the real axis itself, and the entire upper plane are mapped into the vertices z_j , the boundary, and the interior of the polygon, respectively. We will use SC-mapping technique to

solve the transverse fields of CPW and calculate L and C .

3.1.2.1 Zero thickness

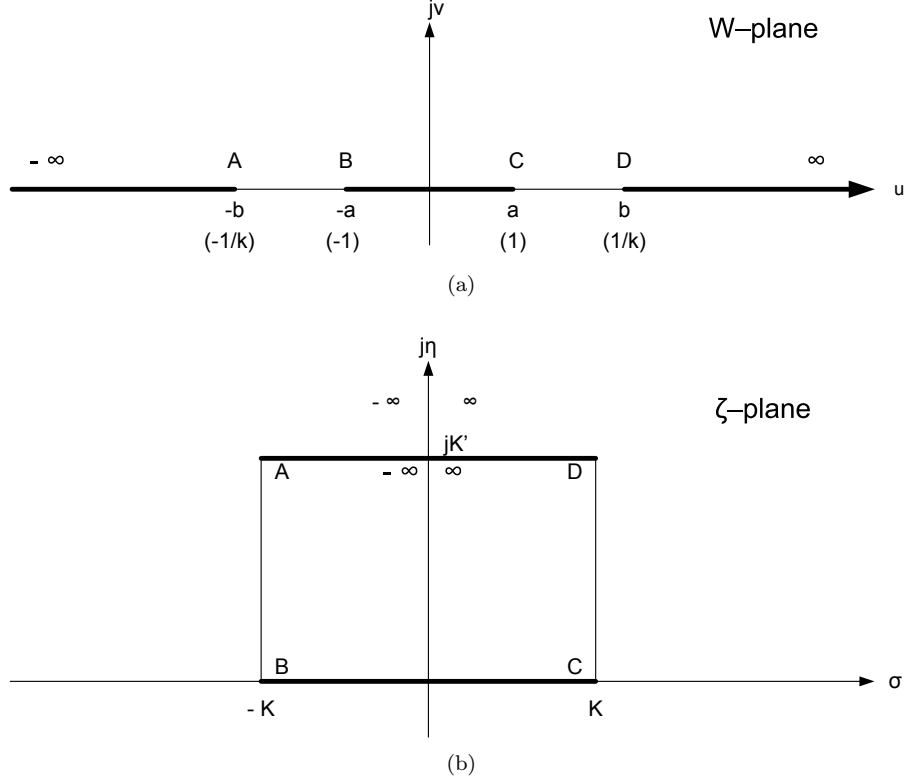


Figure 3.3: SC-mapping of the cross section of a CPW with zero thickness into a parallel-plate capacitor

We begin with a CPW line with zero thickness as shown in Fig. 3.3(a). The center strip has a width of $2a$ and the separation between the two ground planes is $2b$. Because we only care about the capacitance and inductance, the only relevant parameter is the ratio $k = a/b$. Without affecting L and C , we first normalize the CPW dimensions by a so that the center strip width becomes 2 and the ground-plane separation becomes $2/k$, which are also indicated in Fig. 3.3(a).

The upper half of the W -plane can be mapped into the interior of the rectangle in the ξ -plane as shown in Fig. 3.3(b). According to Eq. 3.11, the mapping function with the points $\{-1/k, -1, 1, 1/k\}$ mapping into the four corners of the rectangle is given by

$$\xi = A \int_0^w \frac{1}{\sqrt{(1-w'^2)(1-k^2w'^2)}} dw' \quad (3.12)$$

where A is an unimportant factor that scales the size of the rectangle. By setting $A = 1$, the width

and height of the CPW can be expressed in terms of a special function $K(k)$ called the complete elliptic integral of the first kind [52]:

$$K = K(k) = \int_0^1 \frac{1}{\sqrt{(1-x^2)(1-k^2x^2)}} dx \quad (3.13)$$

$$K' = K(k') = \int_1^{1/k} \frac{1}{\sqrt{(x^2-1)(1-k^2x^2)}} dx \quad (3.14)$$

(3.15)

where $k' = \sqrt{1-k^2}$.

Now the capacitance C between the center strip and the ground planes through upper half plane in free space can be easily obtained from the capacitance of the parallel-plate capacitor in the ξ plane:

$$C_{1/2} = 2\epsilon_0 \frac{K(k)}{K(k')} \quad (3.16)$$

Due to the symmetry, the lower half CPW filled with the substrate which has a dielectric constant ϵ_r , will contribute a capacitance $\epsilon_r C_{1/2}$. Thus, the total capacitance of a zero-thickness CPW line is

$$C = (1 + \epsilon_r) C_{1/2} = \frac{1 + \epsilon_r}{2} \epsilon_0 \frac{4K(k)}{K(k')} \quad (3.17)$$

The factor

$$\epsilon_{\text{eff}} = \frac{1 + \epsilon_r}{2} \quad (3.18)$$

is often referred to as the effective dielectric constant, because the presence of the substrate effectively increases the total capacitance by a factor of ϵ_{eff} , as if the CPW were immersed in a homogenous medium with a dielectric constant of ϵ_{eff} .

Similarly, the total inductance for a zero-thickness CPW line is

$$L_{1/2} = \mu_0 \frac{K(k')}{2K(k)} \quad (3.19)$$

$$L = \frac{L_{1/2}}{2} = \mu_0 \frac{K(k')}{4K(k)} \quad (3.20)$$

We note that the presence of the substrate does not affect the inductance, because both air and the substrate have $\mu = 1$, and the magnetostatic problem does not see the substrate.

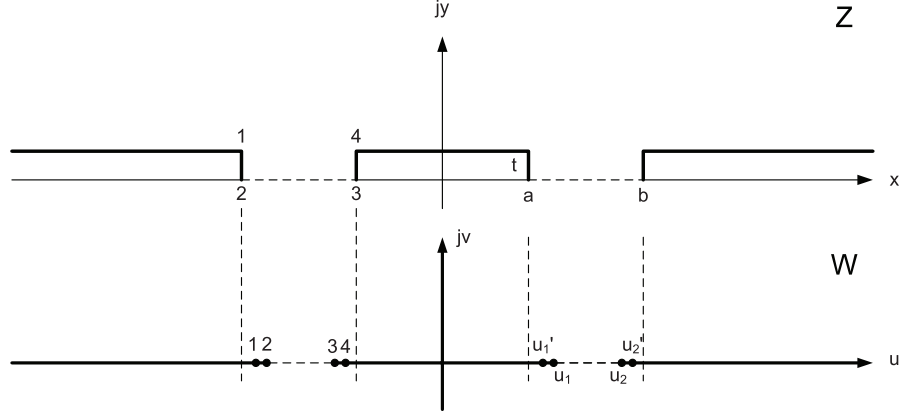


Figure 3.4: SC-mapping of the cross section of a CPW with finite thickness t into a parallel plate capacitor

3.1.2.2 Finite thickness with $t \ll a$

We now consider a CPW line with finite thickness t as shown in Fig. 3.4. The center-strip width and the separation between ground planes are still $2a$ and $2b$ as before. The strategy here is to “flatten” the structure into a zero-thickness CPW and calculate L and C from the derived formula. The upper half CPW in the Z -plane can be mapped into a zero-thickness CPW in the W -plane with the following mapping function (see Fig. 3.4):

$$Z = \int_0^w \sqrt{\frac{(w'^2 - u_1'^2)(w'^2 - u_2'^2)}{(w'^2 - u_1^2)(w'^2 - u_2^2)}} dw' + jt \quad (3.21)$$

where the four points u_1, u_1', u_2, u_2' on the real axis which defines the mapping have to be derived from the following equations:

$$a = \int_0^{u_1'} G(w') dw' \quad (3.22)$$

$$t = \int_{u_1'}^{u_1} G(w') dw' \quad (3.23)$$

$$b - a = \int_{u_1}^{u_2} G(w') dw' \quad (3.24)$$

$$t = \int_{u_2}^{u_2'} G(w') dw' \quad (3.25)$$

with

$$G(w) = \sqrt{\left| \frac{(w^2 - u_1'^2)(w^2 - u_2'^2)}{(w^2 - u_1^2)(w^2 - u_2^2)} \right|}. \quad (3.26)$$

These non-linear equations have no analytical solutions in general. When the thickness is very small, however, approximate solutions can be derived. When $t \rightarrow 0$, $u_1, u_1' \rightarrow a$ and $u_2, u_2' \rightarrow b$,

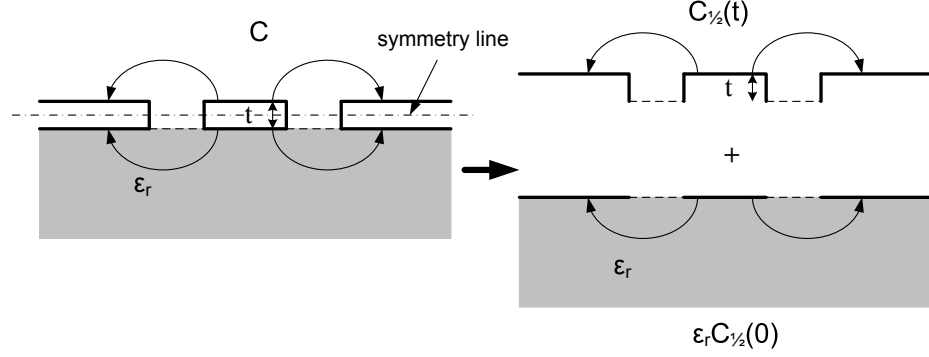


Figure 3.5: Constructing the capacitance C of a CPW with thickness t

keeping terms up to the first order in t/a , we find the solutions of u_1, u'_1, u_2, u'_2 (see Appendix D for the derivation¹⁾)

$$\begin{aligned}
 d &= \frac{2t}{\pi} \\
 u_1 &= a + \frac{d}{2} + \frac{3\log 2}{2}d - \frac{d}{2}\log \frac{d}{a} + \frac{d}{2}\log \frac{b-a}{a+b} \\
 u_2 &= b - \frac{d}{2} - \frac{3\log 2}{2}d + \frac{d}{2}\log \frac{d}{b} + \frac{d}{2}\log \frac{b-a}{a+b} \\
 u'_1 &= u_1 - d \\
 u'_2 &= u_2 + d.
 \end{aligned} \tag{3.27}$$

Then the capacitance and inductance of the upper half CPW (in free space) is given by

$$C_{1/2}(t) = \epsilon_0 \frac{2K(k_t)}{K(k'_t)} \tag{3.28}$$

$$L_{1/2}(t) = \mu_0 \frac{K(k'_t)}{2K(k_t)} \tag{3.29}$$

where $k_t = u_1(t)/u_2(t)$ and $k'_t = \sqrt{1 - k_t^2}$.

There is a subtlety in constructing the total capacitance and inductance. Because the substrate does not exactly fill half of CPW to the symmetry line (see the dashed line in Fig. 3.5), it is found that the total capacitance is better approximated by the sum of the half capacitance of a CPW with thickness t in free space ($\epsilon = 1$) and the half capacitance of a zero-thickness CPW in dielectric ($\epsilon = \epsilon_r$):

$$C = C_{1/2}(t) + \epsilon_r C_{1/2}(0) = \epsilon_0 \frac{2K(k_t)}{K(k'_t)} + \epsilon_r \epsilon_0 \frac{2K(k)}{K(k')} \tag{3.30}$$

And the total inductance is

$$L = \frac{L_{1/2}(t/2)}{2} = \mu_0 \frac{K(k'_{t/2})}{4K(k_{t/2})}. \tag{3.31}$$

¹I have derived these formulas myself, but I am not sure if they already exist in the massive literature on coplanar waveguide.

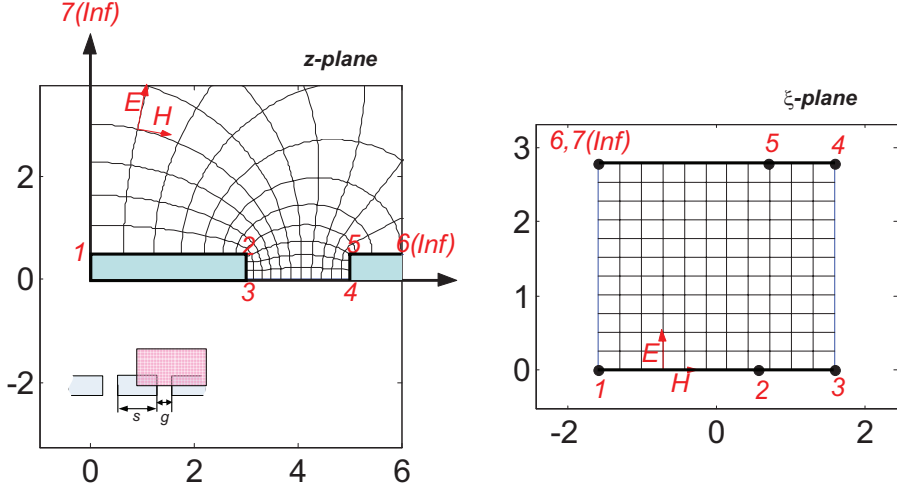


Figure 3.6: Mapping a quadrant of a finite-thickness CPW into a rectangle using Matlab SC toolbox

3.1.2.3 General case of finite thickness from a numerical approach

The SC-mapping can also be solved by numerical programs. One of the basic tasks for such a numerical program is to solve the nonlinear equations like those in Eq. 3.22–3.25 and determine the mapping parameter to the requested precision. We find the Schwarz-Christoffel toolbox (SC-toolbox) for MATLAB developed at University of Delaware [53] to be very flexible and accurate for our purpose.

With the SC-toolbox we directly map a quadrant of the CPW geometry with finite thickness t into a rectangle (parallel-plate capacitor) without the intermediate step of flattening the CPW (see Fig. 3.6). The vertices of the rectangle ξ_i are given by the toolbox and L, C are calculated by

$$C_{1/4} = \epsilon_0 \frac{|\xi_3 - \xi_1|}{|\xi_4 - \xi_3|} \quad (3.32)$$

$$L_{1/4} = \mu_0 \frac{|\xi_4 - \xi_3|}{|\xi_3 - \xi_1|}. \quad (3.33)$$

The total capacitance and inductance from the same approximation as used in Eq. 3.30 and shown in Fig. 3.5 is

$$\begin{aligned} C &= 2[C_{1/4}(t) + \epsilon_r C_{1/4}(0)] \\ L &= \frac{L_{1/4}(t/2)}{4}. \end{aligned} \quad (3.34)$$

The approximation used in the electrostatic problem applies a magnetic wall boundary condition at the exposed substrate surface and solves Laplace's equation in the free space and substrate regions independently. It is also possible to solve for the capacitance accurately without approximation. In

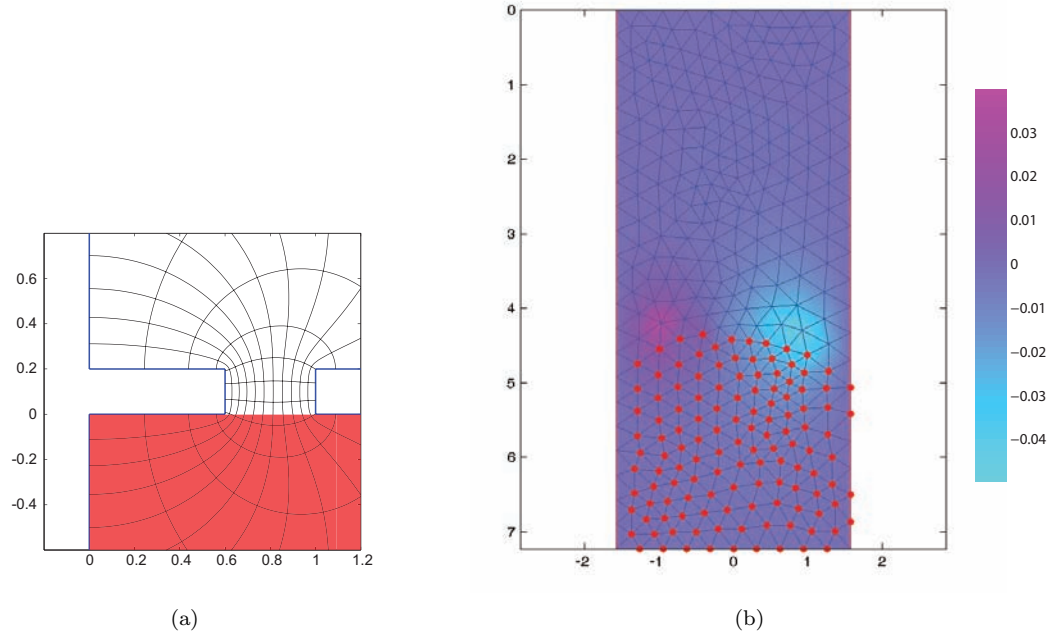


Figure 3.7: Calculating the exact capacitance of a CPW by solving Laplace's equation in the W-plane

order to do this, we first map the right-hand-side half of the CPW into a parallel plate capacitor partially filled with dielectric (see Fig. 3.7). Then we solve Laplace's equation faithfully in the parallel-plate structure by the partial differential equation (PDE) toolbox of Matlab. The PDE toolbox internally implements the finite element method (FEM) and is capable of solving equations of the general type [54]

$$-\nabla \cdot (c\nabla\Phi) + a\Phi = f. \quad (3.35)$$

The equation compatible with PDE toolbox and appropriate for our electrostatic problem is

$$\nabla \cdot [\epsilon(\sigma, \eta) \nabla \Phi(\sigma, \eta)] = 0 \quad (3.36)$$

which comes from one of Maxwell's equations: $\nabla \cdot \vec{D} = 0$. $\epsilon(\sigma, \eta)$ is set to 1 (vertices in blue in Fig. 3.7(b)) or ϵ_r (vertices in red in Fig. 3.7(b)) depending on whether (σ, η) maps to a point (x, y) in the free space region or the substrate region in Fig. 3.7(a). The boundary conditions $\Phi = 1$ and $\Phi = 0$ are applied on the left and right parallel plates, and $\frac{\partial \Phi}{\partial v} = 0$ on both the top and bottom edges of the rectangle. A typical solution of Φ is shown in Fig. 3.7(b). The difference between Φ as compared to the solution of parallel plates fully filled with dielectric is plotted in Fig. 3.7(b). As we can see, the former differs from the latter only in the air-substrate interface region. From the solution Φ , the total electric energy w_e is calculated and the capacitance is derived.

3.1.2.4 Results of L and C calculated using different methods

t [nm]	300			100		
s [μm]	1.5	3.0	6.0	1.5	3.0	6.0
L_0 [nH/m]	436.8	436.8	436.8	436.8	436.8	436.8
L_1 [nH/m]	345.1	384.7	407.3	399.4	415.8	425.1
L_2 [nH/m]	352.1	386.5	407.8	400.2	416.0	425.2
C_0 [pF/m]	165.6	165.6	165.6	165.6	165.6	165.6
C_1 [pF/m]	173.6	169.0	167.3	167.8	166.8	166.2
C_2 [pF/m]	171.4	168.7	167.2	167.7	166.7	166.2
C_3 [pF/m]	172.0	169.1	167.4	167.9	166.7	166.1

L_0 : L from zero-thickness formula

L_1 : L from finite-thickness approximate formula

L_2 : L from numerical method

C_0 : C from zero-thickness formula

C_1 : C from finite-thickness approximate formula

C_2 : C from numerical method with magnetic wall approximation

C_3 : C from numerical method without approximation

Table 3.1: L and C calculated using different methods for different geometries

Results of L and C calculated using different methods, including zero-thickness formula (L_0 and C_0), approximate formula for $t \ll a$ (L_1 and C_1), numerical SC mapping with magnetic wall approximation (L_2 and C_2), and the numerical SC mapping followed by FEM without any approximation (C_3), are compared in Table 3.1. L and C are evaluated for three center-strip widths 1.5, 3, 6 μm and two film thicknesses 300 nm and 100 nm. The ratio between the center-strip width to the width of the gap is fixed to 3:2.

As expected, we see that the results using different methods converge to the same value as t/a goes to zero. As t/a increases, L_0 and C_0 first break down, which deviate from the most accurate values L_2 and C_3 significantly for larger t . Thus these zero-thickness formulas have large error when applied to thick-film CPW. The approximate formula L_1 and C_1 work quite well for not-so-thick films. The error is only 2 % for $t/a = 1/5$ ($s = 0.6 \mu\text{m}$ and $t = 300 \text{ nm}$). In all these geometries, C_2 is always very close to C_3 , suggesting that the magnetic wall approximation is a good approximation. Because of the presence of the substrate in the electrostatic problem, the errors in C using different methods are much less than the error in L .

3.1.3 Theoretical calculation of α for thick films ($t \gg \lambda_{\text{eff}}$)

3.1.3.1 Kinetic inductance L_{ki} , kinetic inductance fraction α , and geometrical factor g

For a transmission line made of perfect conductor, the magnetic field \vec{H} is completely excluded from the conductor. The inductance L is related to the energy stored in the magnetic field outside the conductor. Because this L purely depends on the geometry, it is referred to as the geometric inductance, denoted by L_m . The calculation of L_m has been discussed intensively in the preceding

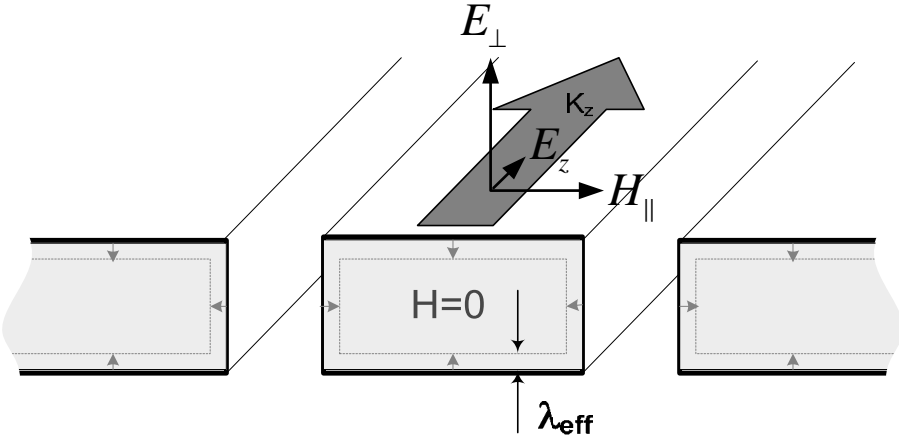


Figure 3.8: \vec{E} field and \vec{H} field near the surface of a thick superconducting CPW.

section of this chapter.

For a superconducting transmission line, the \vec{H} field extends into the superconductor by a distance given by the penetration depth. In this case, the supercurrent flowing in this penetrated layer carries a significant amount of kinetic energy of the Cooper pairs, which will also contribute to L . Because this energy depends on the penetration depth which changes with temperature and quasi-particle density, we usually write the total inductance L as a sum of two parts, a fixed part L_0 and a variable part L_1 .

It can be shown that $L_0 \approx L_m$, because the magnetic field outside the superconductor is usually not too much different from that of a perfect conductor and has little dependence on the penetration depth. L_1 is what we usually refer to as the kinetic inductance L_{ki} .² The total inductance can now be written as

$$L = L_0 + L_{\text{ki}} \approx L_m + L_{\text{ki}}. \quad (3.37)$$

The kinetic inductance fraction α is defined as the ratio of the kinetic inductance L_{ki} to the total inductance L

$$\alpha = \frac{L_{\text{ki}}}{L}. \quad (3.38)$$

In MKIDs, a large α means a large fraction of the inductance is able to change with the quasi-particle density, which usually means a more responsive detector.

Fig. 3.8 shows the \vec{E} and \vec{H} field inside and outside a thick superconducting CPW line. Inside the superconductor, \vec{H} and \vec{J} are zero everywhere except in a surface layer of thickness λ_{eff} . Outside

²Strictly speaking, besides the kinetic energy of the Cooper pairs, the magnetic energy stored in the penetrating magnetic field also contributes to the variable inductance L_1 . In the thick film case, these two contributions are comparable, while in the thin film case, the kinetic energy of Cooper pairs dominates over the magnetic energy. Throughout this thesis, we do not discriminate L_1 and L_{ki} .

the superconductor, the fields are close to a TEM mode, except the \vec{E} field has a small longitudinal component E_z , giving rise to a small component of Poynting vector \vec{S} directed normally into the superconductor surface. This normal component delivers complex power (per unit length) into the superconductor, which is calculated by $\int_{\mathcal{C}} \vec{E}^* \times \vec{H} dl = \int_{\mathcal{C}} E_z^* \cdot H_{\parallel} dl$, where the integral is along the surface contour \mathcal{C} of the superconductor in the cross-sectional plane. On the other hand, the dissipation and stored magnetic energy inside the superconductor are represented by $\frac{1}{2}RI^2$ and $\frac{1}{2}L_{ki}I^2$, respectively, in the transmission line model. According to the Poynting theorem,

$$\frac{1}{2}RI^2 = \operatorname{Re} \left[\int_{\mathcal{C}} E_z^* \cdot H_{\parallel} dl \right] \quad (3.39)$$

$$\frac{1}{2}\omega L_{ki}I^2 = \operatorname{Im} \left[\int_{\mathcal{C}} E_z^* \cdot H_{\parallel} dl \right]. \quad (3.40)$$

With the relationship between E_z and H_{\parallel} given by the surface impedance

$$Z_s = \frac{E_z}{H_{\parallel}} = R_s + j\omega L_s. \quad (3.41)$$

We finally derive

$$R = gR_s \quad (3.42)$$

$$L_{ki} = gL_s = g\mu_0\lambda_{\text{eff}} \quad (3.43)$$

where

$$g = \frac{\int_{\mathcal{C}} H_{\parallel}^2 dl}{I^2} \quad (3.44)$$

Eq. 3.44 shows that the kinetic inductance is related to the effective penetration depth λ_{eff} by a factor g , which depends only on the geometry. The calculation of λ_{eff} is discussed in great detail in Chapter 2. The calculation of the geometrical factor g requires the evaluation of the contour integral of H_{\parallel}^2 . As discussed at the beginning of this chapter, H_{\parallel} can be derived by treating the superconductor as a perfect conductor and solving the Laplace's equation outside. This allows us to use the same conformal mapping technique as used in the calculation of L and C .

3.1.3.2 Approximate formula of g under the condition of $t \ll a$

The contour integral of H_{\parallel}^2 in Eq. 3.44 diverges for a zero-thickness CPW, because a $1/x$ type of singularity will be encountered at the edges of center strip and ground planes. For finite thickness CPW, a $1/\sqrt{x}$ type of singularity will be encountered instead, which is integrable.

To evaluate the integral, we use the same two-step SC-mapping as used in Section 3.1.2.3: the

finite-thickness CPW in the Z -plane is first mapped into a zero-thickness CPW in the W -plane by Eq. 3.21, which is then mapped into a parallel-plate structure in the ξ -plane by Eq. 3.12. It's most convenient to work on the integral in the W -plane. Assume a uniform magnetic field $H = 1$ between the parallel plates in the ξ -plane. The magnetic field H_{\parallel} in the W -plane and Z -plane are $|d\xi/dw|$ and $|d\xi/dz| = |d\xi/dw| / |dz/dw|$, respectively. The current on the center strip I and the geometrical factor g can be written as

$$I = 4 \int_0^{u_1} \left| \frac{d\xi}{dw} \right| dw \quad (3.45)$$

$$g = \frac{4}{I^2} \left\{ \int_0^{u_1} + \int_{u_2}^{\infty} \right\} \left[\left| \frac{d\xi}{dw} \right| / \left| \frac{dz}{dw} \right| \right]^2 \left| \frac{dz}{dw} \right| dw \quad (3.46)$$

with

$$\left| \frac{d\xi}{dw} \right| = \frac{1}{\sqrt{(w^2 - u_1^2)(w^2 - u_2^2)}} \quad (3.47)$$

$$\left| \frac{dz}{dw} \right| = \left| \frac{\sqrt{(w^2 - u_1'^2)(w^2 - u_2'^2)}}{\sqrt{(w^2 - u_1^2)(w^2 - u_2^2)}} \right|. \quad (3.48)$$

In the case of $t \ll a$, approximate solutions for u_1 , u'_1 , u_2 , u'_2 are available (see Eq. 3.27). Using the lowest-order approximations: $u_1 = a$, $u'_1 = a - 2t/\pi$, $u_2 = b$, $u'_2 = b + 2t/\pi$, a formula of g has been derived by Collins[55]

$$\begin{aligned} g &= g_{ctr} + g_{gnd} \\ g_{ctr} &= \frac{1}{4aK^2(k)(1-k^2)} \left[\pi + \log \frac{4\pi a}{t} - k \log \frac{1+k}{1-k} \right] \\ g_{gnd} &= \frac{k}{4aK^2(k)(1-k^2)} \left[\pi + \log \frac{4\pi b}{t} - k \log \frac{1+k}{1-k} \right] \end{aligned} \quad (3.49)$$

where g_{ctr} and g_{gnd} are the contribution from the center strip and the ground planes, respectively, and $k = a/b$ as before. This formula is estimated to be accurate to within 10 percent for $t < 0.05a$ and $k < 0.8$.

3.1.3.3 Numerical calculation of g for general cases

The geometrical factor g can be evaluated numerically with the help of SC-toolbox. To do this, one must first determine the values of the mapping parameters of u_1 , u'_1 , u_2 , u'_2 using the SC-toolbox. With these parameters available, the integrals in Eq. 3.46 can be evaluated numerically.

t [nm]	300			200			100		
s [μm]	0.6	3	6	0.6	3	6	0.6	3	6
L_m [nH/m]	255.7	387.7	408.7	309.4	401.3	416.7	363.2	416.7	425.5
g [μm^{-1}]	1.525	0.391	0.214	1.633	0.4127	0.2249	1.819	0.4498	0.2434
L_{ki} [nH/m]	95.81	24.57	13.45	102.6	25.93	14.13	114.3	28.26	15.29
α	0.2726	0.0596	0.03186	0.2491	0.06069	0.0328	0.2393	0.06351	0.03469

Table 3.2: L_m , g , L_{ki} , and α calculated from the approximate formula Eq. 3.49. $\lambda_{\text{eff}} = 50$ nm is assumed in the calculation.

t [nm]	300			200			100		
s [μm]	0.6	3	6	0.6	3	6	0.6	3	6
L_m [nH/m]	280.5	386.5	407.8	315.9	400.2	416	362.6	416	425.2
g [μm^{-1}]	1.209	0.3673	0.2066	1.385	0.3945	0.2193	1.655	0.4385	0.24
L_{ki} [nH/m]	75.98	23.08	12.98	86.99	24.79	13.78	104	27.55	15.08
α	0.2132	0.05635	0.03085	0.2159	0.05832	0.03206	0.2229	0.06212	0.03426

Table 3.3: L_m , g , L_{ki} , and α calculated from the numerical method. $\lambda_{\text{eff}} = 50$ nm is assumed in the calculation.

3.1.3.4 A comparison of g calculated using different methods

The geometrical factor g , the kinetic inductance fraction α , as well as the geometric inductance L_m and the kinetic inductance L_{ki} are calculated using the two methods and are compared in Table 3.2 and 3.3. We see that the approximate formula of g gives less than 10% error for $t/a < 0.1$. We also find that L_{ki} increases as t or s decreases. Furthermore, g scales as $1/s$. This is because H_{\parallel} scales as $1/s$ while the integration interval scales as s (Eq. 3.44).

3.1.4 Theoretical calculation of α for thin films ($t < \lambda_{\text{eff}}$)

For thin films with $t < \lambda_{\text{eff}}$, the geometrical factor g and the kinetic inductance L_{ki} can no longer be evaluated from the contour integral of H_{\parallel} that is derived for a perfect conductor. The reason has been discussed at the beginning of this chapter. There, we also show that in this case the vector potential A_z satisfies the Laplace equation outside the superconductor and the London equation inside the superconductor, as given by

$$\nabla^2 \vec{A} = \begin{cases} \frac{1}{\lambda_L^2} \vec{A}, & \text{inside the superconductor} \\ 0, & \text{outside the superconductor.} \end{cases} \quad (3.50)$$

A numerical program ‘‘induct’’ developed by Chang [56] is useful in this case. The program uses a variational method to find the current distribution in superconducting strips and calculates the inductance by minimizing the total magnetic and kinetic energy. It can be shown that the variational method used in ‘‘induct’’ is equivalent to solving the equations 3.50. ‘‘Induct’’ takes one parameter, the London penetration depth (effective) λ_L , and outputs the total inductance L . By comparing

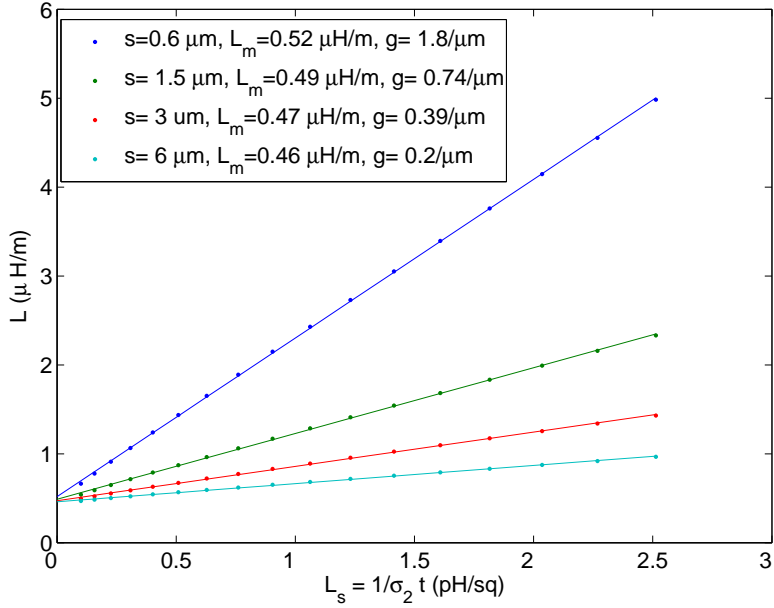


Figure 3.9: Calculated total inductance L as a function of the surface inductance $L_s = 1/\sigma_2 t$ for a thin-film CPW. The film thickness used in the calculation is $t = 20$ nm. Four curves from top to bottom correspond to four CPW geometries with center strip widths of 0.6, 1.5, 3, 6 μm and with the ratio between the center strip width and the gap width fixed at 3 to 2. Data marked with “+” are calculated from “induct”. The four lines show linear fits to the data.

the local equation in the normal form and in the London form at low temperatures,

$$\vec{J} = \frac{1}{i\omega\mu_0\lambda_L^2} \vec{E} = -i\sigma_2 \vec{E}, \quad (\sigma_1 \ll \sigma_2 \text{ for } T \ll T_c) \quad (3.51)$$

we find that λ_L is related to σ_2 by

$$\lambda_L = \sqrt{\frac{1}{\omega\mu_0\sigma_2}}. \quad (3.52)$$

On the other hand, we have shown in Section 2.4.1.3 that the surface inductance of a superconducting thin film with $t < \lambda_{\text{eff}}$ is given by

$$L_s = \frac{1}{\sigma_2 t} \quad (3.53)$$

By varying σ_2 in Eq. 3.52 and Eq. 3.53, and inserting λ_L into “induct”, we can derive the total inductance L as a function of the surface inductance L_s . The results calculated for CPW with four different geometries are shown in Fig. 3.9. We find that L almost has a linear dependence on L_s ,

which allows us to extend the thick-film formula

$$L = L_m + gL_s \quad (3.54)$$

to the thin film case. The equivalent geometrical inductance L_m and geometrical factor g can be determined from the intercept and slope of a linear fit to the data. The linear fits are indicated by the solid lines in Fig. 3.9, with the derived values of L_m and g listed in the legend. The equivalent kinetic inductance L_{ki} and kinetic inductance fraction α for the thin film case are still given by

$$\begin{aligned} L_{ki} &= gL_s \\ \alpha &= \frac{gL_s}{L_m + gL_s} \end{aligned} \quad (3.55)$$

Thus, we have unified formulation for both the thick film and thin film cases.

For a specific CPW, the relevant quantities (L , L_m , L_{ki} , g , and α) can be derived using the following procedures:

1. Calculate the total inductance L as a function of the surface inductance L_s for the specific film thickness t , and from a linear fit, derive L_m and g ;
2. Measure the sheet resistance of the film above its T_c (e.g., at 4 K for Al films), from which derive σ_n ;
3. Calculate $\sigma_2(\omega, T)$ from the formula of σ_2/σ_n derived in Chapter 2 (Eq. 2.92);
4. Insert σ_2 into Eq. 3.53, and from Eq. 3.54 and Eq. 3.55 derive L_{ki} and α .

3.1.5 Partial kinetic inductance fraction

It is often the case that the quasiparticles are only generated in the center strip of CPW instead of the whole superconducting film. In this situation, although the entire superconducting film contributes to L_{ki} , only the center strip where quasiparticle density has a change δn_{qp} contributes to δL_{ki} . Thus we define a partial kinetic inductance fraction α^* as

$$\alpha^* = \frac{L_{ki}^*}{L} = \frac{L_{ki}^*}{L_{ki}}\alpha \quad (3.56)$$

where L_{ki}^* is the partial kinetic inductance contributed from the center strip of the CPW. In the thick film case ($t \gg \lambda_{\text{eff}}$), L_{ki}^* is calculated by

s [μm]	0.6	3	6	5	5	5
g [μm]	0.4	2	4	1	2	3
r_1	0.7309	0.7244	0.7224	0.6133	0.6713	0.7118
r_2	0.6528	0.6986	0.7074	0.5911	0.6513	0.6939

r_1 : ratio of α^*/α from Eq. 3.49

r_2 : ratio of α^*/α from numerical method

Table 3.4: Ratio of α^*/α calculated using the two methods. A film thickness of $t = 200$ nm is used in these calculations.

s [μm]	3			5		
g [μm]	2			2		
λ_L [nm]	100	150	200	100	150	200
$t = 40$ nm	0.8174	0.858	0.8863	0.7613	0.8066	0.8412
$t = 60$ nm	0.7978	0.8368	0.8664	0.7412	0.7821	0.8162
$t = 100$ nm	0.7762	0.8107	0.8395	0.7192	0.754	0.7851

Table 3.5: Ratio of α^*/α calculated using “induct” program

$$\begin{aligned} L_{\text{ki}}^* &= g^* L_s \\ g^* &= \frac{\int_{C^*} H_{\parallel}^2 dl}{I^2} \end{aligned} \quad (3.57)$$

where the contour C^* only runs along the surface of the center strip. In Eq. 3.49 we already give an approximate formula for g^* , and numerical evaluation of g^* is also straightforward. The ratios of $L_{\text{ki}}^*/L_{\text{ki}}$ (or α^*/α) evaluated from both the approximate formula and numerical method for a number of geometries are listed in Table 3.4. We can see that the center strip accounts for more than half of the kinetic inductance. As $t/a \rightarrow 0$, the ratio approaches a constant $L_{\text{ki}}^*/L_{\text{ki}} \rightarrow 1/(1+k) = 0.7$ for CPW geometries with center-strip-to-gap ratio of 3:2, according to Eq. 3.49.

In the thin film case ($t < \lambda_{\text{eff}}$), α^*/α can still be calculated by using the “induct” program. The “induct” program allows users to assign different London penetration depths to the center strip and the ground planes. We first calculate the total inductance L and its increment δL by assigning both the center strip and the ground planes with the actual λ_L and $\lambda_L + \delta\lambda_L$. Then we calculate the partial inductance increment δL^* by only increasing the London penetration depth of the center strip to $\lambda_L + \delta\lambda_L$ while keeping the ground planes at λ_L . The ratio of $\delta L^*/\delta L$ yields the ratio of α^*/α . The ratios of $\delta L^*/\delta L$ are calculated for a number of combinations of geometry, thickness, and London penetration depth, and are listed in Table 3.5. We find that for these geometries the ratios are between 80 % to 90 %, and are higher than the thick film case.

3.2 Experimental determination of α

In this section, we describe an experimental method to determine the kinetic inductance fraction α of a superconducting CPW.

3.2.1 Principle of the experiment

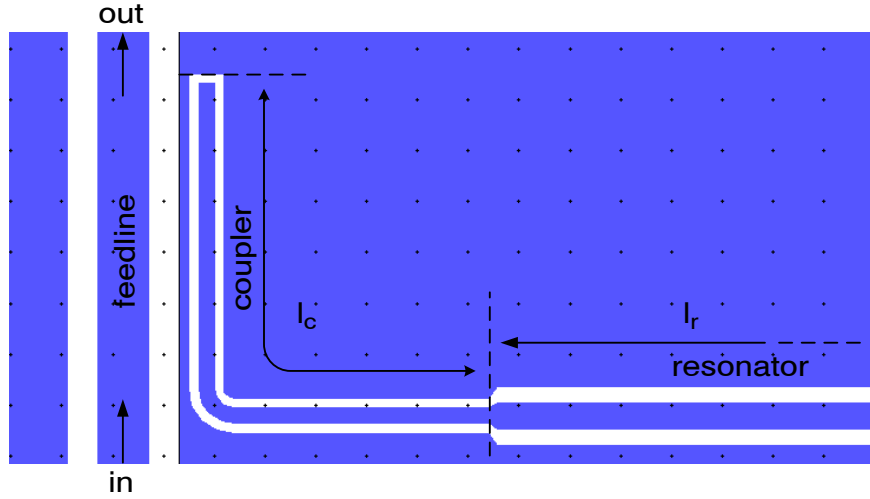


Figure 3.10: Coupler structure of the α -test device

The resonant frequency f_r of a quarter-wave resonator of length l_r is given by

$$f_r = \frac{1}{4l_r\sqrt{LC}}. \quad (3.58)$$

According to Eq. 3.58 and Eq. 3.37, a straightforward way of determining α is to compare the measured resonance frequency of a superconducting CPW resonator f_r^{sc} , with the calculated resonant frequency f_r^{m} of the same resonator assuming only the magnetic inductance L_m :

$$\alpha = 1 - \left(\frac{f_r^{\text{sc}}}{f_r^{\text{m}}}\right)^2. \quad (3.59)$$

This method, however, is only accurate for CPW with large α , because the relative error in Eq. 3.59 is:

$$\frac{\sigma_\alpha}{\alpha} = 2 \frac{1-\alpha}{\alpha} \sqrt{\left(\frac{\sigma_{f_r^{\text{m}}}}{f_r^{\text{m}}}\right)^2 + \left(\frac{\sigma_{f_r^{\text{sc}}}}{f_r^{\text{sc}}}\right)^2}. \quad (3.60)$$

For example, if f_r^{sc} or f_r^{m} has a relative error of 1%, the relative error in α will be 6% for $\alpha = 25\%$ which is acceptable, and 98% for $\alpha = 2\%$ which is too large to be useful.

For a CPW geometry with small α , we resort to the temperature dependence of the resonant

Res#	Group#	s [μm]	L_c [μm]	L_r [mm]	f_r^m [GHz]	Q_c
0	1	0.6	168.60	4558.42	6.466	1.0107E+05
1	1	0.6	168.60	4533.42	6.500	1.0000E+05
2	1	0.6	168.60	4508.42	6.535	9.8937E+04
3	2	1.5	130.45	4408.41	6.713	2.0222E+05
4	2	1.5	130.45	4383.41	6.750	2.0000E+05
5	2	1.5	130.45	4358.41	6.788	1.9779E+05
6	3	3.0	156.56	4180.82	6.960	1.0116E+05
7	3	3.0	156.56	4155.82	7.000	1.0000E+05
8	3	3.0	156.56	4130.82	7.041	9.8844E+04
9	4	6.0	173.75	4004.95	7.163	6.8670E+04
10	4	6.0	148.75	4004.95	7.206	1.0886E+05
11	4	6.0	123.75	4004.95	7.250	2.0000E+05
12	4	6.0	123.75	3979.95	7.294	1.9759E+05
13	4	6.0	123.75	3954.95	7.339	1.9519E+05
14	5	24.0	263.41	3713.70	7.453	2.0254E+04
15	5	24.0	263.41	3663.70	7.548	1.9748E+04

Table 3.6: Design parameters of the α -test device. f_r^m is calculated assuming a film thickness of 200 nm.

frequency f_r and quality factor Q_r (see Eq. 2.54):

$$\begin{aligned} \frac{\delta f_r(T)}{f_r} &= \frac{f_r(T) - f_r(0)}{f_r(0)} = -\frac{\alpha}{2} \frac{\delta X_s(T)}{X_s} \\ \delta \frac{1}{Q_r(T)} &= \frac{1}{Q_r(T)} - \frac{1}{Q_r(0)} = \alpha \frac{R_s(T)}{X_s}. \end{aligned} \quad (3.61)$$

Because the temperature dependence of the surface impedance is an intrinsic property of the superconductor, $X_s(T)$ and $R_s(T)$ are common for resonators of all geometries made from the same superconducting film. The ratio of $\delta f_r/f_r$ or $\delta(1/Q_r)$ between two CPW geometries, with the common temperature dependence canceled out, gives the ratio of α :

$$\frac{\alpha_i}{\alpha_j} = \frac{(\delta f_r/f_r)_i}{(\delta f_r/f_r)_j} = \frac{\delta(1/Q_r)_i}{\delta(1/Q_r)_j}. \quad (3.62)$$

If α_i is large and can be determined with a good accuracy from Eq. 3.59, the small α_j can also be determined with fairly good accuracy by scaling α_i with the ratio given by Eq. 3.62.

3.2.2 α -test device and the experimental setup

For this experiment, we designed two α -test devices which are made of Al films with two different thicknesses: 200 nm and 20 nm. In each device, an Al film was deposited on a silicon substrate and patterned into 16 CPW quarter-wavelength resonators with 5 different geometries. As shown in Fig. 3.10, each resonator has a coupler of length l_c and a common center-strip width of 6 μm , which capacitively couples the resonator body to the feedline for readout. The coupler is then widened (or

narrowed) into the resonator body, with center-strip widths s_r of 0.6 μm , 1.5 μm , 3 μm , 6 μm , or 24 μm , and a length l_r . The ratio between center strip width s and the gap g in both the coupler and the resonator body section is fixed to 3:2, to maintain a constant impedance at $Z_0 \approx 50 \Omega$. The relevant design parameters of the α -test device are listed in Table 3.2.2. Because the smaller geometries are expected to have larger α , they are designed to have smaller f_r^m . This guarantees the actual resonance frequencies f_r^{sc} are always in a fixed order easy to recognize, with smaller geometries at lower frequencies regardless of the film thickness.

The device is mounted in a dilution fridge and cooled down to T as low as 100 mK. A microwave synthesizer is used to excite the resonators. The signal transmitted past the resonator is amplified with a cryogenic HEMT amplifier and compared with the original signal using an IQ-mixer. As the excitation frequency f is swept through the resonance, the I-Q output from the IQ-mixer, after corrections, gives the complex transmission S_{21} through the device and HEMT. The readout system used in this experiment is described in more detail in Section 5.2 and shown in Fig. 5.1. The resonance frequency f_r is obtained by fitting the complex S_{21} data to its theoretical model. The IQ-mixer correction and resonance curve fitting are given in the Appendix E and F.

3.2.3 Results of 200 nm Al α -test device ($t \gg \lambda_{\text{eff}}$ and $t \ll a$)

The 200 nm device was cooled in the dilution fridge and T_c was measured to be 1.25 K. All the 16 resonators were observed.

3.2.3.1 α of the smallest geometry

We first measured the resonant frequency and quality factor of all the resonators at 150 mK. α are immediately calculated from Eq. 3.59 for each resonator and the group mean value is listed in Table 3.7 in the column “ α^1 ”. We will only take $\alpha_1^1 = 27.6\%$ of group 1 as a reliable value and abandon the rest, based on the previous discussion.

3.2.3.2 Retrieving values of α from $f_r(T)$ and $Q_r(T)$

α of the remaining four geometries are determined from the temperature sweep data. $\delta f_r(T)/f_r$ and $\delta(1/Q_r)$ for all the resonators are measured from 150 mK to 480 mK in steps of 10 mK and plotted in Fig. 3.11(a) and Fig 3.11(b). In both plots, the curves fall onto 5 trajectories corresponding to the 5 geometries. We normalize them by the value of group-1. The normalized curves appear to be flat in the temperature range between 220 mK and 300 mK (see Fig. 3.12), where the ratios α_i/α_1 are retrieved. The ratios as well as the values of α_i scaling down from α_1 are listed in Table 3.7 in the two columns “ α_i/α_1 ” and “ α^2 ”.

The ratio of α_i/α_1 can also be derived by fitting $\delta f_r/f_r$ and $\delta(1/Q_r)$ to Eq. 3.61, with $\delta X_s/X_s$

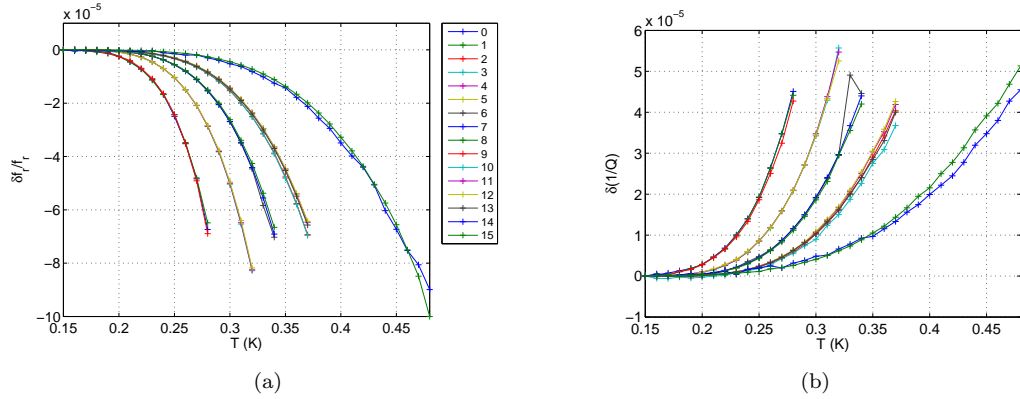


Figure 3.11: Measured $\delta f_r/f_r$ and $\delta(1/Q_r)$ as a function of T from the 200 nm α -test device
 (a)Plot of $\delta f_r/f_r$ vs. T (b)Plot of $\delta(1/Q_r)$ vs. T

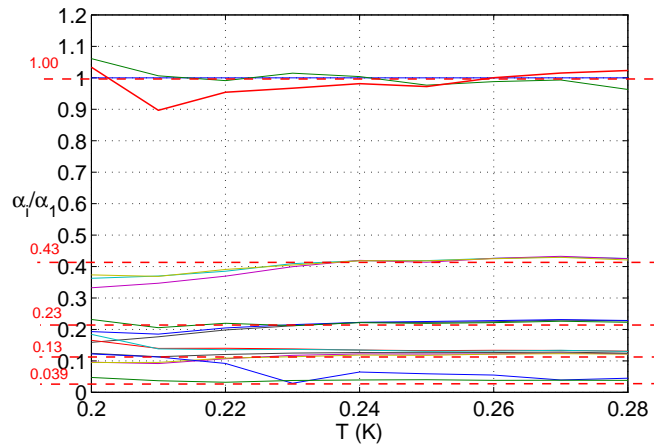


Figure 3.12: $\delta f_r/f_r$ normalized by group-1 from the 200 nm α -test device

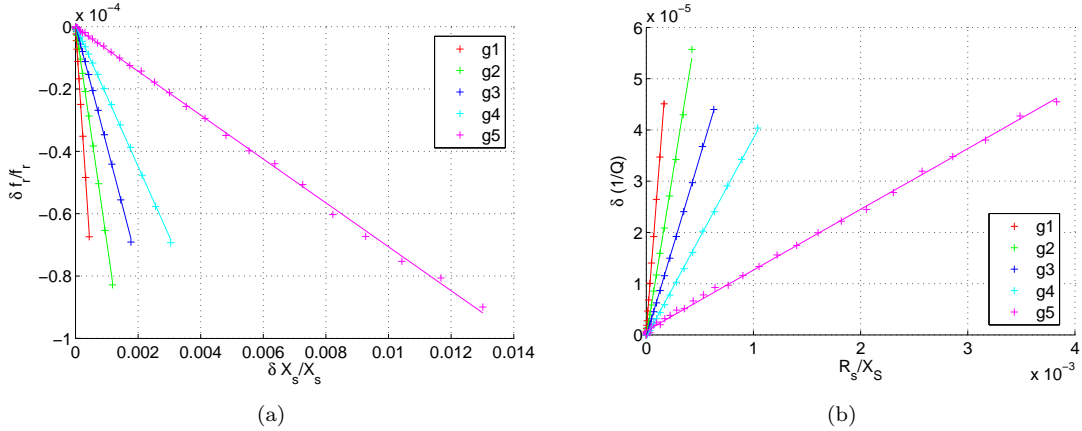


Figure 3.13: Fitting (a) $\delta f_r/f_r$ with $\delta X_s/X_s$ and (b) $\delta(1/Q_r)$ with R_s/X_s from the 200 nm α -test device

group#	α^1	α_i/α_1	α^2	α^3	α^4	α^5
1	27.6%	1.000	27.6%	27.6%	27.6%	30.8%
2	12.3%	0.430	11.9%	12.6%	13.1%	14.5%
3	4.3%	0.230	6.3%	7.0%	7.2%	7.8%
4	0.3%	0.130	3.6%	4.1%	4.0%	4.2%
5	-6.5%	0.039	1.1%	1.3%	1.2%	1.2%

Table 3.7: Results from the 200 nm α -test device

α^1 : α from Eq. 3.59

α_i/α_1 : α ratio between the i th group and the group 1

α^2 : α from scaling the largest alpha with α_i/α_1

α^3 : α from fitting $\delta f_r/f_r$ to $\delta X_s/X_s$

⁵ See also the discussion in the previous section.

α^3 : α from a numerical calculation of g and $\lambda \approx 64$ nm from “surimp”

and R_s/X_s calculated from Martis-Bardeen theory by our “surimp” program described in Chapter 2. As for the five material-dependent parameters required by “surimp”, we take values of v_f and λ_L from reference[40], $T_c = 1.25$ K, and $l = 200$ nm (limited by the film thickness). The parameter $\Delta(0)/k_b T_c$ is chosen such that the fitting yields 27.6% for the smallest 0.6–0.4 geometry. Once determined, the same five parameters are used to fit for the other four geometries. The results are listed in Table 3.7 in the column “ α^3 ” and “ α^4 ”. We see that “ α^3 ” and “ α^4 ” agree with “ α^2 ”. The advantage of the fitting approach (α_3, α_4) over the direct ratio approach (α_2) is that the former takes into account of the frequency dependence of the surface impedance which does not cancel completely in Eq. 3.62 between two resonators.

3.2.3.3 Comparing with the theoretical calculations

The experimental results of α are compared with the theoretical calculations. The kinetic inductance fraction can be calculated from Eq. 3.44 and Eq. 3.43 because the film thickness is several times

larger than the penetration depth. With $\lambda_{\text{eff}} = 64$ nm calculated from “surimp”, calculated values of α are listed in Table 3.7 in the column “ α^5 ”. We find a good agreement, within 10%, between the theoretical results and the experimental results.

3.2.4 Results of 20 nm Al α -test device ($t < \lambda_{\text{eff}}$)

The 20 nm α -test device was cooled in a dilution fridge in another cooldown. T_c was measured to be 1.56 K. 14 out of the 16 resonators showed up (Res 2 and Res 11 fail to show up).

3.2.4.1 α of the smallest geometry

We measured the resonant frequency and quality factor of all the 14 resonators at 120 mK. α calculated from Eq. 3.59 are listed in Table 3.8 under column “ α^1 ”. We see that α of this 20 nm device is significantly larger than the 200 nm device. Even the largest geometry gives an α over 20%. Thus the values of α^1 derived from Eq. 3.59 are all reliable.

3.2.4.2 Retrieving values of α from $f_r(T)$

$\delta f_r/f_r$ as a function of T are measured between 110 mK and 575 mK in steps of 15 mK and plotted in Fig. 3.14. Curves for the 14 resonators still fall onto five trajectories. The quality factors are also measured which appear to be very low. We were unable to distinguish trajectories between geometric groups from the $\delta(1/Q_r)$ curves. So we proceed only with the $\delta f_r/f_r$ data. The results from both the direct ratio approach and the fitting approach are shown in Fig. 3.15 and Fig. 3.16, and are listed in Table 3.8 under columns “ α^2 ” and “ α^3 ”. The parameters used in the fits are: $T_c = 1.56$ K, $l=20$ nm, $v_f = 1.34 \times 10^6$ m/s, $\lambda_L = 15.4$ nm, and $\Delta_0/k_b T_c = 1.71$. We can see that the values of α^2 and α^3 are notably smaller compared to α^1 , for which we do not have an explanation yet.

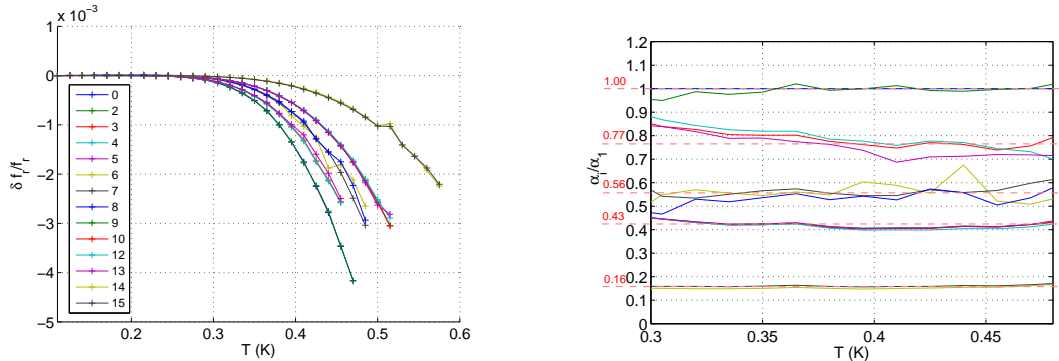


Figure 3.14: Measured $\delta f_r/f_r$ as a function of T from the 20 nm Al device

Figure 3.15: $\delta f_r/f_r$ normalized by group 1 from the 20 nm device

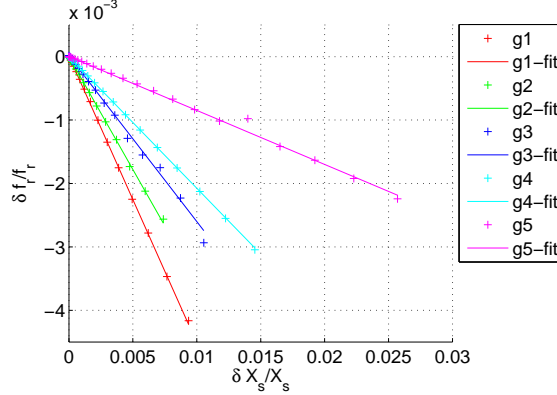


Figure 3.16: Fitting $\delta f_r/f_r$ with $\delta X_s/X_s$ from the 20 nm device

g#	α^1	α_i/α_1	α^2	α^3	α^6
1	89.3%	1.000	89.3%	89.3%	88.3%
2	76.5%	0.770	68.7%	70.2%	75.6%
3	62.7%	0.560	50.0%	51.6%	61.8%
4	45.3%	0.430	38.4%	41.0%	46.4%
5	20.6%	0.160	14.3%	16.8%	20.2%

Table 3.8: Results from the 20 nm α -test device

α^6 : α calculated from “induct” program with $\lambda_L = 165$ nm. Other symbols same as in Table 3.7.

3.2.4.3 Comparing with the theoretical calculations

Since the thickness 20 nm is less than the effective penetration depth, it is appropriate to calculate α from “induct” program, instead of surface integral method. α calculated from “induct” program, assuming a effective London penetration depth of $\lambda_L = 165$ nm, are listed in Table 3.8 in the column “ α^6 ”. Unfortunately, the sheet resistance of the film at 4 K was not measured for this device and λ_L can not be verified from the procedures described in Section 3.1.4.

3.2.5 A table of experimentally determined α for different geometries and thicknesses.

The values of α determined from the two α -test devices described in this section and from another 40 nm geometry-varying device are summarized in Table 3.9. This table is useful for a quick estimation of α for geometries listed or close to those listed in the table. For example, the submm MKID, with a $6\ \mu\text{m}$ width center strip, a $2\ \mu\text{m}$ wide gap, and a 60 nm thick Al film, is estimated to have a kinetic inductance fraction around 20%.

s [μm] \ t [nm]	200	40	20
0.6	27.6%		89.3%
1.5	12.6%		76.5%
3	7%	45%	62.7%
5		26%	
6	4.1%		45.3%
10		17%	
24	1.3%		20.6%

Table 3.9: Summary of experimentally determined α for different center-strip widths and thicknesses. Values of α are reported using α^1 for 20 nm and 40 nm devices, and α^3 for 200 nm device.

Chapter 4

Analysis of the resonator readout circuit

In this chapter, we discuss the resonator readout circuit. The basic question to be answered is: if the kinetic inductance of the superconducting resonator has a change δL_{ki} due to a change in the quasiparticle density δn_{qp} , what will be the change in the phase and amplitude of the microwave output signal?

We begin with an introduction of the basics of a quarter-wave transmission line resonator. Then we present a network model of a resonator capacitively coupled to a feedline. To be general, we assume the transmission line resonator is terminated by a small impedance Z_l instead of being shorted. From the network model, we derive the responsivity of MKID both for $Z_l = 0$ case and $Z_l \neq 0$ case. The $Z_l = 0$ case corresponds to the simple short-circuited $\lambda/4$ resonator and the $Z_l \neq 0$ case corresponds to the hybrid resonator, which has a short sensor strip section near the short-circuited end that is made from a different type of superconductor or a different geometry from the rest of the resonator. For the hybrid resonator, both the static and dynamic response are discussed.

4.1 Quarter-wave transmission line resonator

4.1.1 Input impedance and equivalent lumped element circuit

A short-circuited CPW transmission line of length $\lambda/4$ (see Fig. 4.1(a)) makes a simple while useful microwave resonator[57]. According to the transmission line theory, the input impedance of a shorted transmission line of length l is

$$Z_{in} = Z_0 \tanh(\alpha + j\beta)l = Z_0 \frac{1 - j \tanh \alpha l \cot \beta l}{\tanh \alpha l - j \cot \beta l} \quad (4.1)$$

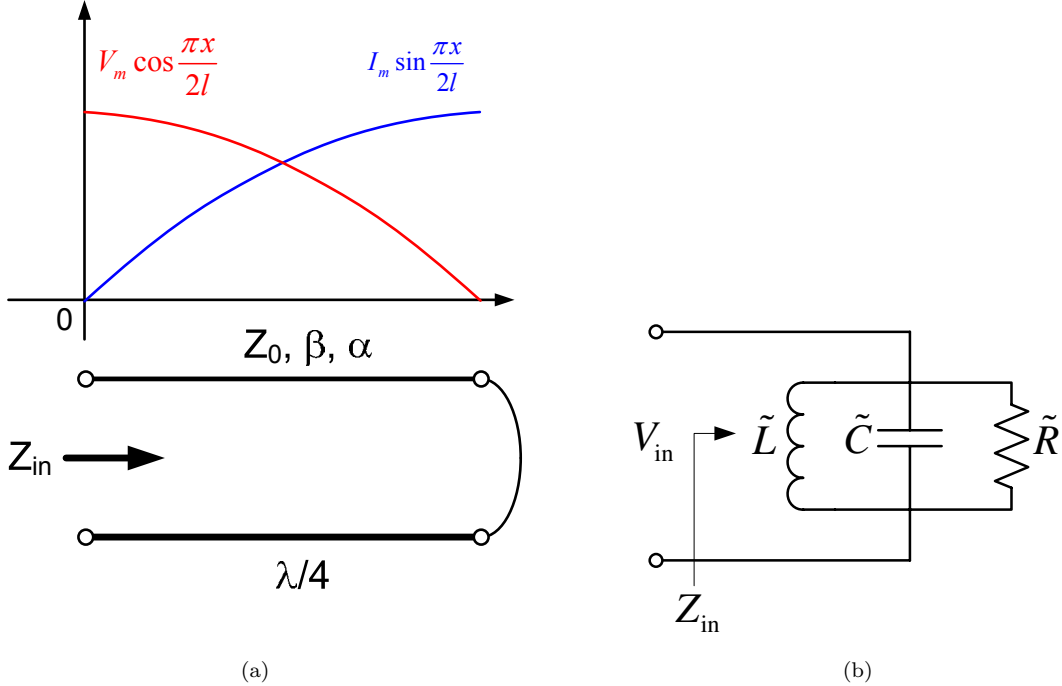


Figure 4.1: A short-circuited $\lambda/4$ transmission line and its equivalent circuit. (a) Illustration of a short-circuited $\lambda/4$ resoantor. The voltage and current distributions show standing wave patterns. (b) The equivalent RLC parallel resonance circuit, valid near resonance

where

$$\gamma = \alpha + j\beta = \sqrt{(R + j\omega L)(j\omega C)} \quad (4.2)$$

is the complex propagation constant, and

$$Z_0 = \sqrt{\frac{L}{C}} \quad (4.3)$$

is the characteristic impedance of the transmission line. Here L , C , and R are the distributed inductance, capacitance, and resistance of the transmission line.

For a lossless line, $\alpha = 0$ and

$$Z_{in} = jZ_0 \tan \beta l. \quad (4.4)$$

At the fundamental resonance frequency

$$\omega_0 = \frac{\pi}{2l\sqrt{LC}} \quad \text{or} \quad f_0 = \frac{1}{4l\sqrt{LC}} \quad (4.5)$$

we have

$$\beta_0 l = \frac{\pi}{2}, \quad Z_{in} = \infty. \quad (4.6)$$

For a transmission line with small loss $\alpha l \ll 1$ at a frequency close to the resonance frequency $\omega = \omega_0 + \Delta\omega$, Eq. 4.1 approximately reduces to

$$Z_{\text{in}} = \frac{Z_0}{\alpha l + j\pi\Delta\omega/2\omega_0}. \quad (4.7)$$

Recall that the impedance of a parallel RLC circuit shown in Fig. 4.1(b) has the same form near the resonance frequency

$$Z_{\text{in}} = \frac{1}{1/\tilde{R} + 2j\Delta\omega\tilde{C}}. \quad (4.8)$$

Thus a short-circuited transmission line of length $\lambda/4$ is equivalent to a parallel RLC resonance circuit, with the equivalent lumped elements \tilde{R} , \tilde{L} , and \tilde{C} related to the distributed R , L , and C of the transmission line by

$$\tilde{R} = \frac{2}{l} \frac{L}{RC}, \quad \tilde{C} = \frac{l}{2} C, \quad \tilde{L} = \frac{8l}{\pi^2} L. \quad (4.9)$$

And the quality factor Q of the circuit is

$$Q = \frac{\pi}{4\alpha l} = \omega_0 \frac{L}{R}. \quad (4.10)$$

4.1.2 Voltage, current, and energy in the resonator

At the resonance frequency $\omega = \omega_0$, the RMS voltage and current have standing-wave distributions along the transmission line

$$V(x) = V_m \cos \frac{\pi x}{2l}, \quad I(x) = I_m \sin \frac{\pi x}{2l} \quad (4.11)$$

where V_m is the maximum voltage at the open end ($x = 0$) and I_m is the maximum current at the shorted end ($x = l$). V_m and I_m are related by $V_m = I_m Z_0$. It follows that the electric energy, magnetic energy and dissipation (per unit length) are

$$\begin{aligned} W_e(x) &= \frac{1}{2} CV(x)^2 = \frac{1}{2} CV_m^2 \cos^2 \frac{\pi x}{2l} \\ W_m(x) &= \frac{1}{2} LI(x)^2 = \frac{1}{2} LI_m^2 \sin^2 \frac{\pi x}{2l} \\ P_l(x) &= \frac{1}{2} RI(x)^2 = \frac{1}{2} RI_m^2 \sin^2 \frac{\pi x}{2l}. \end{aligned} \quad (4.12)$$

The lumped-element relationships in Eq. 4.9 can also be derived by equating the total electric energy and magnetic energy in the RLC tank circuit and in the transmission line resonator,

$$\begin{aligned} \text{Total electric energy} &= \frac{1}{2} \tilde{C} V_{\text{in}}^2 = \frac{1}{2} \int_0^l C V_m^2 \cos^2 \frac{\pi x}{2l} dx \\ \text{Total magnetic energy} &= \frac{1}{2} \frac{V_{\text{in}}^2}{\omega_0^2 L} = \frac{1}{2} \int_0^l L I_m^2 \sin^2 \frac{\pi x}{2l} dx \\ \text{Total dissipation} &= \frac{1}{2} \frac{V_{\text{in}}^2}{R} = \frac{1}{2} \int_0^l R I_m^2 \sin^2 \frac{\pi x}{2l} dx \end{aligned} \quad (4.13)$$

which, by applying $V_{\text{in}} = V_m$ and Eq. 4.5, leads to the same results as in Eq. 4.9.

4.2 Network model of a quarter-wave resonator capacitively coupled to a feedline

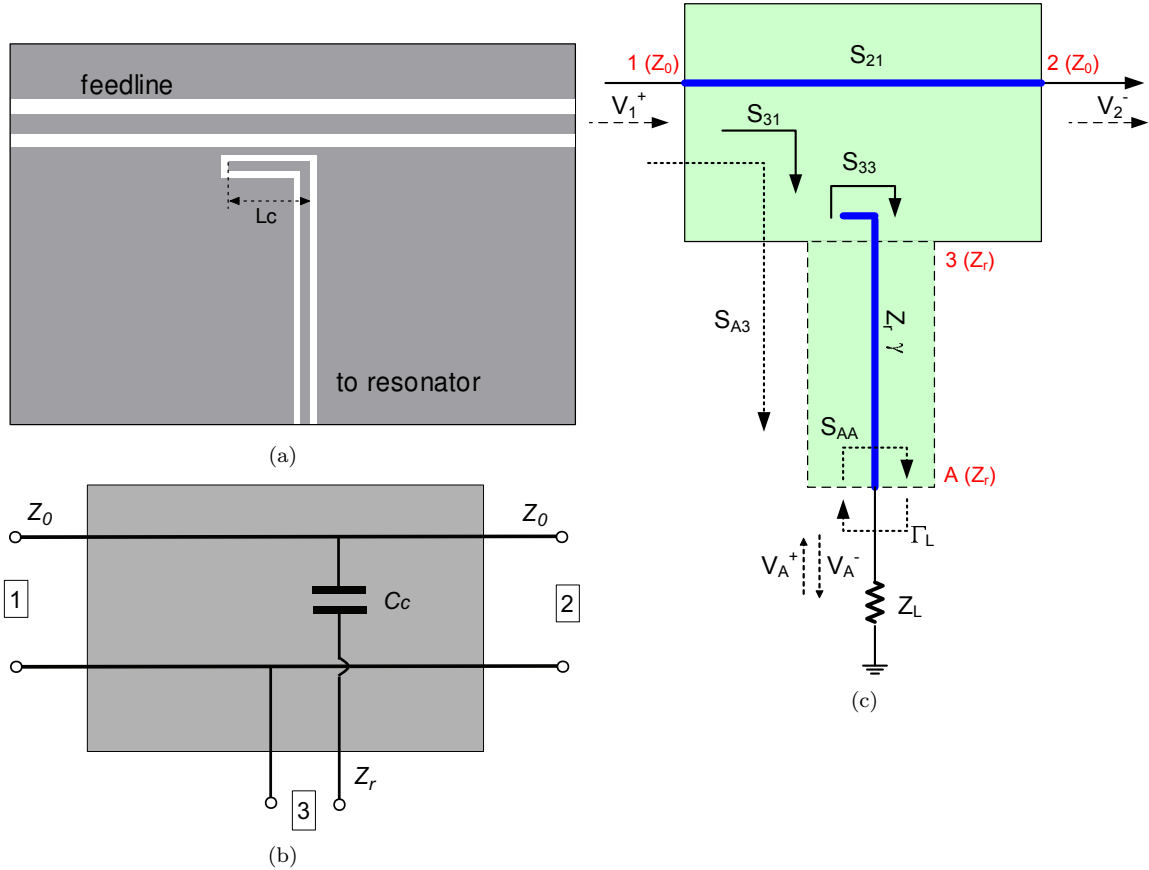


Figure 4.2: Network model of a $\lambda/4$ resonator capacitively coupled to a feedline. (a) The “elbow” coupler. (b) Equivalent lumped element circuit of the coupler. (c) A network model and the signal flow graph

The resonator readout circuit used in MKIDs consists of feedline, coupler, and $\lambda/4$ transmission

line resonator, which is shown in Fig. 4.2(a). Using the equivalent circuit of the coupler shown in Fig. 4.2(b), and by considering the frequency dependent complex impedance of a shorted $\lambda/4$ transmission line (Eq. 4.7), Mazin[16] and Day[14] have derived the resonance condition for the circuit. Here we present an alternative derivation from the network analysis approach.

4.2.1 Network diagram

Fig. 4.2(c) shows a diagram of the equivalent network model, as well as its signal flow graph. In this diagram, the coupler is modeled by a 3-port network block with its port 3 connected to one end of the $\lambda/4$ transmission line. To facilitate future discussions of the hybrid resonator design, we assume the other end of the transmission line is terminated by a load impedance Z_l . For the case of shorted $\lambda/4$ resonator, we shall simply set $Z_l = 0$. We assume that the feedline is a lossless transmission line with characteristic impedance Z_0 , which may be different from the impedance Z_r of the resonator transmission line.

4.2.2 Scattering matrix elements of the coupler's 3-port network

The scattering matrix of the coupler's 3-port network can be easily derived from its equivalent lumped element circuit (Fig. 4.2(b)), in which a coupling capacitor C_c weakly couples the resonator to the feedline. Let $\delta_0 = \omega C_c Z_0$ and $\delta_r = \omega C_c Z_r$. For weak coupling (which is required by a high Q_r resonator), C_c is small and $\delta_0, \delta_r \ll 1$. Under these assumptions, the scattering matrix S is given by¹

$$S = \begin{bmatrix} -j\delta_0/2 & 1 - j\delta_0/2 & j\sqrt{\delta_0\delta_r} \\ 1 - j\delta_0/2 & -j\delta_0/2 & j\sqrt{\delta_0\delta_r} \\ j\sqrt{\delta_0\delta_r} & j\sqrt{\delta_0\delta_r} & 1 - 2j\delta_r - 2\delta_r^2 - \delta_r\delta_0 \end{bmatrix}. \quad (4.14)$$

We find the following general properties for S_{ij} :

$$S_{21} \approx 1 \quad (4.15)$$

$$S_{31} = S_{13}, \quad S_{32} = S_{23} \quad (4.16)$$

$$S_{31} = S_{32}, \quad S_{13} = S_{23} \quad (4.17)$$

$$|S_{33}| = \sqrt{1 - 2|S_{31}|^2}. \quad (4.18)$$

Eq. 4.15 states the fact that the direct transmission through the feedline is close to 1. Eq. 4.16 comes from the reciprocity of the 3-port network. Because the dimension of the coupler is much smaller

¹In the discussion that follows, S-parameters are normalized to the characteristic impedance of Z_0 for port 1 and port 2, and Z_r for port 3 and port A.

than the wavelength, port 1 and port 2 appear to be symmetric and Eq. 4.17 holds. Eq. 4.18 holds because the 3-port network is lossless.

4.2.3 Scattering matrix elements of the extended coupler-resonator's 3-port network

We can extend the coupler's 3-port network to include the $\lambda/4$ transmission line connected to port-3. This can be easily done by shifting the reference plane of port-3 to the other end of the resonator, to port A. The relevant scattering matrix elements are modified to

$$S_{A1} = S_{1A} = S_{A2} = S_{2A} = S_{31}e^{-\gamma l} \quad (4.19)$$

$$S_{AA} = S_{33}e^{-2\gamma l} \quad (4.20)$$

where $l \approx \lambda/4$ is the length of the transmission line section.

4.2.4 Transmission coefficient t_{21} of the reduced 2-port network

When port-A is terminated by the load impedance Z_l , the whole circuit reduces to a 2-port network. With the help of the signal flow graph, the total transmission from port 1 to port 2 can be written as:

$$t_{21} = S_{21} + \frac{S_{A1}\Gamma S_{2A}}{1 - \Gamma S_{AA}} = S_{21} + \frac{S_{31}^2}{e^{2\gamma l}/\Gamma - S_{33}} \quad (4.21)$$

where Γ is the reflection coefficient from the load

$$\Gamma = \frac{Z_l - Z_r}{Z_l + Z_r}. \quad (4.22)$$

For the simple case that the $\lambda/4$ transmission line is shorted at port A, $\Gamma = -1$. In order to further simplify Eq. 4.21, we first introduce a coupling quality factor Q_c defined as:

$$Q_c = 2\pi \frac{\text{energy stored in the resonator}}{\text{energy leak from port 3 to port 1 and 2 per cycle}} = \frac{\pi}{2|S_{31}|^2}. \quad (4.23)$$

The relationship between Q_c and S_{31} can be understood from a power flow point of view: during each cycle the traveling wave inside the $\lambda/4$ resonator is reflected twice at port 3 and upon each reflection a fraction $|S_{13}|^2$ of the stored energy leaks out to port 1 and port 2, respectively. As a result, a total fraction $4|S_{13}|^2$ of the energy leaks out of the resonator per cycle.

With Eq. 4.23, we find

$$S_{31} = j\sqrt{\frac{\pi}{2Q_c}} \quad (4.24)$$

$$S_{33} \approx \sqrt{1 - 2|S_{31}|^2}e^{j\phi} \approx 1 - \frac{\pi}{2Q_c} + j\phi, \quad (\phi \ll 1) \quad (4.25)$$

where $\phi \ll 1$ because the wave is reflected from an open end of the transmission line at port 3. Because of the small coupling capacitance C_c , the input impedance of port 3 is very high. Meanwhile, the propagation constant γ is related to the distributed inductance L , capacitance C , and resistance R by:

$$\gamma = \alpha + j\beta = j\beta(1 - \frac{j}{2Q_{TL}}) = \sqrt{(R + j\omega L)(j\omega C)} \quad (4.26)$$

where

$$\beta = \omega\sqrt{LC} \quad (4.27)$$

$$Q_{TL} = \frac{\omega L}{R}. \quad (4.28)$$

Q_{TL} is the quality factor of the transmission line.

Define a quarter-wave resonance frequency $f_{\lambda/4}$ as,

$$f_{\lambda/4} = \frac{1}{4l\sqrt{LC}}. \quad (4.29)$$

Under the condition that $l \approx \lambda/4$ and $Z_l \ll Z_r$, we have

$$-e^{2\gamma l} \approx 1 + \frac{\pi}{2Q_{TL}} + j\pi \frac{f - f_{\lambda/4}}{f_{\lambda/4}} \quad (4.30)$$

$$\frac{1}{-\Gamma} = \frac{Z_r + Z_l}{Z_r - Z_l} \approx 1 + 2z_l = 1 + 2r_l + 2jx_l = 1 + \frac{\pi}{2Q_l} + 2jx_l \quad (4.31)$$

with

$$z_l = \frac{Z_l}{Z_r} = r_l + jx_l, \quad (|z_l| \ll 1) \quad (4.32)$$

$$Q_l = \frac{\pi}{4r_l} \quad (4.33)$$

where Q_l is the quality factor associated with the dissipation in the load impedance.

With these relationships, Eq. 4.21 can now be reduced to

$$\begin{aligned}
t_{21} &= S_{21} + \frac{S_{31}^2}{e^{2\gamma l}/\Gamma - S_{33}} \\
&= 1 - \frac{\frac{1}{Q_c}}{\left(\frac{1}{Q_c} + \frac{1}{Q_{TL}} + \frac{1}{Q_l}\right) + 2j\left(\frac{f-f_{\lambda/4}}{f_{\lambda/4}} + \frac{2}{\pi}x_L - \frac{\phi}{\pi}\right)} \\
&= 1 - \frac{\frac{Q_r}{Q_c}}{1 + 2jQ_r\frac{f-f_r}{f_r}}
\end{aligned} \tag{4.34}$$

where Q_r is the total quality factor of the resonator given by

$$\frac{1}{Q_r} = \frac{1}{Q_c} + \frac{1}{Q_i} = \frac{1}{Q_c} + \frac{1}{Q_{TL}} + \frac{1}{Q_l}. \tag{4.35}$$

Q_i is the internal quality factor of the resonator which accounts for all the other loss channels (Q_l , Q_{TL}) than through coupling to the feedline (Q_C). The resonance frequency f_r is given by

$$f_r = f_{\lambda/4}\left(1 + \frac{\phi}{\pi} - \frac{2x_L}{\pi}\right). \tag{4.36}$$

4.2.5 Properties of the resonance curves

For a simple shorted $\lambda/4$ resonator, we set $Z_l = 0$ and the resonance frequency and quality factor are given by

$$f_r = f_{\lambda/4}\left(1 + \frac{\phi}{\pi}\right) \tag{4.37}$$

$$\frac{1}{Q_r} = \frac{1}{Q_c} + \frac{1}{Q_i}, \quad Q_i = Q_{TL}. \tag{4.38}$$

According to Eq. 4.34, $t_{21}(f)$ is fully characterized by three parameters Q_c , f_r , Q_r (or Q_i). Q_c depends on the coupling capacitance C_c and is fixed for a certain coupler design. f_r and Q_i are related to the transmission line parameters (R , L , C , and l) of the resonator.

The complex t_{21} as a function of f is plotted in Fig. 4.3(a). When $f \ll f_r$ or $f \gg f_r$, t_{21} is close to $t_{21}(\infty) = 1$ and the feedline is unaffected by the resonator. When f sweeps through the resonance, t_{21} traces out a circle which is referred to as the resonance circle. At the resonance frequency $f = f_r$,

$$t_{21} = 1 - \frac{Q}{Q_c} = \frac{1/Q_i}{1/Q_i + 1/Q_c}. \tag{4.39}$$

The diameter of the circle is

$$d = \frac{Q}{Q_c} = \frac{1/Q_c}{1/Q_i + 1/Q_c}. \tag{4.40}$$

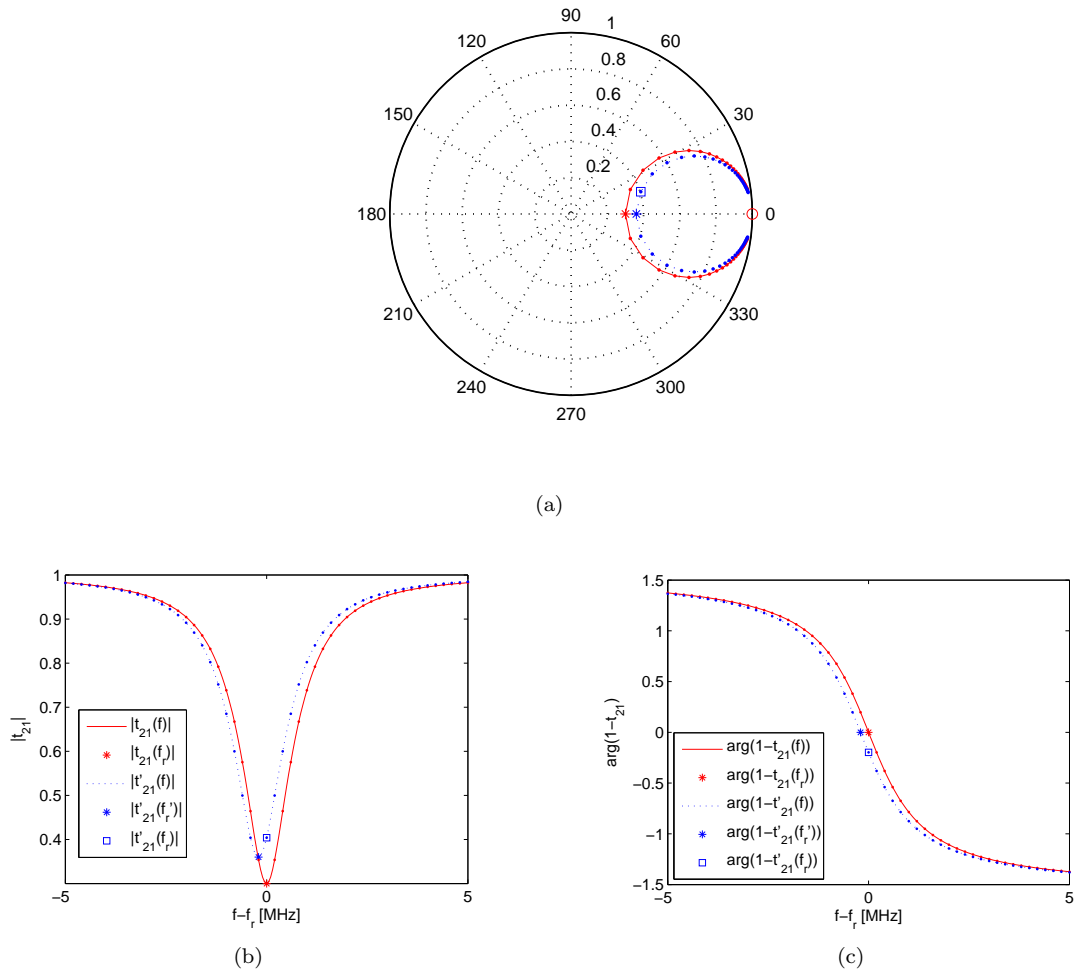


Figure 4.3: Plot of $t_{21}(f)$ (solid line) and its variation $t'_{21}(f)$ (dashed line) due to a small change in δf_r and δQ_r . (a) complex plot (b) magnitude plot (c) phase plot (with respect to $t_{21}(\infty) = 1$)

In the coupling Q limited case where $Q_c \ll Q_i$, we find $Q \rightarrow Q_c$ and $d \rightarrow 1$, while in the internal Q limited case where $Q_c \gg Q_i$, we find $Q \rightarrow Q_i$ and $d \rightarrow 0$. In the critical coupling case we have $Q_c = Q_i$ and $d = 1/2$.

The magnitude of t_{21} as a function of f is plotted in Fig. 4.3(b). According to Eq. 4.34, $|t_{21}(f)|^2$ has a Lorentzian shape

$$|t_{21}(f)|^2 = 1 - \frac{\frac{1}{Q_r^2} - \frac{1}{Q_i^2}}{\frac{1}{Q_r^2} + 4 \left(\frac{f-f_r}{f_r} \right)^2}. \quad (4.41)$$

Again, when $f \gg f_r$ or $f \ll f_r$, the transmission $|t_{21}|$ is close to 1; at the resonance frequency $f = f_r$, $|t_{21}|$ is at the minimum and the feedline is fully loaded by the resonator.

The phase angle θ of t_{21} with respect to the off-resonance point $t_{21}(\infty) = 1$ is plotted in Fig. 4.3(c). θ equals half of the phase angle measured from the center of the circle. According to Eq. 4.34, θ has the following profile

$$\theta = -\arctan 2Q_r \frac{f-f_r}{f_r} \quad (4.42)$$

which changes from $\pi/2$ to $-\pi/2$ when f sweeps from $f \ll f_r$ to $f \gg f_r$. We find that the slope $d\theta/df$ is maximized at the resonance frequency $f = f_r$.

The complex t_{21} can be measured with a vector network analyzer. The resonance parameters Q_c , f_r , Q , and Q_i can be obtained by fitting the t_{21} data to the theoretical models. There are at least two different fitting methods: one can fit the magnitude $|t_{21}|$ to a Lorentzian profile according to Eq. 4.41, or fit the phase angle θ to an “arctan” profile according to Eq. 4.42. Discussion on both methods are given in Appendix E.

4.3 Responsivity of MKIDs I — shorted $\lambda/4$ resonator ($Z_l = 0$)

If the distributed inductance and resistance of the superconducting transmission line have small variations δL and δR , due to a change in the quasiparticle density δn_{qp} , the variation in the resonance frequency and quality factor are given by, according to Eq. 4.28, Eq. 4.36, and Eq. 3.37-3.43,

$$\frac{\delta f_r}{f_r} = -\frac{1}{2} \frac{\delta L}{L} = -\frac{\alpha}{2} \frac{\delta L_{ki}}{L_{ki}} = -\frac{\alpha}{2} \frac{\delta X_s}{X_s} \quad (4.43)$$

$$\delta \frac{1}{Q_i} = \frac{\delta R}{\omega_0 L} = \alpha \frac{\delta R_s}{X_s} \quad (4.44)$$

where $Z_s = R_s + jX_s$ is the surface impedance and α is the kinetic inductance fraction. The variation of t_{21} with the microwave frequency tuned to and fixed at the original resonance frequency f_r is,

from Eq. 4.34,

$$\delta t_{21}|_{f=f_r} = \frac{Q_r^2}{Q_c} \left(\delta \frac{1}{Q_i} - 2j \frac{\delta f_r}{f_r} \right) \approx \alpha \frac{Q_r^2}{Q_c} \frac{\delta Z_s}{|Z_s|}, \quad (R_s \ll X_s \text{ for } T \ll T_c). \quad (4.45)$$

The relationship between δt_{21} and δn_{qp} is, from Eq. 4.45, Eq. 2.80, and Eq. 2.100,

$$\delta t_{21} = \alpha |\gamma| \kappa \frac{Q_r^2}{Q_c} \delta n_{qp} \quad (4.46)$$

where κ is the coefficient defined in Eq. 2.100.

Eq. 4.46 is appropriate for quasiparticles generated uniformly in the entire resonator, both in the center strip and the ground planes. A change in the thermal quasi-particle density caused by a change in the bath temperature will lead to a resonator response that is describable by Eq. 4.46. In the photon detection applications, however, the quasiparticles are usually generated only in the center strip, and so α in Eq. 4.46 should be replaced by the partial kinetic inductance fraction α^* .

We should also take into account the fact that the quasiparticles are usually generated near the shorted end instead of the entire center strip. It can be derived from a modal analysis that the effect to the resonance frequency and internal quality factor due to position dependent variations $\delta L(x)$ and $\delta R(x)$ are weighted by the square of the current distribution in the resonator²:

$$\frac{\delta f_r}{f_r} = -\frac{1}{l} \int_0^l \sin^2 \frac{\pi x}{2l} \frac{\delta L(x)}{L} dx \quad (4.47)$$

$$\frac{\delta \frac{1}{Q_i}}{Q_i} = \frac{2}{l} \int_0^l \sin^2 \frac{\pi x}{2l} \frac{\delta R(x)}{\omega_0 L} dx. \quad (4.48)$$

One can check Eq. 4.47 and 4.48 are consistent with Eq. 4.43 and Eq. 4.44. It follows that, if in general $\delta n_{qp}(x)$ has a position-dependent distribution along the center strip, the response δt_{21} is given by

$$\delta t_{21} = \left\{ \frac{2}{l} \int_0^l \sin^2 \frac{\pi x}{2l} \delta n_{qp}(x) dx \right\} \alpha^* |\gamma| \kappa \frac{Q_r^2}{Q_c}. \quad (4.49)$$

If the quasiparticles are uniformly distributed near the shorted end, with $\sin^2 \frac{\pi x}{2l} \approx 1$ we finally derive

$$\frac{\delta t_{21}}{\delta N_{qp}} \approx \frac{2\alpha^* |\gamma| \kappa Q_r^2}{V Q_c} \quad (4.50)$$

where V is the volume of the entire center strip and N_{qp} is the total number of quasiparticles.

Eq. 4.50 suggests that we can make the MKID more responsive by making α^* , γ , κ , and $\frac{Q_r^2}{Q_c}$ larger,

²For modal analysis, see Section 2.6 of reference [16]. It can also be derived by replacing the $\exp(-2\gamma l)$ factor with $\exp\left\{-2[\gamma l + \int_0^l \delta\gamma(x)dx]\right\}$ (the WKB approximation) in Eq. 4.21 and the derivations that follows.

and the volume V smaller. According to Eq. 2.100, κ is set by the material property (such as N_0 and Δ_0) of the superconductor and has a weak dependence on temperature and frequency. Once a superconductor is selected, κ is almost fixed. Both V and α^* can be largely increased by shrinking the geometry, including making the lateral dimension smaller and reducing the film thickness. When the film thickness is made thinner than the bulk penetration depth, $|\gamma|$ automatically takes its maximum value 1, according to Eq. 2.80. The factor Q_r^2/Q_c can be rewritten as

$$\frac{Q_r^2}{Q_c} = \frac{Q_i^2 Q_c}{(Q_i + Q_c)^2} = \frac{Q_i}{\left(\sqrt{\frac{Q_i}{Q_c}} + \sqrt{\frac{Q_c}{Q_i}}\right)^2} \geq \frac{Q_i}{4} \quad (4.51)$$

which has a maximum at $Q_c = Q_i$ for a fixed Q_i . Usually Q_i is set by the residual resistance of the superconductor or the dielectric loss of the resonator. The factor Q^2/Q_c is maximized by designing a coupling Q_c to match the internal Q_i .

To assess and optimize the overall performance of the detector, one has to take into account other factors such as quasiparticle recombination and noise. A comprehensive discussion of the sensitivity of MKID is given in Chapter 6.

An example response of δt_{21} to an increase in the quasiparticle density δn_{qp} is plotted in Fig. 4.3 by the dashed lines. Because R_s increases with n_{qp} and X_s decreases with n_{qp} , the resonance frequency shifts to lower frequency $f'_r < f_r$ and the quality factor decreases $Q' < Q$, resulting in a smaller resonance circle. Under the fixed driving frequency $f = f_r$, t_{21} moves from the point on the outer circle indicated by “*” to the point on the inner circle indicated by “□”. We note that the displacement δt_{21} in the complex plain has both components in the tangential direction (referred to as the phase direction) and the radial direction (referred to as the amplitude direction) of the resonance circle, which are proportional to δX_s and δR_s , respectively. The displacement in the phase direction is usually several times larger than in the amplitude direction (see Fig. 2.10). However, the noise in MKIDs is found to be almost entirely in the phase direction. Amplitude readout sometimes gives better sensitivity than phase readout. Discussion on noise, sensitivity, and phase readout vs. amplitude readout are the main topics of Chapter 5 and 6.

4.4 Responsivity of MKIDs II — $\lambda/4$ resonator with load impedance ($Z_l \neq 0$)

4.4.1 Hybrid resonators

Recently it has been more popular to use the “hybrid” resonator design for MKIDs. As shown in Fig. 4.4, the resonator consists of two sections, a long transmission line section and a short sensor strip section. The two sections may be made from two different superconductors or two different

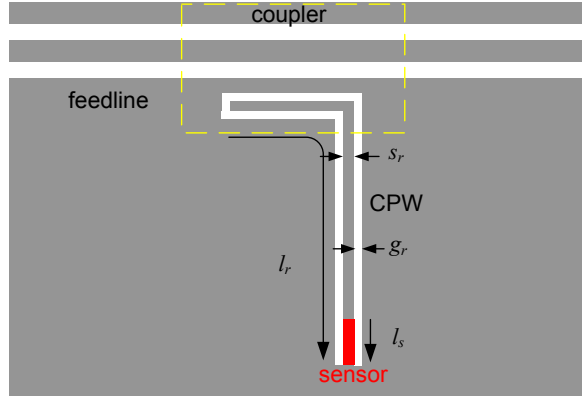


Figure 4.4: A hybrid design of MKID. The total length of the resonator (including the sensor strip) is l_r and the length of the sensor strip is l_s .

geometries. There are several advantages of using a hybrid design. If the sensor strip section is made of a lower gap superconductor (e.g., Al) and the transmission line section is made of a higher gap superconductor (e.g., Nb), it forms a natural quasi-particle trap — the quasiparticles generated on the sensor strip will be confined in the most sensitive region where the current is maximum. If the transmission line section is made of a wider geometry, it will benefit from the noise reduction effect (see Section 5.6).

4.4.2 Static response

The result of δt_{21} due to a static change in the load impedance $\delta z_l = \delta Z_l/Z_r$ is given by, according to Eq. 4.34,

$$\begin{aligned} \delta t_{21}|_{f=f_r} &= \frac{Q_r^2}{Q_c} \left(\delta \frac{1}{Q_r} - 2j \frac{\delta f_r}{f_r} \right) \\ &= \frac{4}{\pi} \frac{Q_r^2}{Q_c} \delta z_l. \end{aligned} \quad (4.52)$$

It is often the case that the total dissipation is dominated by the superconductor loss in the load impedance so that $Q_i \approx Q_l$. For example, in the hybrid submm MKID the sensor strip is made of thin Al (~ 40 nm) film and the rest of the resonator is made of thick Nb (> 100 nm) film. The background optical loading (from the blackbody radiation of the atmosphere) will create a constant density of quasiparticles in the Al strip that is much larger than the thermal quasiparticles density in both Al and Nb sections. In this case, the microwave power in the resonator is mainly dissipated through the surface resistance of Al.

It can be derived from Eq. 4.33, Eq. 4.52 that

$$\delta t_{21}|_{f=f_r} = \frac{Q_r^2}{Q_c Q_i} \frac{\delta z_l}{r_l} = \frac{Q_r^2}{Q_c Q_i} \frac{\delta n_{qp}}{n_{qp}} \left[1 + j \frac{\text{Im}(\kappa)}{\text{Re}(\kappa)} \right] \quad (4.53)$$

which is maximized under critical coupling $Q_c = Q_i$

$$\delta t_{21}|_{f=f_r, Q_c=Q_i} = \frac{1}{4} \frac{\delta n_{qp}}{n_{qp}} \left[1 + j \frac{\text{Im}(\kappa)}{\text{Re}(\kappa)} \right]. \quad (4.54)$$

We can also derive the following formulas

$$Q_i^{-1} = Q_l^{-1} = \frac{4R_l}{\pi Z_r} = \alpha^* |\gamma| \text{Re}(\kappa) n_{qp} \frac{2l_s}{l_r} \quad (4.55)$$

$$\frac{\delta f_r}{f_r} = -\frac{2X_l}{\pi Z_r} = -\frac{\alpha^*}{2} |\gamma| \text{Im}(\kappa) \delta n_{qp} \frac{2l_s}{l_r} \quad (4.56)$$

where l_s is the length of the sensor strip and $l_r \approx \lambda/4$ is the total length of the quarter-wave resonator (including l_s , see Fig. 4.4).

4.4.3 Power dissipation in the sensor strip

Before moving onto a discussion of the dynamic response, we first calculate the power dissipation P_l in the load impedance Z_l (sensor strip).

From a signal flow analysis illustrated in Fig. 4.2(c), the current I_l flowing through Z_l is given by

$$I_l = \frac{V_A^+ - V_A^-}{Z_r} = \frac{V_1^+}{\sqrt{Z_0 Z_r}} \frac{S_{A1}}{1 - \Gamma S_{AA}} (1 - \Gamma) \approx \frac{V_1^+}{\sqrt{Z_0 Z_r}} \frac{-2j\sqrt{\frac{2}{\pi Q_c}}}{\frac{1}{Q_r} + 2j\frac{f-f_r}{f_r}}. \quad (4.57)$$

The power dissipated by Z_l is given by

$$P_l = \frac{1}{2} |I_l|^2 R_l = P_1^+ \frac{\frac{2}{Q_i Q_c}}{1 + 4Q_r^2 \left| \frac{f-f_r}{f_r} \right|^2}. \quad (4.58)$$

Right on resonance $f = f_r$ and under critical coupling $Q_c = Q_i$, the power dissipated in the load impedance is half of the input power to port-1

$$P_l = \frac{1}{2} P_1^+ = \frac{1}{2} P_{\mu w}. \quad (4.59)$$

4.4.4 Dynamic response

Assuming that the load impedance has a slow time-dependent variation $\delta Z_L(t)$, we would like to find the corresponding response in the output voltage $\delta V_2^-(t)$.

Here we apply a perturbation analysis to the circuit. We first replace the load impedance Z_l with a resistor R_l and a inductor L_l in serial connection, and discuss them separately.

Let $V_R(t)$, $I(t)$, and R be the unperturbed voltage, current and resistance of the resistor. And

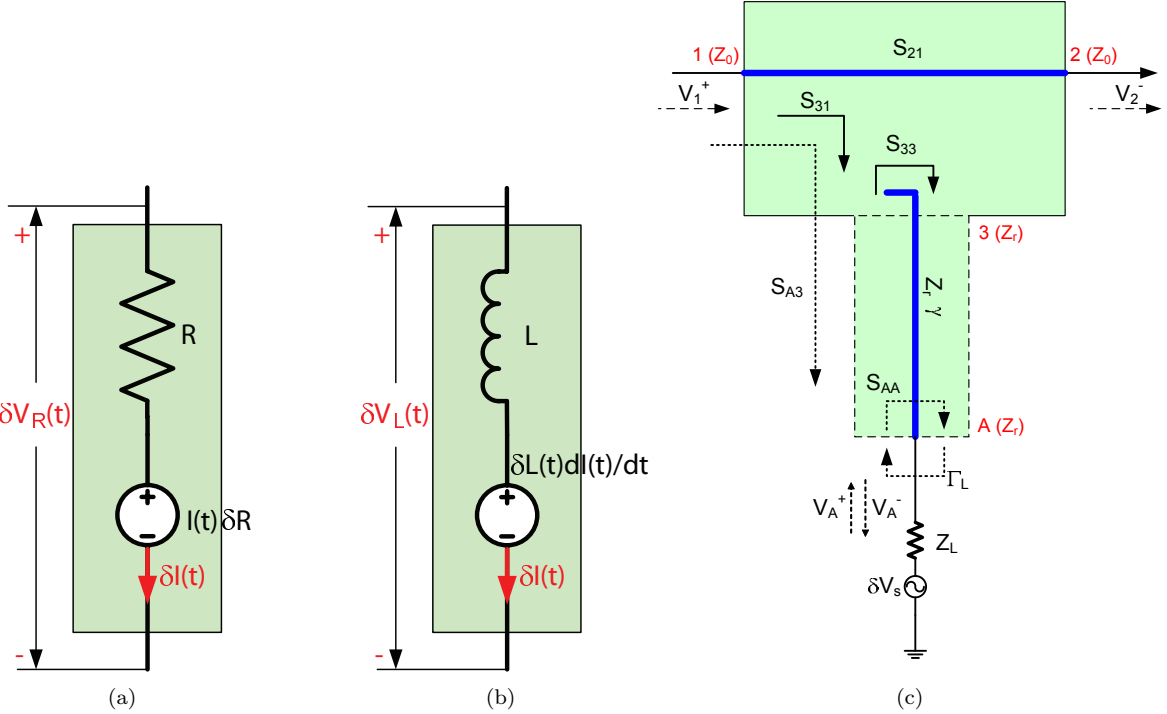


Figure 4.5: Equivalent circuit for (a) $\delta R(t)$ and (b) $\delta L(t)$ perturbations. The equivalent network model is shown in (c).

let $\delta V_R(t)$, $\delta I(t)$, and $\delta R(t)$ be their perturbations. Considering the total voltage, current, and resistance with and without the perturbations, we can write down the following equations,

$$[V_R(t) + \delta V_R(t)] = [I(t) + \delta I(t)][R + \delta R(t)] \quad (4.60)$$

$$V_R(t) = I(t)R. \quad (4.61)$$

Subtracting Eq. 4.61 from Eq. 4.60 and dropping the 2nd-order terms, we get

$$\delta V_R(t) = I(t)\delta R(t) + \delta I(t)R \quad (4.62)$$

which suggests an effective circuit as shown in Fig. 4.5(a).

Similarly, for the inductance perturbation we have

$$\delta V_L(t) = L(t)\frac{d}{dt}\delta I(t) + \delta L(t)\frac{d}{dt}I(t) \quad (4.63)$$

which suggests an effective circuit as shown in Fig. 4.5(b).

Therefore the effect of the perturbation δZ_l can be taken into account by adding an effective

voltage source $\delta V_s(t)$ to the original network model, as illustrated in Fig. 4.5 (c),

$$\delta V_s(t) = \delta R(t)I(t) + \delta L(t)\frac{d}{dt}I(t). \quad (4.64)$$

Assume that $\delta R(t)$ and $\delta L(t)$ are narrow-banded signal with Fourier transforms

$$\begin{aligned}\delta R(t) &= \int_{-\Delta\tilde{f}}^{+\Delta\tilde{f}} \delta R(\tilde{f}) e^{j2\pi\tilde{f}t} d\tilde{f} \\ \delta L(t) &= \int_{-\Delta\tilde{f}}^{+\Delta\tilde{f}} \delta L(\tilde{f}) e^{j2\pi\tilde{f}t} d\tilde{f}.\end{aligned} \quad (4.65)$$

Inserting Eq. 4.65 into Eq. 4.64 and using $I(t) = I_l e^{j2\pi f t}$, we find

$$\delta V_s(f + \tilde{f}) = I_l[\delta R(\tilde{f}) + i2\pi f \delta L(\tilde{f})] = I_l \delta Z_l(\tilde{f}) \quad (4.66)$$

where $\delta V_s(f + \tilde{f})$ is the Fourier transform of $\delta V_s(t)$. $\delta V_2^-(t)$, the voltage response at port 2, is given by,

$$\begin{aligned}\delta V_2^-(f + \tilde{f}) &= V_A^+(f + \tilde{f}) \sqrt{\frac{Z_0}{Z_L}} S_{2A}(f + \tilde{f}) \\ &= \frac{\delta V_s(f + \tilde{f})}{1 - \Gamma S_{AA}} \frac{Z_r}{Z_r + Z_l} \sqrt{\frac{Z_0}{Z_r}} S_{2A}.\end{aligned} \quad (4.67)$$

Now we define a time dependent transmission coefficient $t_{21}(t)$ with its Fourier transform $t_{21}(\tilde{f})$

$$\delta t_{21}(\tilde{f}) = \frac{\delta V_2^-(f + \tilde{f})}{V_1^+}. \quad (4.68)$$

When the output microwave signal V_2^- is homodyne mixed with V_1^+ using a IQ mixer, the dynamic trajectory in the IQ plane is described $t_{21}(t)$.

From Eq. 4.57, 4.66, and 4.67, we derive

$$\delta t_{21}(\tilde{f}) = \frac{4Q_r^2}{\pi Q_c} \frac{1}{1 + 2jQ_r \frac{f-f_r}{f_r}} \frac{1}{1 + 2jQ_r \frac{f+\tilde{f}-f_r}{f_r}} \delta z_l(\tilde{f}). \quad (4.69)$$

When the resonator is driven on resonance $f = f_r$, we find

$$\delta t_{21}(\tilde{f})|_{f=f_r} = \frac{4Q_r^2}{\pi Q_c} \frac{1}{1 + 2jQ_r \frac{\tilde{f}}{f_r}} \delta z_l(\tilde{f}). \quad (4.70)$$

Eq. 4.70 shows that under small perturbation δz_l , the resonator circuit acts as a low-pass filter with a bandwidth equal to the resonator's bandwidth $f_r/2Q$. One can also verify that by setting $\tilde{f} = 0$, Eq. 4.70 gives the same static response as derived in Eq. 4.52.

In the case that Q_i is set by the superconductor loss in the sensor strip, we find

$$\delta t_{21}(\tilde{f})|_{f=f_r} = \frac{Q_r^2}{Q_c Q_i} \frac{\delta z_l(\tilde{f})}{r_l} \frac{1}{1 + 2jQ_r \frac{\tilde{f}}{f_r}}. \quad (4.71)$$

We further assume that at any time the instant load impedance $Z_L(t)$ depends only on the QP density $n_{qp}(t)$ at that time. With this assumption, Eq. 4.71 leads to

$$\delta t_{21}(\tilde{f})|_{f=f_r} = \frac{Q_r^2}{Q_c Q_i} \frac{\delta n_{qp}(\tilde{f})}{n_{qp}} \left[1 + j \frac{\text{Im}(\kappa)}{\text{Re}(\kappa)} \right] \frac{1}{1 + 2jQ_r \frac{\tilde{f}}{f_r}} \quad (4.72)$$

which is maximized at critical coupling $Q_c = Q_i$

$$\delta t_{21}(\tilde{f})|_{f=f_r, Q_c=Q_i} = \frac{1}{4} \frac{\delta n_{qp}(\tilde{f})}{n_{qp}} \left[1 + j \frac{\text{Im}(\kappa)}{\text{Re}(\kappa)} \right] \frac{1}{1 + 2jQ_r \frac{\tilde{f}}{f_r}}. \quad (4.73)$$

It's easy to see that Eq. 4.71, 4.72 and 4.73 are the counterparts of Eq. 4.52, Eq. 4.53, and Eq. 4.54, respectively.

Chapter 5

Excess noise in superconducting microwave resonators

5.1 A historical overview of the noise study

The fundamental noise limit for MKIDs is set by the quasiparticle generation-recombination (g-r) noise (see Section 6.1.1), which decreases exponentially to zero and makes the detector extremely sensitive as the temperature goes to zero. Unfortunately and unexpectedly, a significant amount of excess noise was observed in these resonators, which prevents the detectors from achieving the ultimate sensitivity imposed by the g-r noise. The discovery of this excess noise and a discussion of its influence on detector NEP dates back to 2003[14]. There we have shown, from the noise measurement of a 200 nm thick Al on sapphire MKID, that the NEP limited by the excess noise is two orders of magnitude higher than that limited by the g-r noise, and one order of magnitude higher than that limited by the HEMT amplifier (due to the coupling limited Q). The origin of this excess noise remained largely unknown at that time.

Since then, systematic studies of the excess noise have been carried out both theoretically and experimentally. Early studies were focused on exploring the noise properties and are described in detail in Mazin's thesis[15]. Several interesting properties of the excess noise have been observed in this early work, although some of the discussions and conclusions remained more qualitative than quantitative. We found that the noise is dominantly a phase noise (or a frequency noise, equivalent to a jitter in the resonator's resonance frequency); we observed that the excess noise has a strong dependence on the microwave readout power. An important discovery was that the Al devices made on sapphire substrate gave significant lower noise than those made on the Si substrate. Although in 2003[14] we suggested that the excess noise is too large to be explained by the quasiparticle fluctuations in the superconductor, the apparent substrate dependence of the noise gave stronger evidence that the noise is not related to superconductor.

Meanwhile, we began to search for the candidates of the noise source from the literature of low

temperature physics. We noticed that excess telegraph noise was reported from the single electron transistor (SET) community. In one experiment, they were able to constrain the noise source as being in the substrate by looking at the correlation of the charge fluctuation signals from the two SETs placed close to each other on the same substrate[58]. Fluctuations of similar origins were also found in tunnel junctions and were reported from the quantum computing community. By spring 2005, Peter Day, a JPL member of our MKID group, had described in a proposal the idea that the noise might be generated by two-level tunneling systems in amorphous dielectrics. Our affection to this possibility was substantially increased by the results of Martinis et al. [59], who found that the decoherence of their Josephson qubits could be explained by the dielectric loss caused by the two-level systems (TLS) in the tunnel barrier. TLS are tunneling states in amorphous solids, which have a broad distribution of energy splitting and can be thermally activated at low temperatures, causing anomalous properties (thermal, acoustic and dielectric) and noise. It turns out that TLS were studied as early as in 1960s and a quite established TLS model already existed since the early 1970s[60, 61]. One of the results from Martinis et al. that caught our attention was that the TLS-induced dielectric loss has a strong saturation effect, a behavior perhaps related to the observed power dependence of excess noise in our resonators. Since then, TLS has become a strong candidate for the noise source of our resonators.

The devices tested in the early days were mostly made of Al. In these measurements, the resonator's frequency shift and internal loss are dominated by the conductivity of the superconductor. It was first proposed by Kumar[62, 63] to use Nb resonators to study the low temperature anomalous frequency shift predicted by the TLS theory, and the temperature dependence of excess noise. For this purpose, a Nb on Si CPW resonator was fabricated and tested. From this device, we got two interesting results. First, the noise was seen to decrease dramatically with temperature. Although we do not know what mechanism causes this phenomenon, this is a strong evidence that the excess noise is not from the superconductor, because Nb has $T_c = 9.2$ K and at $T < 1$ K the contribution from the conductivity is negligible. Second, the noise level measured from these resonators were as low as that from the Al on sapphire resonators, contradicting our general experience of higher noise on Si substrate than sapphire substrate. From this experiment, we began to suspect that the TLS noise source might be related to the surface or interface, instead of to the bulk substrate, which was proved to be true in a later experiment.

I started to study the excess noise in 2004, following the early work of Mazin's thesis. In summary, progress in three major areas has been made in my thesis. First, the properties of the excess noise, including power, temperature, material, and geometry dependence, have been quantified; Second, the TLS, responsible for both the low temperature anomalous frequency shift and the excess noise, are confirmed to have a surface distribution, while a bulk distribution in substrate has been ruled out. Three, a semi-empirical noise model has been developed to explain the power and geometry

dependence of the noise, which is useful to predict noise for a specified resonator geometry.

The organization of this chapter follows the historical path of the noise study. Following a brief introduction to the noise measurement setup and the data analysis in Section 5.2, we present the observed general properties of the excess noise in Section 5.3, including its property of being pure frequency (phase) noise, the power dependence, temperature dependence, material dependence, and geometry dependence. These properties give strong evidence that the excess noise is not coming from the superconductor but from the two level-systems in the dielectric materials in the resonator. For this reason, we give a review of the standard TLS theory in the first half of Section 5.4. The established TLS theory may be readily applied to explain the power and temperature dependence of the resonator's frequency shift and dissipation, but not the noise. We dedicate the second half of Section 5.4 to the discussion of the noise model. Because we still do not have a complete TLS noise model yet, in this section we do not go any further than giving some qualitative and semi-quantitative discussions. Nevertheless, based on the TLS theory and experimental observations of the excess noise, we propose a semi-empirical model that is practically useful to predict noise in the resonators. Guided by the TLS theory, several interesting experiments are designed to test the TLS hypothesis, which is discussed in Section 5.5. In the first two experiments, TLS are artificially added into the resonator through a deposited layer of amorphous dielectric material. The behavior of the resonators loaded with TLS is found to be in good agreement with the TLS theory and the observed increase of frequency noise in these resonators demonstrates that TLS are able to act as noise source. The next two experiments, which explore the geometrical scaling of the TLS-induced frequency shift and noise, are the two critical experiments of this chapter. They give direct experimental evidence that the TLS are distributed on the surface of the resonator but not in the bulk substrate. Moreover, the measured geometrical scaling of frequency noise can be satisfactorily explained by the semi-empirical model introduced in Section 5.4.6. With the knowledge about TLS and excess noise, we discuss a number of methods that can potentially reduce the excess noise in Section 5.6, which concludes this chapter.

5.2 Noise measurement and data analysis

The homodyne system used for resonator readout and for noise measurement is illustrated in Fig. 5.1. A microwave synthesizer generates a microwave signal at frequency f which is used to excite a resonator. The transmitted signal is amplified with a cryogenic high electron mobility transistor (HEMT) amplifier mounted at 4 K stage and a room-temperature amplifier, and is then compared to the original signal using an IQ mixer. The output voltages I and Q of the IQ mixer are proportional to the in-phase and quadrature amplitudes of the transmitted signal. As f is varied, the output $\xi = [I, Q]^T$ (the superscript T represents the transpose) traces out a resonance circle (Fig. 5.2(a)).

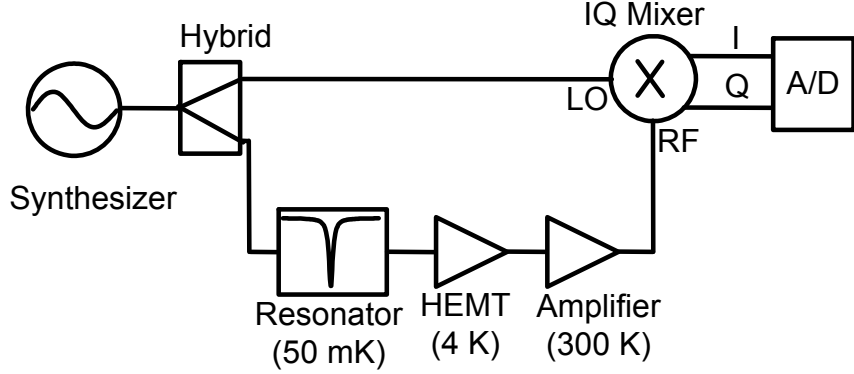


Figure 5.1: A diagram of the homodyne readout system used for the noise measurement

With f fixed, ξ is seen to fluctuate about its mean, and the fluctuations $\delta\xi(t) = [\delta I(t), \delta Q(t)]^T$ are digitized for noise analysis, typically over a 10 s interval using a sample rate $F_s = 250$ kHz.

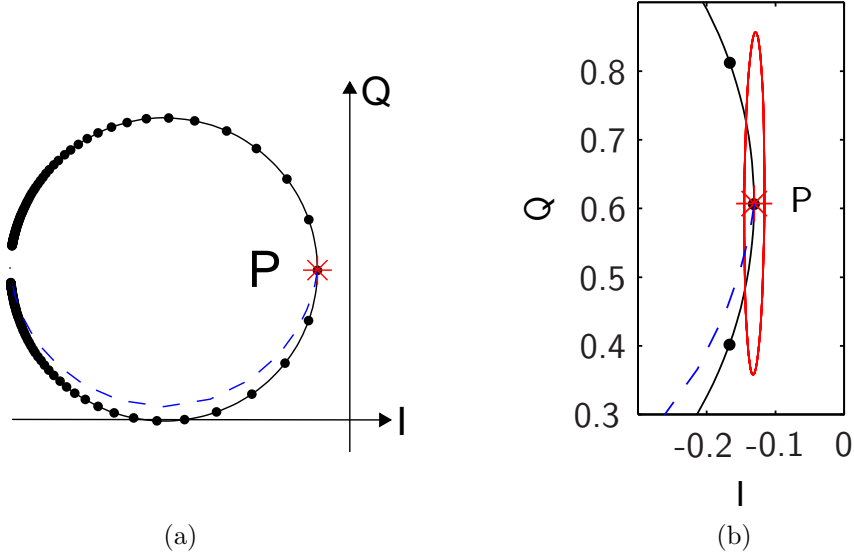


Figure 5.2: (a) Resonance circle of a 200 nm Nb on Si resonator at 120 mK (solid line), quasiparticle trajectory calculated from the Mattis-Bardeen theory[39] (dashed line). For this figure, the readout point $\xi = [I, Q]$ is located at the resonance frequency f_r . (b) Noise ellipse (magnified by a factor of 30). Other parameters are $f_r=4.35$ GHz, $Q_r = 3.5 \times 10^5$ (coupling limited), $w=5$ μm , $g=1$ μm , readout power $P_r \approx -84$ dBm, and internal power $P_{\text{int}} \approx -30$ dBm.

The fluctuations $\delta\xi(t)$ (vector function of t) can be projected into two special directions, the direction tangent to the resonance circle (referred to as the phase direction) and its orthogonal direction (referred to as the amplitude direction). Fluctuation components $\delta\xi_{\parallel}(t)$ and $\delta\xi_{\perp}(t)$ (scalar functions of t) in these two directions correspond to fluctuations in the phase and amplitude of the resonator's electric field \vec{E} , respectively. The voltage noise spectra in the phase and amplitude

direction can be calculated from

$$\begin{aligned}\langle \delta\xi_{\parallel}(\nu)\delta\xi_{\parallel}^*(\nu') \rangle &= S_{\parallel}(\nu)\delta(\nu - \nu') \\ \langle \delta\xi_{\perp}(\nu)\delta\xi_{\perp}^*(\nu') \rangle &= S_{\perp}(\nu)\delta(\nu - \nu')\end{aligned}\quad (5.1)$$

where $\delta\xi_{\parallel}(\nu)$ and $\delta\xi_{\perp}(\nu)$ are the Fourier transform of the time domain fluctuations $\delta\xi_{\parallel}(t)$ and $\delta\xi_{\perp}(t)$, respectively.

The noise data $\delta\xi(t)$ can also be quantified by studying the spectral-domain noise covariance matrix $S(\nu)$, defined by

$$\langle \delta\xi(\nu)\delta\xi^{\dagger}(\nu') \rangle = S(\nu)\delta(\nu - \nu'), \quad S(\nu) = \begin{pmatrix} S_{II}(\nu) & S_{IQ}(\nu) \\ S_{IQ}^*(\nu) & S_{QQ}(\nu) \end{pmatrix}, \quad (5.2)$$

where $\delta\xi(\nu)$ is the Fourier transform of the time-domain data, the dagger represents the Hermitian conjugate, $S_{II}(\nu)$ and $S_{QQ}(\nu)$ are the auto-power spectra, and $S_{IQ}(\nu)$ is the cross-power spectrum.

The matrix $S(\nu)$ is Hermitian and may be diagonalized using a unitary transformation; however, we find that the imaginary part of S_{IQ} is negligible and that an ordinary rotation applied to the real part $\text{Re } S(\nu)$ gives almost identical results. We calculate the eigenvectors and eigenvalues of $S(\nu)$ at every frequency ν :

$$O^T(\nu) \text{Re } S(\nu) O(\nu) = \begin{pmatrix} S_{aa}(\nu) & 0 \\ 0 & S_{bb}(\nu) \end{pmatrix}, \quad (5.3)$$

where $O(\nu) = [v_a(\nu), v_b(\nu)]$ is an orthogonal rotation matrix. We use $S_{aa}(\nu)$ and $v_a(\nu)$ to denote the larger eigenvalue and its eigenvector.

The total noise power in $\delta\xi(t)$ can be quantified and clearly visualized by plotting a noise ellipse, defined by

$$\delta\xi^T C^{-1} \delta\xi = 1 \quad (5.4)$$

where

$$C = \int_{\nu_1}^{\nu_2} \text{Re } S(\nu) d\nu \quad (5.5)$$

is the covariance matrix for δI and δQ filtered for the corresponding bandpass.

The noise in the phase direction can also be described in terms of the phase noise $S_{\theta}(\nu)$ and the (fractional) frequency noise $S_{\delta f_r}(\nu)/f_r^2$, because the voltage fluctuations in the phase direction $\delta\xi_{\parallel}$ can be viewed as being caused by either fluctuations in the phase angle, $\delta\theta$ (with reference to the center of the resonance circle) or jitters in the resonator's resonance frequency, δf_r . The voltage noise $S_{\parallel}(\nu)$, phase noise $S_{\theta}(\nu)$ and the frequency noise $S_{\delta f_r}(\nu)/f_r^2$ are related to each other by the

following relationships:

$$S_{\delta\theta}(\nu) = \frac{S_{||}(\nu)}{r^2}, \quad (\delta\theta = \frac{\delta\xi_{||}}{r}) \quad (5.6)$$

$$S_{\delta f_r}(\nu)/f_r^2 = \frac{S_{\delta\theta}(\nu)}{16Q^2}, \quad (\frac{\delta f_r}{f_r} = \frac{\delta\theta}{4Q}) \quad (5.7)$$

where r is the radius of the resonance circle. They will be used to compare the excess noise in future discussions.

In practice, the calculation of the noise spectra (e.g., $S_{II}(\nu)$ and $S_{QQ}(\nu)$) can be accomplished efficiently using the Matlab function “pwelch”[54]. We use “pwelch” to calculate the power spectrum in three different frequency resolutions for three noise frequency ranges. The noise spectra shown in this chapter usually are plotted with 1 Hz resolution for $1 \text{ Hz} \leq \nu < 50 \text{ Hz}$, 10 Hz resolution for $1 \text{ Hz} \leq \nu < 1 \text{ kHz}$, and 100 Hz resolution for $1 \text{ kHz} \leq \nu < 125 \text{ kHz}$ ($F_s/2$). Unless noted, the noise spectra are calculated as double-sided spectra with $S(\nu) = S(-\nu)$ and only the positive frequencies are plotted.

5.3 General properties of the excess noise

5.3.1 Pure phase (frequency) noise

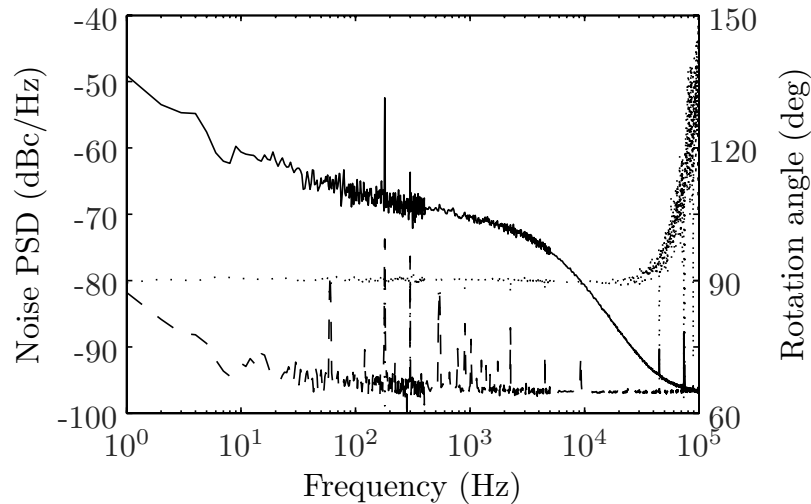


Figure 5.3: Noise spectra in the phase ($S_{aa}(\nu)$, solid line) and amplitude ($S_{bb}(\nu)$, dashed line) directions, and the rotation angle ($\phi(\nu)$, dotted line). The noise data are from the same Nb/Si resonator under the same condition as in Fig. 5.2.

A typical pair of spectra $S_{aa}(\nu)$ and $S_{bb}(\nu)$ are shown in Fig. 5.3, along with the rotation angle $\phi(\nu)$, defined as the angle between $v_a(\nu)$ and the I axis. Three remarkable features are found for

all noise data. First, $\phi(\nu)$ is independent of ν within the resonator bandwidth (the r.m.s. scatter is $\sigma_\phi \leq 0.4^\circ$ per 10 Hz frequency bin from 1 Hz to 5 kHz in Fig. 5.3), which means that only two special directions, v_a and v_b , diagonalize $S(\nu)$. Second, v_a is always tangent to the IQ resonance circle while v_b is always normal to the circle, even when f is detuned from f_r . Because $S_{aa}(\nu)$ and $S_{bb}(\nu)$ are the noise spectra projected into these two constant directions according to Eq. 5.3, they are equal to the voltage noise spectra calculated from Fourier transform of the projected time domain noise data $\delta\xi_{\parallel}(t)$ and $\delta\xi_{\perp}(t)$,

$$\begin{aligned} S_{aa}(\nu) &= S_{\parallel}(\nu) \\ S_{bb}(\nu) &= S_{\perp}(\nu). \end{aligned} \quad (5.8)$$

Third, $S_{aa}(\nu)$ is well above $S_{bb}(\nu)$ (see Fig. 5.3). When we plot the noise ellipse according to Eq. 5.4 and 5.5 using a integration bandpass $\nu_1 = 1$ Hz and $\nu_2 = 1$ kHz, we find the major axis of the noise ellipse is always in the phase direction, and the ratio of the two axes is always very large (8 for the noise ellipse shown in Fig. 5.2(b)).

Fig. 5.3 also shows that the amplitude noise spectrum is flat except for a $1/\nu$ knee at low frequency contributed by the electronics. The amplitude noise is independent of whether the synthesizer is tuned on or off the resonance, and is consistent with the noise temperature of the HEMT amplifier. The phase noise spectrum has a $1/\nu$ slope below 10 Hz, typically a $\nu^{-1/2}$ slope above 10 Hz, and a roll-off at the resonator bandwidth $f_r/2Q_r$ (as is the case in Fig. 5.3) or at the intrinsic noise bandwidth $\Delta\nu_n$, whichever comes first. The phase noise is well above the HEMT noise, usually by two or three orders of magnitude (in rad^2/Hz) at low frequencies. It is well in excess of the synthesizer phase noise contribution or the readout system noise.

Quasi-particle fluctuations in the superconductor, perhaps produced by temperature variations or the absorption of high frequency radiation, can be securely ruled out as the source of the measured noise by considering the direction in the IQ plane that would correspond to a change in quasi-particle density δn_{qp} . According to the discussion in Section 2.4, both the real and inductive parts of the complex conductivity σ respond linearly to δn_{qp} , $\delta\sigma = \delta\sigma_1 - i\delta\sigma_2 = \kappa|\sigma|\delta n_{qp}$, resulting in a trajectory that is always at a nonzero angle $\psi = \tan^{-1}(\delta\sigma_1/\delta\sigma_2)$ to the resonance circle, as indicated by the dashed lines in Fig. 5.2(a) and (b). Mattis-Bardeen calculations yield $\psi = \tan^{-1}[\text{Re}(\kappa)/\text{Im}(\kappa)] > 7^\circ$ for Nb below 1 K, so quasi-particle fluctuations are strongly excluded, since $\psi \gg \sigma_\phi$. Furthermore, ψ is measured experimentally by examining the response to X-ray, optical/UV, or submillimeter photons, and is typically $\psi \approx 15^\circ$ ([24, 50], and see Section 5.6.3).

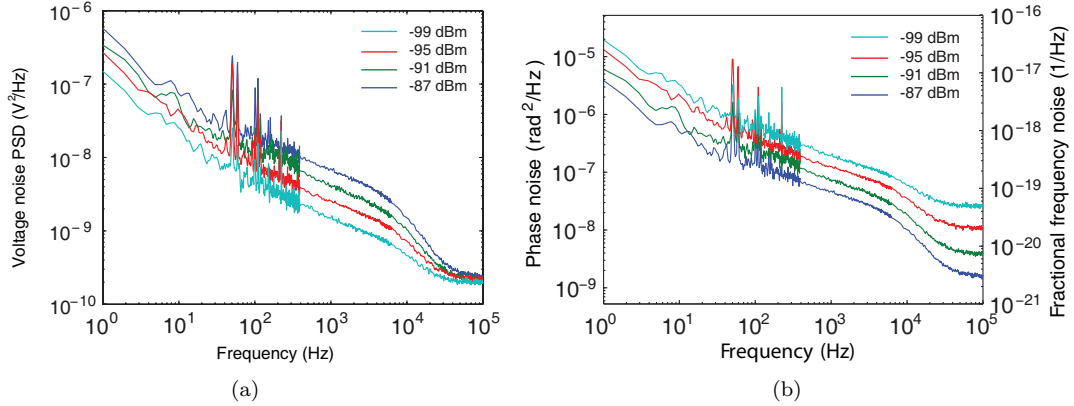


Figure 5.4: Excess noise in the phase direction under different readout powers $P_{\mu w}$. (a) Voltage noise spectrum $S_{||}(\nu)$. (b) Phase noise spectrum $S_{\delta\theta}(\nu)$ (left axis) and fractional frequency noise spectrum $S_{\delta f_r}(\nu)/f_r^2$ (right axis). The readout powers of the 4 curves are $P_{\mu w} = -87$ dBm, -91 dBm, -95 dBm, -99 dBm from top to bottom in (a) and from bottom to top in (b). The data is measured from a 200 nm thick Al on sapphire resonator.

5.3.2 Power dependence

The excess noise has a dependence on the microwave readout power $P_{\mu w}$. Fig. 5.4 compares the measured noise spectra of a resonator under four different readout powers in steps of 4 dBm. We found the voltage noise increases with the readout power, as shown in Fig. 5.4(a). A 2 dB separation is found between the two adjacent noise spectra, suggesting

$$S_{||}(\nu) \propto P_{\mu w}^{\frac{1}{2}}. \quad (5.9)$$

The excess noise, when converted to phase noise or frequency noise, decreases with readout power. The same separation of 2 dB but with a reversed order (top curve with the lowest $P_{\mu w}$) is seen in Fig. 5.4(b), which suggests:

$$S_{\delta\theta}(\nu) \propto P_{\mu w}^{-\frac{1}{2}}, \quad S_{\delta f_r}(\nu)/f_r^2 \propto P_{\mu w}^{-\frac{1}{2}}. \quad (5.10)$$

Eq. 5.9 and Eq. 5.10 are consistent because the radius of the resonance loop r scales as $r \propto P_{\mu w}^{\frac{1}{2}}$.

To compare the excess noise among resonators with different f_r and Q_r , we plot the frequency noise $S_{\delta f_r}(\nu)/f_r^2$ as a function of the microwave power inside the resonator (the internal power). It can be shown that the internal power P_{int} is related to the readout power $P_{\mu w}$ by

$$P_{\text{int}} = \frac{2}{\pi} \frac{Q_r^2}{Q_c} P_{\mu w} \quad (5.11)$$

for a quarter-wave resonator.

The frequency noise vs. internal power for resonators with different f_r and Q_r on the same

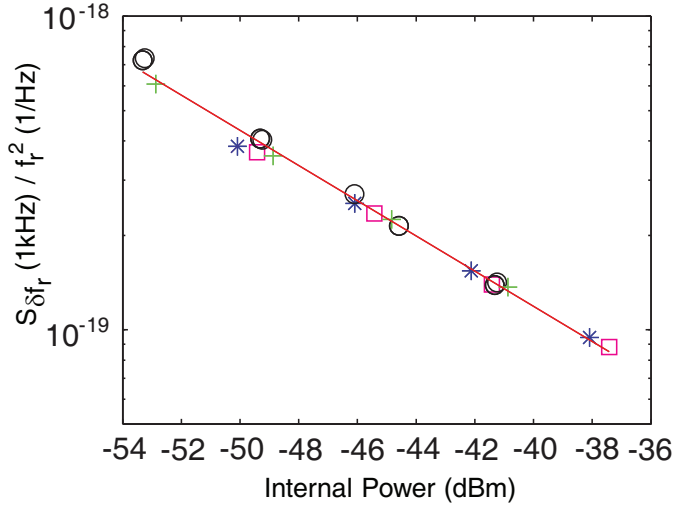


Figure 5.5: Frequency noise at 1 kHz $S_{\delta f_r}(1 \text{ kHz})/f_r^2$ vs. internal power P_{int} falls on to straight lines of slope $-1/2$ in the log-log plot indicating a power law dependance: $S_{\delta f_r/f_r} \propto P_{\text{int}}^{-1/2}$. Data points marked with “+”, “□”, and “*” indicate the on-resonance ($f = f_r$) noise of three different resonators (with different f_r and Q_r on the same chip) under four different $P_{\mu w}$. Data points marked with “○” indicate the noise of resonator 1 (marked with “*”) measured at half-bandwidth away from the resonance frequency ($f = f_r \pm f_r/2Q_r$) under the same four $P_{\mu w}$. The data is measured from a 200 nm thick Al on sapphire device.

substrate are compared in Fig. 5.5. The data points, from three different resonators, four different readout powers, driven on-resonance and detuned, fall nicely onto a straight line of slope $-1/2$ in the log-log plot, suggesting that the frequency noise depends on the internal power P_{int} of the resonator by a power law

$$S_{\delta f_r}(\nu)/f_r^2 \propto P_{\text{int}}^{-\frac{1}{2}}. \quad (5.12)$$

The power law index $-1/2$ in Eq. 5.12 is suggestive. For comparison, amplifier phase noise is a multiplicative effect that would give a constant noise level independent of P_{int} , while the amplifier noise temperature is an additive effect that would produce a $1/P_{\text{int}}$ dependence.

5.3.3 Metal-substrate dependence

The excess noise also depends on the materials used for the resonator. In Fig. 5.6, we plot the frequency noise spectrum at 1 KHz $S_{\delta f_r}(1 \text{ kHz})/f_r^2$ against internal power P_{int} for five resonators made of different metal-substrate combinations (all substrates used are crystalline substrates). In addition to the power dependence $S_{\delta f_r}(\nu)/f_r^2 \propto P_{\text{int}}^{-1/2}$, we find that the noise levels are material dependent. In general, sapphire substrates give lower phase noise than Si or Ge, roughly by an order of magnitude in the noise power. However the Nb/Si resonator showed low noise comparable with Al/sapphire resonator, suggesting that the etching or interface chemistry, which is different for Nb and Al, may play a role. Two Al/Si resonators with very different Al thicknesses and kinetic

inductance fractions[64] fall onto the dashed equal-noise scaling line, strongly suggesting that the superconductor is not responsible for the phase noise.

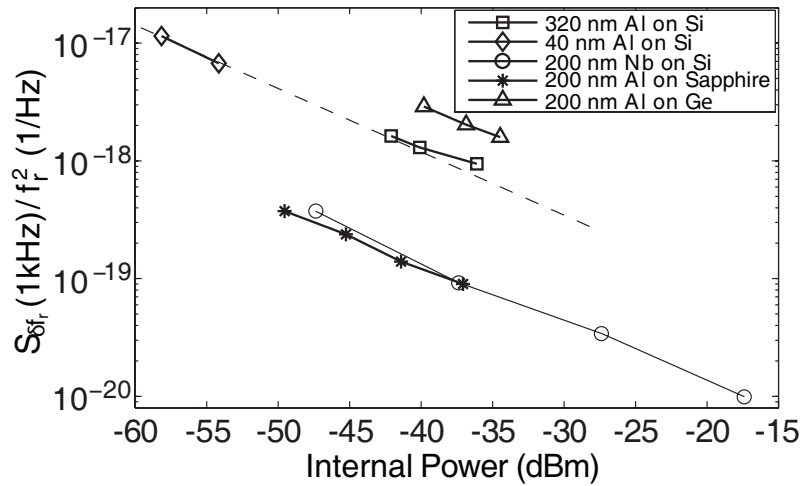


Figure 5.6: Power and material dependence of the frequency noise at $\nu = 1$ kHz. All the resonators shown in this plot have $w=3$ μm , $g=2$ μm and are measured around 120 mK. The spectra used in this plot are single-sided ($\nu > 0$).

As will be discussed in great detail later in this chapter, the TLS on the surface of the resonator, either metal surface or the exposed substrate surface, are responsible for the excess noise. Therefore, the metal-substrate dependence of the excess noise shown in Fig. 5.6 turns out to have nothing to do with the bulk properties of the superconductor or the substrate. Instead, it's their surface or interface properties that make a difference. For example, the metal Al, Nb and crystalline Si, Ge can all form a native oxide layer on the surface, which can be the host material of the TLS. The defects, impurities and chemical residues introduced during etching and other processes of the fabrication may be another source of TLS.

5.3.4 Temperature dependence

The temperature dependence of the excess frequency noise is best demonstrated by the experiment in which the noise of a Nb on Si resonator is measured at temperatures below 1 K. Because Nb has a transition temperature $T_c = 9.2$ K, the noise contribution from superconductor are frozen at $T < 1$ K. Any temperature dependence of noise has to be from other low energy excitations — TLS in the resonator.

Fig. 5.7 shows the measured phase and amplitude noise spectra under readout power $P_{\mu w} = -85$ dBm at several temperatures between 120 mK and 1200 mK. While the amplitude noise ($S_{\perp}(\nu)$, in green) remains almost unchanged, the phase noise ($S_{\parallel}(\nu)$, in blue) decreases steeply with temperature. As mentioned earlier, the amplitude noise spectrum $S_{\perp}(\nu)$ is consistent with the noise floor

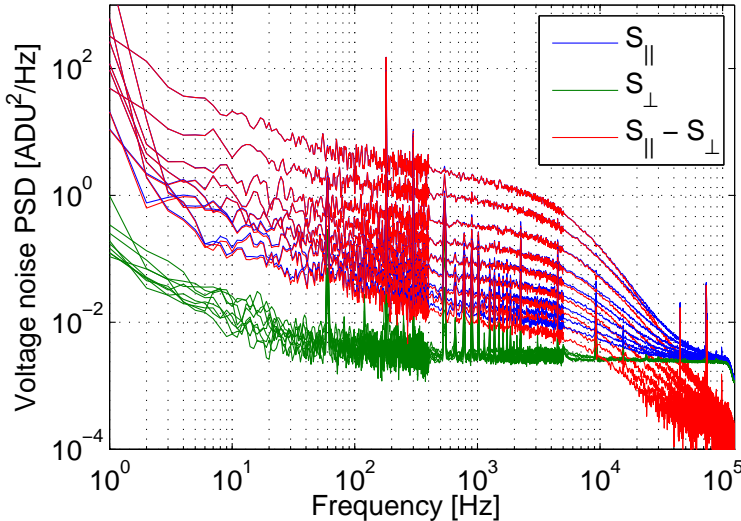


Figure 5.7: Phase noise ($S_{\parallel}(\nu)$, blue curves) and amplitude noise ($S_{\perp}(\nu)$, green curves) spectra measured at $T=120, 240, 400, 520, 640, 760, 880, 1000, 1120$ mK (from top to bottom). The true phase noise can be calculated by subtracting the amplitude noise from the phase noise, which is plotted as the red curves. The voltage unit used here is the unit of our AD card with 1 V = 32767 ADU. The data is measured from a 200 nm Nb on Si resonator under a fixed readout power $P_{\mu w} = -85$ dBm.

of the readout electronics (mainly limited by the noise temperature of our HEMT). Therefore, we calculate the “true” phase noise by subtracting the measured $S_{\perp}(\nu)$ from $S_{\parallel}(\nu)$ and the results are plotted in red curves in Fig. 5.7.

To better quantify the temperature and power dependence of the frequency noise, we retrieve the noise values at 1 kHz from the phase noise spectrum (red curve) at each readout power and each temperature. The 1 kHz frequency noise $S_{\delta f_r}(1 \text{ kHz})/f_r^2$ is plotted as a function of $P_{\mu w}$ and T in Fig. 5.8. The even spacing (~ 2 dB) between any two adjacent noise curves indicates the $P_{\text{int}}^{-1/2}$ dependence of frequency noise as expected. At a fixed $P_{\mu w}$, we find the frequency noise roughly falls onto a power-law relationship and at intermediate temperatures $300 \text{ mK} < T < 900 \text{ mK}$ the temperature dependence is close to

$$S_{\delta f_r}(1 \text{ kHz})/f_r^2 \propto T^{-2} \quad (5.13)$$

as indicated by the parallel solid lines in Fig. 5.8. This scaling is consistent with the $T^{-1.73}$ scaling found by Kumar[63], where he was fitting for a broader range of temperatures.

In addition to the noise, the resonance frequency f_r and quality factor Q_r also show strong temperature dependence, which are shown in Fig. 5.9. Later in this chapter we will see plenty examples of similar $f_r(T)$ and $Q_r(T)$ curves and show that they can be well explained by the TLS theory.

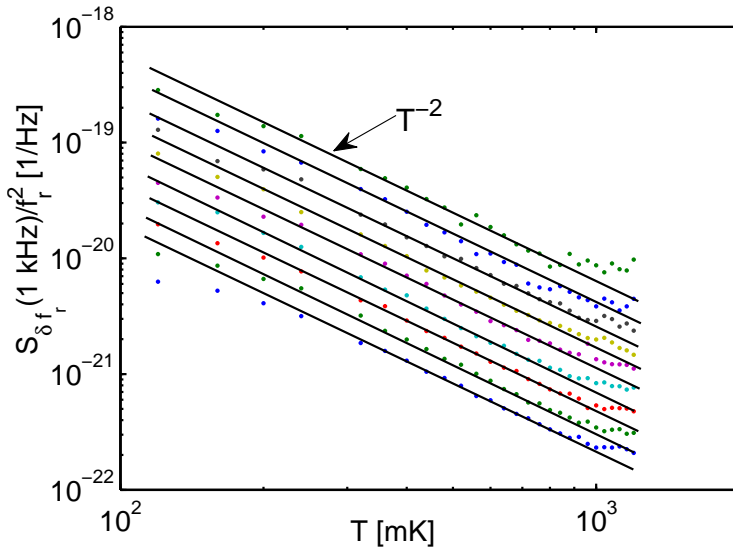


Figure 5.8: Frequency noise at $\nu = 1$ kHz as a function of temperature under several readout powers. The readout powers $P_{\mu\nu}$ are from -105 dBm to -73 dBm in step of 4 dBm from top to bottom. The solid lines indicate T^{-2} temperature dependence. The data is measured from a 200 nm Nb on Si resonator.

In summary, the measured temperature dependence of resonance frequency, quality factor, and frequency noise strongly suggest to us that TLS in the dielectric materials are responsible for the noise.

5.3.5 Geometry dependence

The geometry dependence of the frequency noise was carefully studied with a Nb on sapphire geometry-test device, which contains CPW resonators with five different center strip widths ($s_r = 3 \mu\text{m}, 5 \mu\text{m}, 10 \mu\text{m}, 20 \mu\text{m}, \text{ and } 50 \mu\text{m}$) and with the ratio between the center strip width and the gap width fixed to 3:2. Here we only present the conclusions, while leaving the detailed data and analysis to Section 5.5.2.2, after the introduction of TLS theory and a semi-empirical noise model.

Fig. 5.10 shows the measured frequency noise (before and after the correction for coupler's noise contribution) at $\nu = 2$ kHz as a function of center strip width s_r under the same internal power $P_{\text{int}} = -25$ dBm. We find that the frequency noise has a geometrical scaling

$$S_{\delta f_r}(\nu)/f_r^2 \propto 1/s_r^{1.6}. \quad (5.14)$$

The noise data as well as the temperature-dependent $f_r(T)$ and $Q_r(T)$ data measured from this geometry-test device will be discussed in great detail in Section 5.5.2.2. As we will show there, these data not only confirm the TLS hypothesis but further point to a surface distribution of TLS and rule out a uniform distribution of TLS in the bulk substrate.

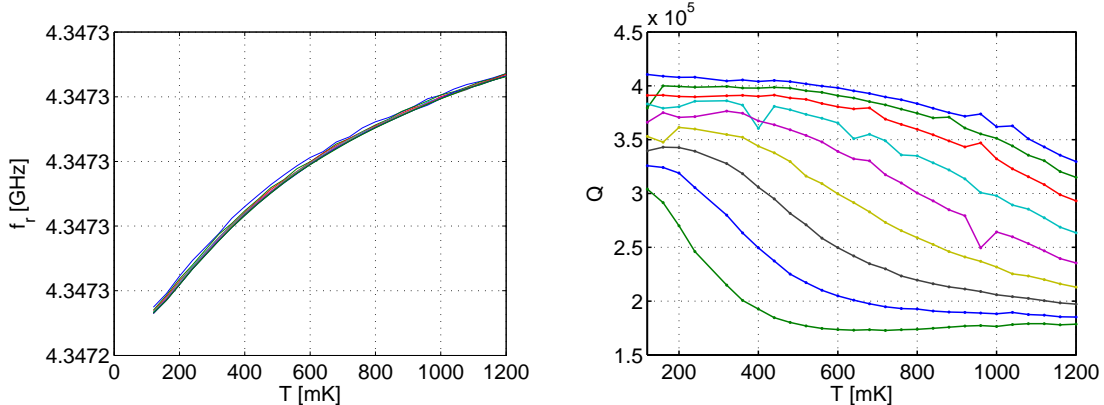


Figure 5.9: Resonance frequency (a) and quality factor (b) as a function of temperature under several readout powers. The readout powers $P_{\mu w}$ are from -105 dBm to -73 dBm in steps of 4 dBm from bottom to top in both plots. The data is measured from a 200 nm Nb on Si resonator.

5.4 Two-level system model

In this section, we first give a review of the standard two-level system (TLS) theory. Then we present a semi-empirical TLS noise model.

5.4.1 Tunneling states

Experiments show that amorphous solids exhibit very different thermal, acoustic, and dielectric properties from crystalline solids at low temperatures. In 1972, the standard two-level system model was independently introduced by Phillips[60] and Anderson[61], which satisfactorily explains the experimental results. This model assumes that a broad spectrum of tunneling states exist in amorphous solids. Although the microscopic nature of the TLS is still unknown, it is often thought that in a disordered solid, one or a group of atoms can tunnel between two sites. These tunneling states have elastic and electric dipole moments that can couple to the elastic and electric fields. Such a tunneling two-level system can be quantum mechanically treated as a particle in a double-well potential, as illustrated in Fig. 5.11.

In the local basis (ϕ_1 and ϕ_2), the system Hamiltonian can be written as

$$H = \frac{1}{2} \begin{pmatrix} -\Delta & \Delta_0 \\ \Delta_0 & \Delta \end{pmatrix}, \quad (5.15)$$

where Δ is called the asymmetric energy which equals the energy difference between the right well and the left well. Δ_0 is the tunneling matrix element.

In the standard TLS theory, a uniform distribution in Δ and a log uniform distribution in Δ_0 is

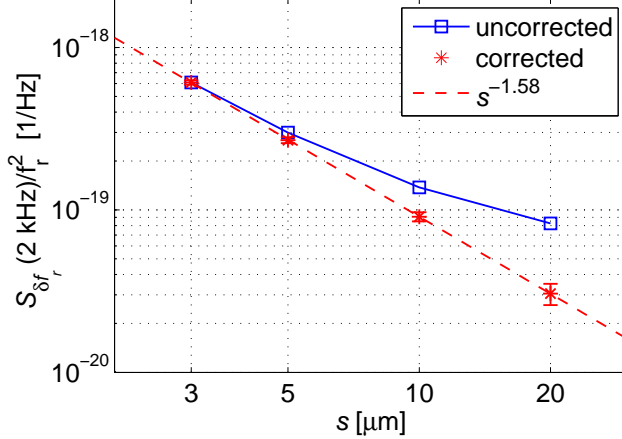


Figure 5.10: The frequency noise $S_{\delta f}(2 \text{ kHz})/f_r^2$ at $P_{\text{int}} = -25 \text{ dBm}$ measured from the geometry-test device is plotted as a function of the center strip width s_r . Values before and after the correction for the coupler's noise contribution are indicated by the squares and stars, respectively. The corrected values of $S_{\delta f}(2 \text{ kHz})/f_r^2$ scale as $s_r^{-1.58}$, as indicated by the dashed line. Refer to Section 5.5.2.2 for details on the device, noise data, and analysis.

assumed

$$P(\Delta, \Delta_0) d\Delta d\Delta_0 = \frac{P_0}{\Delta_0} d\Delta d\Delta_0 \quad (5.16)$$

where P_0 is the two-level density of state found to be on the order of $10^{44}/\text{J}\cdot\text{m}^3$.

The Hamiltonian in Eq. 5.15 can be diagonalized to give the eigenenergies $\pm\varepsilon/2$ where

$$\varepsilon = \sqrt{\Delta^2 + \Delta_0^2}. \quad (5.17)$$

The true eigenstates ψ_1 and ψ_2 can be written in terms of ϕ_1 and ϕ_2 as

$$\psi_1 = \phi_1 \cos \theta + \phi_2 \sin \theta \quad (5.18)$$

$$\psi_2 = \phi_1 \sin \theta - \phi_2 \cos \theta \quad (5.19)$$

where

$$\tan 2\theta = \frac{\Delta_0}{\Delta}. \quad (5.20)$$

In the diagonal representation (ψ_1, ψ_2) the Hamiltonian is in the form of a standard TLS,

$$H_0 = \frac{1}{2}\varepsilon\sigma_z \quad (5.21)$$

where

$$\sigma_x = \begin{pmatrix} 0 & 1 \\ 1 & 0 \end{pmatrix}, \quad \sigma_y = \begin{pmatrix} 0 & -i \\ i & 0 \end{pmatrix}, \quad \sigma_z = \begin{pmatrix} 1 & 0 \\ 0 & -1 \end{pmatrix} \quad (5.22)$$

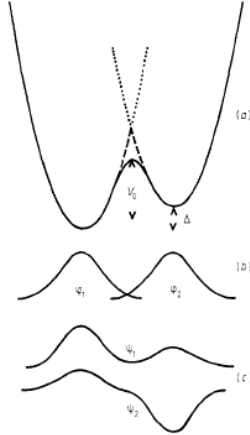


Figure 5.11: A illustration of a particle in a double-well potential

are the Pauli matrices.

5.4.2 Two-level dynamics and the Bloch equations

TLS can interact with an external electric field \vec{E} and strain field e . It can be shown that the dominant effect of the external fields on the TLS is through the perturbation in the asymmetry energy Δ , while changes in the tunnel barrier Δ_0 can usually be ignored[65]. In the electric problem, the interaction Hamiltonian can be written as (in ψ_1, ψ_2 basis)

$$H_{\text{int}}^e = \left[\frac{\Delta}{\varepsilon} \sigma_z + \frac{\Delta_0}{\varepsilon} \sigma_x \right] \vec{d}_0 \cdot \vec{E}. \quad (5.23)$$

We recognize

$$\vec{d}' = 2\vec{d}_0 \frac{\Delta}{\varepsilon} \quad (5.24)$$

as the permanent electric dipole moment and

$$\vec{d} = \vec{d}_0 \frac{\Delta_0}{\varepsilon} \quad (5.25)$$

as the transition electric dipole moment[66]. Because $\Delta_0 \leq \varepsilon$, the maximum transition dipole moment of a TLS with energy splitting ε is \vec{d}_0 . Later we will see that the first term in Eq. 5.23 gives rise to a relaxation response and the second term gives a resonant response to the electric field. In our problem of TLS in a microwave resonator, H_{int}^e gives the coupling between the TLS and the microwave photons.

Similarly, in the acoustic problem, the interaction Hamiltonian can be written as

$$H_{\text{int}}^a = \left[\frac{\Delta}{\varepsilon} \sigma_z + \frac{\Delta_0}{\varepsilon} \sigma_x \right] \gamma e \quad (5.26)$$

where γ is the elastic dipole moment and e is the strain field. In our problem, H_{int}^a couples the TLS to the phonon bath and causes relaxations.

The Hamiltonian of TLS in the electric problem

$$H = H_0 + H_{\text{int}}^e \quad (5.27)$$

has a formal analogy to that of a spin 1/2 system in a magnetic field

$$H = -\hbar\gamma\vec{B} \cdot \vec{S} = -\hbar\gamma(\vec{B}_0 \cdot \vec{S}) - \hbar\gamma(\vec{B}' \cdot \vec{S}) \quad (5.28)$$

where \vec{B}_0 is the static magnetic field, \vec{B}' is the (oscillating) perturbation field, and $\vec{S} = \vec{\sigma}/2$. Comparing Eq. 5.23 to Eq. 5.28, we identify the following correspondence

$$-\hbar\gamma\vec{B} = (0, 0, \varepsilon) \quad \text{and} \quad -\hbar\gamma\vec{B}' = (2\vec{d} \cdot \vec{E}, 0, \vec{d}' \cdot \vec{E}). \quad (5.29)$$

Without relaxation processes, the dynamic equation for a free spin in a magnetic field is simply

$$\frac{d}{dt}\vec{S}(t) = \gamma\vec{S} \times \vec{B} \quad (5.30)$$

where $\vec{S}(t)$ can be either interpreted as the spin operator in Heisenberg picture or as the classical spin (because the quantum mechanical and classical equation take the same form in this problem).

When the relaxation processes are considered, the evolution of the ensemble average of the spin operators $\langle S_i(t) \rangle$ is described by the famous Bloch equations, which were first derived to describe the nuclear magnetic resonance[67]:

$$\begin{aligned} \frac{d}{dt} \langle S_x(t) \rangle &= \gamma (\langle S_y \rangle B_z - \langle S_z \rangle B_y) - \frac{\langle S_x \rangle}{T_2} = 0 \\ \frac{d}{dt} \langle S_y(t) \rangle &= \gamma (\langle S_z \rangle B_x - \langle S_x \rangle B_z) - \frac{\langle S_y \rangle}{T_2} = 0 \\ \frac{d}{dt} \langle S_z(t) \rangle &= \gamma (\langle S_x \rangle B_y - \langle S_y \rangle B_x) - \frac{\langle S_z \rangle - S_z^{\text{eq}}[B_z(t)]}{T_1} \end{aligned} \quad (5.31)$$

where T_1 and T_2 are the longitudinal and transverse relaxation times, respectively, and

$$S_z^{\text{eq}}[B_z(t)] = \frac{1}{2} \tanh\left(\frac{\hbar\gamma B_z(t)}{2kT}\right) \quad (5.32)$$

is the instantaneous equilibrium value of S_z .

5.4.3 Solution to the Bloch equations

To solve the Bloch equations in Eq. 5.31, we first set up the magnetic field as

$$\vec{B}_0 = (0, 0, B_0), \quad \vec{B}' = 2\vec{B}^1 \cos \omega t = (B_x^1, 0, B_z^1) (e^{j\omega t} + e^{-j\omega t}). \quad (5.33)$$

Here we enforce $B_0 < 0$. Next, we linearize the term $S_z^{\text{eq}}[B_z(t)]$ with its Taylor expansion assuming $B_z^1 \ll |B^0|$

$$S_z^{\text{eq}}[B_z(t)] = S_z^{\text{eq}}(B_0) + B_z'(t) dS_z^{\text{eq}}/dB_0. \quad (5.34)$$

Because the perturbation field in Eq. 5.33 is time harmonic, the steady state solution to Eq. 5.31 can be written as a sum of frequency components at $\omega_m = m\omega$ (m is an integer)

$$\langle \vec{S}(t) \rangle = \sum_{m=-\infty}^{m=+\infty} \vec{S}^m \exp(j\omega_m t). \quad (5.35)$$

By inserting Eq. 5.35 and Eq. 5.33 into Eq. 5.31 and equating the coefficient in front of $\exp(j\omega_m t)$ on the left- and right-hand sides of Eq. 5.31, one will obtain a set of coupled linear equations for S_m . It can be shown that only equations for $m = -1, 0, +1$ are important.

The solutions to these equations are given, for example, by Hunklinger[68]. Note that he used S_m to represent the coefficient for the frequency component $e^{-j\omega_m t}$, while here we use it for the frequency component $e^{j\omega_m t}$. Therefore, a substitution of $-\omega$ for ω will convert his results to ours. The magnetic susceptibilities $\chi_i(\omega)$ are defined by

$$\begin{aligned} S_x^1 &= \chi_x(\omega) \hbar \gamma B_x^1 \\ S_z^1 &= \chi_z(\omega) \hbar \gamma B_z^1 \end{aligned} \quad (5.36)$$

and are derived to be

$$\chi_x(\omega) = -\frac{S_z^0}{2\hbar} \left[\frac{1}{\omega_0 - \omega + jT_2^{-1}} + \frac{1}{\omega_0 + \omega - jT_2^{-1}} \right] \quad (5.37)$$

$$\chi_z(\omega) = \frac{dS_z^{\text{eq}}}{d(\hbar\gamma B_0)} \frac{1 - j\omega T_1}{1 + \omega^2 T_1^2} \quad (5.38)$$

where $\omega_0 = -\gamma B_0$ and

$$S_z^0 = \frac{1 + (\omega_0 - \omega)^2 T_2^2}{1 + (\gamma B_x^1)^2 T_1 T_2 + (\omega_0 - \omega)^2 T_2^2} S_z^{\text{eq}}. \quad (5.39)$$

The susceptibilities $\chi_x(\omega)$ and $\chi_z(\omega)$ are of two different origins: $\chi_x(\omega)$ describes the resonant response of the spins to the ac magnetic field, while $\chi_z(\omega)$ has the typical form of a relaxation process. Furthermore, the first term in Eq. 5.37 is the response to the rotating wave and the second term is to the counter rotating wave.

The results for spins in magnetic field can be easily converted to the results for our problem — TLS in an electric field coupled to a phonon bath—by applying the correspondence in Eq. 5.29. For TLS in an electric field, we define an electric susceptibility tensor for the resonance process $\vec{\chi}_{\text{res}}(\omega)$ and a susceptibility tensor for the relaxation process $\vec{\chi}_{\text{rel}}(\omega)$

$$\langle \vec{d} \rangle = \vec{\chi}_{\text{res}}(\omega) \cdot \vec{E} \quad (5.40)$$

$$\langle \vec{d}' \rangle = \vec{\chi}_{\text{rel}}(\omega) \cdot \vec{E}. \quad (5.41)$$

It can be shown that

$$\vec{\chi}_{\text{res}}(\omega) = -\frac{\sigma_z^0}{\hbar} \left[\frac{1}{\omega_\varepsilon - \omega + jT_2^{-1}} + \frac{1}{\omega_\varepsilon + \omega - jT_2^{-1}} \right] \vec{d} \vec{d} \quad (5.42)$$

$$\vec{\chi}_{\text{rel}}(\omega) = -\frac{d\sigma_z^{\text{eq}}(\varepsilon)}{d\varepsilon} \frac{1 - j\omega T_1}{1 + \omega^2 T_1^2} \vec{d}' \vec{d}' \quad (5.43)$$

where

$$\sigma_z^{\text{eq}}(\varepsilon) = -\tanh\left(\frac{\varepsilon}{2kT}\right) \quad (5.44)$$

$$\sigma_z^0 = \frac{1 + (\omega_\varepsilon - \omega)^2 T_2^2}{1 + \Omega^2 T_1 T_2 + (\omega_\varepsilon - \omega)^2 T_2^2} \sigma_z^{\text{eq}}(\varepsilon). \quad (5.45)$$

Here $\omega_\varepsilon = \varepsilon/\hbar$ and $\Omega = 2\vec{d} \cdot \vec{E}/\hbar$ is the Rabi frequency.

5.4.4 Relaxation time T_1 and T_2

In absence of an external field, the Bloch equation for $\langle \sigma_z \rangle$ becomes

$$\frac{d}{dt} \langle \sigma_z \rangle = -\frac{\langle \sigma_z \rangle - \sigma_z^{\text{eq}}}{T_1}. \quad (5.46)$$

Because $\langle \sigma_z \rangle = p_1 - p_2$ is equal to the population difference between the upper and lower states, T_1^{-1} relaxation rate is the rate at which a non-equilibrium population relaxes to its equilibrium value, through the interaction with the phonon bath. Both phonon emission and absorption contribute to this relaxation process. When the two-level population is in thermal equilibrium, the phonon emission and absorption processes are balanced and the population stays unchanged. If the two-level population is out of equilibrium, one phonon process will dominate over the other, always

pulling the system back to its equilibrium. It can be shown that T_1 is given by [66]

$$\frac{1}{T_1} = \left(\frac{\Delta_0}{\varepsilon} \right)^2 \frac{1}{T_{1,\min}} \quad (5.47)$$

$$\frac{1}{T_{1,\min}} = \left[\frac{\gamma_L^2}{v_L^5} + \frac{\gamma_T^2}{v_T^5} \right] \frac{\varepsilon^3}{2\pi\rho\hbar^4} \coth\left(\frac{\varepsilon}{2kT}\right) \quad (5.48)$$

where γ_L and γ_T are the longitudinal and transverse deformation potential, respectively, v_L and v_T are the longitudinal and transverse sound velocity, respectively, and ρ is the mass density. $T_{1,\min}$ is the minimum T_1 time for a TLS with splitting energy ε .

The transverse relaxation time T_2 is also called the dephasing time. In absence of the external field, the transverse spin operators in Heisenberg picture will be precessing about the z axis and the $\sigma_+ = \sigma_x + j\sigma_y$ operator is given by,

$$\sigma_+(t) = \sigma_+(0) \exp(-j\frac{\varepsilon}{\hbar}t). \quad (5.49)$$

If the energy level ε fluctuates with time and the fluctuations $\delta\varepsilon$ are not identical for different TLS, even if an ensemble of TLS starts with the same spin $\sigma_+(0)$ (in phase), they will no longer be in phase after a period of time. Each spin picks up a random phase $\theta(t) = \int_0^t \delta\varepsilon(\tau)d\tau$ and the ensemble average value of $\langle \sigma_+ \rangle$ (or the transverse spin components $\langle \sigma_x \rangle$ and $\langle \sigma_y \rangle$) will decay to zero in a rate that is dictated by $1/T_2$, because usually $\langle e^{-j\theta(t)} \rangle$ has a behavior of exponential decay¹:

$$\left\langle e^{-j \int_0^t \delta\varepsilon(\tau)d\tau} \right\rangle \sim e^{-t/T_2} \quad (5.50)$$

For TLS in an amorphous material, the energy level fluctuation $\delta\varepsilon(t)$ is described by a “diffusion” process, referred to as spectral diffusion. As shown in Fig. 5.12, the energy levels gradually spread out and in the long time limit ($t \gg T_1^*$ with T_1^* being the average T_1 time), $\delta\varepsilon$ reaches a stationary distribution with a width of $\Delta\varepsilon$. And T_2 is inversely proportional to $\Delta\varepsilon$. Roughly speaking, T_2 is the time for which the spread in the random phase θ is of the order $\pi/2$ and can be estimated by

$$T_2^{-1} = \frac{2}{\pi} \frac{\Delta\varepsilon}{\hbar}. \quad (5.51)$$

The major contribution to the energy level fluctuations $\delta\varepsilon$ is through the TLS-TLS interaction. The interaction energy between two TLS (i, j) is given by[65]

$$\delta\varepsilon_{ij} = c \frac{\Delta_i}{\varepsilon_i} \frac{\Delta_j}{\varepsilon_j} \frac{\gamma_i \gamma_j}{\rho v^2 r_{ij}^3} \quad (5.52)$$

¹Depending on the detailed process of $\delta\varepsilon(t)$, the decay generally has a more complicated form than a single exponential and is not always compatible with the single T_2 -rate description used in the Bloch equations.

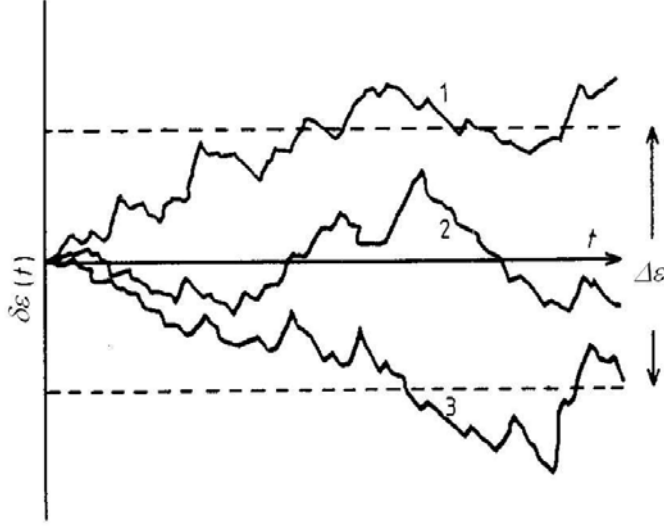


Figure 5.12: An illustration of spectral diffusion. Figure from [65]

where $\gamma_i \Delta / \varepsilon$ and $\gamma_j \Delta / \varepsilon$ are the permanent elastic dipole moments of the two TLS, r_{ij} is the distance between the two TLS, and C is a constant of order unity. Physically, Eq. 5.52 describes the process in which one TLS changes its states and produces a strain field that is felt by another TLS. Replacing $1/r_{ij}^3$ with the volume density of thermally excitable TLS $P_0 kT$ and averaging over the neighboring TLS j leads to

$$\Delta\epsilon \sim C \frac{\gamma^2 P k T}{\rho v^2} \frac{\Delta}{\varepsilon} \quad (5.53)$$

and therefore

$$T_2^{-1} \sim C \frac{2\gamma^2 P k T}{\pi \hbar \rho v^2} \frac{\Delta}{\varepsilon} \quad (5.54)$$

is expected to have a linear dependence on temperature.

5.4.5 Dielectric properties under weak and strong electric fields

At microwave frequencies ($\omega \sim 10^9$ Hz) and at low temperatures ($T < 1$ K, $T_1 > 1$ μ s), $\omega T_1 \gg 1$ and the relaxation contribution given by Eq. 5.43 is much smaller than the resonant contribution given by Eq. 5.43. Therefore, we will give no further discussion on the relaxation contribution.

For the resonant interaction, the TLS contribution to the (isotropic) dielectric function is given by

$$\epsilon_{\text{TLS}}(\omega) = \iiint \left[\hat{e} \cdot \vec{\chi}_{\text{res}}(\omega) \cdot \hat{e} \right] \frac{P}{\Delta_0} d\Delta d\Delta_0 d\hat{d} = \epsilon'_{\text{TLS}}(\omega) - j\epsilon''_{\text{TLS}}(\omega) \quad (5.55)$$

where we have averaged over the TLS asymmetry Δ , tunnel splitting Δ_0 , and dipole orientation \hat{d} .

5.4.5.1 Weak field

If the electric field is weak and the condition $\Omega^2 T_1 T_2 \ll 1$ is satisfied, Eq. 5.55 can be worked out (see Appendix G)

$$\epsilon_{\text{TLS}}(\omega) = \int_0^{\varepsilon_{\max}} \frac{Pd_0^2}{3\hbar} \tanh\left(\frac{\varepsilon}{2k_B T}\right) \left[\frac{1}{\omega_\varepsilon - \omega + jT_2^{-1}} + \frac{1}{\omega_\varepsilon + \omega - jT_2^{-1}} \right] d\varepsilon \quad (5.56)$$

$$= -\frac{2Pd_0^2}{3} \left[\Psi\left(\frac{1}{2} - \frac{\hbar\omega - j\hbar T_2^{-1}}{2j\pi k_B T}\right) - \log \frac{\varepsilon_{\max}}{2\pi k_B T} \right] \quad (5.57)$$

where Ψ is the complex digamma function and ε_{\max} is the maximum energy splitting of TLS.

The TLS contribution to the dielectric loss tangent δ is given by

$$\delta_{\text{TLS}} = \frac{\epsilon''_{\text{TLS}}(\omega)}{\epsilon} = \delta_{\text{TLS}}^0 \tanh\left(\frac{\hbar\omega}{2k_B T}\right) \quad (5.58)$$

where the relationship[52] $\text{Im}\Psi(1/2 + jy) = (\pi/2) \tanh \pi y$ has been applied, and $\delta_{\text{TLS}}^0 = \pi Pd_0^2 / 3\epsilon$ represents the TLS-induced loss tangent at zero temperature in weak electric field. Here ϵ is the dielectric constant of the TLS hosting material.

Similarly, the TLS contribution to the real part of the dielectric constant is given by

$$\frac{\epsilon'_{\text{TLS}}(\omega)}{\epsilon} = -\frac{2\delta_{\text{TLS}}^0}{\pi} \left[\text{Re}\Psi\left(\frac{1}{2} - \frac{\hbar\omega}{2j\pi k_B T}\right) - \log \frac{\varepsilon_{\max}}{2\pi k_B T} \right] \quad (5.59)$$

where $\hbar T^{-1} / 2\pi kT \ll 1/2$ has been neglected and the sign before $\hbar\omega / 2j\pi kT$ can take either “+” or “-”, because $\Psi(\bar{z}) = \overline{\Psi(z)}$.

Eq. 5.58 for the loss tangent can be alternatively derived by considering the imaginary part of the integral in Eq. 5.56. The major contribution to this integral is from the resonant absorption term

$$\text{Im} \left[\frac{1}{\omega_\varepsilon - \omega + jT_2^{-1}} \right] = \frac{T_2^{-1}}{(\omega_\varepsilon - \omega)^2 + (T_2^{-1})^2} \quad (5.60)$$

which is a narrow Lorentzian peak centered at ω with a line width T_2^{-1} . Physically it means only the TLS close to resonance $\omega_\varepsilon \approx \omega$ have significant contribution the loss tangent. Neglecting the $1/(\omega_\varepsilon + \omega + jT_2^{-1})$ term and pulling $\tanh(\varepsilon/2kT)$ out of the integral as $\tanh(\hbar\omega/2kT)$ will yield the same result for δ_{TLS} in Eq. 5.58.

Eq. 5.58 and Eq. 5.59 are the two important results of TLS theory. The predicted temperature dependence is illustrated in Fig. 5.13. The loss tangent δ_{TLS} (blue curve) is highest ($\delta_{\text{TLS}} = \delta_{\text{TLS}}^0$) at low temperatures $T \lesssim \hbar\omega/2k$, and decreases monotonically with T , as $1/T$ at high temperatures $T \gg \hbar\omega/2k$. ϵ'_{TLS} (red curve) has a non-monotonic behavior: ϵ'_{TLS} increases with T when $T < \hbar\omega/2k$; ϵ'_{TLS} decreases when $T > \hbar\omega/2k$; a maximum in ϵ'_{TLS} occurs around $T = \hbar\omega/2k$.

The predicted temperature and frequency dependence of δ_{TLS} and ϵ'_{TLS} have been tested on all

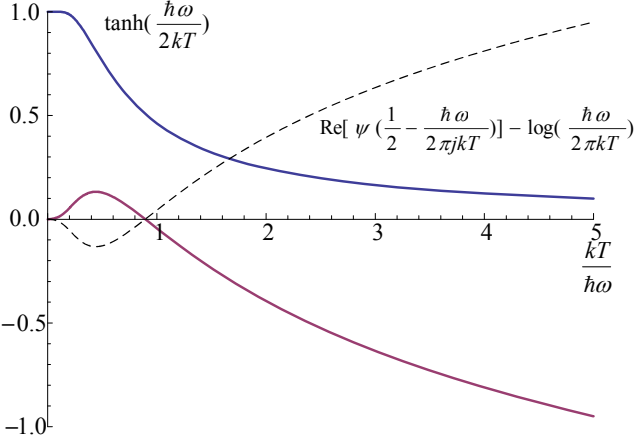


Figure 5.13: Temperature dependence of δ_{TLS} (blue curve) and ϵ'_{TLS} (red curve)

kinds of amorphous solids and are found to be in great agreement with the experiments. Eq. 5.58 and Eq. 5.59 have been used extensively to derive the values of δ_{TLS}^0 for different materials. We use them in the experiments described in Section 5.5 to obtain crucial information of the TLS in our resonators.

5.4.5.2 Strong field

For general and strong electric field, $\epsilon_{\text{TLS}}(\omega)$ has to be evaluated from the full integral

$$\begin{aligned} \epsilon_{\text{TLS}}(\omega) &= \int_0^{\varepsilon_{\max}} \frac{Pd_0^2}{3} \tanh\left(\frac{\varepsilon}{2k_B T}\right) \left[\frac{1 + (\omega_\varepsilon - \omega)^2 T_2^2}{1 + \overline{\Omega}^2 T_1 T_2 + (\omega_\varepsilon - \omega)^2 T_2^2} \right] \\ &\times \left[\frac{1}{\omega_\varepsilon - \omega + jT_2^{-1}} + \frac{1}{\omega_\varepsilon + \omega - jT_2^{-1}} \right] d\varepsilon \end{aligned} \quad (5.61)$$

where

$$\overline{\Omega} = \frac{2d_0 |\vec{E}| \Delta_0}{\sqrt{3} \hbar} \quad (5.62)$$

is the modified Rabi frequency accounting for the orientation integral (see Appendix G).

For the imaginary part of the integral, the main contribution is still from the $1/(\omega_\varepsilon - \omega - jT_2^{-1})$ term. By dropping the other term $1/(\omega_\varepsilon + \omega - jT_2^{-1})$, the integrand now contains a power-broadened absorption profile

$$\left[\frac{1 + (\omega_\varepsilon - \omega)^2 T_2^2}{1 + \overline{\Omega}^2 T_1 T_2 + (\omega_\varepsilon - \omega)^2 T_2^2} \right] \times \text{Im} \left[\frac{1}{\omega_\varepsilon - \omega + jT_2^{-1}} \right] = \frac{-T_2^{-1}}{\left[T_2^{-1} \sqrt{1 + \overline{\Omega}^2 T_1 T_2} \right]^2 + (\omega_\varepsilon - \omega)^2} \quad (5.63)$$

where the width of the Lorentzian is broadened by a factor of $\kappa = \sqrt{1 + \overline{\Omega}^2 T_1 T_2}$. As a result, the

TLS loss tangent

$$\delta_{\text{TLS}} = \delta_{\text{TLS}}^0 \frac{\tanh\left(\frac{\varepsilon}{2k_B T}\right)}{\sqrt{1 + \bar{\Omega}^2 T_1 T_2}} \quad (5.64)$$

is reduced by a factor of κ from the weak field result.

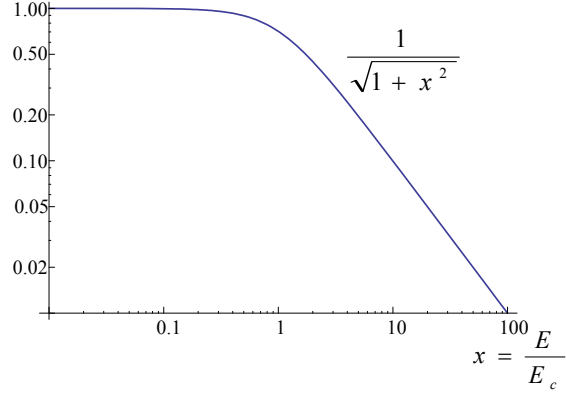


Figure 5.14: Electric field strength dependence of δ_{TLS}

Because $\bar{\Omega} \propto |\vec{E}|$, the loss tangent δ_{TLS} depends on the electric field strength as

$$\delta_{\text{TLS}}(|\vec{E}|) = \frac{\delta_{\text{TLS}}(|\vec{E}|=0)}{\sqrt{1 + |\vec{E}/E_c|^2}} \quad (5.65)$$

where E_c is a critical field for TLS saturation defined as

$$E_c = \frac{\sqrt{3}\hbar}{2d_0|\vec{E}|\sqrt{T_{1,\min}T_2}}. \quad (5.66)$$

The $|\vec{E}|$ dependence of δ_{TLS} is illustrated in Fig. 5.14, where we see that δ_{TLS} scales as $|\vec{E}|^{-1}$ in a strong electric field $|\vec{E}| \gg E_c$.

The real part of the integral in Eq. 5.61 can also be approximately evaluated. Because

$$\text{Re}\left[\frac{1}{\omega_\varepsilon - \omega + jT_2^{-1}}\right] \sim \frac{1}{\omega_\varepsilon - \omega}, \quad \text{Re}\left[\frac{1}{\omega_\varepsilon + \omega - jT_2^{-1}}\right] \sim \frac{1}{\omega_\varepsilon + \omega} \quad (5.67)$$

does not converge (yielding logarithmic divergence) when integrated to a large ε_{\max} , it means that the contribution to ϵ'_{TLS} from large detuned TLS is not negligible. In other words, TLS from a broad range of energy, on-resonance and detuned, all contribute to ϵ'_{TLS} . In addition, we find that the contributions from the two terms in Eq. 5.67 are comparable and therefore none of them can be

neglected. After making a number of mathematical approximations, we derive ²(see Appendix G)

$$\frac{\epsilon'_{\text{TLS}}(\kappa) - \epsilon'_{\text{TLS}}(0)}{\epsilon} = \delta_{\text{TLS}}^0 (1 - \kappa) \operatorname{sech}^2\left(\frac{\hbar\omega}{2kT}\right) \frac{\hbar T_2^{-1}}{2kT} + \delta_{\text{TLS}}^0 \tanh\left(\frac{\hbar\omega}{2kT}\right) \frac{1 - \kappa^2}{\kappa} \frac{T_2^{-1}}{2\omega} \quad (5.68)$$

where $\epsilon'_{\text{TLS}}(0)$ is the weak field result given by Eq. 5.59. Usually $\kappa\hbar T_2^{-1} \ll kT$ and $\kappa T_2^{-1} \ll \omega$, therefore, the power dependence of ϵ'_{TLS} has a very small effect.

5.4.6 A semi-empirical noise model assuming independent surface TLS fluctuators

We assume that the TLS have a uniform spatial distribution within a volume of TLS-host material V_h that occupies some portion of the total resonator volume V . Consider a TLS labeled α , located at a random position $\vec{r}_\alpha \in V_h$ and with an energy level separation $\varepsilon_\alpha = (\Delta_\alpha^2 + \Delta_{0,\alpha}^2)$. The TLS transition dipole moment is given by $\vec{d}_\alpha = \hat{d}_\alpha d_0 \Delta_{0,\alpha} / \varepsilon_\alpha$, where the dipole orientation unit vector \hat{d}_α is assumed to be random and isotropically distributed. In the weak-field, linear response limit, the TLS contribution to the dielectric tensor of the hosting medium is

$$\vec{\epsilon}_{\text{TLS}}(\omega, \vec{r}) = - \sum_{\alpha} \vec{d} \vec{d} \delta(\vec{r} - \vec{r}_\alpha) \left[\frac{1}{\varepsilon_\alpha - \hbar\omega + j\Gamma_\alpha} + \frac{1}{\varepsilon_\alpha + \hbar\omega - j\Gamma_\alpha} \right] \sigma_{z,\alpha}. \quad (5.69)$$

Eq. 5.69 looks very similar to Eq. 5.42 but the interpretations are quite different. In Eq. 5.42 σ_z^0 is the ensemble average of σ_z when the system is in steady-state. Here $\sigma_{z,\alpha}$ is used microscopically to represent the state of an individual TLS at time t which takes values of -1 for the lower state of the TLS and $+1$ for the upper state. We also replaced the dephasing linewidth T_2^{-1} , which is an average effect, with a general linewidth Γ . Averaging over the TLS position, asymmetry, tunnel splitting, and dipole orientation, and assuming a thermal distribution for the level population, Eq. 5.69 gives the same result for the TLS contribution to the (isotropic) dielectric function as in Eq. 5.57

$$\epsilon_{\text{TLS}}(\omega) = -\frac{2Pd_0^2}{3} \left[\Psi\left(\frac{1}{2} - \frac{\hbar\omega - j\Gamma}{2j\pi k_B T}\right) - \log \frac{\varepsilon_{\max}}{2\pi k_B T} \right]. \quad (5.70)$$

As derived earlier, the real (ϵ'_{TLS}) and imaginary (ϵ''_{TLS}) parts of ϵ_{TLS} yield the well-known results for the TLS contribution to the dielectric constant Eq. 5.59 and loss tangent Eq. 5.58. When these TLS are coupled to the resonator, the average effects to the frequency shift and quality factor can be derived both classically from the cavity perturbation theory given by Pozar[57] and quantum-

²I have derived this formula by myself which hasn't been tested by any experiment yet.

mechanically from the cavity QED theory[69]. The results for weak field are

$$\frac{\Delta f_r}{f_r} = -\frac{\int_{V_h} \epsilon'_{\text{TLS}} |\vec{E}|^2 d\vec{r}}{2 \int_V \epsilon |\vec{E}|^2 d\vec{r}} = \frac{F \delta_{\text{TLS}}^0}{\pi} \left[\text{Re} \Psi \left(\frac{1}{2} - \frac{\hbar \omega}{2 j \pi k_B T} \right) - \log \frac{\varepsilon_{\max}}{2 \pi k_B T} \right] \quad (5.71)$$

$$\Delta \frac{1}{Q_r} = -\frac{\int_{V_h} \epsilon''_{\text{TLS}} |\vec{E}|^2 d\vec{r}}{\int_V \epsilon |\vec{E}|^2 d\vec{r}} = F \delta_{\text{TLS}}^0 \tanh \left(\frac{\hbar \omega}{2 k T} \right) \quad (5.72)$$

where $\delta_{\text{TLS}}^0 = 3 P d_0^2 / 2 \epsilon_h$ and

$$F = \frac{\int_{V_h} \epsilon_h \vec{E}(\vec{r})^2 d\vec{r}}{\int_V \epsilon \vec{E}(\vec{r})^2 d\vec{r}} = \frac{w_h^e}{w^e}. \quad (5.73)$$

F is a filling factor which accounts for the fact that the TLS host material volume V_h may only partially fill the resonator volume V , giving a reduced effect on the variation of resonance frequency and quality factor. According to Eq. 5.73, F is the ratio of the electric energy w_h^e stored in the TLS-loaded volume to the total electric energy w^e stored in the entire resonator.

It can be derived from Eq. 5.71 that the TLS-induced temperature variation of frequency shift is given by

$$\frac{f_r(T) - f_r(0)}{f_r} = \frac{F \delta_{\text{TLS}}^0}{\pi} \left[\text{Re} \Psi \left(\frac{1}{2} - \frac{\hbar \omega}{2 j \pi k_B T} \right) - \log \frac{\hbar \omega}{2 \pi k_B T} \right]. \quad (5.74)$$

If the internal loss of the resonator is dominated by the TLS-induced dielectric loss, the internal quality factor Q_i has a temperature dependence given by

$$\frac{1}{Q_i(T)} = F \delta_{\text{TLS}}^0 \tanh \left(\frac{\hbar \omega}{2 k T} \right). \quad (5.75)$$

In Section 5.5, Eq. 5.74 and Eq. 5.75 are directly applied to the experimental data of $\Delta f_r(T)/f_r$ and $1/Q_i(T)$ measured at $T \ll T_c$, to retrieve $F \delta_{\text{TLS}}^0$ for each resonator.

Now, if the dielectric constant fluctuates on time scales $\tau_\epsilon \gg 1/\omega$, according to Eq. 5.71, we would expect to see resonator frequency fluctuations given by

$$\frac{\delta f_r(t)}{f_r} = -\frac{\int_{V_h} \epsilon'_{\text{TLS}}(\vec{r}, t) |\vec{E}|^2 d\vec{r}}{2 \int_V \epsilon |\vec{E}|^2 d\vec{r}}. \quad (5.76)$$

From Eq. 5.69, we see that ϵ'_{TLS} could fluctuate with time if the TLS switch states randomly ($\sigma_{z,\alpha}$ changes sign), for instance due to phonon emission or absorption, or if the the energy level separation E_α is perturbed randomly, for instance due to a collection of nearby TLS that randomly switch states and produce a randomly varying strain field that couples to TLS α . Whatever the mechanism, for independently fluctuating TLS, from Eq. 5.69 we would expect that the Fourier spectra of the $\delta \epsilon_1$

fluctuations to obey

$$\langle \delta\epsilon'_{\text{TLS}}^*(\vec{r}_1, \nu_1) \delta\epsilon'_{\text{TLS}}(\vec{r}_2, \nu_2) \rangle = S_\epsilon(\vec{r}_1, \nu_1, T) \delta(\vec{r}_1 - \vec{r}_2) \delta(\nu_1 - \nu_2). \quad (5.77)$$

Therefore, the resonator frequency power spectrum should be given by

$$\frac{S_{\delta f_r}(\nu)}{f_r^2} = \frac{\int_{V_h} S_\epsilon(\vec{r}, \nu, T) |\vec{E}|^4 d\vec{r}}{4 \left(\int_V \epsilon |\vec{E}|^2 d\vec{r} \right)^2}. \quad (5.78)$$

For weak enough \vec{E} field, the fluctuations in $\delta\epsilon'_{\text{TLS}}$ should not depend on \vec{E} and therefore Eq. 5.78 predicts that the resonator noise is independent of microwave power. Noise in this low power regime is very difficult to measure and the behavior of the noise remains unknown, because the level of the noise usually falls below the HEMT noise floor. While in the familiar high P_{int} regime, in which most MKIDs operate[14] and most of the noise data are taken[70], the frequency noise is observed to scale as $P_{\text{int}}^{-1/2}$ as discussed in Section 5.3.2. This $P_{\text{int}}^{-1/2}$ scaling reminds us of TLS saturation effects discussed in Section 5.4.5.2 which are quantitatively described by Eq. 5.64. We therefore make the ansatz that the noise depends on field strength in a similar manner:

$$S_\epsilon(\vec{r}, \nu, \omega, T) = \kappa(\nu, \omega, T) / \sqrt{|\vec{E}(\vec{r})|^2 + E_{n,c}^2(\omega, T)}, \quad (5.79)$$

where $E_{n,c}(\omega, T)$ is a critical electric field, likely related to the critical field E_c for the saturation of the TLS dissipation (Eq. 5.66), and the noise spectral density coefficient $\kappa(\nu, \omega, T)$ is allowed to vary with (microwave) frequency ω and temperature T [63]. Because we are assuming a uniform distribution of TLS in the volume V_h , we do not expect S_ϵ to have an additional explicit dependence on position \vec{r} . At high power for which $E \gg E_{n,c}$ in the region contributing significantly to the resonator noise, Eq. 5.78 becomes

$$\frac{S_{\delta f_r}(\nu)}{f_r^2} = \kappa(\nu, \omega, T) \frac{\int_{V_h} |\vec{E}|^3 d^3 r}{4 \left(\int_V \epsilon |\vec{E}|^2 d^3 r \right)^2}. \quad (5.80)$$

In Appendix H, we have further derived a noise formula for our transmission line resonators by inserting the appropriate resonator field into Eq. 5.80,

$$\frac{S_{\delta f_r}(\nu)}{f_r^2} = \kappa(\nu, \omega, T) \frac{4 \int_{A_h} \rho(x, y)^3 dx dy}{3\pi C^2 V_0 l}, \quad (5.81)$$

where C is the distributed capacitance of the transmission line, l is the length of the resonator, V_0 is the voltage at the open end, and $\rho(x, y)$ is the electric field distribution in the cross-sectional plane normalized to $V_0 = 1$ V. It is easy to see that Eq. 5.81 exhibits the desired $P_{\text{int}}^{-1/2}$ scaling with power.

The semi-empirical model, especially Eq. 5.80 and Eq. 5.81, will be applied and tested in the experiments in the next section.

5.5 Experimental study of TLS in superconducting resonators

In this section, we present measurements of several devices that are specially designed to study TLS in the resonators. By applying the TLS theory and noise model developed in Section 5.4, we have obtained important information of the TLS which provides new clues to physical mechanism of the TLS noise.

5.5.1 Study of dielectric properties and noise due to TLS using superconducting resonators

In the following two experiments, TLS are known to be in a deposited layer of a known type of amorphous material. Because the thickness of the TLS layer is much larger (hundreds of nm) than the intrinsic TLS layer on a bare CPW resonator (a few nm)³, the TLS effects are more pronounced and easier to measure. From these experiments, we would like to know whether the TLS theory gives a good description of the observed TLS effects and whether these extrinsic TLS are able to produce excess noise that exhibits the same noise properties as observed from the intrinsic TLS.

5.5.1.1 Silicon nitride (SiN_x) covered Al on sapphire device

In this experiment we artificially deposited a $1\mu\text{m}$ thick layer of amorphous SiN_x by plasma-enhanced chemical vapor deposition (PECVD) on top of Al on sapphire CPW resonators. We measured f_r , Q_r and noise before and after the deposition, to study how TLS are coupled to a resonator and how the noise changes before and after the deposition of the SiN_x layer.

- **Device and measurement** The original device is a typical Al on sapphire CPW device: a 200 nm thick Al film is deposited on a crystalline sapphire substrate and patterned into several CPW quarter-wave resonators. All these resonators have center strip width $s_r = 3 \mu\text{m}$, gap $g_r = 2\mu\text{m}$ and resonator lengths $l_r \sim 8 \text{ mm}$ to produce resonance frequencies $f_r \sim 4 \text{ GHz}$. The original device, after various measurements, was deposited with a $\sim 1 \mu\text{m}$ thick layer of SiN_x by plasma-enhanced chemical vapor deposition (PECVD) on its surface, for further testing and measurements (see Fig. 5.15).

As usual, we use a vector network analyzer to measure the S_{21} transmission (through the device, HEMT and a room temperature amplifier). The resonance frequency f_r , total quality factor Q_r , coupling quality factor Q_c , and internal quality factor Q_i are derived from fitting $S_{21}(f)$ data, using

³We will see in Section 5.5.2.1 that the TLS are distributed in a nm-thick surface layer instead of the bulk substrate.

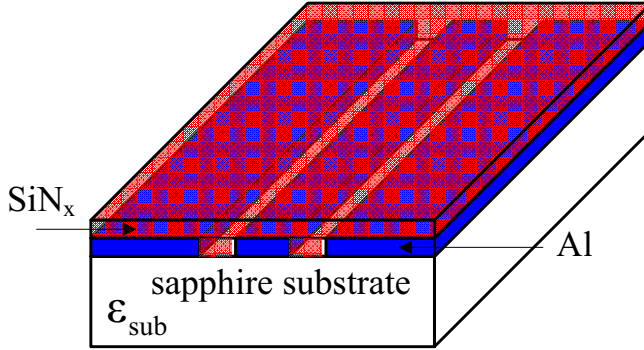


Figure 5.15: An illustration of the SiN_x -covered CPW resonator. The Al film is in blue color and the SiN_x layer is in red color.

the procedures described in Appendix E. For noise characterization, both the measurement setup and the noise data analysis are standard, and have been described in Section 5.2.

- **Resonance Frequency shift before and after the deposition of SiN_x** The fundamental resonance frequency f_r of all resonators (7 resonators with different Q_c) are measured before and after the deposition of SiN_x . After the deposition of SiN_x , we also measured the non-fundamental resonances around $2f_r$ and $3f_r$. The resonance at $2f_r$ is very likely to come from the coupled slot-line mode (also called the odd mode) of CPW line[71]. We include them for two reasons: they have lower Q_c (~ 6000) closer to the TLS-limited Q_i (~ 2000) at low excitation powers, which gives us better sensitivity at those powers; these $2f_r$ - (around 7 GHz) and $3f_r$ - (around 10 GHz) resonances also allow us to study the frequency dependence of various properties.

Table 5.1: f_r before and after the deposition of SiN_x

	f_r (GHz) before	f_r (GHz) after	ratio
Res 1	3.880	3.428	1.13
Res 2	$3.880 \times 2 = 7.760^*$	7.658	1.01
Res 3	$3.880 \times 3 = 11.64^*$	10.167	1.14

The resonance frequency shift of one of the resonators and its $2f_r$, $3f_r$ harmonics (they are referred to as Res 1, Res 2 and Res 3, and treated as if they were three physically independent resonators hereafter) are quantitatively compared in Table 5.1. Because f_r of Res 2 and Res 3 are not measured on the bare device, they are inferred by the doubling and tripling f_r of Res 1. On the other hand, we use EM simulation programs to calculate the effective dielectric constant ϵ_{eff} for the CPW even mode (Res 1 and Res 3) before and after the deposition. With a dielectric constant $\epsilon_h = 7.2$ for SiN_x , the simulation result gives $\epsilon_{\text{eff, before}} = 5.5$ for the bare device and $\epsilon_{\text{eff, after}} = 7.2$ for the SiN_x -covered device. And the ratio

$$\sqrt{\frac{\epsilon_{\text{eff, after}}}{\epsilon_{\text{eff, before}}}} = 1.14 \quad (5.82)$$

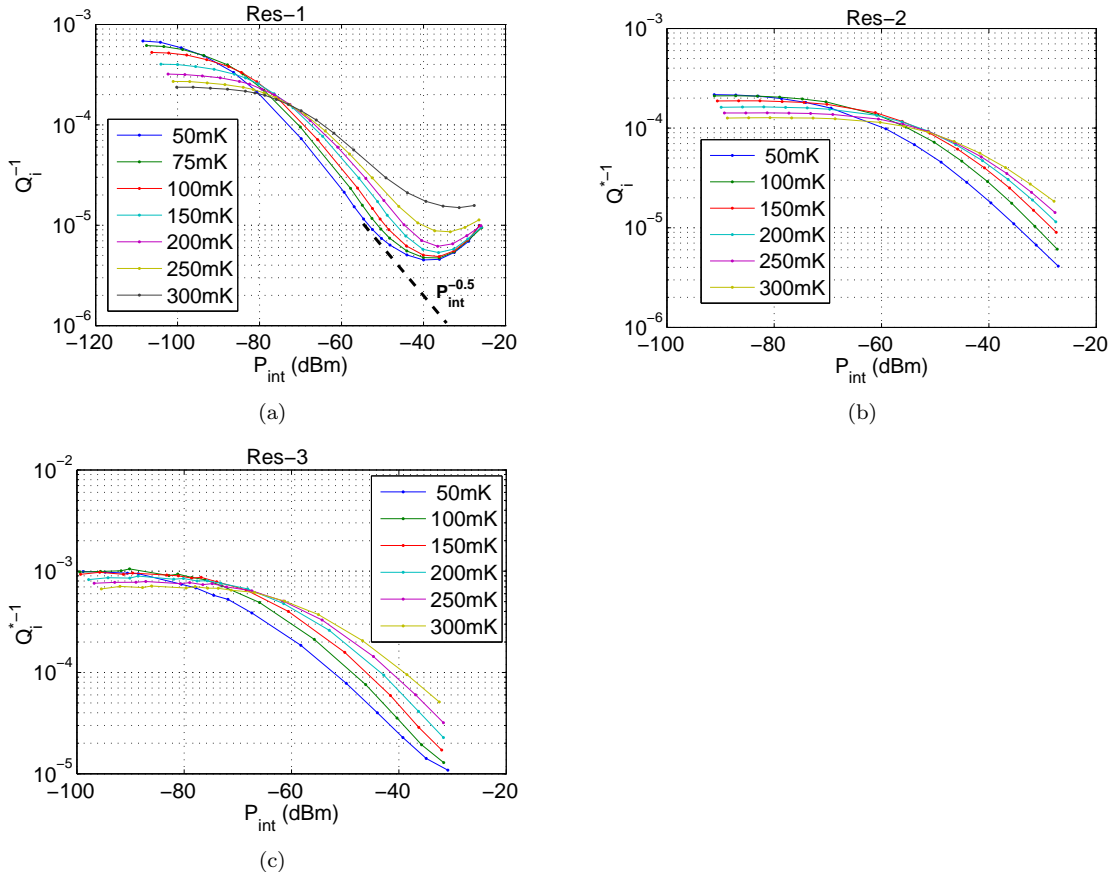


Figure 5.16: Internal loss Q_i^{-1} as a function of P_{int} of the 3 resonators measured at several temperatures between 50 mK to 300 mK. T ranges from 50 mK to 300 mK in steps of 50 mK (or 25 mK) and P_r ranges from -65 dBm and -120 dBm in steps of 4 dBm (or 2 dBm).

agrees very well with the measured f_r ratios of Res 1 and Res 3 in Table 5.1. This result confirms that both the geometric parameters and dielectric constants we assumed are very close to their real values. We notice that the f_r ratio for Res 2 are much less than Res 1 and Res 3, suggesting that the CPW odd mode probably has a field distribution that is less concentrated in the SiN_x layer as compared to the CPW even mode.

- **Power dependence of f_r and Q_i** We measure f_r and Q_i of the 3 resonators in a two-dimensional sweep of bath temperature T and readout power $P_{\mu w}$. Fig. 5.16 shows internal loss Q_i^{-1} as a function of internal power P_{int} at different temperatures.

We can clearly see 3 regimes in Fig. 5.16(a): below -80 dBm (regime I), Q_i^{-1} reaches a constant high value; between -80 dBm and -40 dBm (regime II), Q_i^{-1} decreases with P_{int} and scales as $P_{\text{int}}^{-1/2}$; above -40 dBm (regime III), Q_i^{-1} increases with P_{int} . The regime III behavior is known to be caused by the non-linearity of superconductor at high power and is not TLS-related. Res 2 (Fig. 5.16(b)) and Res 3 (Fig. 5.16(c)) also show the same features, except that we have to subtract 1.3×10^{-5}

Table 5.2: δ_{TLS}^0 and f_r from a joint fit to the $Q_i^{-1}(T)$ and $f_r(T)$ data at the lowest readout power

	f_r (GHz)	$F\delta_{\text{TLS}}^0$	F	δ_{TLS}^0
Res 1	3.4294	7.63×10^{-4}	0.31	2.46×10^{-3}
Res 2	7.6593	2.21×10^{-4}	-	-
Res 3	10.172	9.92×10^{-4}	0.31	3.20×10^{-3}

from Q_i^{-1} for Res 2 and 6×10^{-6} for Res 3 to make them scale as $P_{\text{int}}^{-1/2}$ in regime II. These extra power independent small losses might be related to the interface between Al and SiN_x —for example, from a slightly damaged surface of Al formed during the deposition process. In regime I and II, Q_i^{-1} is limited by the TLS-induced loss tangent δ_{TLS} which displays a typical saturation behavior that is discussed in Section 5.4.5.2.

- **Temperature dependence of f_r and Q_i** To retrieve the value of δ_{TLS}^0 (δ_{TLS} for weak field at zero temperature), we fit the data of $Q_i^{-1}(T)$ and $f_r(T)$ under the lowest readout power at each temperature to their theoretical profiles Eq. 5.75 and Eq. 5.74. For each resonator, $Q_i^{-1}(T)$ and $f_r(T)$ are fitted jointly with two fitting parameters: f_r and the product $F\delta_{\text{TLS}}^0$. As shown in Fig. 5.17, fits to the TLS model generally agree well with the data, except that a large deviation is seen in the f_r fit of Res 3. We find that at the lowest readout powers an adjacent resonator is entering the bandwidth of Res 3 and probably makes the fitting routine report an inaccurate f_r .

The values of $F\delta_{\text{TLS}}^0$ and f_r from the fits are listed in Table 5.2. Because both the CPW geometry and the thickness of SiN_x are known, we can derive the electric field distribution from EM simulations and calculate the filling factor F according to Eq. 5.73. For Res 1 and Res 3 with CPW even mode, we find $F = 0.31$. Using this value of filling factor, Res 1 data yields $\delta_{\text{TLS}}^0 = 2.46 \times 10^{-3}$ and Res 3 data yields $\delta_{\text{TLS}}^0 = 3.2 \times 10^{-3}$ for our SiN_x . These values of δ_{TLS}^0 are pretty reasonable. Typical values of δ_{TLS}^0 for amorphous materials are usually found between 10^{-4} and 10^{-2} in the literature[59]. Even for the same amorphous material, the value of δ_{TLS}^0 depends largely on how the material is prepared. For example, low-loss SiN_x made from PECVD process with $\delta_{\text{TLS}}^0 \approx 10^{-4}$ was reported from another research group[59], which is significantly lower than what we measured from our SiN_x .

The difference between the two values of δ_{TLS}^0 derived from Res 1 and Res 3, though not large, suggests that the TLS density of states P might be frequency dependent, because Res 1 and Res 3 are physically the same resonator with the same filling factor F and the only difference is their resonance frequencies, 3.4 GHz vs. 10.2 GHz.

- **Noise comparison before and after the deposition of SiN_x** Noise, as well as its power and temperature dependence, is measured on both the bare device and the SiN_x -covered device. The noise from the bare device shows the general features of excess noise that have been discussed in

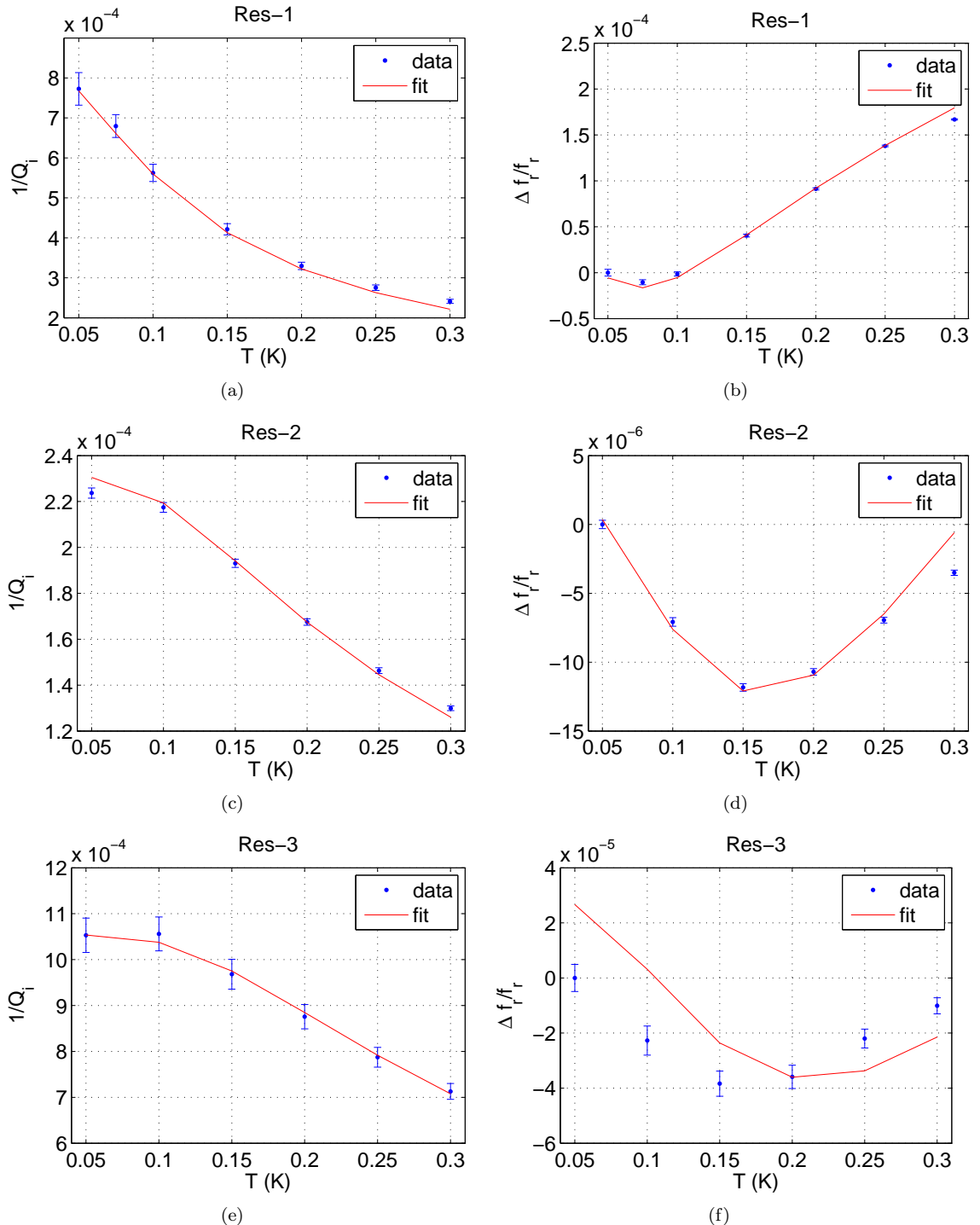


Figure 5.17: Joint fit of Q_i^{-1} and f_r vs. T at lowest readout power into their theoretical profiles Eq. 5.74 and Eq. 5.75

detail in Section 5.3.

Fig. 5.18(a) shows a pair of phase and amplitude noise spectra, measured on Res 1 of the SiN_x -covered device at $T = 50 \text{ mK}$ and $P_{\text{int}} = -50 \text{ dBm}$. It has the same features as the noise from a bare resonator: the noise is dominantly phase noise; amplitude noise is mostly flat and limited by the HEMT noise floor; the phase noise spectrum has a $1/f$ slope below 10 Hz, a $1/f^{-1/2}$ at higher frequencies and a roll-off at around 10 kHz. The frequency noise of Res 1 at $\nu = 500 \text{ Hz}$ as a function of P_{int} is plotted in Fig. 5.18(b) for two different temperatures, $T = 125 \text{ mK}$ (blue) and $T = 200 \text{ mK}$ (red). For comparison, the noise from the bare device measured at $T = 120 \text{ mK}$ is also plotted (black). In addition to the familiar $P_{\text{int}}^{-1/2}$ power dependence, we find that the noise has increased by a factor of 20 after the deposition of SiN_x . This implies that the measured excess noise of the SiN_x -covered device, as shown in Fig. 5.18(a), is mainly produced by the TLS in the SiN_x layer.

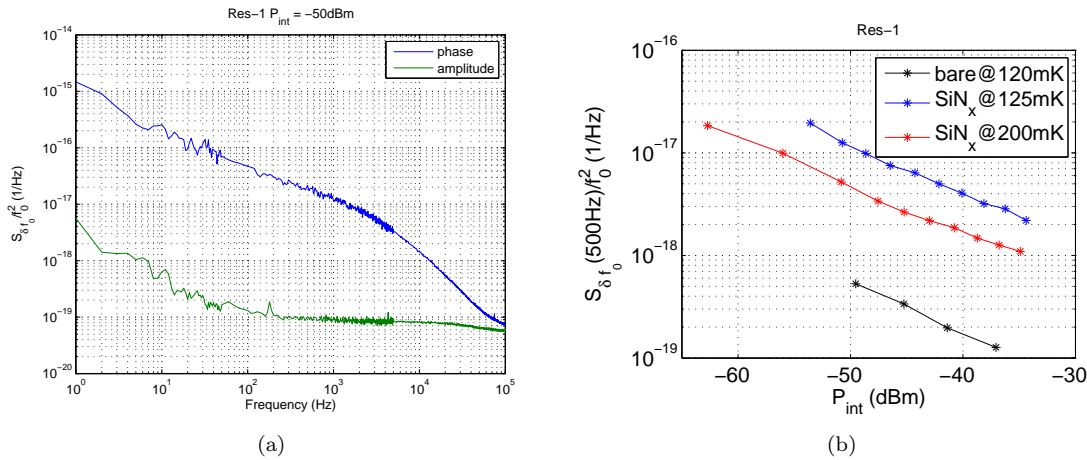


Figure 5.18: Excess noise measured on Res 1 of the SiN_x -covered device. (a) Phase and amplitude noise spectra measured at $T = 50 \text{ mK}$ and $P_{\text{int}} = -50 \text{ dBm}$. (b) Frequency noise at 500 Hz vs. internal power P_{int} . The blue and red lines are measured at $T = 125 \text{ mK}$ and $T = 200 \text{ mK}$, respectively. As a comparison, noise measured at $T = 120 \text{ mK}$ before the deposition of SiN_x is indicated by the black line.

•Temperature dependence of excess phase noise Constrained by the low Q_r at low P_{int} and the nonlinearity effect of superconductor at high P_{int} , we have a very limited window of readout power in which we can measure noise. Also we can not reliably measure noise at $T > 250 \text{ mK}$, because the resonator is made of Al ($T_c = 1.2 \text{ K}$) and the effect from superconductivity will mix in at higher temperatures.

Fig. 5.19 shows the frequency noise at $\nu = 500 \text{ Hz}$ of Res 1 measured between 50 mK and 225 mK and at $P_{\text{int}} = -48 \text{ dBm}$ (interpolated). The noise shows a strong temperature dependence on the temperature, scaling roughly as $T^{-1.5}$ above 125 mK .

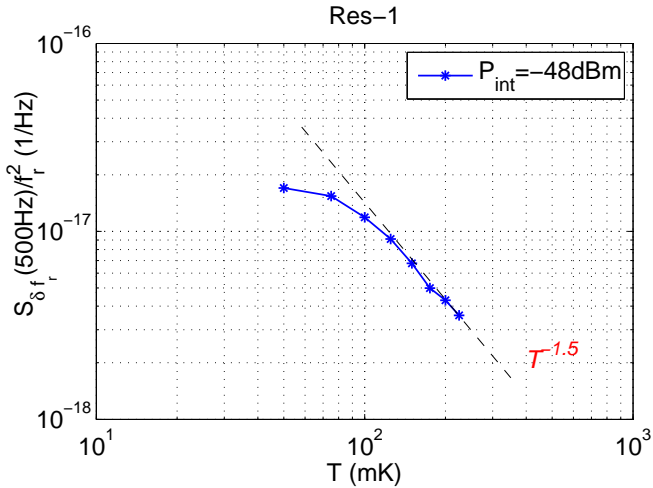


Figure 5.19: Temperature dependence of frequency noise measured on Res 1 at $P_{\text{int}} = -48$ dBm from the SiN_x -covered device

Conclusion The measured temperature dependence of $\Delta f_r/f_r$ and Q_i^{-1} , as well as the power and temperature dependence of Q_i^{-1} , all agree well with the TLS theory. By fitting the $\Delta f_r(T)/f_r$ data and $Q_i(T)^{-1}$ data to Eq. 5.74 and Eq. 5.75, the product $F\delta_{\text{TLS}}^0$ can be derived. If F is known, δ_{TLS}^0 can be determined, which is one of the important parameters of the TLS.

After the deposition of SiN_x , the phase noise is seen to increase by a factor of 20. It also keeps all the general features of phase noise found in a bare resonator. The fact that the noise from a SiN_x -covered device and from a bare device shows the same features is strong evidence that the noise in both cases is of the same origin — TLS.

5.5.1.2 Nb microstrip with SiO_2 dielectric on sapphire substrate

Another device we measured with a large TLS filling factor is a Nb on sapphire half-wavelength microstrip resonator device. Between the top strip (600 nm thick) and the ground plane (150 nm thick), both made of Nb, is a layer of sputtered (amorphous) SiO_2 dielectric (400 nm thick). Other relevant resonator parameters are listed in Table 5.3. Because the electric field is largely confined in the dielectric layer, the microstrip should have a very high filling factor. Indeed, EM simulation shows that $F = 94\%$ for this microstrip device.

- **Power and temperature dependence of f_r and Q_i .** We first measure the power and temperature dependence of f_r and Q_i , and fit the latter to the TLS model to retrieve the value of $F\delta_{\text{TLS}}^0$, as we did in the previous experiment with the SiN_x -covered device.

The results are shown in Fig. 5.20. In Fig. 5.20(a) we plot a group of Q_i^{-1} vs. P_{int} curves at different T , which looks very similar to its counter part in the SiN_x experiment. In Fig. 5.20(b) we plot a group of f_r vs. T curves at different P_{int} , which shows the signature shape of TLS-induced

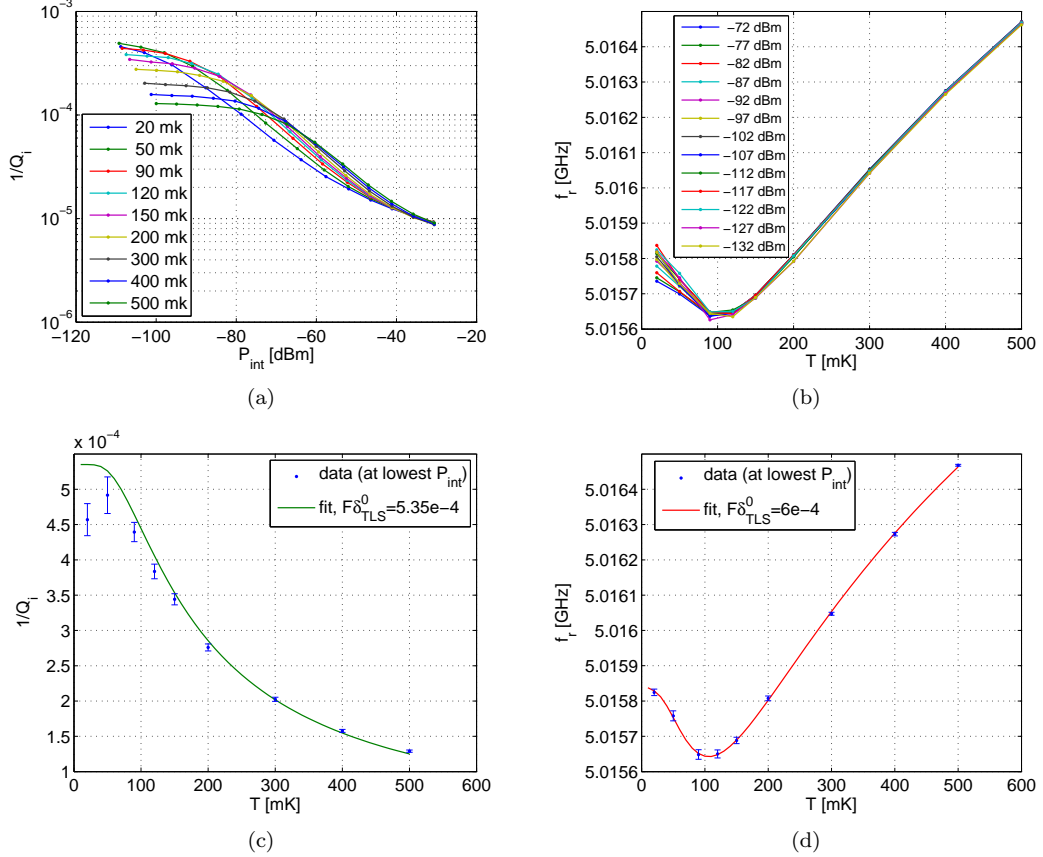


Figure 5.20: Measured power and temperature dependence of f_r and Q_i from Nb on sapphire with SiO_2 dielectric microstrip device. (a) Q_i^{-1} as a function of P_{int} at several temperatures (indicated in the legend) between 20 mK and 500 mK. (b) f_r as a function of T measured at several readout powers $P_{\mu w}$ (indicated in the legend) between -132 dBm and -72 dBm. (c) Fitting $Q_i^{-1}(T)$ at $P_{\mu w} = -132$ (lowest $P_{\mu w}$) to the theoretical model Eq. 5.75 yields $F\delta_{\text{TLS}}^0 = 5.35 \times 10^{-4}$. The first three data points are ignored, because for these data points the electric field is not below the critical field, as shown in (a). (d) Fitting $f_r(T)$ at $P_{\mu w} = -132$ dBm (lowest $P_{\mu w}$) to the theoretical model Eq. 5.74 yields $F\delta_{\text{TLS}}^0 = 6 \times 10^{-4}$.

variation of dielectric constant, as discussed in Section 5.4.5.1. We also see that at temperature above 100 mK, these curves shows very little power dependence, which is expected from Eq. (5.68). The noticeable power dependence under 100 mK is probably due to the heating effect.

The data of $Q_i^{*-1}(T)$ and $f_r(T)$ under the lowest readout power at each temperature are separately fitted to their theoretical profiles Eq. 5.75 and Eq. 5.74. Fairly good fits are obtained as shown in Fig. (5.20(c)) and Fig. (5.20(d)). The value of $F\delta_{\text{TLS}}^0$ is 5.4×10^{-4} derived from the $Q_i^{-1}(T)$ fit and 6×10^{-4} from the $f_r(T)$ fit, which roughly agrees (within 20%) with each other. This means the loss tangent δ_{TLS}^0 of the SiO_2 dielectric is around $\delta_{\text{TLS}}^0 \sim 6 \times 10^{-4}$, which is a factor of 4 better compared to the SiN_x measured in the experiment described in the previous section.

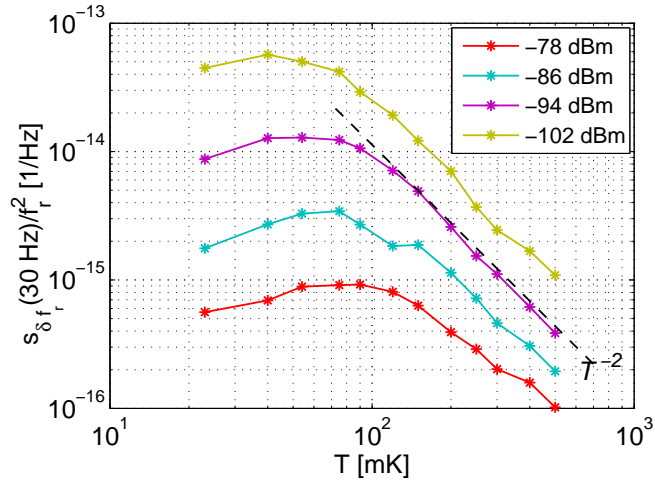


Figure 5.21: Frequency noise at 30 Hz as a function of temperature measured at $P_{\text{int}} = -78, -86, -94$, and -102 dBm from Nb on sapphire with SiO_2 dielectric microstrip device. At $T > 100 \text{ mK}$, the noise roughly scales as T^{-2} .

- **Power and temperature dependence of frequency noise.** The frequency noise measured at temperatures between 20 mK and 500 mK under several readout powers are shown in Fig. (5.5.1.2). We again see that the noise decreases rapidly at high temperature ($T > 100 \text{ mK}$) and roughly scales as T^{-2} , which is also observed in Fig. 5.8 and Fig. 5.19. In addition, we see that the noise decrease slightly at very low temperatures, which is another interesting clue to the physics of the TLS noise.

- **Estimating $\kappa(\nu, \omega, T)$ from noise data.** Because both the spatial distribution of the TLS (uniformly distributed in the dielectric layer) and the electric field (from EM simulation or simply approximated by a parallel plate structure) are known, we are ready to apply the semi-empirical noise model developed in Section 5.4.6 and estimate the noise coefficient $\kappa(\nu, \omega, T)$ for SiO_2 used in our microstrip.

As an example, we will derive the spectrum of $\kappa(\nu, 5 \text{ GHz}, 120 \text{ mK})$ from the frequency noise

Table 5.3: Parameters of Nb/SiO₂/Nb microstrip

resonance frequency	f_r	5.07 GHz
internal power	P_{int}	-43 dBm
Nb top strip width	w	7.5 μm
Nb top strip thickness	d	600 nm
thickness of SiO ₂	h	400 nm
resonator length	l	15 mm (half-wave)
capacitance per unit length	C	7.3e-10 F/m (85 ϵ_0)
characteristic impedance	Z_0	8.66 Ω
effective dielectric constant	ϵ_{eff}	3.6
CPW voltage at open end	V_0	1.86 mV
integral $\int_{A_h} \rho(x, y)^3 dx dy$	I_3	47/ μm

spectrum measured at $T = 120$ mK and $P_{\text{int}} = -38$ dBm shown in Fig. 5.22(a). The 3 parameters, C , V_0 , and l , required by Eq. 5.81 are calculated and listed in Table 5.3. The integral

$$I_3 = \int_{A_h} \rho(x, y)^3 dx dy \approx w/h^2 \quad (5.83)$$

is calculated by approximating the microstrip field with that in a parallel plate structure.

According to Eq. 5.81, the conversion factor from the frequency noise $S_{\delta f_r}(\nu)/f_r^2$ to $\kappa(\nu, \omega, T)$ is given by

$$g = \frac{4I_3}{3\pi C^2 V_0 l} = \frac{9.90 \times 10^7}{\epsilon_0^2} \text{ m}^{-2} \text{V}^{-1}. \quad (5.84)$$

By applying this factor, we finally derive the spectrum $\kappa(\nu, 5 \text{ GHz}, 120 \text{ mK})$ which is shown in the Fig. 5.22(b).

The noise coefficient $\kappa(\nu, \omega, T)$ for other temperatures T and microwave frequencies ω can be derived in a similar way. Because on this device we have only one microstrip resonator with $f_r \sim 5$ GHz, we are unable to obtain κ for other frequencies. In future experiments, it should be easy to design resonators which spread out in the wider frequency range in which we are interested. In fact, according to the TLS picture, the frequency noise should be only dependent on the value of $\hbar\omega/kT$, instead of ω and T individually. Once the values of $\kappa(\nu, \hbar\omega/kT)$ are derived, they can be used to predict the frequency noise in resonators with any geometry, resonance frequency, and at any temperature, as long as the TLS are of the same type, and the spatial distribution of the TLS and the electric field are known in these resonators.

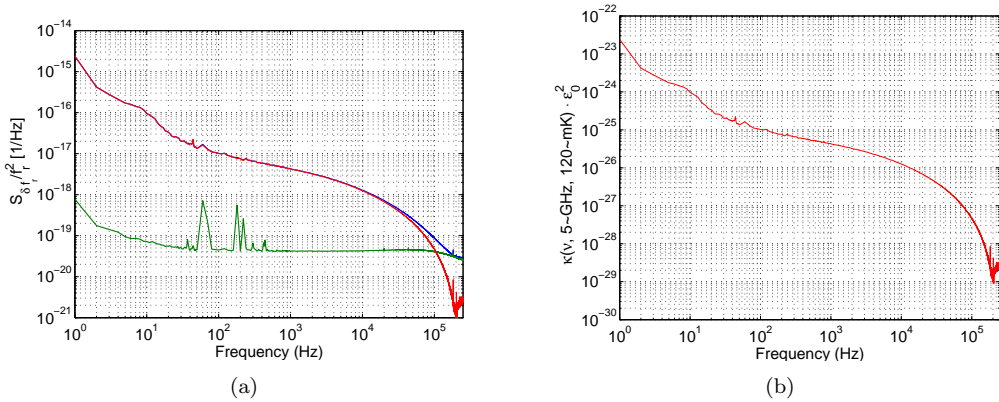


Figure 5.22: Frequency noise spectrum (a) and the derived noise coefficient κ (b). The noise spectra are measured at $T = 120$ mK and $P_{\text{int}} = -38$ dBm from the Nb microstrip device with SiO_2 dielectric.

5.5.2 Locating the TLS noise source

From the experimental and theoretical results presented in the preceding sections of this chapter, we are almost certain that the excess noise is caused by fluctuating TLS in the dielectric materials. So far we have not given any discussion on where the TLS are. As shown in Fig. 5.23, at least four locations in our CPW resonator can host the TLS fluctuators—the bulk substrate or its exposed surface, the interface layers between the metal films and the substrate, and the oxide layers on the metal surfaces. In the next two experiments, we will give experimental evidence that the TLS are distributed on the surface of the resonator but not in the bulk substrate.

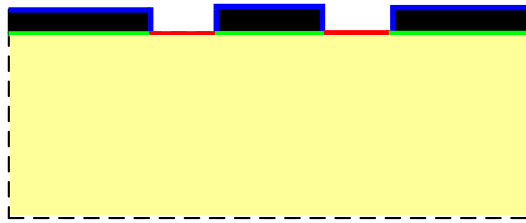


Figure 5.23: Potential locations of TLS noise source: bulk substrate (yellow), exposed substrate surface (red), the interface layers between the metal films and the substrate (green), and oxide layers on the metal surfaces (blue)

5.5.2.1 Evidence for a surface distribution of TLS from frequency shift measurement

We have learned a lot about the TLS effects on the dielectric properties from the study of SiN_x -covered device and SiO_2 dielectric microstrip device. Especially, we are able to determine the product of the TLS loss tangent δ_{TLS}^0 and filling factor F by fitting the TLS models to either the temperature dependence of $\Delta f_r(T)/f_r$ data at any readout power or $Q_i^{-1}(T)$ data at low power. In this experiment, we go back and apply this analysis to study the intrinsic TLS in the bare resonators.

The key idea of this experiment is to measure $\Delta f_r/f_r$ of coplanar waveguide (CPW) resonators with different geometries in order to obtain values of $F\delta_{\text{TLS}}^0$ for each geometry. The frequency-multiplexed resonators are all fabricated simultaneously and are integrated onto a single chip, and are measured in a single cooldown. We can therefore safely assume that a single value of the loss tangent δ_{TLS}^0 applies for all resonator geometries. This allows the variation of the filling factor F with geometry to be determined, providing information on the geometrical distribution of the TLS. If TLS are in the bulk substrate with dielectric constant ϵ_r , Eq. 5.73 applied to the CPW field distribution would yield a filling factor $F \approx \epsilon_r/(\epsilon_r + 1)$ that is independent of the resonator's center strip width s_r . If instead the TLS are in a surface layer, F should be dependent on the CPW geometry, scaling roughly as $1/s_r$.

The geometry test device used in this experiment consists of five CPW quarter-wavelength resonators with different geometries. They are patterned from a 120 nm-thick Nb film deposited on a

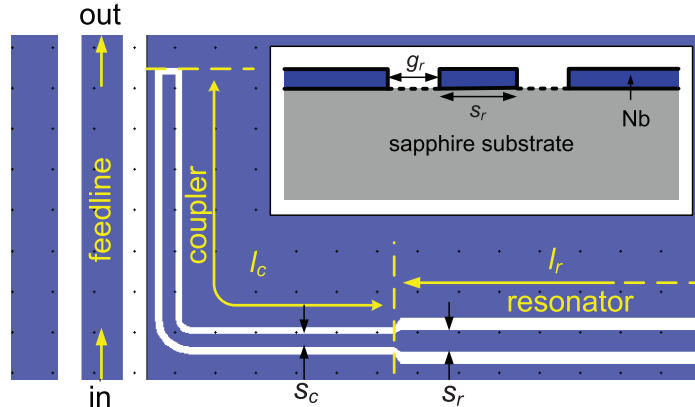


Figure 5.24: An illustration of the CPW coupler and resonator. The inset shows a cross-sectional view of the CPW. The contour of the metal surface and the contour of the exposed surface of the substrate are indicated by the solid line and the dashed line, respectively.

crystalline sapphire substrate. Because Nb has a critical temperature $T_c = 9.2$ K, the effect of superconductivity on the temperature dependence of the resonance frequency is negligible for $T < 1$ K. As shown in Fig. 5.24, each resonator is capacitively coupled to a common feedline using a CPW coupler of length $l_c \cong 200$ μm and with a common center-strip width of $s_c = 3$ μm . The coupler is then widened into the resonator body, with a center-strip width of $s_r = 3$ μm , 5 μm , 10 μm , 20 μm or 50 μm , and a length of $l_r \sim 5$ mm. The ratio between center strip width s and the gap g in both the coupler and the resonator body is fixed to 3:2, to maintain a constant impedance of $Z_0 \approx 50$ Ω . The resonance frequencies are $f_r \sim 6$ GHz, and the coupler is designed to have a coupling quality factor $Q_c \sim 50,000$.

Fig. 5.25 shows the measured frequency shifts $\Delta f_r/f_r$ for the five resonators as a function of temperature over the temperature range 100 mK to 800 mK. Although all of the resonators display a common shape for the variation of frequency with temperature, the magnitude of the effect varies strongly with geometry. As shown by the dashed lines in Fig. 5.25, fits to the TLS model (Eq. 5.74) generally agree quite well with the data. The familiar non-monotonic variation of the dielectric constant with temperature can be clearly seen in Fig. 5.25: f_r increases (ϵ decreases) when $T > \hbar\omega/2k$; a minimum in f_r (a maximum in ϵ) occurs around $T = \hbar\omega/2k$; at lower temperatures ($T < 100$ mK), we would expect to see a decrease in f_r (increase in ϵ) as indicated by the extrapolation of the fit. The largest deviations from the TLS model (about 4%) occur at the lowest temperatures, and are likely due to TLS saturation effects discussed in Section 5.4.5.2. Power-dependent frequency shifts of this size have also been previously observed experimentally[63]. Here, we will ignore these small effects and focus on the geometrical dependence.

With the exception of the 3 μm resonator, the measured values of $F\delta_{\text{TLS}}^0$ from the fits have to be corrected for the coupler because the coupler's center strip width $s_c = 3$ μm differs from that

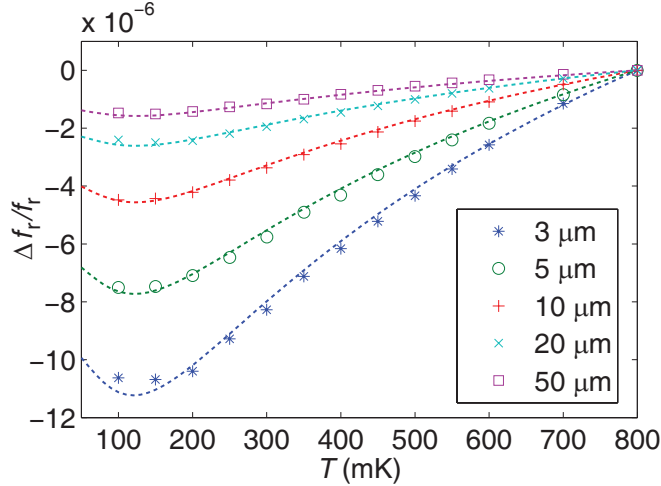


Figure 5.25: Fractional frequency shift $\Delta f_r/f_r$ as a function of temperature. $\Delta f_r/f_r$ is calculated using $\Delta f_r/f_r = [f_r(T) - f_r(800 \text{ mK})]/f_r(800 \text{ mK})$. The temperature sweep is in steps of 50 mK from 100 mK to 600 mK, and in steps of 100 mK above 600 mK. The markers represent different resonator geometries, as indicated by the values of the center strip width s_r in the legend. The dashed lines indicate fits to the TLS model.

of the resonator, $s_c \neq s_r$. In the limit $l_c \ll l_r$, it can be shown that the corrected filling factor is given by,

$$F^* = \frac{F - t F_{3\mu\text{m}}}{1 - t} \quad (5.85)$$

where $t = 2l_c/(l_c + l_r)$. The values of $F^* \delta_{\text{TLS}}^0$ are listed in Table 5.4, as well as the ratios relative to the value for 3 μm resonator.

We also measured the resonance frequencies at 4.2 K (0.46 T_c), allowing the shift $\Delta f_r(4.2 \text{ K}) = f_r(4.2 \text{ K}) - f_r(100 \text{ mK})$ as well as the kinetic inductance fraction to be calculated for each geometry, as shown in Table 5.4.

Fig. 5.26 shows the results for the geometrical scaling of the corrected filling factor F^* and the kinetic inductance fraction α , plotted as ratios relative to their respective values for the resonator with a 3 μm wide center strip. The observed strong variation of F^* with geometry immediately rules out a volume TLS distribution, and favors a surface distribution. We investigate this in more detail by comparing the data to two theoretically calculated geometrical factors g_m and g_g , which have units of inverse length and are calculated from contour integrals in a cross-sectional plane given by

$$g_m = \frac{1}{V^2} \int_{\text{metal}} \vec{E}^2 dl \quad (5.86)$$

$$g_g = \frac{1}{V^2} \int_{\text{gap}} \vec{E}^2 dl \quad (5.87)$$

where V is the CPW voltage. The first integral is actually a sum of three contour integrals, taken over the surfaces of the three metal conductors, the center strip and the two ground planes. The

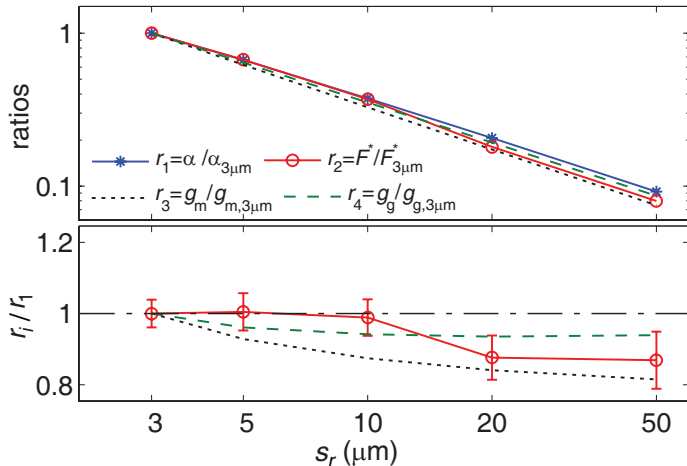


Figure 5.26: The scaling of the measured values of the kinetic inductance α and TLS filling factor F^* , as well as the calculated values of the CPW geometrical factors g_m and g_g , are shown, as a function of the resonator center strip width s_r . The top panel shows the ratios of α (r_1), F^* (r_2), g_m (r_3), and g_g (r_4) to their values for the $3\ \mu\text{m}$ resonators. The bottom panel shows these ratios normalized by the kinetic inductance ratio r_1 .

second contour integral is taken over the two ‘‘gaps’’, the surface of the exposed substrate in between the conductors. These contours are illustrated in the inset of Fig. 5.24. The integrals are evaluated numerically using the electric field derived from a numerical conformal mapping solution to the Laplace equation, where the conformal mapping procedure is identical to that used in the calculation of α described in Section 3.1.3.1.

According to Eq. 5.73, F^* should have the same scaling as g_m if the TLS are distributed on the metal surface (or at the metal-substrate interface), or as g_g if the TLS are located on the surface of the exposed substrate. The kinetic inductance of the CPW may also be calculated using a contour integral similar to that of g_m , except that the integrand is replaced by \vec{H}^2 [64]. Because the magnetic field \vec{H} is proportional to \vec{E} for a quasi-TEM mode, we expect the kinetic inductance fraction α to have the same geometrical scaling as g_m .

Fig. 5.26 shows that the four quantities, F^* , α , g_m , and g_g , all scale as $s_r^{-\gamma}$ with $\gamma = 0.85 - 0.91$. The finite thickness of the superconducting film is responsible for the deviations from $\gamma = 1$. This is very strong evidence that the TLS have a surface distribution and are not uniformly distributed in the bulk substrate. These data, however, cannot discriminate between a TLS distribution on the metal surface and a TLS distribution on the exposed substrate surface (the gap), because the corresponding theoretical predictions (g_m and g_g) are very similar and both agree with the data. Future measurements of resonators with various center-strip-to-gap ratios may allow these two TLS distributions to be separated.

The absolute values of $F^* \delta_{\text{TLS}}^0$ are also of interest. Assuming a typical value of $\delta_{\text{TLS}}^0 \sim 10^{-2}$ for the TLS-loaded material[59], the measured value of $F^* \delta_{\text{TLS}}^0 = 3 \times 10^{-5}$ for the $3\ \mu\text{m}$ resonator yields

a filling factor of $F^* \sim 0.3\%$. Numerical calculations show that this is consistent with a ~ 2 nm layer of the TLS-loaded material on the metal surface or a ~ 3 nm layer on the gap surface, suggesting that native oxides or adsorbed layers may be the TLS host material[72].

Table 5.4: Values and ratios

s_r [μm]	$f_r(100 \text{ mK})$ [GHz]	$\Delta f_r(4.2 \text{ K})$ [MHz]	$\frac{\alpha}{\alpha_{3\mu\text{m}}}$	$F^* \delta_{\text{TLS}}^0 \times 10^{-5}$	$\frac{F^*}{F^*_{3\mu\text{m}}}$	$\frac{g_m}{g_{m,3\mu\text{m}}}$	$\frac{g_g}{g_{g,3\mu\text{m}}}$
3 μm	5.666	11.1	1	2.98 ± 0.12	1	1	1
5 μm	5.735	7.41	0.67	2.00 ± 0.07	0.67	0.62	0.64
10 μm	5.800	4.15	0.37	1.10 ± 0.03	0.37	0.33	0.35
20 μm	5.836	2.28	0.21	0.54 ± 0.03	0.18	0.17	0.19
50 μm	5.851	1.02	0.092	0.24 ± 0.02	0.08	0.075	0.086

5.5.2.2 More on the geometrical scaling of frequency noise

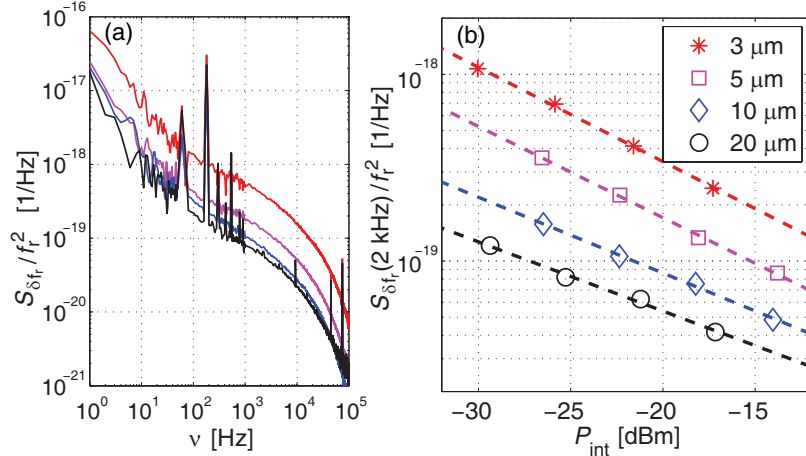


Figure 5.27: Frequency noise of the four CPW resonators measured at $T = 55$ mK. (a) Frequency noise spectra at $P_{\mu\text{w}} = -65$ dBm. From top to bottom, the four curves correspond to CPW center strip widths of $s_r = 3 \mu\text{m}$, $5 \mu\text{m}$, $10 \mu\text{m}$, and $20 \mu\text{m}$. The various spikes seen in the spectra are due to pickup of stray signals by the electronics and cabling. (b) Frequency noise at $\nu = 2$ kHz as a function of P_{int} . The markers represent different resonator geometries, as indicated by the values of s_r in the legend. The dashed lines indicate power law fits to the data of each geometry.

In addition to the low-temperature frequency shift data, we also measured the frequency noise data on the same geometry test device as described in the previous section in the same cooldown.

The frequency noise spectra $S_{\delta f_r}(\nu)/f_r^2$ of the five resonators are measured for microwave readout power $P_{\mu\text{w}}$ in the range -61 dBm to -73 dBm. As an example, the frequency noise spectra measured at $P_{\mu\text{w}} = -65$ dBm are shown in Fig. 5.27(a). Apart from a common spectral shape, we clearly see that the level of the noise decreases as the center strip becomes wider. Unfortunately the noise of the $50 \mu\text{m}$ -resonator is not much higher than that of our cryogenic HEMT amplifier, and therefore those measurements are less reliable, so we exclude the $50 \mu\text{m}$ -resonator from further discussion.

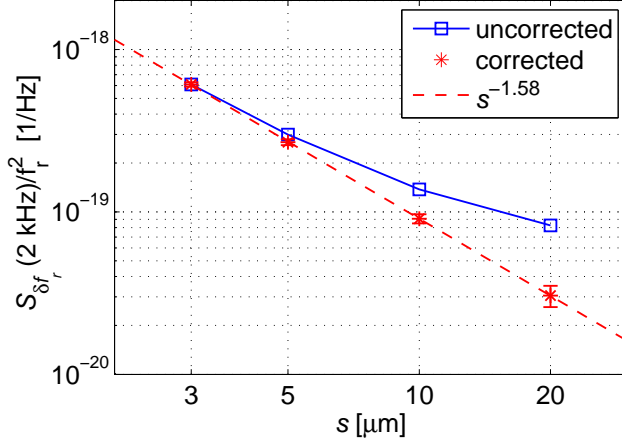


Figure 5.28: The measured frequency noise $S_{\delta f}(2 \text{ kHz})/f_r^2$ at $P_{\text{int}} = -25 \text{ dBm}$ is plotted as a function of the center strip width s_r . Values directly retrieved from power-law fits to the data in Fig. 5.27 are indicated by the open squares. Values corrected for the coupler's contribution are indicated by the stars. The corrected values of $S_{\delta f}(2 \text{ kHz})/f_r^2$ scale as $s_r^{-1.58}$, as indicated by the dashed line.

The noise levels at $\nu = 2 \text{ kHz}$ were retrieved from the noise spectra and are plotted as a function of resonator internal power $P_{\text{int}} = 2Q_r^2P_{\mu w}/\pi Q_c$ in Fig. 5.27(b). All resonators display a power dependence close to $S_{\delta f}/f_r^2 \propto P_{\text{int}}^{-1/2}$, as we have previously observed[73, 70, 63]. In order to study the geometrical scaling of the noise in more detail, we first fit the noise vs. power data for each resonator to a simple power law, and retrieve the values of the noise $S_{\delta f}(2 \text{ kHz})/f_r^2$ at $P_{\text{int}} = -25 \text{ dBm}$ for each geometry. These results (Fig. 5.28) again show that the noise decreases with increasing s_r , although not (yet) as a simple power law.

To make further progress, we apply the semi-empirical noise model (Eq. 5.80) to the coupler correction. For the resonators that are wider than the coupler ($s_r > s_c = 3 \text{ } \mu\text{m}$), the measured values of $S_{\delta f_r}/f_r^2$ need to be corrected for the coupler's noise contribution. A similar procedure was applied in the frequency shift data in the previous section (Eq. 5.85). In the limit $l_c \ll l_r$, the correction is given by

$$S_{\delta f_r}^* = (S_{\delta f_r} - \eta S_{\delta f_r, 3\mu\text{m}})/(1 - \eta) \quad (5.88)$$

where $\eta = 3\pi l_c/4(l_c + l_r)$. The corrected values are plotted in Fig. 5.28 (with symbol stars) and are found to have a simple power-law scaling $1/s_r^{1.58}$. We find a similar noise scaling, $1/s_r^\alpha$, with α between 1.49 and 1.6, for noise frequencies $400 \text{ Hz} < \nu < 3 \text{ kHz}$.

While the fact that an $|E|^3$ -weighted coupler noise correction leads to a simple power law noise scaling is already quite encouraging, we will now go further and show that the observed $s_r^{-1.58}$ power-law slope can be reproduced by our semi-empirical noise model. Measurements of the anomalous

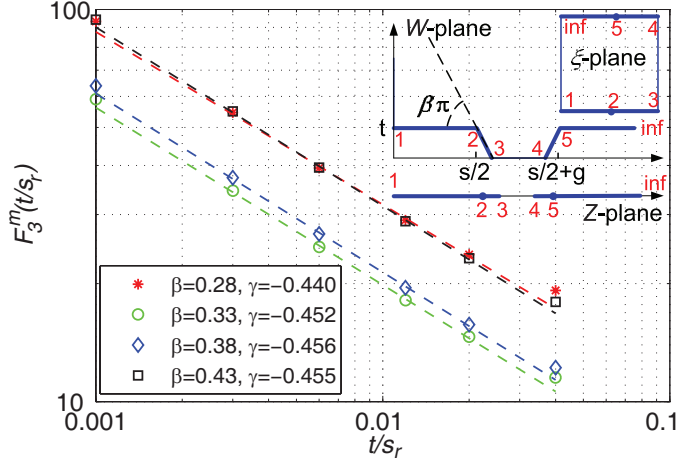


Figure 5.29: The calculated dimensionless noise scaling function $F_3^m(t/s_r)$ is plotted as a function of the ratio between the CPW half film thickness t and the center strip width s_r . The inset shows the conformal mapping used to derive the electric field. The contour integral for $F_3^m(t/s_r)$ is evaluated on the surface of the metal, as outlined by the solid lines in the W -plane. Results are shown for four different values of the parameter $\beta = 0.28, 0.33, 0.38, 0.43$ that controls the edge shape (see inset). The dashed lines indicate power law $(t/s_r)^\gamma$ fits to $F_3^m(t/s_r)$.

low temperature frequency shift described in the previous section have already pointed to a surface distribution of TLS. If these TLS are also responsible for the frequency noise, according to Eq. 5.80 we would expect the noise to have the same geometrical scaling as the contour integral $I_3 = \int |\vec{E}|^3 ds$ evaluated either on the metal surface (I_3^m) or the exposed substrate surface (I_3^g). For zero-thickness CPW, although the integral is divergent, the expected scaling can be shown to be $I_3 \propto 1/s_r^2$. For CPW with finite thickness, we can evaluate I_3 numerically using the electric field derived from a numerical conformal mapping solution. The two-step mapping procedure used here is modified from that given by Collin[55] and is illustrated in the inset of Fig. 5.29. We first map a quadrant of finite-thickness CPW with half thickness t (in the W -plane) to a zero-thickness CPW (in the Z -plane) and then to a parallel-plate capacitor (in the ξ -plane). To avoid non-integrable singularities, we must constrain all internal angles on the conductor edges to be less than $\pi/2$, which leads to the condition $0.25 < \beta < 0.5$, where $\beta\pi$ is the angle defined in Fig. 5.29. Instead of evaluating I_3 directly, we define a normalized dimensionless integral $F_3(t, s_r) = \int |\vec{E}/E^*|^3 ds^*$, where $s^* = s/s_r$ is a normalized integration coordinate and $E^* = V/s_r$ is a characteristic field strength for a CPW with voltage V . Now F_3 depends only on the ratio t/s_r and is related to the original contour integral by $I_3(s_r, t, V) = (V^3/s_r^2)F_3(t/s_r)$. The results $F_3^m(t/s_r)$ calculated for the metal surface are plotted in Fig. 5.29, and show a power law scaling $F_3^m \sim (t/s_r)^\gamma$ with $\gamma \approx -0.45$ for $0.003 < t/s_r < 0.02$, the relevant range for our experiment. We also find that for a wide range of β , $0.27 < \beta < 0.43$, although the absolute values of $F_3^m(t/s_r)$ vary significantly, the scaling index γ remains almost constant, $-0.456 < \gamma < -0.440$. Therefore, γ appears to depend little on the edge shape.

From Eq. 5.80, the noise scaling is predicted to be $I_3^m(t, s_r, V) \propto s_r^{-2-\gamma} \sim s_r^{-1.55}$ (at fixed V), which agrees surprisingly well with the measured $s_r^{-1.58}$ scaling. We also investigated the case for TLS located on the exposed substrate surface, and found that F_3^g has almost identical scaling ($\gamma \approx -0.45$) as F_3^m . While we still cannot say whether the TLS are on the surface of the metal or the exposed substrate, we can safely rule out a volume distribution of TLS fluctuators in the bulk substrate; this assumption yields a noise scaling of $\sim s_r^{-1.03}$, significantly different than that measured.

In summary, the scaling of the frequency noise with resonator power and CPW geometry can be satisfactorily explained by the semi-empirical model developed in Section 5.4.6 and with the assumption of a surface distribution of independent TLS fluctuators. These results allow the resonator geometry to be optimized, which will be discussed in the next section. Had we known the exact \vec{E} field distribution and the exact TLS distribution for our CPW resonators, we would be able to derive the noise coefficient $\kappa(\nu, \omega, T)$ as we did for the SiQ₂ microstrip experiment discussed earlier. Unfortunately, the two parameters, the edge shape and the thickness of the TLS layer, required for calculating $\kappa(\nu, \omega, T)$ are not easily available. However, they are expected to be common among resonators fabricated simultaneously on the same wafer, and more or less stable for resonators fabricated through the same processes. Since we have shown that the ratio of $|\vec{E}|^3$ integral between two resonator geometries is insensitive to the edge shape, we can still predict the scaling of the noise among different resonator geometries[74].

5.6 Method to reduce the noise

Based on our knowledge of the excess noise, we propose several methods that may potentially reduce the noise. Some of them have already been put into the action and proved to be effective. Of course, a better understanding of the physics of the TLS noise may lead to more effective noise reduction methods.

5.6.1 Hybrid geometry

5.6.1.1 Two-section CPW

Our noise model (Eq. 5.80) implies that the noise contributions are weighted by $|\vec{E}|^3$, so TLS fluctuators located near the coupler end of a quarter-wave resonators should give significantly larger noise contributions than those located near the shorted end. Meanwhile, the noise measurement of the geometry test device has demonstrated that the noise decreases rapidly with increasing s_r , scaling as $s_r^{-1.6}$. This leads us to a two-section CPW resonator design for MKID. As shown in Fig. 5.30, the resonator has a wider section (with center strip width s_1 , gap g_1 , and length l_1) on

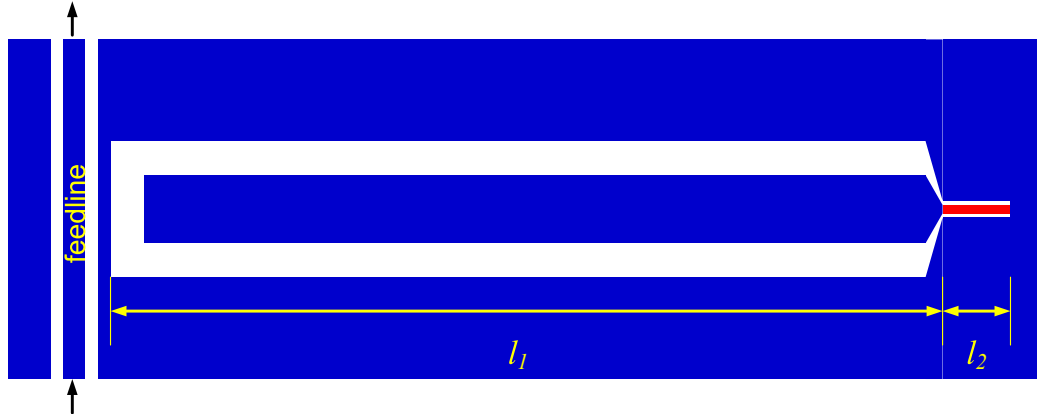


Figure 5.30: An illustration of the two-section CPW MKID design. Quasiparticles are generated and confined in the effective sensor area indicated by the red strip.

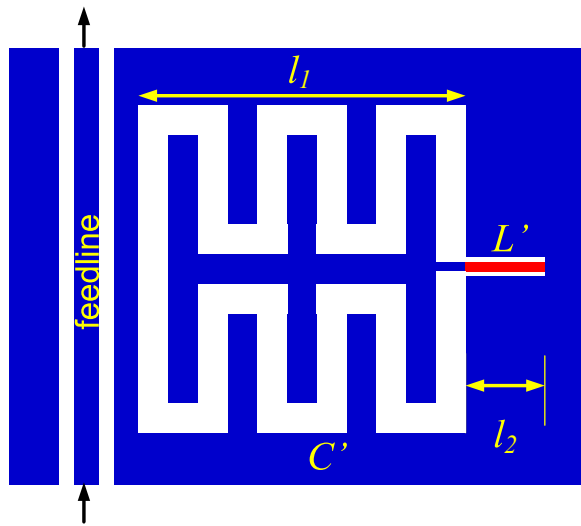


Figure 5.31: An illustration of the MKID design using interdigitated capacitor. Quasiparticles are generated and confined in the effective sensor area indicated by the red strip.

the coupler end to benefit from the noise reduction, but a narrower section (with center strip width s_2 , gap g_2 , and length l_2) at the low- $|\vec{E}|$ shorted end to maintain a high kinetic inductance fraction and responsivity. Meanwhile, we can make the section 1 CPW from a higher gap superconductor (e.g., Nb) and section 2 from a lower gap superconductor (e.g., Al), to confine the quasiparticles in section 2. To maximize the noise reduction effect and the responsivity, we should also make $l_1 \gg l_2$.

In the example design as shown in Fig. 5.30, we have $s_1/s_2 = g_1/g_2 = 4$. According to the $s_r^{-1.6}$ noise scaling, this detector design is expected to give 9 times lower frequency noise and therefore 3 times better NEP as compared to the conventional one-section CPW with s_2 and g_2 .

5.6.1.2 A design using interdigitated capacitor

The wider geometry section in the two-section CPW design can be replaced by a interdigitated planar capacitor section, as shown in Fig. 5.31. Such an interdigitated design makes the resonator more compact and easier to fit into a detector array where the space is limited. The strips and gaps in the interdigitated capacitor should be made as wide as is allowed by the space in order to maximize the noise reduction effect. Because the dimension of the capacitor ($l_1 \sim 1$ mm) is designed to be much smaller than the wavelength $\lambda > 10$ mm, the voltage distribution on the interdigitated capacitor structure is almost in phase and such a structure indeed acts as a lumped-element capacitor C' . The length of the shorted sensor strip in section 2 is also much smaller than the wavelength, so the sensor strip acts as an inductor with inductance $L' = Ll_1$, where L is the inductance per unit length of the CPW in section 2. The entire structure shown in Fig. 5.31 virtually becomes a parallel RLC resonant circuit and can be conveniently described by a lumped-element circuit model.

5.6.2 Removing TLS

An obvious way of reducing excess noise is to remove the TLS fluctuators from the resonator, partially or completely.

5.6.2.1 Coating with non-oxidizing metal

If the TLS are in the oxide layer of the superconductor, coating the superconductor with a layer of non-oxidizing metal (for example, Au) may get rid of some of the TLS on the metal surface and reduce noise. However, it can not remove all the TLS because the superconducting film will still be exposed to air and form oxides at the edges where they are etched off. Because the electric field strength is usually peaked at these edges, the noise contributions from these remaining TLS, according to the $|\vec{E}|^3$ weighting, are still significant. EM simulation shows that this method may only moderately reduce the noise by a factor of a few.

5.6.2.2 Silicides

The surface oxide can only be avoided if the superconducting film is not exposed to air. This is almost impossible for standard lithographed planar structures but may be possible by using superconducting silicides (such as PtSi[75], CoSi[76]). These silicides are made by ion implantation of metal into silicon substrate. With this process, for example, one can bury a entire CPW into the crystalline Si up to ~ 100 nm deep beneath the surface. One can bury it even deeper by regrowing crystalline Si on the surface. Because the crystalline structure of Si will not be destroyed and no amorphous material will be created in these processes, the devices made from these silicides are expected to be free of TLS fluctuators and excess noise.

5.6.3 Amplitude readout

As has been shown earlier in this chapter, no excess noise is observed in the amplitude direction and the amplitude noise, set by the noise temperature of HEMT, can be orders of magnitude lower than the phase noise at low noise frequencies. Therefore, using amplitude readout may avoid the excess noise and in some cases give better sensitivity.

Recall from Chapter 2 and 4 that a change in the quasiparticle will cause a change in both the real (σ_1) and imaginary (σ_2) part of the conductivity, resulting in an *IQ* trajectory that is always at a nonzero angle $\psi = \tan^{-1}(\delta\sigma_1/\delta\sigma_2)$ to the resonance circle. Calculation from Martis-Bardeen's theory shows that $\tan\psi = 1/4 \sim 1/3$ for the temperature and frequency range that MKIDs usually operate in. This means as soon as the phase noise exceeds the amplitude noise (HEMT noise floor) by about a factor of 10 (in power), amplitude readout may yield a better NEP than the phase readout.

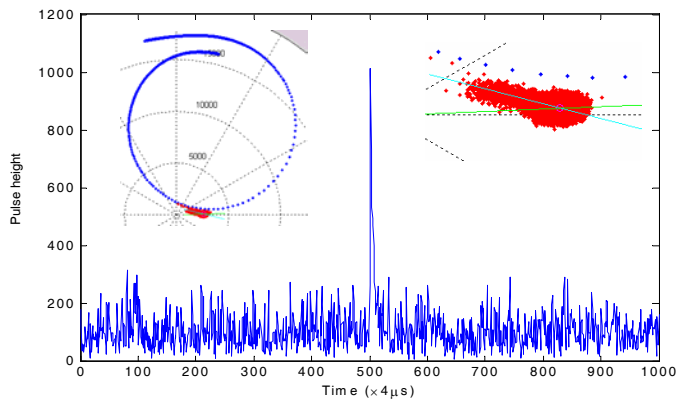


Figure 5.32: Detector response to a single UV photon event. The data is measured from a 40 nm Al on sapphire MKID illuminated by monochromatic UV photons ($\lambda = 254$ nm) at around 200 mK. The quasi-particle recombination time is measured to be $20 \mu\text{s}$. The inset shows the resonance circle and the pulse response in the IQ plane. In the zoom-in view of the pulse response, one can identify the pulse and the noise ellipse. The angle between the average pulse direction and the major axis of the noise ellipse is 15° .

Fig. 5.32 shows the measured detector response to a 254 nm UV photon. From the average pulse trajectory and the major axis of the noise ellipse, we determine $\psi \approx 15^\circ$. Applying the standard optimal filtering analysis to these data, we derived the NEP for both the phase and amplitude readout, which is plotted in Fig. 5.33. We see that amplitude NEP is a factor of 4 lower than the phase NEP at low frequency (below 10 Hz). At high frequency (above 5 kHz), the phase NEP becomes better than the amplitude NEP again. To take advantage of the signal in both directions, one can analyze the data using a two-dimensional optimal filtering algorithm. It can be shown that

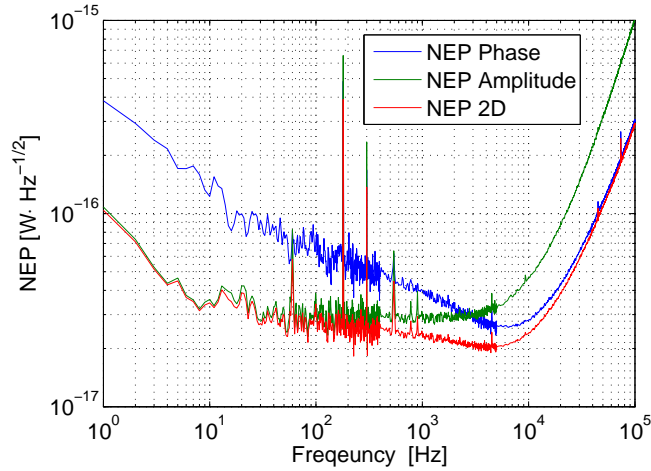


Figure 5.33: NEP calculated for the phase readout (blue), amplitude readout (green), and a combined readout (red)

the two-dimensional NEP is given by

$$\text{NEP}_{\text{2D}}^{-2} = \text{NEP}_{\text{pha}}^{-2} + \text{NEP}_{\text{amp}}^{-2} \quad (5.89)$$

which is indicated by the lowest curve in Fig. 5.33.

Chapter 6

Sensitivity of submm kinetic inductance detector

In this chapter, we will discuss the sensitivity of submm MKIDs, as an example of applying the models and theories of superconducting resonators developed in the previous chapters.

As the first stage of the detector development, these submm MKIDs are to be deployed in the Caltech Submillimeter Observatory (CSO), a ground-based telescope. For ground-based observations, it is inevitable that the detector will be exposed to the radiations from the atmosphere and have a background photon signal. Once the intrinsic noise of the detector is made smaller than the shot noise of this background photon signal, the sensitivity of the detector is adequate. This requirement is called background limited photon (BLIP) detection.

One of the important questions to be answered in this chapter is whether our submm MKIDs can achieve the background limited photon detection on the ground, or in other words, whether the intrinsic detector noise (g-r noise, HEMT amplifier noise, and TLS noise) is below the photon noise of the background radiation from the atmosphere.

6.1 The signal chain and the noise propagation

In our submm MKID design, we have adopted the hybrid resonator architecture as discussed in Section 4.4, Section 5.6.1, and shown in Fig. 5.30.

For the purpose of a sensitivity analysis, the signal chain of the detector is illustrated in Fig. 6.1: the submm photon stream (with optical power p) breaks the Cooper pairs and generates quasiparticles (with density n_{qp}), which changes the impedance of the sensor strip Z_l and the microwave output signal V_2^- (the microwave voltage seen at the input port of the HEMT). We would like to derive the fluctuations in the output voltage δV_2^- when the sensor strip is under the optical loading p .

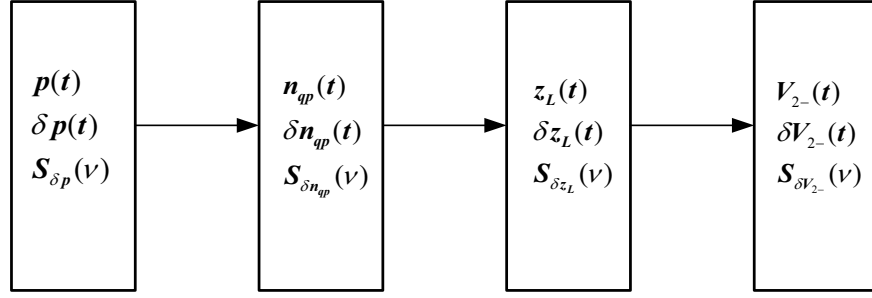


Figure 6.1: A diagram of the signal chain and noise propagation in a hybrid submm detector. p : optical power; Z_L : load impedance of the sensor strip n_{qp} : quasiparticle density; V_{2^-} : output microwave voltage seen at the input port of the HEMT

6.1.1 Quasiparticle density fluctuations δn_{qp} under an optical loading p

When the sensor strip is under optical loading, the total quasiparticle density n_{qp} is the sum of the thermal quasiparticle density n_{qp}^{th} (generated by thermal phonons) and the excess quasiparticle density n_{qp}^{ex} (generated by optical photons).

$$n_{qp} = n_{qp}^{th} + n_{qp}^{ex} \quad (6.1)$$

Three independent physical processes are involved in changing n_{qp} and must be modeled: thermal quasiparticle generation, excess quasiparticle generation, and quasiparticle recombination. We can write out the following rate equation,

$$\frac{dn_{qp}(t)}{dt} = [g^{th}(t) + g^{ex}(t) - r(t)] \quad (6.2)$$

where $g^{th}(t)$, $g^{ex}(t)$, and $r(t)$ are the rates for the 3 processes.

6.1.1.1 Quasiparticle recombination $r(t)$

The average quasiparticle recombination rate only depends on the total quasiparticle density n_{qp} and is calculated by[77]

$$\langle r(t) \rangle = r(n_{qp}) = Rn_{qp}^2. \quad (6.3)$$

With this definition, the quasiparticle lifetime is given by¹

$$\frac{1}{\tau_{qp}(n_{qp})} = 2Rn_{qp} \quad (6.4)$$

¹We usually express the quasiparticle lifetime as $\tau_{qp}^{-1} = \tau_0^{-1} + 2Rn_{qp}$, to account a finite lifetime τ_0 at low n_{qp} . In the regime that submm MKIDs operate, n_{qp} from the background loading is usually large enough so that the Rn_{qp} term will dominate over the τ_0^{-1} term. For this reason, we ignore the τ_0^{-1} term throughout the calculations in this chapter.

where R is the recombination constant.

We write

$$r(t) = \frac{2R(t)}{V} = \langle r(t) \rangle + \delta r(t) \quad (6.5)$$

where V is the volume of the sensor strip and $R(t)$ represents the recombination events in the volume V . $R(t)$ is often modeled by a Poisson point process[78] and it can be shown that the auto-correlation function of $\delta r(t)$ is a delta function

$$\langle \delta r(t) \delta r(t') \rangle = \frac{4}{V^2} \langle R(t) \rangle \delta(t - t') = \frac{2}{V} R n_{qp}^2 \delta(t - t') \quad (6.6)$$

and the power spectrum is white

$$S_{\delta r}(\tilde{f}) = \frac{2}{V} R n_{qp}^2. \quad (6.7)$$

6.1.1.2 Thermal quasiparticle generation $g^{th}(t)$

The average thermal generation rate only depends on the bath temperature T and is in balance with the thermal recombination rate when the system is in thermal equilibrium and without excess quasiparticles

$$\langle g^{th}(t) \rangle = g^{th}(T) = r(n_{qp}^{th}(T)) = R n_{qp}^{th}(T)^2 \quad (6.8)$$

where n_{qp}^{th} is the thermal quasiparticle density given by Eq. 2.93.

We write

$$g^{th}(t) = \frac{2G^{th}(t)}{V} = \langle g^{th}(t) \rangle + \delta g^{th}(t) \quad (6.9)$$

where $G^{th}(t)$ represents the thermal generation events, which is also modeled by a Poisson point process. The power spectrum of $\delta g^{th}(t)$ is

$$S_{\delta g^{th}}(\tilde{f}) = \frac{2}{V} R n_{qp}^{th}(T)^2. \quad (6.10)$$

6.1.1.3 Excess quasiparticle generation $g^{ex}(t)$ under optical loading

We assume that the number of excess quasiparticles generated by each detected submm photon is given by $\zeta(\nu, \Delta)$, which in general, depends both on the photon energy $h\nu$ and the gap energy Δ (binding energy of the Cooper pair). An empirical assumption about $\zeta(\nu, \Delta)$ often adopted for photon to quasiparticle conversion is that a fraction of $\eta_e \approx 60\%$ of the photon energy goes to the

quasiparticles,

$$\eta_e = \frac{\zeta \Delta}{h\nu} \quad (6.11)$$

Thus, the excess quasiparticle generation rate $g^{ex}(t)$ and the photon detection rate $G^{ph}(t)$ (number of photons detected per unit time) are related by

$$g^{ex}(t) = \frac{\zeta}{V} G^{ph}(t). \quad (6.12)$$

The statistical properties of $G^{ex}(t)$ can be found in photon counting theory. In addition, to simplify the discussion, we make the following assumptions:

1. The optical loading is from the black body radiation with mean photon occupation number $\bar{n}_{ph} = (e^{\frac{h\nu}{kT}} - 1)^{-1}$;
2. The photon numbers and their fluctuations of different modes are independent;
3. The detector has a narrow band of response ($\int d\nu \rightarrow \Delta\nu$);
4. The detector is single mode ($A\Omega = \lambda^2$, where A is the area of the detector and Ω is diffraction limited solid angle) and is only sensitive to one of the two polarizations;
5. The detector has a quantum efficiency of 1. (A reduced quantum efficiency η can be introduced with the substitution $\bar{n}_{ph} \rightarrow \eta\bar{n}_{ph}$.)

Under these assumptions, we can derive

$$\langle G^{ph}(t) \rangle = \Delta\nu \bar{n}_{ph} \quad (6.13)$$

$$p = \langle G^{ph}(t) \rangle h\nu = \Delta\nu \bar{n}_{ph} h\nu \quad (6.14)$$

$$\langle \delta G^{ph}(t) \delta G^{ph}(t') \rangle = \Delta\nu \bar{n}_{ph} (1 + \bar{n}_{ph}) \delta(t - t') \quad (6.15)$$

where p is the average optical power received by the detector. Therefore

$$\langle g^{ex}(t) \rangle = g^{ex}(p) = \frac{\zeta}{V} \Delta\nu \bar{n}_{ph} = \frac{\zeta p}{h\nu V} \quad (6.16)$$

$$S_{\delta g^{ex}}(\tilde{f}) = \left(\frac{\zeta}{V} \right)^2 \Delta\nu \bar{n}_{ph} (1 + \bar{n}_{ph}) = \left(\frac{\zeta}{V} \right)^2 \frac{p}{h\nu} \left(1 + \frac{p}{h\nu \Delta\nu} \right). \quad (6.17)$$

6.1.1.4 Steady state quasiparticle density \bar{n}_{qp}

The steady state quasiparticle density \bar{n}_{qp} can be derived by solving

$$\frac{dn_{qp}(t)}{dt} = 0 \quad (6.18)$$

which leads to a quadratic equation

$$R\bar{n}_{qp}^2 - Rn_{qp}^{th}(T)^2 - \frac{\zeta p}{h\nu V} = 0. \quad (6.19)$$

We usually operate at a low enough temperature so that the excess quasiparticle generation rate dominates over the thermal quasiparticle generation rate

$$g^{ex}(p) \gg g^{th}(T). \quad (6.20)$$

Under this condition, the thermal generation terms can be neglected and the steady-state equation reduces to,

$$R\bar{n}_{qp}^2 = \frac{\zeta p}{h\nu V} \quad (6.21)$$

and the positive root is

$$\bar{n}_{qp} = \sqrt{\frac{\zeta p}{h\nu RV}} \quad (6.22)$$

6.1.1.5 Fluctuations in quasiparticle density δn_{qp}

The fluctuations in the quasiparticle density $\delta n_{qp}(t) = n_{qp}(t) - \bar{n}_{qp}$ can be shown to satisfy the following equation,

$$\frac{d\delta n_{qp}(t)}{dt} = -2R\bar{n}_{qp}\delta n_{qp}(t) + [\delta g^{th}(t) + \delta g^{ex}(t) - \delta r(t)] \quad (6.23)$$

This allows us to calculate the power spectrum of δn_{qp} in the Fourier domain as,

$$S_{\delta n_{qp}}(\tilde{f}) = \frac{\tau_{qp}^2}{1 + (2\pi\tilde{f}\tau_{qp})^2} [S_{\delta g^{th}}(\tilde{f}) + S_{\delta g^{ex}}(\tilde{f}) + S_{\delta r}(\tilde{f})] = \frac{\tau_{qp}^2}{1 + (2\pi\tilde{f}\tau_{qp})^2} S_{gr}(\tilde{f}) \quad (6.24)$$

where $\tau_{qp} = \tau_{qp}(\bar{n}_{qp})$ and we have used the fact that the 3 processes are independent. Under the condition that the excess quasiparticle generation dominates over thermal generation,

$$\begin{aligned} S_{gr}(\tilde{f}) &\approx S_{\delta r}(\tilde{f}) + S_{\delta g^{ex}}(\tilde{f}) \\ &\approx \frac{2\zeta p}{h\nu V^2} + \left(\frac{\zeta}{V}\right)^2 \frac{p}{h\nu} \left(1 + \frac{p}{h\nu\Delta\nu}\right) \end{aligned} \quad (6.25)$$

where Eq. 6.14 and Eq. 6.21 have been applied. By applying Eq. 6.3 and Eq. 6.22 we can further derive the spectral density of the fractional quasiparticle density fluctuations,

$$S_{\frac{\delta n_{qp}}{\bar{n}_{qp}}}(\tilde{f}) = \frac{S_{\delta n_{qp}}(\tilde{f})}{\bar{n}_{qp}^2} = \frac{1/4}{1 + (2\pi\tilde{f}\tau_{qp})^2} \left[\frac{(2/\zeta + 1)h\nu}{p} + \frac{1}{\Delta\nu} \right]. \quad (6.26)$$

Note that the power spectra derived above are double-sided with $-\infty < \tilde{f} < \infty$.

6.2 Noise equivalent power (NEP)

Now we are ready to calculate NEP of our submm MKIDs limited by different noise sources.

Throughout the derivation that follows, we make the assumption that the noise frequency \tilde{f} of interest is small compared to both the resonator bandwidth $\tilde{f} \ll f_r/2Q_r$ and the recombination bandwidth $\tilde{f} \ll f_r/2\pi\tau_{qp}$.

We also assume that the maximum microwave power allowed to be dissipated in the sensor strip equals the submm optical power absorbed in the sensor strip times a fudge factor $\xi \geq 1^2$

$$P_t = \xi \eta_e p. \quad (6.27)$$

This ensures that the microwave readout power will not overwhelm the optical power in generating quasiparticles and so the quasi-particle population in the sensor strip is always dominated by the submm photon generated quasiparticles. For simplicity, we assume $\xi = 1$ in future derivations.

6.2.1 Background loading limited NEP

The directive of the logarithm of Eq. 6.21 yields a very simple and useful relationship

$$\frac{d\bar{n}_{qp}/\bar{n}_{qp}}{dp} = \frac{1}{2p}. \quad (6.28)$$

The background loading limited NEP can be calculated by

$$\text{NEP}^{\text{BLIP}}(\tilde{f}) = \sqrt{S_{\delta n_{qp}/n_{qp}}^{\text{BLIP}}(\tilde{f})} \left| \frac{d\bar{n}_{qp}/\bar{n}_{qp}}{dp} \right|^{-1} \quad (6.29)$$

$$\begin{aligned} &= \sqrt{\left(\frac{2}{\zeta} h\nu + h\nu + \frac{p}{\Delta\nu} \right) p} \\ &= \sqrt{\left(\frac{2\Delta}{\eta_e} + h\nu + \frac{p}{\Delta\nu} \right) p} \end{aligned} \quad (6.30)$$

where Eq. 6.26 and Eq. 6.11 have been used.

²In theory, the microwave frequency (< 10 GHz) is far below the gap frequency of Al (~ 90 GHz) and can not directly break Cooper pairs. However, in experiments we have observed both a shift in the resonance frequency and a decrease in the quality factor as the microwave power increases, which suggests that the microwave power (dissipated by the surface resistance) is able to increase the quasiparticle density in the superconductor through some unknown mechanism. Because part (perhaps most part) of this dissipated microwave power goes to the phonon bath, the fudge factor must be larger (perhaps much larger) than 1.

6.2.2 Detector NEP limited by the HEMT amplifier

The HEMT noise temperature T_n is equivalent to a voltage fluctuation δV_{2-} seen at the input port of the HEMT, with the noise power spectrum given by

$$S_{\delta V_{2-}}^{\text{HEMT}}(f + \tilde{f}) = kT_n Z_0 \quad (6.31)$$

which, after IQ demodulation, leads to a (isotropic) noise

$$S_{\text{IQ}}^{\text{HEMT}}(\tilde{f}) = kT_n Z_0 / 2 \quad (6.32)$$

in either the phase or amplitude quadrature of the IQ voltage output. In order to calculate NEP utilizing Eq. 6.28, we would like to convert the HEMT noise to an equivalent fluctuation in the quasiparticle density $\delta n_{qp}/n_{qp}$.

In Section 4.4, we have discussed the dynamic response of a hybrid resonator. According to Eq. 4.73 and 4.58, under the optimal condition (which maximizes the responsivity)

$$Q_c = Q_i \text{ and } f = f_r \quad (6.33)$$

the spectrum of the fluctuations in the microwave output voltage δV_2^- , due to fluctuations in quasiparticle density $\delta n_{qp}/n_{qp}$, is given by

$$\delta V_2^-(f + \tilde{f}) = V_1^+ \delta t_{21}(\tilde{f}) = \sqrt{\frac{Z_0 P_l}{4}} \frac{\delta n_{qp}(\tilde{f})}{n_{qp}} \left[1 + j \frac{\text{Im}(\kappa)}{\text{Re}(\kappa)} \right] \quad (6.34)$$

where P_l is the power dissipated in the sensor strip. After IQ demodulation, the voltage noise in the IQ output is³

$$S_{\text{IQ}}(\tilde{f}) = \frac{Z_0 P_l}{8} S_{\delta n_{qp}/n_{qp}} r_\kappa^2 \quad (6.35)$$

where $r_\kappa = \text{Re}(\kappa)/\text{Im}(\kappa)$ for phase readout and $r_\kappa = 1$ for amplitude readout. Therefore, the equivalent noise spectrum of the HEMT amplifier, in terms of quasi-particle fluctuations $\delta n_{qp}/n_{qp}$, is given by

$$S_{\delta n_{qp}/n_{qp}}^{\text{HEMT}}(\tilde{f}) = \frac{4kT_n}{P_l r_\kappa^2}. \quad (6.36)$$

With Eq. 6.28, 6.27, and 6.36, the HEMT limited NEP for both amplitude readout and phase

³Note that the noise power delivered to the load by δV_2 is $|\delta V_2|^2/2Z_0$ and a factor of 1/2 arises.

readout can be calculated by

$$\text{NEP}^{\text{HEMT}}(\tilde{f}) = \sqrt{S_{\delta n_{qp}/n_{qp}}^{\text{HEMT}}(\tilde{f})} \left| \frac{d\bar{n}_{qp}/\bar{n}_{qp}}{dp} \right|^{-1} \quad (6.37)$$

$$= \sqrt{\frac{16kT_n p}{\xi \eta_e r_\kappa^2}}. \quad (6.38)$$

6.2.3 Requirement for the HEMT noise temperature T_n in order to achieve BLIP detection

The condition for background limited detection is that the detector noise is dominated by the background photon noise but not the HEMT amplifier, or equivalently, the HEMT limited NEP should be below the BLIP NEP:

$$\text{NEP}^{\text{BLIP}} > \text{NEP}^{\text{HEMT}} \quad (6.39)$$

which leads to the following criteria,

$$\left(\frac{2\Delta}{\eta_e} + h\nu + \frac{p}{\Delta\nu} \right) p > \frac{16kT_n p}{\xi \eta_e r_\kappa^2}. \quad (6.40)$$

This imposes a requirement for the HEMT noise temperature,

$$T_n < \frac{\xi r_\kappa^2 (2\Delta + \eta_e h\nu + \eta_e p / \Delta\nu)}{16k}. \quad (6.41)$$

We assume that the optical loading is equivalent to a blackbody of temperature T_{load} in front of the telescope and the telescope has an optical efficiency of η_{opt} , so that the optical power the detector directly sees can be calculated from

$$p = \eta_{\text{opt}} k T_{\text{load}} \Delta\nu \quad (6.42)$$

which leads to

$$T_n < \frac{\xi r_\kappa^2}{16} (2\Delta/k + \eta_e h\nu/k + \eta_e \eta_{\text{opt}} T_{\text{load}}). \quad (6.43)$$

The required HEMT noise temperature T_n in order to achieve BLIP detection is calculated for the four mm/submm bands used in MKIDcam and are listed in Table 6.1. The appropriate effective loading temperatures T_{load} quoted for CSO, a photon to quasiparticle conversion factor of $\eta_e = 0.6$, a fudge factor of $\xi = 1$, an overall optical efficiency of $\eta_{\text{opt}} = 25\%$, and a ratio of 3 between the phase signal and the amplitude signal ($r_\kappa = 3$) are assumed in these calculations. For each

band, the detector sees an optical loading around 10 pW. Also listed in Table 6.1 are the BLIP NEP (NEP^{BLIP}), HEMT amplifier limited NEPs for the phase readout ($\text{NEP}_{\text{pha}}^{\text{HEMT}}$) and amplitude readout ($\text{NEP}_{\text{amp}}^{\text{HEMT}}$), where $T_n = 5 \text{ K}$ is assumed in these NEP calculations.

We find that the values of T_n^{amp} listed in Table 6.1 are all less than 5 K, while T_n^{pha} all greater than 5 K, the noise temperature of the HEMT currently in use. This means that the BLIP detection is not achieved in the amplitude readout; it would be achieved by using the phase readout, if there were no excess phase noise. However, the fudge factor we assumed in the calculation was very conservative $\xi = 1$. In reality, ξ could be much larger than 1 and the amplitude readout might have already been or very close to be background limited, using the hybrid resonator design under the optimal operation conditions.

Band	λ_0 [μm]	ν_0 ($\Delta\nu$) [GHz]	T_{load} [K]	T_n^{amp} [K]	T_n^{pha} [K]	NEP^{BLIP} [$10^{-17} \frac{\text{W}}{\sqrt{\text{Hz}}}$]	$\text{NEP}_{\text{amp}}^{\text{HEMT}}$ [$10^{-17} \frac{\text{W}}{\sqrt{\text{Hz}}}$]	$\text{NEP}_{\text{pha}}^{\text{HEMT}}$ [$10^{-17} \frac{\text{W}}{\sqrt{\text{Hz}}}$]	$\text{NEP}_{\text{pha}}^{\text{TLS}}$ [$10^{-16} \frac{\text{W}}{\sqrt{\text{Hz}}}$]
1	1300	230 (60)	50	1.2	10.6	6.7	13.8	4.6	4.6
2	1050	285 (50)	60	1.4	12.3	7.2	13.8	4.6	4.6
3	860	350 (30)	102.5	1.9	17.0	8.6	14.0	4.7	4.7
4	740	405 (20)	162.5	2.5	23.0	10.3	14.4	4.8	4.8

Table 6.1: Requirement for the HEMT noise temperature T_n in order to achieve BLIP detection calculated from Eq. 6.43. λ_0 : center wavelength; ν_0 : center frequency; $\Delta\nu$: bandwidth; T_{load} : effective loading temperature in front of the telescope; T_n^{amp} , T_n^{pha} : required HEMT noise temperature T_n for amplitude and phase readout; NEP^{BLIP} : background loading limited NEP; $\text{NEP}_{\text{amp}}^{\text{HEMT}}$, $\text{NEP}_{\text{pha}}^{\text{HEMT}}$: HEMT limited detector NEP for amplitude readout and phase readout, calculated using $T_n = 5 \text{ K}$ and a phase-to-amplitude signal ratio of $r_\kappa = 3$; $\text{NEP}_{\text{pha}}^{\text{TLS}}$: TLS limited detector NEP for phase readout. All NEPs are quoted at $\tilde{f} = 1 \text{ Hz}$ with \tilde{f} defined in $-\infty < \tilde{f} < \infty$.

In deriving the results in Table 6.1, we have made several assumptions. One of the important assumptions is that Q_i is set by the superconductor loss in the sensor strip. As long as this condition is satisfied, we find the BLIP criteria Eq. 6.43 does not depend on the detailed resonator design parameters, such as the film thickness, the resonator geometry, or the kinetic inductance fraction.

6.2.4 Detector NEP limited by the TLS noise

Because there is no excess noise in the amplitude direction, $\text{NEP}_{\text{amp}}^{\text{HEMT}}$ quoted in Table 6.1 are directly achievable when implementing the amplitude readout. For phase readout, however, the NEP will be greatly degraded due to the excess phase noise caused by the TLS.

To predict the TLS limited detector NEP, we need to estimate the frequency noise for our submm MKID. This can be done by scaling the measured noise according to Eq. H.6. The noise level of Nb on Si resonator at the internal power of -40 dBm shown in Fig. 5.6 is chosen as the noise standard, from which the noise will be scaled. According to Eq. H.6, the noise of different resonators should scale with a noise scaling factor $N_f = I_g^3 / (C_r^2 V_0 l_r)$. So the parameters C_r , l_r , V_0 , and I_g^3 are directly relevant to the noise scaling.

The detailed design parameters of a hybrid resonator used in the submm MKID array, as well as the relevant parameter of the Nb on Si resonator, are shown in Table 6.2. In this table Band 1 parameters are used in the calculations. Those parameters directly relevant to the noise scaling are marked with the stars. The values of I_3^g are evaluated using the conformal mapping solution as described in Section 3.1.2.3, assuming $\beta = 0.33$ (internal angles of $2\pi/3$).

From the evaluation of the noise factor N_f , we find the frequency noise of the hybrid resonator at its optimal operation power ($P_{\text{int}} = -46$ dBm) is larger than that of the Nb on Si resonator at the internal power of -40dBm by a factor of 4.2. The predicted frequency noise for the hybrid resonators are $2.1 \times 10^{-19}/\text{Hz}$ at 1kHz and $6.6 \times 10^{-18}/\text{Hz}$ at 1Hz, if a $1/\sqrt{\tilde{f}}$ spectral shape is assumed.

To calculate NEP, the following frequency responsivity factor is needed

$$\frac{\delta f_r/f_r}{\delta p} = \frac{\delta f_r/f_r}{\delta n_{qp}/n_{qp}} \frac{\delta n_{qp}/n_{qp}}{\delta p} = -\frac{r_\kappa}{2Q_i} \frac{1}{2p} \quad (6.44)$$

where the following formula, derived from Eq. 4.55 and 4.56, is applied:

$$\delta \frac{1}{Q_i} - 2j \frac{\delta f_r}{f_r} = \frac{1}{Q_i} \left[1 + j \frac{\text{Im}(\kappa)}{\text{Re}(\kappa)} \right] \frac{\delta n_{qp}}{n_{qp}}. \quad (6.45)$$

Finally, the TLS noise limited detector NEP for phase readout is given by

$$\text{NEP}_{\text{pha}}^{\text{TLS}} = \sqrt{S_{\delta f_r}(\tilde{f})/f_r^2} \left| \frac{\delta f_r/f_r}{\delta p} \right|^{-1} = \frac{4pQ_i}{r_\kappa} \sqrt{S_{\delta f_r}(\tilde{f})/f_r^2}. \quad (6.46)$$

The results of $\text{NEP}_{\text{pha}}^{\text{TLS}}$ are listed in Table 6.1 for all four bands and in Table 6.2 for Band 1. We can see that for phase readout, the TLS limited detector NEP is a factor of 10 higher than the HEMT limited NEP and is a factor of 5 – 7 higher than the BLIP NEP. Therefore, the BLIP detection is not achieved using the current design with the phase readout.

One way of achieving a better $\text{NEP}_{\text{pha}}^{\text{TLS}}$ is to make the film thinner. As the result of a thinner film, the kinetic inductance fraction α , the quasiparticle density n_{qp} , and the fractional frequency noise $S_{\delta f_r}/f_r^2$ will increase, while the internal Q_i , the internal power P_{int} , and the quasiparticle lifetime τ_{qp} will decrease. It can be shown that $S_{\delta f_r}/f_r^2$ increases as $\sqrt{1/Q_i}$ and $\text{NEP}_{\text{pha}}^{\text{TLS}}$ decreases at a fixed optical loading, according to Eq. 6.46. Currently we are also working on modifying the design to implement a interdigitated capacitor scheme, as discussed in Sec. 5.6.1.2, to reduce the TLS noise.

Parameter	Meaning	Nb/Si	hybrid	Reference
f_r [GHz]	resonance frequency	4	7.5	
s_r [μm]	center strip width	3	6	Fig. 4.4
g_r [μm]	gap width	2	2	Fig. 4.4
t [nm]	film thickness	200	60	
l_s [mm]	length of the sensor strip (Al)	-	1	Fig. 4.4
V [μm^3]	volume of the sensor strip (Al)	-	360	
$*l_r$ [mm]	total length of resonator	8.3	4.3	Eq. 4.29
$*C_r$ [pF/m]	capacitance per unit length	142	171	Sec. 3.1.2.3
L_r [H/m]	inductance per unit length	-	349	Sec. 3.1.2.3
Z_r [Ω]	characteristic impedance	-	45	Eq. 4.3
α^*	partial kinetic inductance fraction	-	0.2	Sec. 3.2.5
T_c [K]	transition temperature	-	1.35	
Δ_0 [meV]	superconducting gap	-	0.2	
T [K]	operation temperature	0.12	0.22	
κ [$10^{-7}\mu\text{m}^3$]	$\frac{\delta\sigma/ \sigma }{\delta n_{qp}}$	-	$1.19 + 3.35j$	Eq. 2.100
γ	a power index	-	-1	Eq. 2.80
p [pW]	detector optical loading	-	1.03	Eq. 6.42
R [$\mu\text{m}^{-3}\text{s}^{-1}$]	recombination constant	-	9.6	Ref. [77]
$n_{qp,0}$ [μm^{-3}]	steady-state quasiparticle density	-	7403	Eq. 6.22
τ_{qp} [μs]	quasiparticle recombination time	-	7	Eq. 6.4
Q_i	internal quality factor	-	12200	Eq. 4.55
Q_c	coupling quality factor	-	12200	Eq. 6.33
Q_r	resonator quality factor	-	6100	Eq. 4.35
$P_{\mu w}$ [dBm]	readout power	-	-79	Eq. 4.59
P_{int} [dBm]	internal power	-40	-46	Eq. H.4
$*V_0$ [mV]	voltage at open (coupler) end	6.5	3	Eq. H.4
$*I_q^3$ [$\text{V}^3\mu\text{m}^{-2}$]	contour integral on metal surface	1.35	1.95	Sec. 5.5.2.2
$*N_f = I_g^3/(C_r^2 V_0 l_r)$	noise scaling factor	1.24	5.2	Eq. H.6
$S_{\delta f_r}(1\text{kHz})/f_r^2$ [$10^{-19}/\text{Hz}$]	noise level at 1 kHz	0.5	2.1	Fig. 5.6
$S_{\delta f_r}(1\text{Hz})/f_r^2$ [$10^{-18}/\text{Hz}$]	noise level at 1 Hz ($1/\sqrt{f}$ shape)	1.6	6.6	Sec. 5.3.1
$\frac{\delta f_r/f_r}{\delta p}$ [1/W]	responsivity	-	5.6×10^6	Eq. 6.44
$\text{NEP}_{\text{pha}}^{\text{TLS}}$ [$10^{-16}\text{W}/\sqrt{\text{Hz}}$]	TLS limited NEP for phase readout	-	4.6	Eq. 6.46

Table 6.2: Design parameters and derived quantities involved in the calculation of TLS limited detector NEP

Appendix A

Several integrals encountered in the derivation of the Mattis-Bardeen kernel $K(q)$ and $K(\eta)$

A.1 Derivation of one-dimensional Mattis-Bardeen kernel $K(\eta)$ and $K(q)$

The Mattis-Bardeen non-local equation 2.11 is a vector equation in the general form of three-dimensional convolution

$$\vec{J}(\vec{r}) = \int \tilde{K}(\vec{R}) \cdot \vec{A}(\vec{r}') d\vec{r}' \quad (\text{A.1})$$

where

$$\tilde{K}(\vec{R}) = C \frac{\vec{R} \vec{R} I(\omega, R, T) e^{-R/l}}{R^4} \quad (\text{A.2})$$

$$\vec{R} = (x' - x)\hat{x} + (y' - y)\hat{y} + (z' - z)\hat{z}. \quad (\text{A.3})$$

$\tilde{K}(\vec{R})$ is a tensor and C is an unimportant constant. In the configuration of a plane wave polarized in the x direction incident onto the surface of a bulk superconductor in the $x - y$ plane as shown in Fig. 2.1, we need to derive the one-dimensional form of Eq. A.1. With

$$\vec{J} = J_x \hat{x}, \quad \vec{A} = A_x \hat{x} \quad (\text{A.4})$$

we can rewrite Eq. A.1 in Cartesian coordinates as

$$J_x(z) = \int \int \int C \frac{(\hat{x} \cdot \vec{R})^2 I(\omega, R, T) e^{-R/l}}{R^4} A_x(z') dx' dy' dz' \quad (\text{A.5})$$

$$= \int K(z' - z) A_x(z') dz' \quad (\text{A.6})$$

where

$$K(z' - z) = C \int \int \frac{(\hat{x} \cdot \vec{R})^2 I(\omega, R, T) e^{-R/l}}{R^4} dx' dy'. \quad (\text{A.7})$$

$$(\text{A.8})$$

Using the property that

$$f(z') = \int f(z'') \delta(z' - z'') dz'' \quad (\text{A.9})$$

we get

$$K(z' - z) = C \int \int \int \frac{(\hat{x} \cdot \vec{R}_1)^2 I(\omega, R_1, T) e^{-R_1/l}}{R_1^4} \delta(z' - z'') dx' dy' dz'' \quad (\text{A.10})$$

$$= C \int \frac{(\hat{x} \cdot \vec{R}_1)^2 I(\omega, R_1, T) e^{-R_1/l}}{R_1^4} \delta((z' - z) - (z'' - z)) d\vec{R}_1 \quad (\text{A.11})$$

$$\vec{R}_1 = (x' - x)\hat{x} + (y' - y)\hat{y} + (z'' - z)\hat{z}. \quad (\text{A.12})$$

This integral can be worked out in spherical coordinates

$$\begin{aligned} K(z' - z) &= C \int_0^\infty dR_1 \int_0^\pi \sin \theta d\theta \int_0^{2\pi} d\phi \sin^2 \theta \cos^2 \phi I(\omega, R_1, T) e^{-R_1/l} \delta(z' - z - R \cos \theta) \\ &= C\pi \int_0^\infty dR_1 \int_0^\pi d\theta \sin^3 \theta I(\omega, R_1, T) e^{-R_1/l} \delta(z' - z - R_1 \cos \theta) \\ &= C\pi \int_0^\infty dR_1 \int_{-1}^1 dt (1 - t^2) I(\omega, R_1, T) e^{-R_1/l} \delta(z' - z - R_1 t) \\ &= C\pi \int_{-1}^1 dt \frac{1 - t^2}{|t|} \int_0^\infty dR_1 I(\omega, R_1, T) e^{-R_1/l} \delta(R_1 - \frac{z' - z}{|t|}) \\ &= \begin{cases} C\pi \int_0^1 dt \frac{1 - t^2}{|t|} I(\omega, \frac{z' - z}{t}, T) e^{-\frac{z' - z}{|t|}} & z' - z > 0 \\ C\pi \int_{-1}^0 dt \frac{1 - t^2}{|t|} I(\omega, \frac{z' - z}{t}, T) e^{-\frac{z' - z}{|t|}} & z' - z < 0 \end{cases} \\ &= C\pi \int_0^1 dt \frac{1 - t^2}{t} I(\omega, \frac{|z' - z|}{t}, T) e^{-\frac{|z' - z|}{t}} \\ &= C\pi \int_1^\infty du \left(\frac{1}{u} - \frac{1}{u^3} \right) I(\omega, |z' - z| u, T) e^{-\frac{|z' - z| u}{t}}. \end{aligned} \quad (\text{A.13})$$

Finally, we have

$$K(\eta) = C\pi \int_1^\infty du \left(\frac{1}{u} - \frac{1}{u^3} \right) I(\omega, |\eta| u, T) e^{-|\eta| u/l} \quad (\text{A.14})$$

with $\eta = z' - z$.

The one-dimensional kernel in Fourier space $K(q)$ can be worked out by Fourier transform of Eq. A.14. Instead of working on the final result, we start from one of the intermediate results in Eq. A.13:

$$\begin{aligned} K(q) &= - \int_{-\infty}^\infty K(\eta) e^{jq\eta} d\eta \\ &= -C\pi \int_0^\infty dR_1 \int_{-1}^1 dt (1-t^2) I(\omega, R_1, T) e^{-R_1/l} \left\{ \int_{-\infty}^\infty \delta(\eta - R_1 t) e^{jq\eta} d\eta \right\} \\ &= -C\pi \int_0^\infty dR_1 \int_{-1}^1 dt (1-t^2) I(\omega, R_1, T) e^{-R_1/l} e^{jqR_1 t} \end{aligned} \quad (\text{A.15})$$

where the minus sign arises from the definition $J_x(q) = -K(q)A_x(q)$ in Eq. 2.15. The integral with respect to t can be easily carried out

$$\int_{-1}^1 (1-t^2) e^{jqR_1 t} dt = \frac{4}{(qR_1)^2} \left[\frac{\sin qR_1}{qR_1} - \cos(qR_1) \right]. \quad (\text{A.16})$$

Finally, we get

$$K(q) = -C\pi \int_0^\infty \left[\frac{\sin qR_1}{(qR_1)^3} - \frac{\cos qR_1}{(qR_1)^2} \right] I(\omega, R_1, T) e^{-R_1/l} dR_1. \quad (\text{A.17})$$

A.2 $R(a, b)$ and $S(a, b)$

We encounter the following two integrals in solving for $K(q)$:

$$\int_0^\infty e^{-bx} \left(\frac{\sin x}{x^3} - \frac{\cos x}{x^2} \right) \cos ax dx = R(a, b) \quad (\text{A.18})$$

$$\int_0^\infty e^{-bx} \left(\frac{\sin x}{x^3} - \frac{\cos x}{x^2} \right) \sin ax dx = S(a, b). \quad (\text{A.19})$$

They can be worked out by method of Laplace transform. Let $s = b - ia$ and

$$\begin{aligned} W(s) &= R(a, b) + iS(a, b) \\ &= \int_0^\infty \frac{1}{x^2} \left(\frac{\sin x}{x} - \cos x \right) e^{-(b-ia)x} dx \\ &= \int_0^\infty \left\{ \frac{1}{x^2} \left(\frac{\sin x}{x} - \cos x \right) \right\} e^{-sx} dx. \end{aligned} \quad (\text{A.20})$$

Now the problem becomes finding the Laplace transform of the term in the curly brackets. From the two tabulated Laplace transforms:

$$L(\sin x) = \frac{1}{1+s^2} \quad (\text{A.21})$$

$$L(\cos x) = \frac{s}{1+s^2} \quad (\text{A.22})$$

and by iteratively applying the property of Laplace transform:

$$L(f(x)) = \int_0^s L(f'(x))ds + f(0) \quad (\text{A.23})$$

$W(s)$ works out to be

$$W(s) = -\frac{s}{2} + \frac{s^2+1}{2} \arctan \frac{1}{s}. \quad (\text{A.24})$$

It follows that

$$\begin{aligned} R(a, b) &= \operatorname{Re}[W(b - ia)] \\ &= -\frac{b}{2} + \frac{ab}{4} \ln \left[\frac{b^2 + (1+a)^2}{b^2 + (1-a)^2} \right] + \frac{1}{4}(1+b^2-a^2)\{\arctan[\frac{2b}{b^2+a^2-1}] + n_x\pi\} \end{aligned} \quad (\text{A.25})$$

$$\begin{aligned} S(a, b) &= \operatorname{Im}[W(b - ia)] \\ &= \frac{a}{2} - \frac{ab}{2}\{\arctan[\frac{2b}{b^2+a^2-1}] + n_x\pi\} + \frac{1}{8}(1+b^2-a^2)\ln \left[\frac{b^2 + (1+a)^2}{b^2 + (1-a)^2} \right] \\ n_x &= 0 \text{ for } b^2 + a^2 - 1 \geq 0, \quad n_x = 1 \text{ for } b^2 + a^2 - 1 < 0. \end{aligned} \quad (\text{A.26})$$

In our numerical program, $R(a, b)$ and $S(a, b)$ are evaluated by Eq. A.25 and Eq. A.26.

A.3 $RR(a, b)$, $SS(a, b)$, $RRR(a, b, t)$, and $SSS(a, b, t)$

The following two integrals are encountered in solving for $K(\eta)$ in the thin film surface impedance calculation:

$$\int_1^\infty \left(\frac{1}{u} - \frac{1}{u^3} \right) e^{-au} \cos(bu) du = RR(a, b) \quad (\text{A.27})$$

$$\int_1^\infty \left(\frac{1}{u} - \frac{1}{u^3} \right) e^{-au} \sin(bu) du = SS(a, b). \quad (\text{A.28})$$

Let $s = a + jb$ and define

$$\begin{aligned} X(s) &= RR(a, b) - jSS(a, b) \\ &= \int_1^\infty \left(\frac{1}{u} - \frac{1}{u^3} \right) e^{-su} du. \end{aligned} \quad (\text{A.29})$$

The complex-valued integral of $X(s)$ can be worked out and the result is

$$X(s) = \frac{s-1}{2}e^{-s} - \frac{s^2-2}{2}E_1(s) \quad (\text{A.30})$$

where $E_1(s)$ is a special function called exponential integral. In our numerical program, $RR(a, b)$ and $SS(a, b)$ are evaluated from first evaluating $X(s)$ from Eq. A.29 and then taking the real and imaginary part. Separate expressions of the real and imaginary part are also available and given by Popel[40].

When solving for

$$K_{nn'}(\eta) = \frac{2}{t} \int_0^{\frac{t}{2}} K(\eta) d\eta \quad (\text{A.31})$$

two other integrals are encountered

$$\frac{2}{t} \int_0^{t/2} SS(a\eta, b\eta) d\eta = RRR(a, b, t) \quad (\text{A.32})$$

$$\frac{2}{t} \int_0^{t/2} SS(a\eta, b\eta) d\eta = SSS(a, b, t). \quad (\text{A.33})$$

With $s = a + jb$, we define

$$\begin{aligned} Y(s, t) &= RRR(a, b, t) - jSSS(a, b, t) \\ &= \frac{2}{t} \int_0^{t/2} \int_1^\infty \left(\frac{1}{u} - \frac{1}{u^3} \right) e^{-s\eta u} du d\eta. \end{aligned} \quad (\text{A.34})$$

The complex-valued integral $Y(s, t)$ works out to be

$$\begin{aligned} Y(s, t) &= \int_1^\infty \left(\frac{1}{u} - \frac{1}{u^3} \right) \frac{2(1 - e^{stu/2})}{stu} du \\ &= \frac{4}{3st} + \left(\frac{st}{12} - \frac{1}{6} - \frac{4}{3st} \right) e^{-st/2} + \left(1 - \frac{s^2 t^2}{24} \right) E_1(st/2). \end{aligned} \quad (\text{A.35})$$

In our numerical program, $RRR(a, b, t)$ and $SSS(a, b, t)$ are evaluated from first evaluating the complex $Y(s)$ from Eq. A.35 and then taking the real and imaginary parts of $Y(s)$. Separated expressions of the real and imaginary parts are also available and given by Popel.

Appendix B

Numerical tactics used in the calculation of surface impedance of bulk and thin-film superconductors

B.1 Dimensionless formula

The integrals of $K(q)$ in Eq. 2.19 and Eq. 2.20 are made dimensionless by redefining the following normalized variables:

$$\bar{\omega} = \frac{\hbar\omega}{\Delta}, \quad \bar{q} = \frac{\hbar v_0 q}{\Delta}, \quad \bar{b}_q = \frac{\hbar v_0}{\Delta l}, \quad \bar{b} = \frac{\bar{b}_q}{\bar{q}} \quad (\text{B.1})$$

$$\bar{\epsilon} = \frac{E}{\Delta}, \quad \bar{\Delta}_1 = \sqrt{|\bar{\epsilon}^2 - 1|}, \quad \bar{\Delta}_2 = \sqrt{|(\bar{\epsilon} + \bar{\omega})^2 - 1|} \quad (\text{B.2})$$

$$\bar{a}_1 = \frac{\bar{\Delta}_1}{\bar{q}}, \quad \bar{a}_2 = \frac{\bar{\Delta}_2}{\bar{q}}, \quad \bar{a}^+ = \bar{a}_1 + \bar{a}_2, \quad \bar{a}^- = \bar{a}_1 - \bar{a}_2 \quad (\text{B.3})$$

and $K(q)$ becomes

$$\begin{aligned} \text{Re}\{\lambda_{L0}^2 K(q)\} &= \frac{3}{\bar{q}} \times \\ &\left\{ \int_{\max\{1-\bar{\omega}, -1\}}^1 [1 - 2f(\bar{\epsilon} + \bar{\omega})] \left\{ \frac{\bar{\epsilon}(\bar{\epsilon} + \bar{\omega}) + 1}{\sqrt{1 - \bar{\epsilon}^2} \sqrt{(\bar{\epsilon} + \bar{\omega})^2 - 1}} R(\bar{a}_2, \bar{a}_1 + \bar{b}) + S(\bar{a}_2, \bar{a}_1 + \bar{b}) \right\} d\bar{\epsilon} \right. \\ &+ \frac{1}{2} \int_{1-\bar{\omega}}^{-1} [1 - 2f(\bar{\epsilon} + \bar{\omega})] \{[g(\bar{\epsilon}) + 1]S(\bar{a}^-, \bar{b}) - [g(\bar{\epsilon}) - 1]S(\bar{a}^+, \bar{b})\} d\bar{\epsilon} \\ &- \int_1^\infty [1 - f(\bar{\epsilon}) - f(\bar{\epsilon} + \bar{\omega})][g(\bar{\epsilon}) - 1]S(\bar{a}^+, \bar{b}) d\bar{\epsilon} \\ &\left. + \int_1^\infty [f(\bar{\epsilon}) - f(\bar{\epsilon} + \bar{\omega})][g(\bar{\epsilon}) + 1]S(\bar{a}^-, \bar{b}) d\bar{\epsilon} \right\} \end{aligned} \quad (\text{B.4})$$

(B.5)

$$\begin{aligned} \text{Im}\{\lambda_{L0}^2 K(q)\} &= \frac{3}{q} \times \\ &\left\{ -\frac{1}{2} \int_{1-\bar{\omega}}^{-1} [1 - 2f(\bar{\epsilon} + \bar{\omega})] \{[g(\bar{\epsilon}) + 1]R(\bar{a}^-, \bar{b}) + [g(\bar{\epsilon}) - 1]R(\bar{a}^+, \bar{b})\} d\bar{\epsilon} \right. \\ &+ \left. \int_1^\infty [f(\bar{\epsilon}) - f(\bar{\epsilon} + \bar{\omega})] \{[g(\bar{\epsilon}) + 1]R(\bar{a}^-, \bar{b}) + [g(\bar{\epsilon}) - 1]R(\bar{a}^+, \bar{b})\} d\bar{\epsilon} \right\}. \end{aligned} \quad (\text{B.6})$$

B.2 Singularity removal

The integrals in Eq. B.4 and Eq. B.6 involves finite and infinite integrals with singularity at lower or upper limit. They can be pre-removed by the following change of variables:

$$\begin{aligned} \int_a^b \frac{f(x)}{\sqrt{x-a}} dx &= 2 \int_0^{\sqrt{b-a}} f(y^2 + a) dy, \quad x = y^2 + a \\ \int_a^b \frac{f(x)}{\sqrt{x-b}} dx &= 2 \int_0^{\sqrt{b-a}} f(b - y^2) dy, \quad x = b - y^2 \\ \int_a^b \frac{f(x)}{\sqrt{x-a}\sqrt{x-b}} dx &= \int_a^{\frac{a+b}{2}} \frac{f(x)}{\sqrt{x-a}\sqrt{x-b}} dx + \int_{\frac{a+b}{2}}^b \frac{f(x)}{\sqrt{x-a}\sqrt{x-b}} dx \\ \int_{-a}^a \frac{f(x)}{\sqrt{x^2-a^2}} dx &= \int_{\pi/2}^{-\pi/2} f(\sin y) dy, \quad x = \sin y. \end{aligned} \quad (\text{B.7})$$

We also encounter a singularity in the integral of Eq. 2.36 at $Q = 0$. To remove it, we first split the integration interval of $[0, \infty]$ into $[0, 1]$ and $[1, \infty]$. Then the first integral can be rewritten as

$$\begin{aligned} &\int_0^1 \ln(1 + \frac{\lambda_{L0}^2 K(Q/\lambda_{L0})}{Q^2}) dQ \\ &= \int_0^1 \ln(Q^2 + \lambda_{L0}^2 K(Q/\lambda_{L0})) dQ - \int_0^1 \ln Q^2 dQ \\ &= \int_0^1 \ln(Q^2 + \lambda_{L0}^2 K(Q/\lambda_{L0})) dQ + 2 \end{aligned} \quad (\text{B.8})$$

which is no longer singular at $Q = 0$.

B.3 Evaluation of $K(\eta)$

It can be derived that the expression of $K(\eta)$ ($\eta > 0$) can be obtained from the expression of $K(q)$ with the following substitutions

$$\begin{aligned} 1/q &\rightarrow \eta \\ R(a, b) &\rightarrow RR(a, b) \\ S(a, b) &\rightarrow SS(a, b) \\ -\frac{qK(q)}{4} &\rightarrow K(\eta) \end{aligned} . \quad (\text{B.9})$$

Similarly, K_{nn} can be obtained from the expression of $K(q)$ with the following substitutions

$$\begin{aligned} 1/q &\rightarrow t/2 \\ R(a, b) &\rightarrow RRR(a, b, t) \\ S(a, b) &\rightarrow SSS(a, b, t) \\ -\frac{qK(q)}{4} &\rightarrow K_{nn} \end{aligned} . \quad (\text{B.10})$$

Thus the numerical integrals of $K(q)$ developed for the bulk case can be largely reused with slight modifications for the thin film case.

Appendix C

j_t/j_z in quasi-TEM mode

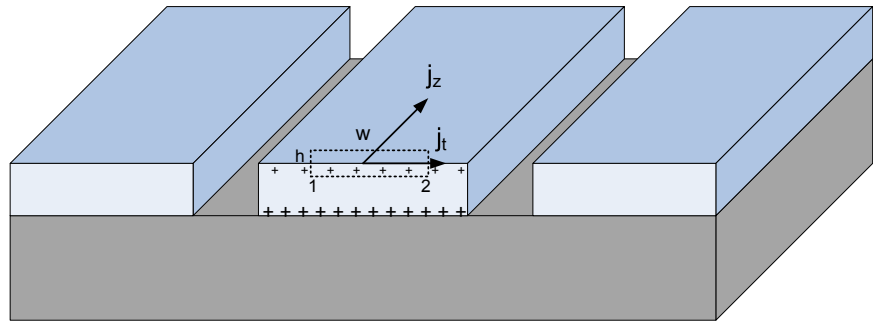


Figure C.1: Current and charge distribution on the surface of the center strip

The continuity equation of charge reads

$$\nabla \cdot \vec{J} + \frac{\partial \rho}{\partial t} = 0 \quad (\text{C.1})$$

which can be rewritten into the following form

$$\nabla_t \cdot \vec{j}_t = j\beta j_z - j\omega\rho. \quad (\text{C.2})$$

For a CPW in a homogenous media, a pure TEM mode exists. In this mode,

$$\beta j_z = \omega\rho \quad (\text{C.3})$$

$$j_t = 0 \quad (\text{C.4})$$

holds on every point on the conductor surface. From an integral of Eq. C.3 along an arbitrary contour enclosing the center conductor, we get

$$\beta I_z = \omega Q \quad (\text{C.5})$$

where Q is the total charge (per unit length) on the center strip. For a CPW with substrate-air inhomogeneity, Eq. C.5 still holds macroscopically. From the solution to the magnetostatic problem, I_z splits into equal halves on the bottom and top sides of the center strip and j_z is symmetric on the two sides. From the solution to the electrostatic problem, we have an unequal distribution of total charge Q , with $Q/(1 + \epsilon_r)$ and $Q\epsilon_r/(1 + \epsilon_r)$ on the top and bottom sides (see Fig. C.1). In this case, Eq. C.3 and C.4 no longer hold on every point and the magnitude of $\nabla_t \cdot \vec{j}_t$ may be on the same order of βj_z at some points:

$$\nabla_t \cdot \vec{j}_t \sim \beta j_z. \quad (\text{C.6})$$

Integrating Eq. C.6 in the rectangular area as shown in Fig. C.1 and applying the divergence theorem, we find

$$\begin{aligned} (j_t^2 - j_t^1)h &\sim \beta j_z wh \\ j_t &\sim j_t^2 - j_t^1 \sim \beta j_z w \end{aligned} \quad (\text{C.7})$$

which leads to

$$\frac{j_t}{j_z} \sim \frac{w}{\lambda}. \quad (\text{C.8})$$

The result in Eq. C.8 can be understood by looking at the charge redistribution: j_z redistributes the charges along the propagation direction (z direction) and j_t redistributes the charges within the cross-sectional plane; in a cycle, j_z effectively moves the charges by the distance of a wavelength λ while j_t moves the charges by a distance no greater than the transverse dimension w . Therefore, the ratio of j_z to j_t is on the order of the ratio of the wavelength to the transverse dimension of the transmission line.

Appendix D

Solution of the conformal mapping parameters in the case of $t \ll a$

We first write u_1, u'_1, u_2, u'_2 as

$$u_1 = a + \delta_1 \quad (\text{D.1})$$

$$u_2 = b + \delta_2 \quad (\text{D.2})$$

$$u'_1 = u_1 - d_1 \quad (\text{D.3})$$

$$u'_2 = u_2 + d_2. \quad (\text{D.4})$$

δ_1, δ_2, d_1 and d_2 all go to zero as t goes to zero. To solve the integral equations in Eq. 3.22–3.25, we rewrite the integrand $G(u)$ as

$$G(w) = \sqrt{\left| \frac{w - u'_1}{w - u_1} \cdot \frac{w + u'_1}{w + u_1} \cdot \frac{w - u'_2}{w - u_2} \cdot \frac{w + u'_2}{w + u_2} \right|} \quad (\text{D.5})$$

which is the square-root of a product of 4 fractions. Because $u_1 \approx u'_1$ and $u_2 \approx u'_2$, the pair of zero and pole in each fraction are very close to each other. Whenever the pair of zero and pole are far away from the integration interval, we replace the fraction with its first-order Taylor expansion, e.g.,

$$\sqrt{\frac{w - u'_1}{w - u_1}} \approx 1 - \frac{d_1}{2(w - u_1)}. \quad (\text{D.6})$$

Eq. 3.23 can be approximately worked out

$$\begin{aligned}
t &= \int_{u'_1}^{u_1} G(w') dw' \\
&\approx \int_{u'_1}^{u_1} \sqrt{\frac{w' - u'_1}{u_1 - w'}} dw' + o(t) \\
&= \frac{\pi d_1}{2}.
\end{aligned} \tag{D.7}$$

In the same way Eq. 3.25 yields $t = \pi d_2/2$. Therefore

$$d_1 = d_2 = d = \frac{2t}{\pi}. \tag{D.8}$$

Eq. 3.22 and Eq. 3.24 can be worked out with a few more steps

$$\begin{aligned}
a &\approx \int_0^{u'_1} \sqrt{\frac{u'_1 - w'}{u_1 - w'}} \left[1 - \frac{d}{2(w' + u_1)} + \frac{d}{2(w' - u_2)} + \frac{d}{2(w' + u_2)} \right] dw' \\
&\approx \int_0^{u'_1} \sqrt{\frac{u'_1 - w'}{u_1 - w'}} + \frac{d}{2} \int_0^{u'_1} \left(-\frac{1}{w' + u_1} + \frac{1}{w' - u_2} + \frac{1}{w' + u_2} \right) dw' \\
&= \left(\sqrt{u_1(u_1 - d)} + d \log \frac{\sqrt{d}}{\sqrt{u_1} + \sqrt{u_1 - d}} \right) + \frac{d}{2} \left(-\log 2 + \log \frac{u_1 + u_2}{u_2} + \log \frac{u_2}{u_2 - u_1} \right) \\
&= u_1 - \frac{d}{2} - \frac{3 \log 2}{2} + \frac{d}{2} \log \frac{d}{a} + \frac{d}{2} \log \frac{a+b}{b-a} \\
b - a &\approx \int_{u_1}^{u_2} \sqrt{\frac{w' - u'_1}{w' - u_1} \frac{u'_2 - w'}{u_2 - w'}} \left[1 - \frac{d}{2(w' + u_1)} + \frac{d}{2(w' + u_2)} \right] dw' \\
&\approx \int_{u_1}^{u_2} \sqrt{\frac{w' - u'_1}{w' - u_1} \frac{u'_2 - w'}{u_2 - w'}} + \int_{u_1}^{u_2} \frac{d}{2} \left[-\frac{1}{w' + u_1} + \frac{1}{w' + u_2} \right] dw' \\
&\approx \left(u_2 - u_1 + d - \log \frac{d}{4(u_2 - u_1)} \right) + \frac{d}{2} \left(-\log \frac{u_1 + u_2}{2u_1} + \log \frac{2u_2}{u_1 + u_2} \right) \\
&= \left(u_2 - u_1 + d - \log \frac{d}{4(b-a)} \right) + \frac{d}{2} \left(-\log \frac{a+b}{2a} + \log \frac{2b}{a+b} \right).
\end{aligned} \tag{D.9}$$

The sum of the two equations gives

$$b = u_2 + \frac{d}{2} + \frac{3 \log 2}{2} - \frac{d}{2} \log \frac{d}{b} + \frac{d}{2} \log \frac{b-a}{a+b}. \tag{D.10}$$

Therefore

$$\begin{aligned}
\delta_1 &= \frac{d}{2} + \frac{3 \log 2}{2} d - \frac{d}{2} \log \frac{d}{a} + \frac{d}{2} \log \frac{b-a}{a+b} \\
\delta_2 &= \frac{d}{2} + \frac{3 \log 2}{2} d - \frac{d}{2} \log \frac{d}{b} + \frac{d}{2} \log \frac{b-a}{a+b}
\end{aligned} \tag{D.11}$$

and Eq. 3.27 is derived.

Appendix E

Fitting the resonance parameters from the complex t_{21} data

In this appendix, we discuss how to determine the resonance parameters f_r , Q_r , and Q_c by fitting to the measured complex t_{21} data from the network analyzer.

E.1 The fitting model

The total transmission t_{21} through the device, amplifiers, and cables measured by the network analyzer, can be written as

$$t_{21}(f) = ae^{-2\pi j f \tau} \left[1 - \frac{Q_r/Q_c e^{j\phi_0}}{1 + 2jQ(\frac{f-f_r}{f_r})} \right]. \quad (\text{E.1})$$

Eq. E.1 is our fitting model which contains seven parameters: $\arg[a], |a|$, τ , f_r , Q_r , Q_c , and ϕ_0 . Here a is a complex constant accounting for the gain and phase shift through the system. The constant τ accounts for the cable delay related with the path length of the cables. The other parameters have been introduced in Chapter 4.

E.2 The fitting procedures

Although it is possible to use Eq. E.1 and directly fit for all the 7 parameters simultaneously, such a nonlinear multi-parameter fitting problem is non-robust and extremely sensitive to the initial values. For this reason, we usually break down the 7-parameter fitting problem into several independent fitting problems, each only containing one or two parameters. The fitting results obtained from this step-by-step method are usually quite good. If further accuracy is needed or the statistics of the fitting results are required, we will finally run a 7-parameter refined fitting, using the results obtained from the step-by-step method as initial values.

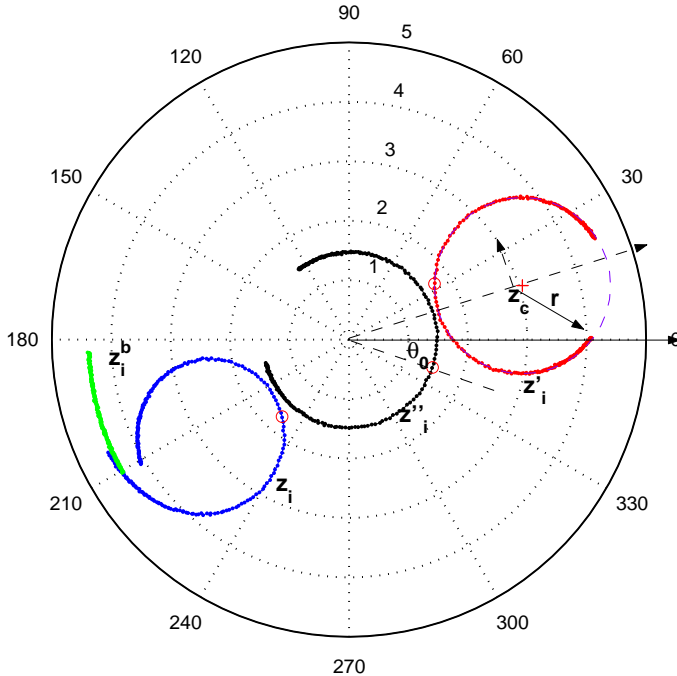


Figure E.1: Fitting the resonance circle step by step in the complex plain. The data in this plot is from a Al on Si resonator.

E.2.1 Step 1: Removing the cable delay term

Let $\{(f_i, z_i)\}$ be the set of transmission data we would like to fit, which is measured by a network analyzer at a low temperature (usually between 50 mK and 200 mK for Al devices).

The cable delay time τ can be measured directly using the network analyzer's "electronic delay" function. At off-resonance frequencies the t_{21} data reflects the pure cable term $e^{2\pi j f \tau}$, which is usually a circle or an arc centered at the origin. When the electronic delay τ is set to an optimal value, these circles (arcs) should shrink to a blob of minimal size. For example, in our current setup τ is usually around 30 ns, which depends on the length of the coaxial cables in use. Another way to remove the cable effect is to normalize the low temperature transmission data z by the transmission data z_b measured at a much higher temperature (above $T_c/2$). At this high temperature, the superconductor loss becomes so large that almost all the resonances have died out, leaving only the trace of the cable delay term (see the green curve in Fig. E.1).

After this step, with the cable delay term removed, the new data z' should now appear as a circle (see the red curve in Fig. E.1).

E.2.2 Step 2: Circle fit

In this step, we will determine the center $z_c = x_c + jy_c$ and the radius r of the circle z' resulted from the previous step. For this circle fitting problem, we use the method described by Chernov

and Lesort[79]. In this method, the objective function to be minimized is

$$\mathcal{F}(x_c, y_c, r) = \sum_{i=1}^n [Aw_i'^2 + Bx_i' + Cy_i' + D]^2 \quad (\text{E.2})$$

which is subject to the constraint $B^2 + C^2 - 4AD = 1$. Here $w_i'^2 = x_i'^2 + y_i'^2$. In matrix form, $\mathcal{F} = \mathbf{A}^T \mathbf{M} \mathbf{A}$ and the constraint is $\mathbf{A}^T \mathbf{B} \mathbf{A} = 1$, where

$$\mathbf{A} = (A, B, C, D)^T$$

$$\mathbf{M} = \begin{pmatrix} M_{ww} & M_{xw} & M_{yw} & M_w \\ M_{xw} & M_{xx} & M_{xy} & M_x \\ M_{yw} & M_{xy} & M_{yy} & M_y \\ M_w & M_x & M_y & n \end{pmatrix} \quad (\text{E.3})$$

$$\mathbf{B} = \begin{pmatrix} 0 & 0 & 0 & -2 \\ 0 & 1 & 0 & 0 \\ 0 & 0 & 1 & 0 \\ -2 & 0 & 0 & 0 \end{pmatrix} \quad (\text{E.4})$$

(E.5)

where M_{ij} are the moments of the data. For example, $M_{xw} = \sum_{i=1}^n x_i w_i$ and $M_x = \sum_{i=1}^n x_i$.

This is a constrained nonlinear minimization problem which can be solved by the standard Lagrange multiplier method. With the introduction of a Lagrange multiplier η we minimize the function

$$\mathcal{F}_* = \mathbf{A}^T \mathbf{M} \mathbf{A} - \eta(\mathbf{A}^T \mathbf{B} \mathbf{A} - 1) \quad (\text{E.6})$$

Differentiating with respect to \mathbf{A} leads to the linear equation

$$\mathbf{M} \mathbf{A} - \eta \mathbf{B} \mathbf{A} = 0 \quad (\text{E.7})$$

η can be solved from the equation

$$\det(\mathbf{M} - \eta \mathbf{B}) = 0 \quad (\text{E.8})$$

$Q(\eta) = \det(\mathbf{M} - \eta \mathbf{B}) = 0$ is a polynomial equation of 4-th degree. It can be shown that $Q(\eta) = 0$ has 3 positive roots and the smallest one minimizes \mathcal{F}_* . Thus η can be efficiently found by a numerical root searching algorithm with start value of $\eta = 0$. Once η is determined, other parameters $A, B, C,$

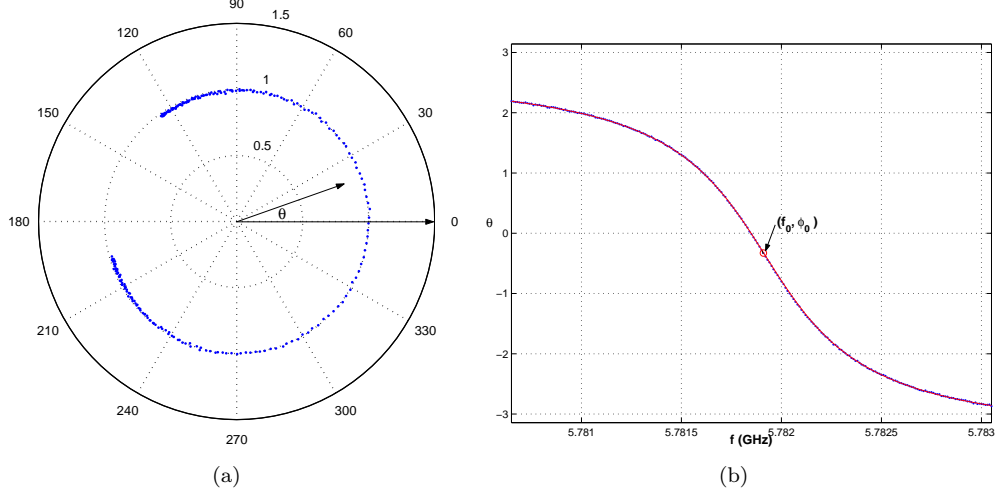


Figure E.2: Fitting the phase of z_i'' (a) Z'' (b) $\theta_i(f)$ (blue) and its fit (red)

D can be obtained from Eq. E.7 and the circle parameters are given by

$$\begin{aligned} x_c &= -\frac{B}{2A} \\ y_c &= -\frac{C}{2A} \\ r &= \frac{1}{4A^2} \end{aligned} \quad (\text{E.9})$$

The purple dashed curve in Fig. E.1 shows the result from this circle fitting procedure.

E.2.3 Step 3: Rotating and translating to the origin

In this step, we translate the circle to the origin and align it along real axis by the following transformation:

$$z_i'' = (z_c - z_i') \exp(-j\alpha) \quad (\text{E.10})$$

where z_c and $\alpha = \arg(z_c)$ are the results from circle fitting. This is equivalent to setting up a new coordinate system at the center of the circle as shown in Fig. E.1.

E.2.4 Step 4: Phase angle fit

In this step, the phase angle θ of z_i'' as a function of f is fit to the following profile:

$$\theta = -\theta_0 + 2 \tan^{-1} [2Q_r(1 - \frac{f}{f_r})] \quad (\text{E.11})$$

where $\theta_i = \arg(z''_i)$. We use Matlab curve fitting toolbox to carry out a robust non-linear minimization:

$$\min \left\{ \sum_{i=1}^n \left| \theta_i + \theta_0 - 2 \tan^{-1} [2Q_r(1 - \frac{f_i}{f_r})] \right|^2 \right\}. \quad (\text{E.12})$$

f_r , Q_r , and θ_0 are determined from the fit. The phase angle data and fit are shown in Fig. E.2(b).

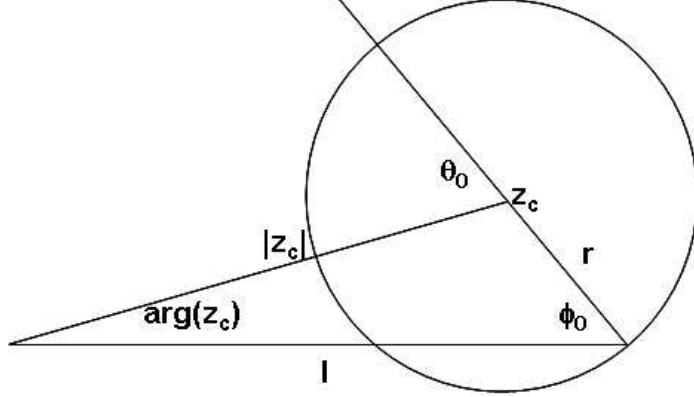


Figure E.3: Geometric relationships used to determine Q_c and ϕ_0

E.2.5 Step 5: Retrieving other parameters

The parameters Q_c and ϕ_0 can be found from the geometric relationships illustrated in Fig. E.3. According to Eq. 4.40, Q_c is

$$Q_c = \frac{|z_c| + r}{2r} Q_r. \quad (\text{E.13})$$

And ϕ_0 is related to θ_0 by

$$\phi_0 = \theta_0 - \arg(z_c). \quad (\text{E.14})$$

E.3 Fine-tuning the fitting parameters

The parameters obtained from the step-by-step fitting procedures can be used as the initial values to run a refined multi-parameter non-linear fitting. This time we fit z_i directly to Eq. (E.1). We use Matlab curve fitting toolbox to do a robust non-linear least-squared fitting. One of the advantages of using the curve fitting toolbox is that the confidence interval for each parameter is automatically reported by the toolbox. To evaluate and compare the goodness of the fits, we calculate the reduced χ^2 by

$$\chi^2 = \frac{1}{n-7} \frac{\sum_{i=1}^n |z_i - z_{\text{fit}}|^2}{\sigma_z^2}. \quad (\text{E.15})$$

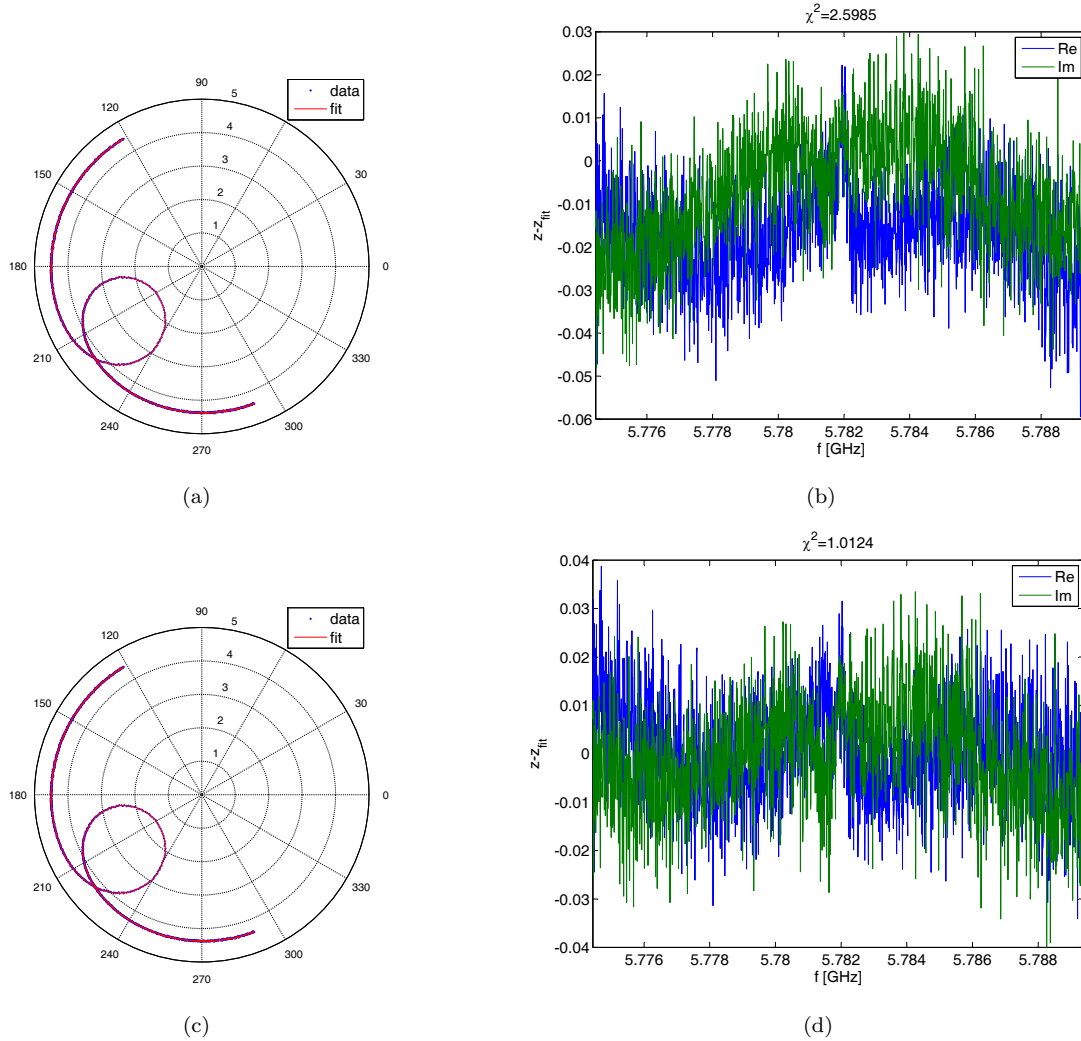


Figure E.4: Refining the fitting result from the step-by-step fitting procedures. The result from the step-by-step fitting procedures is plotted in (a) and (b), while the result from the refined fitting procedure is plotted in (c) and (d). Data z (blue) and its fit z_{fit} (red) are plotted in (a) and (c). Real (blue) and imaginary (green) part of the residues ($z_{\text{fit}} - z$) are plotted in (b) and (d).

where $n - 7$ is the degree of freedom in the fitting problem. σ_z^2 is estimated from the mean square distance between two adjacent data points of the first m data points

$$\sigma_z^2 = \frac{\sum_{i=1}^m |z_i - z_{i+1}|^2}{2m} \quad (\text{E.16})$$

This method of estimating σ_z^2 works quite well because the first m data points are usually at off resonance frequencies with the Gaussian-distributed noise from the measurement system.

As shown in Fig. E.4, both the initial fit and the refined fit usually have small χ^2 . The refined fit yields a χ^2 close to 1, which means the fitting model Eq. E.1 is a good model.

E.4 Fitting $|t_{21}|^2$ to the skewed Lorentzian profile

Resonance parameters can also be found by fitting the $|t_{21}|^2$ data to the following skewed Lorentzian model

$$|t_{21}(f)|^2 = A_1 + A_2(f - f_r) + \frac{A_3 + A_4(f - f_r)}{1 + 4Q_r^2 \left(\frac{f - f_r}{f_r} \right)^2}. \quad (\text{E.17})$$

The fitting result is shown in Fig. E.5. For the data set used throughout this appendix, we find that the result of f_r from this skewed Lorentzian fit agrees with the previous fitting method within 10^{-7} and Q within 0.1%.

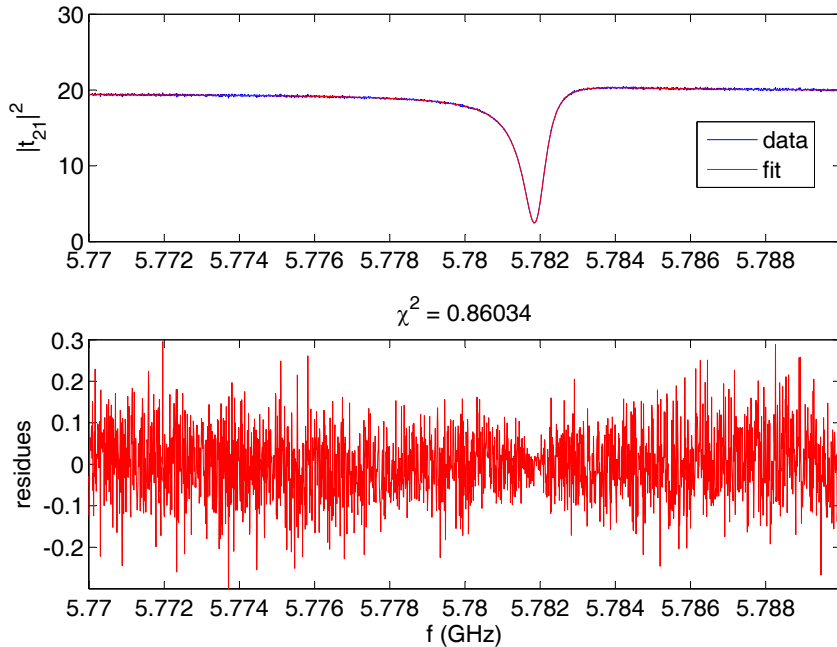


Figure E.5: Fitting $|t_{21}|$ to skewed Lorentzian model

Appendix F

Calibration of IQ-mixer and data correction

Assume that the LO port of the IQ mixer is fed with a microwave signal of complex amplitude $A_{\text{LO}} = 1$ and the RF port with $A_{\text{RF}} = re^{i\theta}$. The output voltages can be written as

$$I = I_0 + A_I \cos \theta \quad (\text{F.1})$$

$$Q = Q_0 + A_Q \cos(\theta + \gamma). \quad (\text{F.2})$$

Here γ is the phase difference between the I and Q channels. I_0, Q_0 account for the DC offset and A_I, A_Q account for the unbalanced gains in the two channels. For an ideal IQ-mixer, $\gamma = -\pi/2$, $I_0 = Q_0 = 0$, $A_I = A_Q = A$, and as θ goes from 0 to 2π , the IQ output traces out a circle centered at the origin in the IQ plane. For a nonideal IQ-mixer, the output traces out an ellipse which is off the origin, as shown in Fig. F.1. Easy to see that the center of the ellipse is at (I_0, Q_0) . It can be shown that the other 3 mixer parameters A_I, A_Q , and γ are related to the half long axis a , half short axes b , and the orientation angle Φ by

$$\begin{aligned} A_I &= \sqrt{a^2 \cos^2 \Phi + b^2 \sin^2 \Phi} \\ A_Q &= \sqrt{a^2 \sin^2 \Phi + b^2 \cos^2 \Phi} \\ \gamma &= \alpha_1 - \alpha_2 \\ \alpha_1 &= \arctan \frac{b \sin \Phi}{a \cos \Phi} \\ \alpha_2 &= \pi - \arctan \frac{b \cos \Phi}{a \sin \Phi}. \end{aligned} \quad (\text{F.3})$$

These relationships are illustrated in Fig. F.2 by two triangles.

According to Eq. F.3, the 3 parameters A_I, A_Q , and γ , which characterize a non-ideal IQ mixer, can be fully determined from the IQ ellipses. This provides us a way to experimentally measure these parameters. One can use a phase shifter to produce a θ sweep and obtain the IQ ellipse.

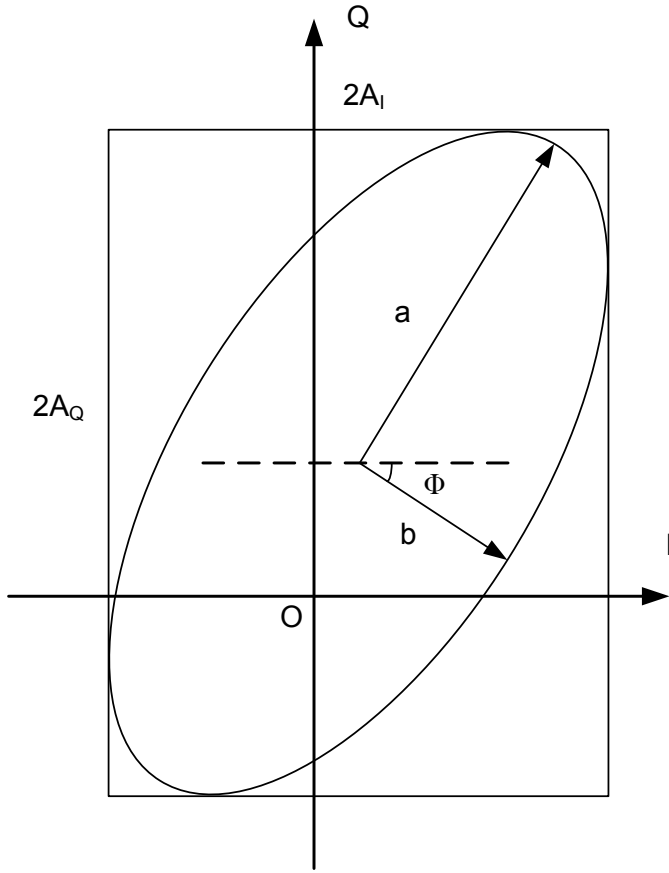


Figure F.1: IQ mixer output tracing out an ellipse

Unfortunately, we do not have a programmable phase shifter. Instead, we obtain the IQ ellipse by beating two synthesizers. The output frequencies of the two synthesizers are set to be 1 kHz apart and the IQ ellipses are digitized at a sample rate of 2 kHz for 1 second (two circles are recorded). The data is then fit to a ellipse by standard routines to give a , b , and Φ .

The IQ ellipses measured at a number of frequencies and RF input powers by beating two synthesizers are plotted in Fig. F.3. The ratio of A_I/A_Q and γ are indicated in these plots. As expected, the A_I/A_Q is close to but not exactly 1. γ varies between -85° and -113° at frequencies between 2 GHz and 10 GHz. The ellipses under different RF input powers at the same frequency are concentric and the long and short axes scale linearly with RF amplitude. From these ellipses, we obtain A_I , A_Q , and γ at discrete frequencies and powers from Eq. F.3. These values are then interpolated at arbitrary frequency and power in the measurement range to generate the continuous functions $A_I(f, P_{RF})$, $A_Q(f, P_{RF})$, and $\gamma(f, P_{RF})$. Using these functions, the amplitude and phase

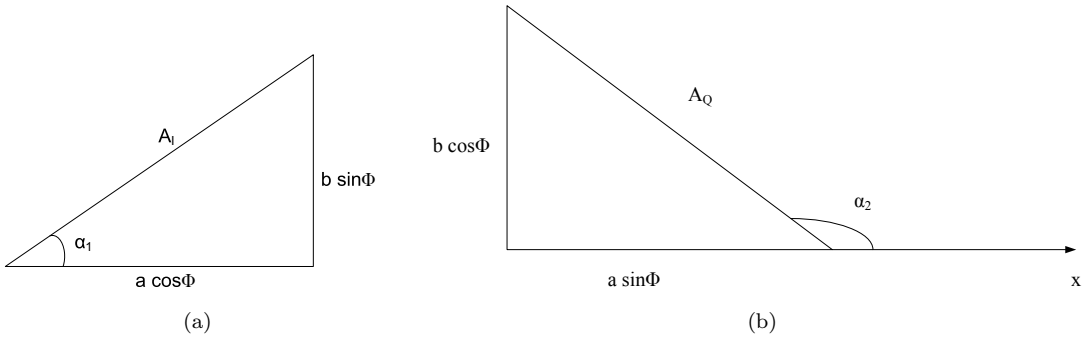


Figure F.2: Relationships between A_I , A_Q , γ and a, b, Φ illustrated in two triangles

of the original RF input microwave signal can be recovered by

$$\begin{aligned} g &= \frac{\cos(\theta + \gamma)}{\cos \theta} = \frac{A_I Q}{A_Q I} \\ \theta &= \begin{cases} \arctan \frac{\cos \gamma - g}{\sin \gamma} & (I > 0) \\ \arctan \frac{\cos \gamma - g}{\sin \gamma} + \pi & (I < 0) \end{cases} \\ r &= \begin{cases} \frac{I}{A_I \cos \theta} & (\text{if } \cos \theta \neq 0) \\ \frac{Q}{A_Q \cos(\theta + \gamma)} & (\text{if } \cos \theta = 0) \end{cases} . \end{aligned} \quad (\text{F.4})$$

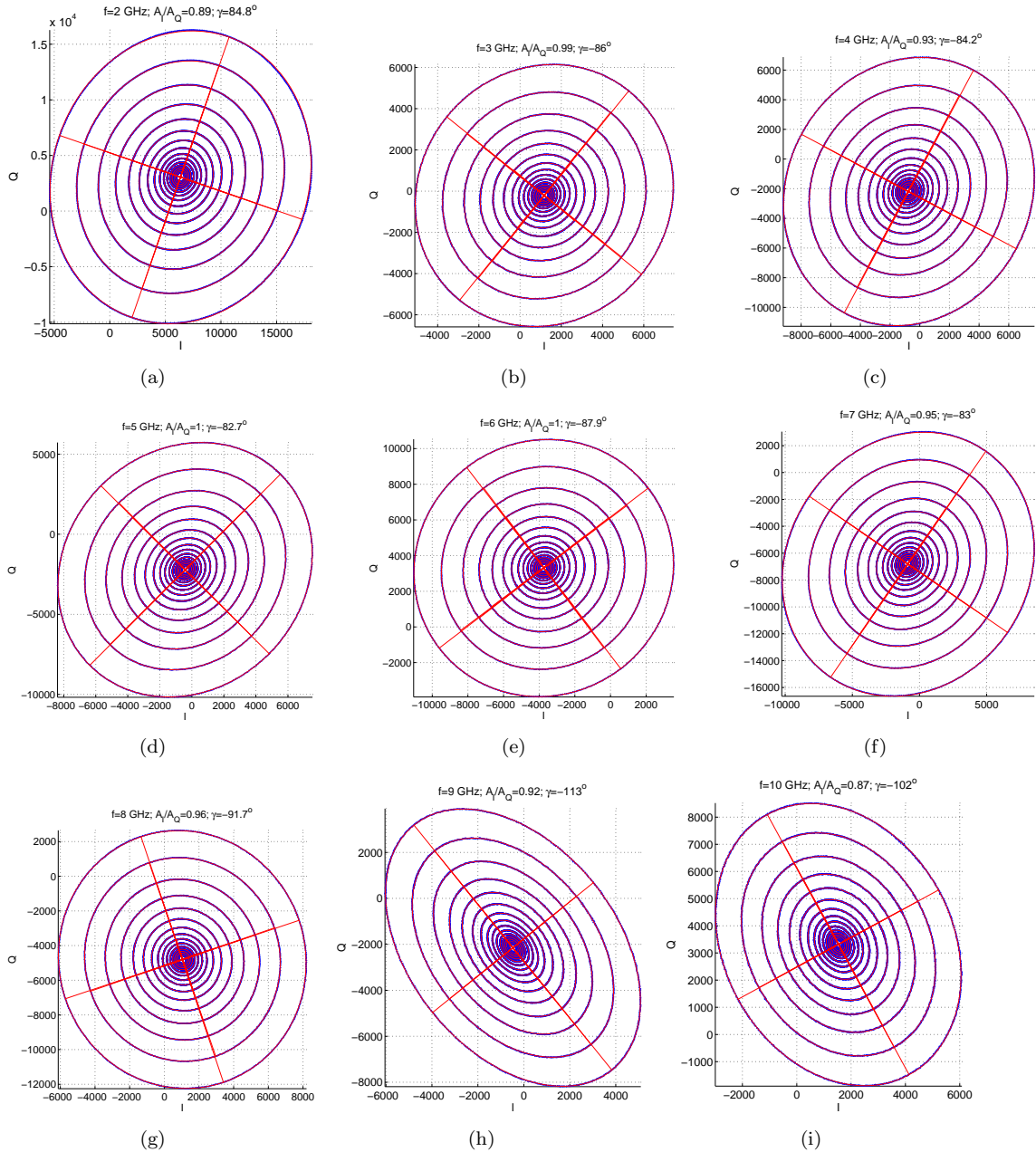


Figure F.3: IQ ellipses from beating two synthesizers. Data and fits are plotted in blue and red, respectively. Ellipses for each frequency are measured with LO power of 13 dBm and RF power in steps of 2 dBm.

Appendix G

Several integrals encountered in the calculation of $\epsilon_{\text{TLS}}(\omega)$

G.1 Integrating $\vec{\chi}_{\text{res}}(\omega)$ over TLS parameter space

Here we evaluate the integral of Eq. 5.55. Let

$$\chi(\omega_\varepsilon, \omega) = \frac{1}{\hbar(\omega_\varepsilon - \omega + jT_2^{-1})} + \frac{1}{\hbar(\omega_\varepsilon + \omega - jT_2^{-1})}. \quad (\text{G.1})$$

The full integral reads

$$\begin{aligned} \epsilon_{\text{TLS}}(\omega) &= \iint \left[\hat{e} \cdot \vec{\chi}_{\text{res}}(\omega) \cdot \hat{e} \right] \frac{P}{\Delta_0} d\Delta_0 d\Delta d\hat{d} \\ &= \int_0^{\Delta_{\max}} d\Delta \int_{\Delta_{0,\min}}^{\Delta_{0,\max}} \frac{P}{\Delta_0} d\Delta_0 \int_0^{\frac{\pi}{2}} \sin \theta d\theta \\ &\times \left\{ \left(\frac{\Delta_0}{\varepsilon} \right)^2 d_0^2 \cos^2 \theta \tanh \left(\frac{\varepsilon}{2kT} \right) \left[\frac{1 + (\omega_\varepsilon - \omega)^2 T_2^2}{1 + \Omega^2 T_1 T_2 + (\omega_\varepsilon - \omega)^2 T_2^2} \right] \chi(\omega_\varepsilon, \omega) \right\}. \end{aligned} \quad (\text{G.2})$$

Let $u = \Delta_0/\varepsilon$. By applying the following change of variables

$$\int_0^{\Delta_{\max}} \int_{\Delta_{0,\min}}^{\Delta_{0,\max}} \frac{P}{\Delta_0} d\Delta_0 d\Delta \longrightarrow \int_0^{\varepsilon_{\max}} \int_{u_{\min}}^1 \frac{P}{u \sqrt{1-u^2}} du d\varepsilon \quad (\text{G.3})$$

the integral reduces to

$$\begin{aligned} \epsilon_{\text{TLS}}(\omega) &= P d_0^2 \int_0^{\varepsilon_{\max}} d\varepsilon \int_{u_{\min}}^1 \frac{u}{\sqrt{1-u^2}} du \int_0^{\frac{\pi}{2}} \cos^2 \theta \sin \theta d\theta \\ &\times \left\{ \tanh \left(\frac{\varepsilon}{2kT} \right) \left[\frac{1 + (\omega_\varepsilon - \omega)^2 T_2^2}{1 + \Omega^2 T_1 T_2 + (\omega_\varepsilon - \omega)^2 T_2^2} \right] \chi(\omega_\varepsilon, \omega) \right\}. \end{aligned} \quad (\text{G.4})$$

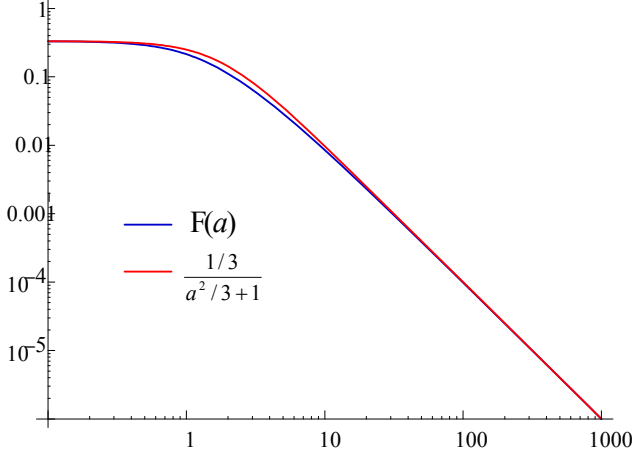


Figure G.1: Comparison between $F(a)$ and $1/(a^2/3 + 1)$

Note that

$$\Omega^2 T_1 = \left(\frac{2d_0 |\vec{E}| \cos \theta}{\hbar} \frac{\Delta_0}{\varepsilon} \right)^2 \times T_{1,\min} \left(\frac{\varepsilon}{\Delta_0} \right)^2 = 2d_0^2 |\vec{E}|^2 \cos^2 \theta T_{1,\min} / \hbar^2 \quad (\text{G.5})$$

has dependence on θ but no dependence on u . Therefore, the integral of u can be separately worked out

$$\int_{u_{\min}}^1 \frac{u}{\sqrt{1-u^2}} du = \sqrt{1-u_{\min}^2} \approx 1 \quad (\text{G.6})$$

reducing the integral to

$$\begin{aligned} \epsilon_{\text{TLS}}(\omega) &= P d_0^2 \int_0^{\frac{\pi}{2}} \cos^2 \theta \sin \theta d\theta \\ &\times \left\{ \int_0^{\varepsilon_{\max}} d\varepsilon \tanh \left(\frac{\varepsilon}{2kT} \right) \left[\frac{1 + (\omega_\varepsilon - \omega)^2 T_2^2}{1 + \Omega^2 T_1 T_2 + (\omega_\varepsilon - \omega)^2 T_2^2} \right] \chi(\omega_\varepsilon, \omega) \right\}. \end{aligned} \quad (\text{G.7})$$

The integral on θ is of the following form

$$\int_0^1 \frac{t^2}{a^2 t^2 + 1} dt = \frac{a - \arctan(a)}{a^3} = F(a). \quad (\text{G.8})$$

In fact, for all range of a , $F(a)$ can be well approximated by a simpler function, as shown in Fig. G.1

$$F(a) \sim \frac{1}{3} \frac{1}{a^2/3 + 1}. \quad (\text{G.9})$$

According to Eq. G.9, the θ -integral and θ -dependence of Ω can be effectively removed by substi-

tuting $d_0/\sqrt{3}$ for d_0 in the ε integral

$$\epsilon_{\text{TLS}}(\omega) = \frac{Pd_0^2}{3} \int_0^{\varepsilon_{\max}} d\varepsilon \tanh\left(\frac{\varepsilon}{2kT}\right) \left[\frac{1 + (\omega_\varepsilon - \omega)^2 T_2^2}{1 + \overline{\Omega}^2 T_1 T_2 + (\omega_\varepsilon - \omega)^2 T_2^2} \right] \chi(\omega_\varepsilon, \omega) \quad (\text{G.10})$$

where the effective Rabi frequency is modified to

$$\overline{\Omega} = \frac{2d_0|\vec{E}|}{\sqrt{3}} \frac{\Delta_0}{\varepsilon}. \quad (\text{G.11})$$

G.2 $\epsilon_{\text{TLS}}(\omega)$ for weak field ($|\vec{E}| \rightarrow 0$).

If the electric field is weak and $\overline{\Omega}^2 T_1 T_2 \ll 1$ is satisfied, we can set $\overline{\Omega} = 0$ in Eq. G.7. The integral of θ can now be separated to yield 1/3. The integral simplifies to

$$\epsilon_{\text{TLS}}(\omega) = \frac{Pd_0^2}{3\hbar} \int_0^{\varepsilon_{\max}} \tanh\left(\frac{\varepsilon}{2kT}\right) \left[\frac{1}{\omega_\varepsilon - \omega + jT_2^{-1}} + \frac{1}{\omega_\varepsilon + \omega - jT_2^{-1}} \right] d\varepsilon. \quad (\text{G.12})$$

Now let $x = \varepsilon/kT$, $z = (\hbar\omega - j\hbar T_2^{-1})/kT$ and $x_m = \varepsilon_{\max}/kT$. We rewrite the integral as

$$\epsilon_{\text{TLS}}(\omega) = \frac{Pd_0^2}{3} \int_0^{x_m} \tanh\left(\frac{x}{2}\right) \frac{2x}{x^2 - z^2} dx. \quad (\text{G.13})$$

The following are pure mathematical derivations

$$\begin{aligned} & \int_0^{x_m} \tanh\left(\frac{x}{2}\right) \frac{2x}{x^2 - z^2} dx \\ &= \int_0^{x_m} \left[\tanh\left(\frac{x}{2}\right) - 1 \right] \frac{2x}{x^2 - z^2} dx + \int_0^{x_m} \frac{2x}{x^2 - z^2} dx \\ &\approx \int_0^\infty \frac{-2}{e^x + 1} \frac{2x}{x^2 - z^2} dx + \log\left(\frac{-x_m^2}{z^2}\right) \\ &= -2 \int_0^\infty \left(\frac{1}{e^x - 1} - \frac{2}{e^{2x} - 1} \right) \frac{2x}{x^2 - z^2} dx + \log\left(\frac{-x_m^2}{z^2}\right) \\ &= -2 \left[\int_0^\infty \frac{1}{e^x - 1} \frac{2x}{x^2 - z^2} dx - \int_0^\infty \frac{2}{e^{2x} - 1} \frac{2x}{x^2 - z^2} dx - \log\left(\frac{jx_m}{z}\right) \right] \\ &= -2 \left[\int_0^\infty \frac{1}{e^{2\pi t} - 1} \frac{2t}{t^2 + (jz/2\pi)^2} dt - \int_0^\infty \frac{2}{e^{2\pi t} - 1} \frac{2t}{t^2 - (jz/\pi)^2} dt - \log\left(\frac{jx_m}{z}\right) \right] \\ &= -2 \left[\int_0^\infty \frac{1}{e^{2\pi t} - 1} \frac{2t}{t^2 + (\frac{-z}{2\pi j})^2} dt - \int_0^\infty \frac{2}{e^{2\pi t} - 1} \frac{2t}{t^2 + (\frac{-2z}{2\pi j})^2} dt - \log\left(\frac{jx_m}{z}\right) \right] \\ &= -2 \left\{ \left[\log\left(\frac{-z}{2\pi j}\right) + \frac{2\pi j}{2z} - \psi\left(\frac{-z}{2\pi j}\right) \right] - 2 \left[\log\left(\frac{-z}{\pi j}\right) + \frac{\pi j}{2z} - \psi\left(\frac{-z}{\pi j}\right) \right] - \log\left(\frac{jx_m}{z}\right) \right\} \\ &= -2 \left[\psi\left(\frac{1}{2} - \frac{z}{2\pi j}\right) - \log\left(\frac{x_m}{2\pi}\right) \right]. \end{aligned} \quad (\text{G.14})$$

In the derivations above, we have applied the following two formula found in Abramowitz and Stegun (page 259)[52], to express the integral in terms of complex digamma function ψ :

$$\begin{aligned}\psi(z) &= \log z - \frac{1}{2z} - 2 \int_0^\infty \frac{tdt}{(t^2 + z^2)(e^{2\pi t} - 1)} \\ \psi(2z) &= \frac{1}{2}\psi(z) + \frac{1}{2}\psi(z + \frac{1}{z}) + \log 2.\end{aligned}\quad (\text{G.15})$$

Therefore in the weak field limit,

$$\epsilon_{\text{TLS}}(\omega) = -\frac{2Pd_0^2}{3} \left[\psi\left(\frac{1}{2} - \frac{\hbar\omega - jT_2^{-1}}{2\pi jkT}\right) - \log\left(\frac{\varepsilon_{\max}}{2\pi kT}\right) \right]. \quad (\text{G.16})$$

G.3 $\epsilon_{\text{TLS}}(\omega)$ for nonzero \vec{E} field.

For general nonzero electrical field, we evaluate the real part (ϵ'_{TLS}) and the imaginary part (ϵ''_{TLS}) separately.

For the integral of ϵ''_{TLS} , the major contribution is from the first term in $\chi(\omega_\varepsilon, \omega)$ and the second term can be neglected. After dropping the second term, the integral becomes

$$\epsilon''_{\text{TLS}}(\omega) = \frac{Pd_0^2}{3\hbar} \int_0^{\varepsilon_{\max}} d\varepsilon \tanh\left(\frac{\varepsilon}{2kT}\right) \left[\frac{-T_2^{-1}}{(T_2^{-1}\sqrt{1 + \overline{\Omega}^2 T_1 T_2})^2 + (\omega_\varepsilon - \omega)^2} \right]. \quad (\text{G.17})$$

The factor in the square brackets is a Lorentzian centered at ω_ε with a line width of $T_2^{-1}\sqrt{1 + \overline{\Omega}^2 T_1 T_2}$. Because within the width of the Lorentzian $\tanh(\varepsilon/2kT)$ is almost constant, it can be taken out of the integral leading to

$$\begin{aligned}\epsilon''_{\text{TLS}}(\omega) &\approx -\frac{Pd_0^2}{3\hbar} \tanh\left(\frac{\hbar\omega}{2kT}\right) \int_0^{\varepsilon_{\max}} d\varepsilon \left[\frac{-T_2^{-1}}{(T_2^{-1}\sqrt{1 + \overline{\Omega}^2 T_1 T_2})^2 + (\omega_\varepsilon - \omega)^2} \right] \\ &\approx -\frac{\pi Pd_0^2}{3} \frac{\tanh\left(\frac{\hbar\omega}{2kT}\right)}{\sqrt{1 + \overline{\Omega}^2 T_1 T_2}}.\end{aligned}\quad (\text{G.18})$$

The field-dependent loss tangent is given by

$$\delta_{\text{TLS}} = \delta_0 \frac{\tanh\left(\frac{\hbar\omega}{2kT}\right)}{\sqrt{1 + (|E|/E_c)^2}} \quad (\text{G.19})$$

where the critical electric field is

$$E_c = \frac{\sqrt{3}\hbar}{2d_0|\vec{E}|\sqrt{T_{1,\min}T_2}}. \quad (\text{G.20})$$

Next, we work on the real part of the integral in Eq. G.7 for $\epsilon'_{\text{TLS}}(\omega)$. Let $\kappa(|\vec{E}|) = \sqrt{1 + \bar{\Omega}^2 T_1 T_2}$ be the saturation factor. The difference in $\epsilon'_{\text{TLS}}(\omega)$ between strong field and zero field is calculated by

$$\begin{aligned}\delta\epsilon'(\kappa) &= \epsilon'_{\text{TLS}}(\kappa) - \epsilon'_{\text{TLS}}(0) \\ &= \frac{Pd_0^2}{3\hbar} \int_0^{\varepsilon_{\max}} \tanh\left(\frac{\varepsilon}{2kT}\right) \left[\frac{1 + (\omega_\varepsilon - \omega)^2 T_2^2}{1 + \bar{\Omega}^2 T_1 T_2 + (\omega_\varepsilon - \omega)^2 T_2^2} - 1 \right] \\ &\quad \times \left\{ \frac{(\omega_\varepsilon - \omega)}{(\omega_\varepsilon - \omega)^2 + (T_2^{-1})^2} + \frac{(\omega_\varepsilon + \omega)}{(\omega_\varepsilon + \omega)^2 + (T_2^{-1})^2} \right\} d\varepsilon.\end{aligned}\quad (\text{G.21})$$

Now we calculate the contribution from the two terms in the curly brackets separately.

$$\begin{aligned}\delta\epsilon'_1 &= \frac{Pd_0^2}{3\hbar} \int_0^{\varepsilon_{\max}} \tanh\left(\frac{\varepsilon}{2kT}\right) \left[\frac{1 + (\omega_\varepsilon - \omega)^2 T_2^2}{1 + \bar{\Omega}^2 T_1 T_2 + (\omega_\varepsilon - \omega)^2 T_2^2} - 1 \right] \frac{\omega_\varepsilon - \omega}{(\omega_\varepsilon - \omega)^2 + (T_2^{-1})^2} d\varepsilon \\ &= \frac{Pd_0^2}{3\hbar} \int_0^{\varepsilon_{\max}} \tanh\left(\frac{\varepsilon}{2kT}\right) \left[\frac{\Delta\omega}{\Delta\omega^2 + (\kappa T_2^{-1})^2} - \frac{\Delta\omega}{\Delta\omega^2 + (T_2^{-1})^2} \right] d\varepsilon.\end{aligned}\quad (\text{G.22})$$

Because the term in the square brackets

$$\frac{\Delta\omega}{\Delta\omega^2 + (\kappa T_2^{-1})^2} - \frac{\Delta\omega}{\Delta\omega^2 + (T_2^{-1})^2} = \frac{(1 - \kappa^2)(T_2^{-1})^2 \Delta\omega}{[\Delta\omega^2 + (T_2^{-1})^2][\Delta\omega^2 + (\kappa T_2^{-1})^2]} \quad (\text{G.23})$$

is an odd function of $\Delta\omega$ which has significant contribution to the integral only when $|\omega_\varepsilon - \omega| \lesssim \kappa T_2^{-1}$, we can replace $\tanh\left(\frac{\varepsilon}{2kT}\right)$ by its Taylor expansion at $\varepsilon = \hbar\omega$ and extend the integral limits to $\pm\infty$,

$$\begin{aligned}\delta\epsilon'_1 &\approx \frac{Pd_0^2}{3} \int_{-\infty}^{\infty} \left[\tanh\left(\frac{\hbar\omega}{2kT}\right) + \operatorname{sech}^2\left(\frac{\hbar\omega}{2kT}\right) \frac{\hbar\Delta\omega}{2kT} \right] \left[\frac{\Delta\omega}{\Delta\omega^2 + (\kappa T_2^{-1})^2} - \frac{\Delta\omega}{\Delta\omega^2 + (T_2^{-1})^2} \right] d\Delta\omega \\ &= \frac{\pi Pd_0^2}{3} \operatorname{sech}^2\left(\frac{\hbar\omega}{2kT}\right) \frac{\hbar T_2^{-1}}{2kT} (1 - \kappa)\end{aligned}\quad (\text{G.24})$$

The contribution from the second term in the curly brackets is Eq. G.21.

$$\delta\epsilon'_2 = \frac{Pd_0^2}{3\hbar} \int_0^{\varepsilon_{\max}} \tanh\left(\frac{\varepsilon}{2kT}\right) \left[\frac{-\bar{\Omega}^2 T_1 T_2}{1 + \bar{\Omega}^2 T_1 T_2 + (\omega_\varepsilon - \omega)^2 T_2^2} \right] \frac{\omega_\varepsilon + \omega}{(\omega_\varepsilon + \omega)^2 + (T_2^{-1})^2} d\varepsilon \quad (\text{G.25})$$

where the term in the square brackets is only nonzero within a small range around $\omega_\varepsilon \sim \omega$ in which

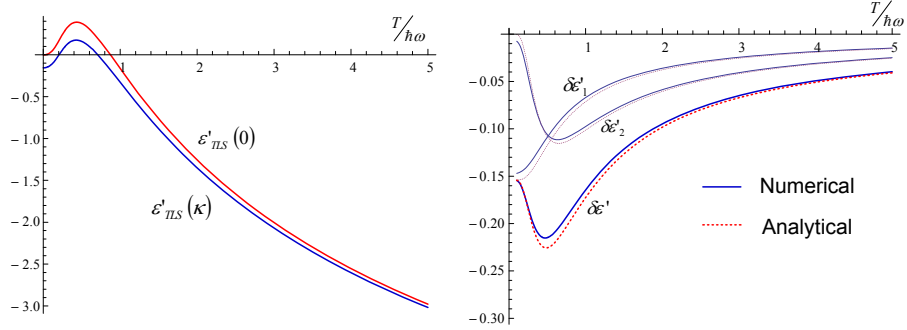


Figure G.2: $\delta\epsilon'$, $\delta\epsilon'_1$ and $\delta\epsilon'_2$ as a function of temperature. Left panel shows ϵ'_{TLS} for zero field $\kappa = 0$ (blue) and nonzero field $\kappa = 3$ (red). Their difference is plotted by the bottom curve in the right panel, as well as the two contributions $\delta\epsilon'_1$ and $\delta\epsilon'_2$. In the right panel, solid lines are calculated from evaluating the exact integrals numerically while the dashed line are calculated from the derived approximate formula.

all other terms are almost constant. Therefore

$$\begin{aligned}\delta\epsilon'_2 &\approx \frac{Pd_0^2}{3\hbar} \tanh\left(\frac{\hbar\omega}{2kT}\right) \frac{1}{2\omega} \int_{-\infty}^{\infty} \left[\frac{-\bar{\Omega}^2 T_1 T_2}{1 + \bar{\Omega}^2 T_1 T_2 + (\omega_\varepsilon - \omega)^2 T_2^2} \right] d\varepsilon \\ &= \frac{\pi P d_0^2}{3} \tanh\left(\frac{\hbar\omega}{2kT}\right) \frac{T_2^{-1}}{2\omega} \frac{1 - \kappa^2}{\kappa}\end{aligned}\quad (\text{G.26})$$

Finally, we have derived

$$\begin{aligned}\epsilon'_{\text{TLS}}(\kappa) - \epsilon'_{\text{TLS}}(0) &= \delta\epsilon'_1 + \delta\epsilon'_2 \\ &= \frac{\pi P d_0^2}{3} \left[\operatorname{sech}^2\left(\frac{\hbar\omega}{2kT}\right) \frac{\hbar T_2^{-1}}{2kT} (1 - \kappa) + \tanh\left(\frac{\hbar\omega}{2kT}\right) \frac{T_2^{-1}}{2\omega} \frac{1 - \kappa^2}{\kappa} \right]\end{aligned}\quad (\text{G.27})$$

The temperature variation of ϵ'_{TLS} for zero field $\kappa = 0$ and nonzero field $\kappa = 3$ are plotted in the left panel in Fig. G.2. We can see that ϵ'_{TLS} decreases with the field strength. The difference between the two curves $\delta\epsilon' = \epsilon_{\text{TLS}}(\kappa = 3) - \epsilon_{\text{TLS}}(\kappa = 0)$, separated into the two contributions $\delta\epsilon'_1$ and $\delta\epsilon'_2$, evaluated both numerically from the exact integrals and analytically from the derived approximate formula, are plotted in the right panel of Fig. G.2. There we see that the approximate formula works pretty well.

Appendix H

Semi-empirical frequency noise formula for a transmission line resonator

In this appendix, we derive the formula of frequency noise in the high power regime for a transmission line resonator from the semi-empirical noise model Eq. 5.80

$$\frac{S_{\delta f_r}(\nu)}{f_r^2} = \kappa(\nu, \omega, T) \frac{\int_{V_h} |\vec{E}|^3 d^3r}{4 \left(\int_V \epsilon |\vec{E}|^2 d^3r \right)^2} \quad (\text{H.1})$$

We consider a m -wave transmission line resonator in general. For example, for a quarter-wave resonator $m = 1/4$ and for a half-wave resonator $m = 1/2$. Assume that the transmission line goes in the z -direction with $z = 0$ and $z = l$ represents the coupler end (always an open end) and the opposite end, respectively. The cross-section of the transmission line is in the $x-y$ plane, with x -axis parallel to surface of the metal film and y -axis perpendicular to the surface. The spatial distribution of the electric field in the resonator has a standing wave pattern given by

$$|E(x, y, z)| = V_0 \rho(x, y) \left| \cos\left(\frac{2\pi m z}{l}\right) \right| \quad (\text{H.2})$$

where V_0 is the voltage at $z=0$ (a harmonic time dependence of $e^{j\omega t}$ is assumed and omitted as usual), which is related to the internal power P_{int} and readout power $P_{\mu w}$ by,

$$P_{\text{int}} = \frac{V_+^2}{2Z_r} = \frac{(V_0/2)^2}{2Z_r} = \frac{1}{2\pi m} P_{\mu w} \frac{Q^2}{Q_c} \quad (\text{H.3})$$

$$V_0 = \sqrt{\frac{4Z_r Q_r^2}{\pi m Q_c} P_{\mu w}} \quad (\text{H.4})$$

$\rho(x, y)$ is the field distribution in the cross-sectional plane normalized by V_0 . The denominator in Eq. H.1 is related to the electric energy in the system and can be expressed in terms of transmission

line parameters

$$2 \int_V \epsilon E(\vec{r})^2 d\vec{r} = CV_0^2 l \quad (\text{H.5})$$

Inserting Eq. H.2 and Eq. H.5 to Eq. H.1 yields

$$\frac{S_{\delta f_r}(\nu)}{f_r^2} = \kappa(\nu, \omega, T) \frac{4 \int_{A_h} \rho(x, y)^3 dx dy}{3\pi C^2 V_0 l} \quad (\text{H.6})$$

Because of the term V_0 in the denominator, Eq. H.6 gives the correct $P_{\text{int}}^{-1/2}$ power dependence of noise. Eq. H.6 also predict that the noise scales inversely with length, which arises from the incoherent sum of the contribution from independent fluctuators along the z -axis.

The most important part of the noise formula Eq. H.6 is the following integral

$$I_3 = \int_{A_h} \rho(x, y)^3 dx dy \quad (\text{H.7})$$

which is taken in the area A_h occupied by the TLS host material in the cross-sectional plane. It can be shown that for microstrip transmission line

$$I_3 = \int_{A_h} \rho(x, y)^3 dx dy \approx \frac{w}{h^2} \quad (\text{H.8})$$

where the field is approximated by that of a parallel plate capacitor. Here w and h are the width and the thickness of the dielectric in the microstrip. For a surface distribution of TLS,

$$I_3 = \int_{A_h} \rho(x, y)^3 dx dy \approx t \int_{C_h} \rho(\xi)^3 d\xi \quad (\text{H.9})$$

where the contour C_h runs over the TLS distributed surface and t is the thickness of the TLS layer.

Bibliography

- [1] P. de Bernardis, P. A. R. Ade, J. J. Bock, J. R. Bond, J. Borrill, A. Boscaleri, K. Coble, B. P. Crill, G. De Gasperis, P. C. Farese, P. G. Ferreira, K. Ganga, M. Giacometti, E. Hivon, V. V. Hristov, A. Iacoangeli, A. H. Jaffe, A. E. Lange, L. Martinis, S. Masi, P. V. Mason, P. D. Mauskopf, A. Melchiorri, L. Miglio, T. Montroy, C. B. Netterfield, E. Pascale, F. Piacentini, D. Pogosyan, S. Prunet, S. Rao, G. Romeo, J. E. Ruhl, F. Scaramuzzi, D. Sforna, and N. Vittorio, “A flat universe from high-resolution maps of the cosmic microwave background radiation,” *Nature* **404** (2000), no. 6781, 955–959.
- [2] A. E. Lange, P. A. R. Ade, J. J. Bock, J. R. Bond, J. Borrill, A. Boscaleri, K. Coble, B. P. Crill, P. de Bernardis, P. Farese, P. Ferreira, K. Ganga, M. Giacometti, E. Hivon, V. V. Hristov, A. Iacoangeli, A. H. Jaffe, L. Martinis, S. Masi, P. D. Mauskopf, A. Melchiorri, T. Montroy, C. B. Netterfield, E. Pascale, F. Piacentini, D. Pogosyan, and S. Prunet, “Cosmological parameters from the first results of boomerang,” *Physical Review D* **63** (2001), no. 4, 042001.
- [3] F. Simon, “Application of low temperature calorimetry to radioactive measurements,” *Nature* **135** (1935) 763.
- [4] F. J. Low, “Low-temperature geranium bolometer,” *Journal of the Optical Society of America A* **51** (1961), no. 11, 1300.
- [5] J. Glenn, J. J. Bock, G. Chattopadhyay, S. F. Edgington, A. E. Lange, J. Zmuidzinas, P. D. Mauskopf, B. Rownd, L. Yuen, and P. A. R. Ade, “Bolocam: a millimeter-wave bolometric camera,” in *Proceedings SPIE—the International Society of Optical Engineering*, T. G. Phillips, ed., vol. 3357, pp. 326–334. 1998.
- [6] K. D. Irwin, G. C. Hilton, D. A. Wollman, and J. M. Martinis, “X-ray detection using a superconducting transition-edge sensor microcalorimeter with electrothermal feedback,” *Applied Physics Letters* **69** (1996), no. 13, 1945–1947.
- [7] K. D. Irwin and G. C. Hilton, “Cryogenic particle detection,” in *Topics in Applied Physics*, C. Enss, ed., vol. 99, pp. 63–149. Springer, Berlin, Germany, 2005.

- [8] B. Cabrera, R. M. Clarke, P. Colling, A. J. Miller, S. Nam, and R. W. Romani, "Detection of single infrared, optical, and ultraviolet photons using superconducting transition edge sensors," *Applied Physics Letters* **73** (1998), no. 6, 735–737.
- [9] K. D. Irwin, G. C. Hilton, J. M. Martinis, S. Deiker, N. Bergren, S. W. Nam, D. A. Rudman, and D. A. Wollman, "A mo-cu superconducting transition-edge microcalorimeter with 4.5 ev energy resolution at 6 kev," *Nuclear Instruments and Methods in Physics Research Section A: Accelerators, Spectrometers, Detectors and Associated Equipment* **444** (2000) 184–187.
- [10] S. F. Lee, J. M. Gildemeister, W. Holmes, A. T. Lee, and P. L. Richards, "Voltage-biased superconducting transition-edge bolometer with strong electrothermal feedback operated at 370 mk," *Applied Optics* **37** (1998), no. 16, 3391–3397.
- [11] A. Fleischmann, C. Enss, and G. M. Seidel, "Cryogenic particle detection," in *Topics in Applied Physics*, C. Enss, ed., vol. 99, pp. 151–216. Springer, Berlin, Germany, 2005.
- [12] D. Twerenbold, "Giaever-type superconducting tunneling junctions as high-resolution X-ray-detectors," *Europhysics Letters* **1** (1986), no. 5, 209–214.
- [13] A. Peacock, P. Verhoeve, N. Rando, A. vanDordrecht, B. Taylor, C. Erd, M. Perryman, R. Venn, J. Howlett, D. Goldie, J. Lumley, and M. Wallis, "Single optical photon detection with a superconducting tunnel junction," *Nature* **381** (1996), no. 6578, 135–137.
- [14] P. K. Day, H. G. LeDuc, B. A. Mazin, A. Vayonakis, and J. Zmuidzinas, "A broadband superconducting detector suitable for use in large arrays," *Nature* **425** (2003), no. 6960, 817–821.
- [15] B. A. Mazin, P. K. Day, J. Zmuidzinas, and H. G. LeDuc, "Multiplexable kinetic inductance detectors," *AIP Conference Proceedings* **605** (2002) 309–312.
- [16] B. A. Mazin, *Microwave kinetic inductance detectors*. PhD thesis, Caltech, 2004.
- [17] J. Baselmans, S. J. C. Yates, R. Barends, Y. J. Y. Lankwarden, J. R. Gao, H. Hoevers, and T. M. Klapwijk, "Noise and sensitivity of aluminum kinetic inductance detectors for sub-mm astronomy," *Journal of Low Temperature Physics* **151** (2008) 524–529.
- [18] G. Vardulakis, S. Withington, D. J. Goldie, and D. M. Glowacka, "Superconducting kinetic inductance detectors for astrophysics," *Measurement Science and Technology* **19** (2008), no. 1, 015509.
- [19] M. Tinkham, *Introduction to Superconductivity*, 2nd ed. McGraw-Hill, New York, 1996.

- [20] B. A. Mazin, B. Bumble, P. K. Day, M. E. Eckart, S. Golwala, J. Zmuidzinas, and F. A. Harrison, “Position sensitive X-ray spectrophotometer using microwave kinetic inductance detectors,” *Applied Physics Letters* **89** (2006), no. 22, 222507.
- [21] P. K. Day, H. G. Leduc, A. Goldin, T. Vayonakis, B. A. Mazin, S. Kumar, J. Gao, and J. Zmuidzinas, “Antenna-coupled microwave kinetic inductance detectors,” *Nuclear Instruments and Methods in Physics Research Section A: Accelerators, Spectrometers, Detectors and Associated Equipment* **559** (2006) 561–563.
- [22] J. Schlaerth, A. Vayonakis, P. Day, J. Glenn, J. Gao, S. Golwala, S. Kumar, H. LeDuc, B. Mazin, J. Vaillancourt, and J. Zmuidzinas, “A millimeter and submillimeter kinetic inductance detector camera,” *Journal of Low Temperature Physics* **151** (2008) 684–689.
- [23] B. A. Mazin, M. E. Eckart, B. Bumble, S. Golwala, P. K. Day, J. Gao, and J. Zmuidzinas, “Optical/UV and X-ray microwave kinetic inductance strip detectors,” *Journal of Low Temperature Physics* **151** (2008) 537–543.
- [24] B. A. Mazin, P. K. Day, K. D. Irwin, C. D. Reintsema, and J. Zmuidzinas, “Digital readouts for large microwave low-temperature detector arrays,” *Nuclear Instruments and Methods in Physics Research Section A: Accelerators, Spectrometers, Detectors and Associated Equipment* **559** (2006) 799–801.
- [25] S. Golwala, J. Gao, D. Moore, B. Mazin, M. Eckart, B. Bumble, P. Day, H. G. LeDuc, and J. Zmuidzinas, “A wimp dark matter detector using mkids,” *Journal of Low Temperature Physics* **151** (2008) 550–556.
- [26] M. Daal, B. Sadoulet, and J. Gao, “Kinetic inductance phonon sensors for the cryogenic dark matter search experiment,” *Journal of Low Temperature Physics* **151** (2008) 544–549.
- [27] K. W. Lehnert, K. D. Irwin, M. A. Castellanos-Beltran, J. A. B. Mates, and L. R. Vale, “Evaluation of a microwave SQUID multiplexer prototype,” *IEEE Transactions on Applied Superconductivity* **17** (2007), no. 2, 705–709.
- [28] J. A. B. Mates, G. C. Hilton, K. D. Irwin, L. R. Vale, and K. W. Lehnert, “Demonstration of a multiplexer of dissipationless superconducting quantum interference devices,” *Applied Physics Letters* **92** (2008), no. 2, 023514.
- [29] I. Hahn, B. Bumble, H. Leduc, M. Weilert, and P. Day, “An X-band squid multiplexer,” *AIP Conference Proceedings* **850** (2006) 1613–1614.
- [30] I. Hahn, P. K. Day, B. Bumble, and H. G. Leduc, “Recent results of a new microwave SQUID multiplexer,” *Journal of Low Temperature Physics* **151** (2008) 934–939.

- [31] A. Wallraff, D. I. Schuster, A. Blais, L. Frunzio, R.-S. Huang, J. Majer, S. Kumar, S. M. Girvin, and R. J. Schoelkopf, “Strong coupling of a single photon to a superconducting qubit using circuit quantum electrodynamics,” *Nature* **431** (2004), no. 7005, 162–167.
- [32] E. Jaynes and F. Cummings, “Comparison of quantum and semiclassical radiation theories with application to the beam maser,” *Proceedings of IEEE* **51** (1963), no. 1, 89–109.
- [33] J. Majer, J. M. Chow, J. M. Gambetta, J. Koch, B. R. Johnson, J. A. Schreier, L. Frunzio, D. I. Schuster, A. A. Houck, A. Wallraff, A. Blais, M. H. Devoret, S. M. Girvin, and R. J. Schoelkopf, “Coupling superconducting qubits via a cavity bus,” *Nature* **449** (2007) 443.
- [34] A. A. Houck, D. I. Schuster, J. M. Gambetta, J. A. Schreier, B. R. Johnson, J. M. Chow, L. Frunzio, J. Majer, M. H. Devoret, S. M. Girvin, and R. J. Schoelkopf, “Generating single microwave photons in a circuit,” *Nature* **449** (2007) 328.
- [35] D. I. Schuster, A. A. Houck, J. A. Schreier, A. Wallraff, J. M. Gambetta, A. Blais, L. Frunzio, J. Majer, B. R. Johnson, M. H. Devoret, S. M. Girvin, and R. J. Schoelkopf, “Resolving photon number states in a superconducting circuit,” *Nature* **445** (2007) 515.
- [36] C. A. Regal, J. D. Teufel, and K. W. Lehnert, “Measuring nanomechanical motion with a microwave cavity interferometer,” *Nature Physics advanced online publication* (2008).
- [37] R. G. Chambers, “The anomalous skin effect,” *Proceedings of the Royal Society of London. Series A, Mathematical and Physical Sciences* **215** (1952), no. 1123, 481–497.
- [38] F. London, “Electrodynamics of macroscopic fields in supraconductors,” *Nature* **137** (1936), no. 3476, 991–992.
- [39] D. C. Mattis and J. Bardeen, “Theory of the anomalous skin effect in normal and superconducting metals,” *Physical Review* **111** (1958), no. 2, 412–417.
- [40] R. Popel, “Electromagnetic properties of superconductors,” in *Superconducting Quantum Electronics*, V. Kose, ed., ch. 3, pp. 44–78. Springer-Verlag, Berlin, Germany, 1989.
- [41] A. B. Pippard, “An experimental and theoretical study of the relation between magnetic field and current in a superconductor,” *Proceedings of the Royal Society of London. Series A, Mathematical and Physical Sciences* **216** (1953), no. 1127, 547–568.
- [42] J. Bardeen, L. N. Cooper, and J. R. Schrieffer, “Microscopic theory of superconductivity,” *Physical Review* **106** (1957), no. 1, 162–164.
- [43] G. E. H. Reuter and E. H. Sondheimer, “The theory of the anomalous skin effect in metals,” *Proceedings of the Royal Society of London. Series A, Mathematical and Physical Sciences* **195** (1948), no. 1042, 336–364.

- [44] J. R. Hook, “A method for calculating the microwave surface impedance of superconducting films,” *Journal of Low Temperature Physics* **23** (1976), no. 5, 645–661.
- [45] J. Ward, F. Rice, G. Chattopadhyay, and J. Zmuidzinas, “Supermix: A flexible software library for high-frequency circuit simulation, including sis mixers and superconducting elements,” in *Proceedings SPIE—the International Society of Optical Engineering*, pp. 269–281. 1999.
- [46] B. Mhlschlegel, “Die thermodynamischen funktionen des supraleiters,” *Zeitschrift fr Physik A Hadrons and Nuclei* **155** (1959) 313–327.
- [47] S. Sridhar, “Microwave response of thin-film superconductors,” *Journal of Applied Physics* **63** (1988), no. 1, 159–166.
- [48] R. E. Glover and M. Tinkham, “Conductivity of superconducting films for photon energies between 0.3 and $4kT_c$,” *Physical Review* **108** (1957), no. 2, 243–256.
- [49] C. S. Owen and D. J. Scalapino, “Superconducting state under the influence of external dynamic pair breaking,” *Physical Review Letters* **28** (1972), no. 24, 1559–1561.
- [50] J. Gao, J. Zmuidzinas, A. Vayonakis, P. K. Day, B. A. Mazin, and H. G. Leduc, “Equivalence of the effects on the complex conductivity of superconductor due to temperature change and external pair breaking,” *Journal of Low Temperature Physics* **151** (2008) 557–563.
- [51] C. P. Wen, “Coplanar waveguide: A surface strip transmission line suitable for nonreciprocal gyromagnetic device applications,” *IEEE Transactions on Microwave Theory and Techniques* **17** (Dec 1969), no. 12, 1087–1090.
- [52] M. Abramowitz and I. A. Stegun, *Handbook of Mathematical Functions: with Formulas, Graphs, and Mathematical Tables*. Dover Publications, New York, 1965.
- [53] <http://www.math.udel.edu/~driscoll/software/SC>.
- [54] Matlab user manual.
- [55] R. E. Collin, *Foundations for Microwave Engineering, 2nd edition*. IEEE Press, New York, 2000.
- [56] W. H. Chang, “The inductance of a superconducting strip transmission line,” *Journal of Applied Physics* **50** (1979), no. 12, 8129–8134.
- [57] D. M. Pozar, *Microwave Engineering, 2nd edition*. John Wiley and Sons, New York, 1998.
- [58] A. B. Zorin, F.-J. Ahlers, J. Niemeyer, T. Weimann, and H. Wolf, “Background charge noise in metallic single-electron tunneling devices,” *Physical Review B* **53** (1996), no. 20, 13682–13687.

- [59] J. M. Martinis, K. B. Cooper, R. McDermott, M. Steffen, M. Ansmann, K. D. Osborn, K. Cicak, S. Oh, D. P. Pappas, R. W. Simmonds, and C. C. Yu, “Decoherence in Josephson qubits from dielectric loss,” *Physical Review Letters* **95** (2005), no. 21, 210503.
- [60] W. A. Phillips, “Tunneling states in amorphous solids,” *Journal of Low Temperature Physics* **7** (1972), no. 3-4, 351–360.
- [61] P. W. Anderson, B. I. Halperin, and C. M. Varma, “Anomalous low-temperature thermal properties of glasses and spin glasses,” *Philosophical Magazine* **25** (1972) 1–9.
- [62] S. Kumar, P. Day, H. LeDuc, B. Mazin, M. Eckart, J. Gao, and J. Zmuidzinas, “Frequency noise in superconducting thin-film resonators,” *APS March Meeting abstract* (2006). <http://meetings.aps.org/link/BAPS.2006.MAR.B38.2>.
- [63] S. Kumar, J. Gao, J. Zmuidzinas, B. A. Mazin, H. G. Leduc, and P. K. Day, “Temperature dependence of the frequency and noise of superconducting coplanar waveguide resonators,” *Applied Physics Letters* **92** (2008) 123503.
- [64] J. Gao, J. Zmuidzinas, B. A. Mazin, P. K. Day, and H. G. Leduc, “Experimental study of the kinetic inductance fraction of superconducting coplanar waveguide,” *Nuclear Instruments and Methods in Physics Research, Section A* **559** (2006) 585–587.
- [65] W. A. Phillips, “Two-level states in glasses,” *Reports on Progress in Physics* **50** (1987) 1657–1708.
- [66] W. A. Phillips, *Amorphous solids: low-temperature properties*. Springer-Verlag, Berlin, and New York, 1981.
- [67] F. Bloch, “Nuclear induction,” *Physical Review* **70** (1946), no. 7-8, 460–474.
- [68] S. Hunklinger and W. Arnold, *Physical Acoustics*, vol. 12, ch. 3, p. 155. Academic, New York, 1976.
- [69] L. Hilico, C. Fabre, S. Reynaud, and E. Giacobino, “Linear input-output method for quantum fluctuations in optical bistability with two-level atoms,” *Physical Review A* **46** (1992), no. 7, 4397–4405.
- [70] J. Gao, J. Zmuidzinas, B. A. Mazin, P. K. Day, and H. G. LeDuc, “Noise properties of superconducting coplanar waveguide microwave resonators,” *Applied Physics Letters* **90** (2007), no. 102507, 817–821.
- [71] R. N. Simons, *Coplanar Waveguide Circuits Components and Systems*. John Wiley and Sons, New York, 2001.

- [72] J. Gao, M. Daal, A. Vayonakis, S. Kumar, J. Zmuidzinas, B. Sadoulet, B. A. Mazin, P. K. Day, and H. G. Leduc, “Experimental evidence for a surface distribution of two-level systems in superconducting lithographed microwave resonators,” *Applied Physics Letters* **92** (2008), no. 15, 152505.
- [73] J. Gao, B. Mazin, M. Daal, P. Day, H. LeDuc, and J. Zmuidzinas, “Power dependence of phase noise in microwave kinetic inductance detectors,” in *Proceedings SPIE—the International Society of Optical Engineering*, J. Zmuidzinas, W. S. Holland, S. Withington, and W. D. Duncan, eds., vol. 6275, p. 627509. 2006.
- [74] J. Gao, M. Daal, J. M. Martinis, A. Vayonakis, J. Zmuidzinas, B. Sadoulet, B. A. Mazin, P. K. Day, and H. G. Leduc, “A semiempirical model for two-level system noise in superconducting microresonators,” *Applied Physics Letters* **92** (2008), no. 21, 212504.
- [75] K. Oto, S. Takaoka, K. Murase, and S. Ishida, “Superconductivity in ptsi ultrathin films,” *Journal of Applied Physics* **76** (1994), no. 9, 5339–5342.
- [76] K. Radermacher, D. Monroe, A. E. White, K. T. Short, and R. Jebasinski, “Quantum transport of buried single-crystalline *cosi2* layers in (111)si and (100)si substrates,” *Phys. Rev. B* **48** (1993), no. 11, 8002–8015.
- [77] M. C. Gaidis, *Superconducting Tunnel Junctions as Single Photon X-Ray Detector*. PhD thesis, Yale University, 1994.
- [78] D. L. Snyder, *Random Point Processes*. John Wiley and Sons, New York, 1975.
- [79] N. Chernov and C. Lesort, “Least squares fitting of circles,” *Journal of Mathematical Imaging and Vision* **23** (2005), no. 3, 239–252.